Université Libre de Bruxelles

Ecole Polytechnique de Bruxelles

Formation doctorale en Sciences de l'ingénieur et technologie

Université de Liège

Faculté des Sciences Appliquées

Collège de doctorat en Électricité, électronique et informatique

Energy-Based Magnetic Hysteresis Models

- Theoretical Development and Finite Element Formulations -

Doctoral Dissertation presented by

Kevin JACQUES

in fullfilment of the requirements for the degree of
Docteur en Sciences de l'Ingénieur

November 2018

Thesis committee:

Prof. Christophe GEUZAINE (Université de Liège), Advisor
Prof. Johan GYSELINCK (Université Libre de Buxelles), Advisor
Dr. Zacharie DE GREVE (Université de Mons)
Prof. François HENROTTE (Université Catholique de Louvain - Université de Liège)
Prof. Artem NAPOV (Université Libre de Buxelles)
Prof. Afef KEDOUS LEBOUC (CNRS, G2Elab - Université Grenoble Alpes)
Prof. Paavo RASILO (Tampere University of Technology)
Prof. Benoît VANDERHEYDEN (Université de Liège), President

Author contact information:

Kevin Jacques

BEAMS - Bio Electro and Mechanical Systems,
Dept. of Engineering,
Université Libre de Bruxelles

Campus du Solbosch, Bâtiment L,
Av. F. Roosevelt 50,
1050 Brussels, Belgium

Email: Kevin.Jacques@ulb.ac.be

ACE - Applied and Computational Electromagnetics,
Dept. of Electrical Engineering and Computer Science,
University of Liège

Montefiore Institute B28,
Quartier Polytech 1,
Allée de la Découverte 10,
4000 Liège, Belgium

Email: Kevin.Jacques@uliege.be

Funding:

This work was supported in part by the Belgian Science Policy under grant IAP P7/02 and the Walloon Region of Belgium under grant RW-1217703 (WBGreen FEDO).
Computational resources have been provided by the Consortium des Équipements de Calcul Intensif (CÉCI), funded by the Fonds de la Recherche Scientifique de Belgique (F.R.S.-FNRS) under Grant No. 2.5020.11.

This version was generated on November 23, 2018

Abstract

This work focuses on the development of a highly accurate energy-based hysteresis model for the modeling of magnetic hysteresis phenomena. The model relies on an explicit representation of the magnetic pinning effect as a dry friction-like force acting on the magnetic polarization. Unlike Preisach and Jiles-Atherton models, this model is vectorial from the beginning and derives from thermodynamic first principles.

Three approaches are considered: the first one, called vector play model, relies on a simplification that allows an explicit, and thus fast, update rule, while the two others, called the variational and the differential approaches, avoid this simplification, but require a non-linear equation to be solved iteratively. The vector play model and the variational approach were already used by other researchers, whereas the differential approach introduced in this thesis, is a new, more efficient, exact implementation, which combines the efficiency of the vector play model with the accuracy of the variational approach. The three hysteresis implementations lead to the same result for purely unidirectional or rotational excitation cases, and give a rather good approximation in all situations in-between, at least in isotropic material conditions.

These hysteresis modeling approaches are incorporated into a finite-element code as a local constitutive relation with memory effect. The inclusion is investigated in detail for two complementary finite-element formulations, magnetic field **h** or flux density **b** conforming, the latter requiring the inversion of the vector hysteresis model, naturally driven by **h**, for which the Newton-Raphson method is used. Then, at the finite-element level, once again, the Newton-Raphson technique is adopted to solve the nonlinear finite-element equations, leading to the emergence of discontinuous differential reluctivity and permeability tensors, requiring a relaxation technique in the Newton-Raphson scheme. To the best of the author's knowledge, the inclusion of an energy-based hysteresis model has never been successfully achieved in a **b**-conform finite-element formulation before.

Résumé

Ce travail se concentre sur le développement d'un modèle d'hystérésis précis basé sur l'énergie pour la modélisation du phénomène d'hystérésis magnétique. Ce modèle repose sur une représentation de l'effet d'ancrage (pinning) comme une force de friction agissant sur la polarisation magnétique. Contrairement aux modèles de Preisach et de Jiles-Atherton, ce modèle est vectoriel dés le début et dérive des premiers principes de la thermodynamique.

Trois approches sont considérées: la première, qui se rapproche d'un modèle de type "vector-play", repose sur une simplification qui permet de dégager une loi de mise à jour explicite, et donc rapide, alors que les deux autres, appelées approche variationelle et approche différentielle, évitent cette simplification mais nécessitent la résolution d'une équation non-linéaire par un processus itératif. Le modèle "vector-play" et l'approche variationelle ont déjà été utilisés par d'autres chercheurs, alors que l'approche différentielle introduite dans cette thèse, est une nouvelle implémentation exacte, plus efficace, qui combine l'efficacité du modèle "vector-play" avec la précision de l'approche variationelle. Les trois implémentations d'hystérésis mènent au même résultat pour des cas d'excitation purement unidirectionel ou rotationel, et donnent une assez bonne approximation dans toutes les situations intermédiaires, du moins dans les conditions où le matériau est isotrope.

Ces approches de modélisation de l'hystérésis sont incorporées dans un code d'éléments finis comme une relation constitutive locale avec effet de mémoire. L'inclusion fait l'objet d'un examen détaillé dans deux formulations complémentaires d'éléments finis, conformes en champ magnétique **h** ou en densité de flux **b**, cette dernière nécessitant l'inversion du modèle d'hystérésis vectorial, naturellement piloté par **h**, pour laquelle la méthode de Newton-Raphson est utilisée. Ensuite, au niveau éléments finis, une nouvelle fois, la technique de Newton-Raphson est adoptée pour résoudre les équations non-linéaires des éléments-finis, conduisant à l'émergence de tenseurs discontinus de réluctivité et perméabilité différentielles, qui nécessitent une technique de relaxation dans le schéma de Newton-Raphson. A la connaissance de l'auteur, l'inclusion d'un modèle d'hystérésis basé sur l'énergie n'a jamais été réalisée avec succès dans une formulation éléments finis conforme en **b** auparavant.

Remerciements

Je tiens à remercier mes promoteurs Christophe Geuzaine et Johan Gyselinck de m'avoir fait confiance et donné l'opportunité de mener ce travail avec une grande liberté, dans d'excellentes conditions, au sein des équipes de recherche ACE de l'Université de Liège et BEAMS de l'Université de Bruxelles. Je vous suis reconnaissant de m'avoir fait découvrir le monde de la recherche scientifique, chacun avec votre vision personnelle, et de m'avoir guidé par vos conseils et votre soutien. Cela a été un plaisir de travailler avec vous durant ces cinq années. Christophe, je suis particulièrement admiratif de ton inébranlable optimisme et ta passion communicative pour ton travail qui ont été des sources de motivation et d'avancement continuels. Johan, je te remercie d'avoir partagé ton expertise technique et ta rigueur scientifique, et j'ai apprécié la disponibilité et l'implication dont tu as fait preuve pour contribuer à l'amélioration de mes productions scientifiques.

Je remercie également les membres de mon comité de thèse, Christophe Geuzaine, Johan Gyselinck, Zacharie De Greve, François Henrotte, Artem Napov, Afef Kedous Lebouc, Paavo Rasilo et Benoît VanderHeyden, pour leur participation, l'intérêt porté sur mon travail et leurs conseils prodigués pour la révision du présent manuscrit. Plus particulièrement, je tiens à remercier François Henrotte avec qui j'ai eu la chance de collaborer plus étroitement et d'échanger de nombreuses idées lors de discussions techniques ou philosophiques. J'ai ainsi pu compter sur ton expérience pour démarrer et poursuivre ma recherche dans la continuité de tes travaux précédents sur l'hystérésis.

Je souhaite aussi remercier toutes les personnes avec qui j'ai eu la chance de cosigner des articles scientifiques. Plus spécifiquement, je pense ici à Patrick Dular et Ruth V. Sabariego qui m'ont donné leur précieuse aide pour le développement de modèles sur les supports Gmsh et GetDP. J'ai beaucoup appris de leur savoir et de leurs conseils. Dans cette continuité, je remercie également Innocent Niyonzima, avec qui j'ai partagé mon bureau au début de ma thèse; Christophe Guérin, pour nos enrichissants échanges de point de vue; et Simon Steentjes, pour son suivi par correspondance et ses données expérimentales fournies. Je remercie aussi sincèrement Laurent Stainier de m'avoir accueilli à l'École centrale de Nantes, pour ses idées et suggestions intéressantes, issues de sa longue expérience dans la résolution de systèmes non-linéaires et qui m'ont été profitables dans mon travail.

En outre, je tiens à souligner l'excellente atmosphère de travail qui a régné au sein du groupe ACE depuis le départ et à remercier chaleureusement tous les collègues actuels et anciens que j'ai eu l'opportunité de côtoyer, à savoir Anthony Royer, Alexandre Halbach, Alexandre Vion, Amaury Johnen, Ariel Lozano, Axel Modave, Christophe Geuzaine, David Colignon, Erin Kuci, Fabrice Frebel, François Henrotte, Frédéric Olivier, Frédéric Plumier, Innocent Niyonzima, Isabel Molenberg, Jean-Fernand Arban, Jean de Dieu Nshimiyimana, Jonathan Velasco, Maryse Ledent, Maxime Graulich, Maxime Spirlet, Nicolas Marsic, Patrick Dular, Pierre Beerten, Ruth V. Sabariego, Simon Tournier, Sophie Cimino, Steven Roman, Valera Biangani, Vanessa Mattesi, Véronique Beauvois, Vincent Nivoliers et Yannick Paquay.

Par ailleurs, je remercie la Région wallonne de Belgique pour la subvention RW1217703 associée au projet WBGreen FEDO, la Politique scientifique fédérale belge (BELSPO) dans le cadre de la subvention PAI/IAP P7/02 et la subvention du partenariat d'innovation technologique TRACTION 2020, qui ont toutes soutenu, en partie, le développement de cette thèse. Je tiens également à remercier le Consortium des Équipements de Calcul Intensif (CÉCI), pour la mise à disposition des clusters informatiques que j'ai eu la chance d'utiliser.

Je souhaite également adresser une pensée à toutes les personnes qui m'ont entouré et soutenu à un moment où un autre au cours de cette aventure. Merci à mes amis, ma belle-famille et ma famille pour tous les bons moments passés ensemble. Je remercie du fond du coeur mes parents qui ont toujours cru en moi et sur qui j'ai pu compter en toutes circonstances. Merci pour vos encouragements, votre soutien, et votre compréhension, y compris dans les moments ou j'avais besoin de m'isoler pour me concentrer sur mon travail. J'espère être à la hauteur de vos sacrifices et vous rendre fiers. Enfin, je remercie ma compagne Stéphanie qui a partagé mon quotidien et a su me pousser à avancer toujours plus loin. Merci pour ton amour et ta patience. J'ai de la chance de t'avoir rencontré et me réjouis de savoir ce que nous réserve la suite. A tes côtés, tout me paraît surmontable et le champ des possibles s'élargit.

Kevin Jacques,
Novembre 2018.

Contents

List of Figures

List of Tables

List of Symbols

Alphanumeric symbols

$\mathbf{a}$	Magnetic vector potential (Wb/m)
$\mathbf{b}$	Magnetic flux density (T)
$\mathbf{d}$	Electric flux density (C/m^2)
$\mathbf{e}$	Electric field (V/m)
$\mathbb{E}^3$	Three-dimensional oriented Euclidean space
$\mathbf{h}$	Magnetic field (A/m)
$\mathbf{j}$	Current density (A/m^2)
$\mathbf{J}$	Magnetic polarization (T)
$\mathbf{m}$	Magnetization (A/m)
n	Time step
$\mathbf{p}$	Electric polarization (C/m^2)
q	Electric charge density (C/m^3)
t	Time instant
v	Electric scalar potential (V)
$\mathbf{x} = (x, y, z)$	Point of $\mathbb{E}^3$

Greek symbols

Ω	Bounded open set of $\mathbb{E}^3$
Γ	Boundary of Ω ($= \partial\Gamma$)
ϕ	Magnetic scalar potential (A)
σ	Electric conductivity (S/m)
μ	Magnetic permeability (H/m)
μ_0	Magnetic permeability of vacuum ($= 4\pi \times 10^{-7}$ H/m)
μ_r	Relative magnetic permeability ($= \mu/\mu_0$)
χ	Magnetic susceptibility
χ_r	Relative magnetic susceptibility ($= \chi/\mu_0$)
ϵ	Electric permittivity (F/m)
ϵ_0	Electric permittivity of vacuum ($\simeq 8.854187817\ 10^{-12}$F/m)
ϵ_r	Relative electric permittivity ($= \epsilon/\epsilon_0$)

Abbreviations

1D	One-dimensional , 4, 42, 47, 153, 195
2D	Two-dimensional , 4, 47, 93, 153, 196
3D	Three-dimensional , 42, 47, 92, 193, 198
accelerated	Accelerated search technique , 159
anhy	Anhysteretic law , 172
BFGS	Broyden–Fletcher–Goldfarb–Shanno , 96
brent	Brent , 53
cg	Conjugate gradient , 52
CPU	Central processing unit , 6, 60, 98, 160, 198
DC	Direct current , 26, 178
DFP	Davidon-Fletcher-Powell Formula , 95

diff	Differential approach , 5, 59, 71, 113, 159, 195
dir	Direct form , 5, 177, 196
DOF	Degree of freedom , 121, 158
EB	Energy-based , 3, 37, 47, 71, 109, 131, 153, 195
FE	Finite element , 2, 71, 109, 140, 153, 195
GO	Grain-oriented , 23
GoodBFGS	Good Broyden–Fletcher–Goldfarb–Shanno algorithm , 96, 159
GSE	Generalized Steinmetz equation , 26
heavy	Heavy search technique , 159
iGSE	Improved generalized Steinmetz equation , 26
inv	Inverse form , 5, 177, 196
JA	Jiles-Atherton , 146, 187, 196
JAC_{ana}	Jacobian matrix evaluated analytically , 159
JAC_{num}	Jacobian matrix evaluated numerically by finite differences , 159
MSE	Modified Steinmetz equation , 26
MSF	Mesh scale factor , 176
naive	Naive , 53
NGO	Non-grain-oriented , 23, 133, 197
NSE	Natural Steinmetz extension , 26
NR	Newton-Raphson , 5, 72, 113, 152, 158, 195
NR_{ana}	Newton-Raphson with Jacobian matrix evaluated analytically , 73, 159
NR_{num}	Newton-Raphson with Jacobian matrix evaluated numerically , 92, 159
sd	Steepest descent , 52
SE	Steinmetz equation , 25
SST	Single sheet tester , 131
standard	Standard search technique , 159
RD	Rolling direction , 23, 133, 187, 197
RMS	Root mean square , 178

RMSD	Root mean square deviation , 147
RMSDN	Root mean square deviation norm , 60, 97
$RMSD_r$	Relative root mean square deviation , 147
TD	Transverse direction , 23, 133, 187, 197
TEAM	Test electromagnetic analysis methods , 145, 153
ts	Time step , 60, 97
var	Variational approach , 5, 52, 71, 113, 159, 195
vpm	Vector Play Model , 4, 50, 71, 113, 154, 195
wolfe	Wolfe , 53

Operators

∂	Boundary operator
^{C}	Complement
$\partial_x, \partial_y, \partial_z$	Space derivatives
∂_t	Time derivative
curl	Curl
div	Divergence
grad	Gradient
$\cdot$	Scalar product
$\times$	Vector product

Introduction

Context and Motivations

Magnetic materials are central components in the design of electromagnetic energy conversion applications, where they allow the establishment and circulation of magnetic fields, which is essential for electric motors, generators, transformers, actuators, sensors, etc. The properties of the magnetic materials have thus a significant impact on the operating characteristics, current, torque, response time, power density, and efficiency of all these electromagnetic energy converters.

In particular, electrical machines are exploited in almost all industrial sectors, where they account for about 60% of the electrical energy consumed [73], and are widely present in domestic applications. They are also a crucial technology for conversion of renewable energy, such as wind turbines, and are increasingly present in the world of transport, where hybrid cars and buses, trains, trams and planes integrate a growing number of electric drives and actuators [93, 163]. Functional magnetic materials are used under different forms in electrical machine applications, from soft ferromagnetic cores, which are generally laminated or powdered in order to reduce eddy current losses, to hard permanent magnets, where their ability to resist demagnetization in operating conditions is then fundamental. Magnetic materials are also extremely important in electronic energy conversion systems such as high-frequency switched-mode power supplies and inverters, where they condition the efficiency of the passive magnetic components (transformers and inductors) in power electronic circuits [89]. Ferrites are widely used in such applications in order to limit magnetic losses at these high frequencies.

The manufacturers of electromagnetic energy converters are facing new conceptual, economic and ecological challenges for the 21st century, where the need for stronger, lighter and more energy efficient devices is ever growing [93]. In particular, there is the important issue of the minimization of the weight to power ratio in the design of electrical drives for new developments in transportation technologies. For efficient designs, it is important to accurately evaluate losses, either by experimental measure-

ment or by numerical simulation, as thermal aspects are eventually the dimensioning factor. Beside the environmentally questionable use of rare-earth materials to manufacture permanent magnets, ecological awareness has also led to increasing environmental legislation with strict directives demanding better energy efficiency of equipment. These guidelines place manufacturers under the obligation to reconsider all their product ranges from the point of view of efficiency and to review their design methodologies to integrate this new dimension. Due to the ubiquity of magnetic materials, even a small improvement in the efficiency of the energy converter devices can result in a massive reduction of the global electrical energy consumption, with large economical and environmental savings.

Size and weight reductions can be realized for a given output power by operating at higher frequencies, which is made possible by recent advances in power electronics. As both magnetic losses (iron losses) and Joule losses in conductors (copper losses) increase with frequency, estimating these losses is paramount for the design of modern compact conversion devices. While in many applications iron losses are predominant compared to copper losses, the former are much more difficult to estimate given the complexity of the behavior of magnetic materials, due to the hysteresis phenomenon combined with the high harmonic content induced by electronic supply systems.

Traditional methods of designing electrical energy conversion devices combine semi-empirical rules with often simplistic modeling assumptions allowing a decoupling between the different phenomena and the different scales involved, in order to treat separately different aspects of the problem. Therefore, the real response of the magnetic materials, their hysteretic nature and temperature dependence, as well as their complex geometric structuring (e.g. with laminations), are not taken into account, and the losses themselves are only assessed a posteriori. This pragmatic approach is dissociated, quick and easy to implement, but is essential in the preliminary design phase. However, its limited accuracy is insufficient to enable a truly effective optimization of the energy consumption of electrical machines. Such optimization requires the use of modern numerical simulation tools. Techniques based on the finite element (*FE*) method, initially developed in the field of solid mechanics, have proven their worth for the simulation of electrical machines. However, at the level of magnetic losses, laminated magnetic cores are usually modeled as non-conductive and homogeneous materials, with a single non-linear and non-hysteretic constitutive law, linking the flux density $\mathbf{b}$ and the magnetic field $\mathbf{h}$. The losses are then calculated through a post-processing formula of the solution [24].

Having design tools that offer rigorous and precise loss calculation functionalities with accurate signal predictions is thus a glaring demand that is still far from being sufficiently covered.

The modeling of iron losses with a complete description of the magnetic material behavior is however a very difficult problem. The iron loss phenomena is the result of complex microscopic mechanisms, related to the microstructure of the magnetic material, summarized by Fig. 0.1, that manifest themselves at the macroscale through several interdependent physical phenomena, like eddy currents, skin effect, saturation

and, crucially, hysteresis.

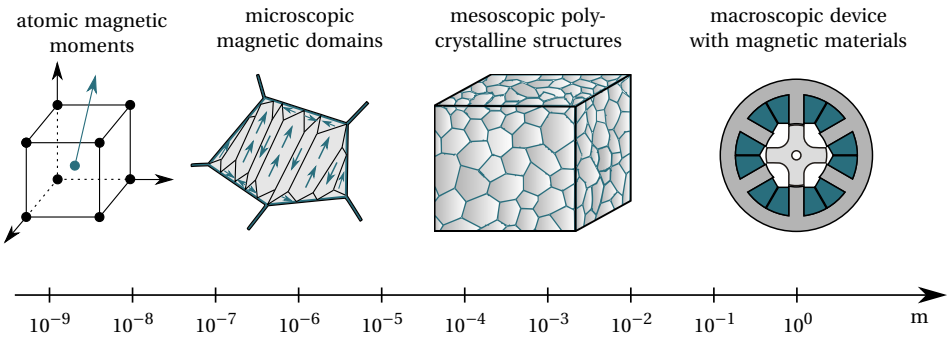

Figure 0.1: *Different spatial scales involved in the magnetic properties, adapted from [48].*

In this context, it is needed to include a hysteresis model within the simulation tools in order to represent more accurately the magnetization curves, and eventually the estimation of iron losses. Hysteresis phenomenon may indeed have a strong influence on current, torque and naturally iron losses in the results of time stepping simulations of electromechanical devices.

Presently, the most widely used hysteresis models are usually the Preisach [176, 157] or the Jiles-Atherton models [125]. The Preisach model describes, probably, the most accurately the shape of hysteresis loops but is only based on a mathematical formalism with no direct interpretation in terms of energy and requires a large collection of experimental data. The Jiles-Atherton model is much easier to implement but can sometimes provide unphysical behavior which prompted many ad-hoc modifications [41, 123, 160, 9, 140], while the physical assumptions underlying its derivation are still questionable [217]. Furthermore, both models are natively scalar and their various vector extensions lack real physical background. However, for the study of coupled phenomena and in the evaluation of losses or forces in electric machines, it is relevant that the hysteresis model remains coherent with thermodynamic principles for a straightforward energy balance validation.

Bergqvist introduced in [17] a new quasi-static magnetic hysteresis model, intrinsically vectorial, built on consistent thermodynamic principles, and inspired by dry-friction like mechanisms in visco-plasticity to represent the pinning effect of magnetic domain walls. The so-called energy-based (*EB*) hysteresis model [103] offers the possibility to calculate directly the stored and dissipated energy at any time, not only after the closure of minor hysteresis loops, as it is usually the case. It combines the simplicity of the Jiles-Atherton model with the Preisach model point of view, where the magnetization curve is constructed as a superposition of several pseudoparticle contributions, whose number can be adequately chosen to reach a given level of accuracy.

The Bergqvist model along with the derived *EB* hysteresis models [103], have been fur-

ther studied in several works, developing simple parameter identification strategies [15, 132, 104], correlating model parameters with microstructural features of electrical steels [120], dealing with anisotropy [198] and temperature influences [14, 196], extending to a dynamical model [102, 197] or proposing slight modifications for the improvement of core loss computation and including in *FE* simulations [145].

Originally, Bergqvist simplified the non-linear differential equation deduced from the energy balance of the magnetic material to arrive at an explicit magnetization update rule, transforming the *EB* model into a Vector Play Model (*vpm*). This simplification is employed in almost all following works. However, there is not yet much discussion in the literature on the different implementation aspects of the *EB* hysteresis model, and a quantitative comparison between them in terms of accuracy and computational cost within a practical *FE* environment is still missing. Moreover, the inclusion of the model as a constitutive relation in *FE* simulations remains also challenging due to strong nonlinearities and potential inconsistencies between the input vector variable of the model, which is natively driven by the magnetic field $\mathbf{h}$, and the basic variable of the *FE* formulation, which may be expressed in terms of the flux density vector $\mathbf{b}$.

Dissertation goals

The global objective of the research is to contribute to the efficient modeling of magnetic losses in complex electromagnetic energy conversion devices. More precisely, the thesis aims at developing advanced methods for the accurate prediction of vector hysteresis behavior observed in ferromagnetic materials of electrical machines, by coupling the *EB* hysteresis model with *FE* magnetostatic and magnetodynamic field analyses.

The first goal of the research project is to implement and verify the hysteresis model behavior at material level, by taking care of the stability and efficiency of the different implementations investigated. The second goal is to generalize and implement the *EB* model within an open source Gmsh/GetDP *FE* code [56, 85], in magnetostatic and magnetodynamic formulations, first in one-dimensional (*1D*), then in two-dimensional (*2D*) situations. A third goal is to propose an easy and automatic identification strategy for the *EB* model parameters, based only on standard experimental measurements on material samples. The final goal consists in validating the implementation and the identification of the vector *EB* hysteresis model by comparing the simulation results with measurement data for a practical transformer application, with harmonic or rotating fields excitations. The classical Jiles-Atherton hysteresis model is also inspected in this context to illustrate the advantages of the *EB* model over the latter.

As key information on the performance of the proposed modeling strategy, the accuracy, robustness, and speed of each numerical implementation is carefully analyzed throughout the work.

Dissertation outline

This dissertation is divided into seven chapters.

Chapter 1 starts with a review of the physical concepts underlying the magnetic hysteresis phenomenon. The physics of ferromagnetic materials are first briefly reviewed. The chapter continues with a literature overview of simple iron loss models used in electrical machines and then with a presentation of existing hysteresis models, based on different empirical, phenomenological, or physical types of modeling that can be included in *FE* simulations.

In Chapter 2, the derivation of the energy-based hysteresis model from thermodynamics is given. The model decomposes the magnetic field into a sum of two components: a reversible part and an irreversible one related to magnetic losses in the material. The presence of defects introduces potential wells in the free energy responsible for hysteresis phenomenon. A pseudo-potential of dissipation can then be defined, which in combination with the potential energy leads to an energetically consistent formulation to define the behavior of ferromagnetic material. The model is then improved by considering an infinite number of pseudo-particles and different homogenization strategies are discussed.

Then, after discretization in a finite number of pseudo-particles, three direct numerical implementations of the model are detailed in Chapter 3. The first one is the *vpm* approximation originally proposed by Bergqvist [17]. The second one corresponds to the variational approach (*var*), initially proposed in [79] and further developed in personal works [116, 113], where there is no simplification employed. The third approach is a new update rule, called differential approach (*diff*) which avoids the *vpm* approximation for solving the non-linear implicit differential equation governing the hysteresis magnetization. The three approaches are extensively compared with various types of magnetic field excitation sources, from unidirectional to purely rotational cases.

In Chapter 4, the direct form (*dir*) of the three approaches, all driven by the magnetic field $\mathbf{h}$, are inversed by means of specifically adapted and approximated Newton-Raphson (*NR*) techniques in order to have access to the corresponding inverse form (*inv*), driven by the induction field $\mathbf{b}$. The different investigated inversion techniques are thoroughly compared on their stability and computation efficiency.

Chapter 5 deals with the inclusion of the three different model approaches as constitutive relations in complementary $\mathbf{b}$-conform or $\mathbf{h}$-conform, magnetodynamic or magnetostatic *FE* formulations, the hysteresis model being used either under their *inv* or *dir* forms respectively. Some strategies to improve the nonlinear resolution of the systems at the *FE* level are suggested.

Chapter 6 proposes a systematic procedure for identifying the parameters of the ferromagnetic *EB* hysteresis model. The identification process also makes it possible to give insight into the microscopic nature of the materials. The technique is validated with experimental measurements.

Chapter 7 concerns the application of the *FE* formulations coupled with the *EB* hysteresis model for different time stepped simulations. By way of illustration, it starts with a simple *1D FE* time stepping modeling of a lamination sheet [104], presenting already all the main complexity encountered in the iron losses modeling, combining eddy currents, skin effect and hysteresis influences. Then, subsequent more complex *FE* models are simulated. A simple academic square model with a **b**-conform *FE* formulation allows to examine the behavior of the inverse *EB* model in a simple *FE* context. A T-joint model is then used to expose the complementarity of the two dual *FE* formulations with rotating hysteresis. The chapter considers then a more practical application with the *2D FE* simulations of a three-phase transformer core, analyzing the two complementary **b**-conform and **h**-conform *FE* formulations, including the hysteresis model. The accuracy between the different implementations, regarding also the influence of the mesh density, is highlighted as well as the central processing unit (*CPU*) times that are observed and put in perspective with the *CPU* times obtained with the anhysteretic constitutive law. Finally, a reference test case from the scientific community, specially built to study vector hysteresis models, is examined. It allows to validate with available measurement data the results of the *FE* simulations with the *EB* hysteresis model. Furthermore, this test case is also used to compare the *EB* hysteresis model with the classical Jiles-Atherton model.

Original contributions

Hereafter is a list of contributions that are considered to be original:

1. The derivation in Chapter 2 of a new multi-scale representation of the pinning field distribution based on the homogenization of the magnetic field, instead of the homogenization of the energy balance, useful for parameter identification.

2. The elaboration of the new *diff* approach for the energy-based hysteresis model, driven by the magnetic field, and its detailed comparison with the two other approaches (*vpm* and *var*) on a large set of illustrative examples in Chapter 3.

3. The inversion of the energy-based hysteresis model in order to drive it with the flux density as input, thanks to the use of relaxed or approximated Newton-Raphson methods, with a detailed study on the efficiency of the different inversion techniques applied on a representative range of several magnetization change situations in Chapter 4.

4. The inclusion of the energy-based hysteresis model in complementary finite-element formulations (magnetic field or flux density conforming), requiring either the direct or the inverse model forms respectively, for magnetostatic and magnetodynamic analyses, with general improvements in the resolution of nonlinear systems associated to the finite-element method in Chapter 5.

5. The automatization and validation of a procedure for the parameter identification of the energy-based hysteresis model, based on standard material measurements in Chapter 6.

6. The application of the aforementioned various implementations of the energy-based hysteresis model in a finite-element context, for the simulations of several one-dimensional or two-dimensional finite-element models, from academic towards further realistic examples of increasing geometric complexity, with a permanent comparing study between the different implementation possibilities, at the hysteresis model level, at the inversion technique level, or at the finite-element formulation level, with validation on available experimental measurement data for the final practical transformer application in Chapter 7.

All the models and finite element formulations have been implemented in the open source Gmsh/GetDP *FE* code [56, 85]. Full models ready for testing are available online on the website of the ONELAB project.

The main original contributions of this thesis have been presented in the following peer-reviewed journals and conference proceedings.

Journals or Proceedings

- K. Jacques, R. V. Sabariego, C. Geuzaine, and J. Gyselinck. "Inclusion of a Direct and Inverse Energy-Consistent Hysteresis Model in Dual Magnetostatic Finite-Element Formulations". In: *IEEE Transactions on Magnetics* 52.3 (Mar. 2016), pp. 1–4
- K. Jacques, C. Geuzaine, F. Henrotte, and J. Gyselinck. "Comparison between differential and variational forms of an energy-based hysteresis model". In: *IEEE International Energy Conference (ENERGYCON)*. Belgium, Apr. 2016, pp. 1–6
- C. Guérin, K. Jacques, R. V. Sabariego, P. Dular, C. Geuzaine, and J. Gyselinck. "Using a Jiles-Atherton vector hysteresis model for isotropic magnetic materials with the finite element method, Newton-Raphson method, and relaxation procedure". In: *International Journal of Numerical Modelling: Electronic Networks, Devices and Fields* 30.5 (2017), e2189
- K. Jacques, S. Steentjes, F. Henrotte, C. Geuzaine, and K. Hameyer. "Representation of microstructural features and magnetic anisotropy of electrical steels in an energy-based vector hysteresis model". In: *AIP Advances* 8.4 (2018), p. 047602
- I. Niyonzima, R. Sabariego, P. Dular, K. Jacques, and C. Geuzaine. "Multiscale Finite Element Modeling of Nonlinear Magnetoquasistatic Problems using Magnetic Induction Conforming Formulations". In: *Multiscale Modeling & Simulation* 16.1 (2018), pp. 300–326

Conferences

- K. Jacques, R. V. Sabariego, C. Geuzaine, and J. Gyselinck. "Inclusion of a Direct and Inverse Energy-Consistent Hysteresis Model in Dual Magnetostatic Finite-Element Formulations". In: *20th International Conference on the Computation of Electromagnetic Fields (COMPUMAG)*. Montréal, Canada, July 2015

- S. Steentjes, F. Henrotte, K. Jacques, and K. Hameyer. “Energy-Based Ferromagnetic Material Model with Magnetic Anisotropy and Magnetostriction”. In: *Conf. Proc. 1st IEEE Conference Advances in Magnetics (AIM)*. Bormio, Italy, Mar. 2016
- K. Jacques, C. Geuzaine, F. Henrotte, and J. Gyselinck. “Comparison between differential and variational forms of an energy-based hysteresis model”. In: *IEEE International Energy Conference (ENERGYCON)*. Leuven, Belgium, Apr. 2016
- K. Jacques, C. Geuzaine, and J. Gyselinck. “Using an Energy-Based Hysteresis Model in Magnetodynamic Finite Element Simulations of a Three-Phase Transformer”. In: *10th International Symposium on Electric and Magnetic Fields (EMF)*. Lyon, France, Apr. 2016
- K. Jacques, P. Dular, C. Geuzaine, and J. Gyselinck. “Dual Magnetodynamic Finite Element Formulations with Inclusion of an Energy-Based Hysteresis Model”. In: *17th Biennal Conference on Electromagnetic Field Computations (CEFC)*. Miami, FL, United States, Nov. 2016
- K. Jacques, F. Henrotte, J. Gyselinck, R. V. Sabariego, and C. Geuzaine. “Comparison between The Energy-Based Hysteresis Model and The Jiles-Atherton Model in Finite Element Simulations”. In: *The 18th International Symposium on Applied Electromagnetics and Mechanics (ISEM)*. Chamonix, Mont-Blanc, France, Sept. 2017
- K. Jacques, F. Henrotte, C. Geuzaine, and J. Gyselinck. “Improved Energy-Based Hysteresis Model and Parameter Identification for Magnetic Hysteresis Materials”. In: *The 11th International Symposium on Electric and Magnetic Fields (EMF)*. Darmstadt, Germany, Apr. 2018

CHAPTER

1 Magnetic Losses Modelling - State of the Art -

THE purpose of this chapter is to give an overview of some general aspects of the theory of magnetism, introducing units, terms and quantities that are used throughout this thesis. The physics of ferromagnetic materials and the mechanism behind the hysteresis effect are recalled in order to understand the nature of the underlying approximations that must be made to build practical models which will be presented afterwards.

1. Physical Origins of Magnetism

1.1. Review of Definitions and Notations

The study of magnetic phenomena relies on the definition of two related vector field quantities: the magnetic flux density (or magnetic induction) **b**, and the magnetic field **h**. Vectors are depicted in bold characters in this thesis. The fields **b** and **h** differ in how they account for magnetization. The former is an extensive material property, which means that its magnitude is proportional to the size of the system it describes. On the other hand, the latter is an intensive property, because its value does not depend on the amount of the substance for which it is measured.

In vacuum, **b** and **h** translate the same property, aside from units, such that it is natural to establish a proportionality relationship between them

$$\mathbf{b} = \mu_0 \mathbf{h}, \tag{1.1}$$

where μ_0 is called the permeability of vacuum. In this thesis, the International System of Units is selected such that **b** and **h** are expressed in tesla (T) and ampere per meter (A/m) respectively, which determines the proportionality constant $\mu_0 = 4\pi \times 10^{-7}$ H/m.

Magnetic fields arise from electric currents, but more fundamentally from the movement of electric charges.

1

Subjected to a magnetic field, certain substances start to produce themselves, in the volume they occupy and in their surrounding, a magnetic induction. It is said that the substance magnetizes or magnetically polarizes itself. This is a general property of matter that manifests itself more notably for certain materials called magnetic materials.

The spin of electrons and, to a small extent, their orbital motion around the nucleus are responsible for this phenomenon, the very essence of which can only be studied by quantum physics. However, from the engineer's point of view, the detailed behavior of electrons in the magnetization process is more usefully described by the concept of atomic magnetic moment than by that of wave function from quantum theory. The magnetic moment $\mathbf{m}_0$ is a quantity that represents the magnetic strength and orientation of an elementary entity that produces a magnetic field, such as electrons. The unit of magnetic moment is ampere meter squared ($\mathrm{A\,m^2}$).

In matter, the magnetic induction can be expressed by the equation

$$\mathbf{b} = \mu_0 \mathbf{h} + \mu_0 \mathbf{m}. \tag{1.2}$$

This equation defines the magnetization vector field $\mathbf{m}$ which is a measure of the net magnetic moment per unit volume of matter. In particular, if a given elementary volume ΔV of a medium consists of a collection of elementary magnetic moments $\mathbf{m}_0$, the definition of the magnetization $\mathbf{m}$ is

$$\mathbf{m} = \frac{\sum \mathbf{m}_0}{\Delta V}, \tag{1.3}$$

where the sum runs over all the moments contained in ΔV. The unit of $\mathbf{m}$ is ampere per meter (A/m).

The magnetic induction in matter can also be expressed by the equation

$$\mathbf{b} = \mu_0 \mathbf{h} + \mathbf{J}. \tag{1.4}$$

This equation defines this time the magnetic polarization vector $\mathbf{J}$, whose unit is tesla (T). The vector fields $\mathbf{J}$ and $\mathbf{m}$ report the same phenomenon and are related by

$$\mathbf{J} = \mu_0 \mathbf{m}. \tag{1.5}$$

In this thesis, the quantity $\mathbf{J}$ will be usually preferred to $\mathbf{m}$, as is customary in the study of ferromagnetism.

Given the general relationships (1.2) and (1.4) connecting $\mathbf{b}$, $\mathbf{h}$, $\mathbf{m}$ and $\mathbf{J}$, the magnetic properties of a medium are defined once a functional dependence $\mathbf{b}(\mathbf{h})$, $\mathbf{m}(\mathbf{h})$ or $\mathbf{J}(\mathbf{h})$ is known. These are called the magnetic constitutive laws of the medium. In their simple expression, they write

$$\mathbf{b} = \mu \mathbf{h}, \qquad \mathbf{m} = \chi_r \mathbf{h}, \qquad \mathbf{J} = \chi \mathbf{h}, \tag{1.6, 1.7, 1.8}$$

where μ, χ_r and χ are the magnetic permeability, the relative and the absolute magnetic susceptibilities of the medium, respectively. These are medium-specific properties which indicate the ability of a material to support a magnetic field and measure

how they respond to a magnetic excitation. The quantities μ, χ and χ_r are connected by the relations

$$\mu = \mu_0 + \chi = \mu_0 (1 + \chi_r) = \mu_0 \mu_r \,. \tag{1.9}$$

The values μ and χ are expressed in henry per meter (H/m), while χ_r is a dimensionless parameter. The relative magnetic permeability, denoted by μ_r, is the dimensionless analogue of μ. It can be shown that in order to ensure thermodynamic stability, the inequalities $\mu \geq 0$ and $\chi_r \geq -1$ must be satisfied.

It is assumed in (1.6)-(1.8) that **b**, **h**, **m** and **J** are co-linear. It is under this condition, verified by definition in isotropic materials, at least on a macroscopic scale, that susceptibility is a scalar quantity. In anisotropic materials, for which the properties may vary with field direction, susceptibility and permeability are characterized by second rank tensors, $\underline{\boldsymbol{\mu}}$, $\underline{\boldsymbol{\mu_r}}$, $\underline{\boldsymbol{\chi}}$ and $\underline{\boldsymbol{\chi_r}}$. Tensors are highlighted in bold underlined characters in this thesis. The generalization of (1.9) for anisotropic medium is then

$$\underline{\boldsymbol{\mu}} = \mu_0 \underline{\boldsymbol{I}} + \underline{\boldsymbol{\chi}} = \mu_0 \left(\underline{\boldsymbol{I}} + \underline{\boldsymbol{\chi_r}} \right) = \mu_0 \underline{\boldsymbol{\mu_r}} \,, \tag{1.10}$$

where $\underline{\boldsymbol{I}}$ is the identity tensor. In the following of this introductory chapter, susceptibility and permeability are, in many cases, viewed as scalar quantities, restricting the analysis to a single field direction of interest. All the vector fields $\mathbf{h}, \mathbf{b}, \mathbf{m}$ and $\mathbf{J}$ are then co-linear and it is reasonable to treat them also as scalar quantities, h, b, m and J.

The laws given by (1.6)-(1.8) have the advantage of simplicity but are clearly not adapted to describe more advanced magnetization processes. In general, the value of the material property χ, and thus of χ_r, μ and μ_r, is not constant and may depend on many factors such as the magnetic field and its history, but also, for example, on the temperature and the stress state of the sample [173]. In this thesis, thermal and mechanical influences are not investigated further. Nevertheless, this work aims to describe ferromagnetic systems with the non-linear magnetic dependence of the material properties that includes saturation and hysteresis effects. For that purpose, it is necessary to develop more complex laws that will be gradually introduced in the following.

1.2. Classes of Magnetic Materials

Materials are classified in different categories depending on how they respond under the influence of magnetism. This information is precisely indicated by their magnetic susceptibility which provides insights into the nature of their atomic structure.

Diamagnetism

Diamagnetic materials are characterized by a very weak magnetization that is opposed to the applied magnetic field, and therefore by a low negative χ_r value ($\mu_r < 1$), typically $\chi_r \approx -10^{-5}$.

Diamagnetism is due to an orbital movement of electrons, caused by the applied magnetic field. The classical explanation assimilates this movement to a microscopic current comparable to that of an induced current in a solenoid. Under Lenz's law, the

induced current opposes the field that produces it, such that the electron reacts by inducing a magnetic moment opposite to the applied field, which is consistent with the fact that χ_r is negative.

Diamagnetism is a phenomenon present in all atomic matter, but which can be masked by the more important effects of paramagnetism or ferromagnetism when these coexist in the material.

Paramagnetism

Paramagnetic materials are also characterized by a weak magnetization which is, on the other hand, in the direction of the magnetic field, which gives a low positive χ_r value ($\mu_r > 1$), typically $\chi_r \approx 10^{-6}$ to 10^{-3}.

A paramagnetic material can be described as a set of uncoupled magnetic moments. These moments exist due to the presence of atoms with unpaired electrons. Usually, each atomic orbital of an atom contains a maximum of two electrons with opposite spins, in accordance with the Pauli exclusion principle, so that their magnetic moments are in opposite directions and cancel out. However, an atomic orbital occupied solely by an unpaired electron presents an uncompensated permanent magnetic moment free to align in any direction. Under the action of a magnetic field, these moments tend to align in the same direction, reinforcing the field. Nevertheless, the resulting polarization remains very low, because the effect of thermal agitation, which randomly orients the magnetic moments, remains preponderant.

The small amplitudes encountered for the susceptibilities with diamagnetism and paramagnetism are of little interest in electrical engineering. In reality, their susceptibility can often be neglected such that $\mu_r \approx 1$, which amounts to considering that the medium behaves magnetically as vacuum.

Ferromagnetism

Ferromagnetic materials are bodies that have the ability to magnetize themselves under the effect of an external magnetic field and to keep this magnetization. The relationship between the magnetization and the magnetic field is no longer linear, such that the susceptibility is a function of the field $\chi_r(h)$, that can go through very high values, typically $\chi_r \approx 10^2$ to 10^6, before reaching a saturated regime at higher fields.

As in paramagnetic materials, ferromagnetism comes from the presence of atoms that carry a permanent magnetic moment. However these moments are no longer independent of each other but are, on the contrary, strongly linked. This mutual interaction, which is called ferromagnetic coupling, results in a parallel arrangement of moments. Therefore, ferromagnetic materials present a spontaneous polarization, existing in the absence of an applied magnetic field.

Under the effect of an increase in temperature, the thermal agitation becomes more important and favors the return to a random distribution of magnetic moments, resulting in a decrease in the net maximal magnetization. Each ferromagnetic material

has a specific temperature, called the Curie temperature, above which the substance loses its ferromagnetic property and exhibits a paramagnetic behavior.

The phenomenon of orientation of magnetic moments inside ferromagnetic materials occurs in a localized manner. A sample of macroscopic size is therefore divided into a large number of small volumes, called magnetic domains, each having a spontaneous polarization oriented differently from those of its neighbors. Magnetic-domain structure plays a key role in the hysteresis phenomenon encountered in ferromagnetic materials. This is discussed in more detail in the following sections.

Ignoring the hysteresis effect at this stage, the typical shape of a ferromagnetic polarization $J(h)$ is illustrated next to paramagnetic and diamagnetic responses in Fig. 1.1. A saturation state appears in the ferromagnetic response where an increase in the magnetic field cannot increase the polarization. This happens when all magnetic moments in the structure are already aligned in the magnetic field direction. The induction field b is simply the polarization field added to the empty space contribution $\mu_0 h$. Therefore, the b field continues to increase, even above saturation for a ferromagnetic material, but at a rate comparable to paramagnetism, which is several orders of magnitude smaller than the rate observed below saturation.

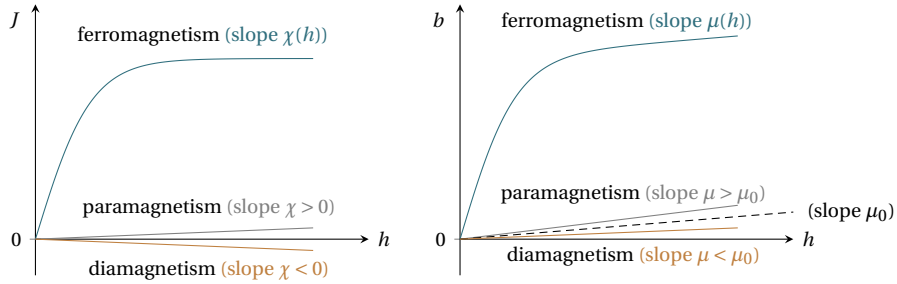

Figure 1.1: *Simplified comparison of magnetic susceptibilities χ (left) and magnetic permeabilities μ (right) for ferromagnetic, paramagnetic and diamagnetic responses.*

Antiferromagnetism

Antiferromagnetism is the type of magnetism where the exchange interaction between neighboring atoms leads to an antiparallel alignment of the atomic magnetic moments. The total magnetization of the material is then zero in that configuration. When the magnetic field is increased, the magnetization tends to align in the same direction but the strong exchange interaction opposes it. The susceptibility is thus in general very low, $\chi_r \approx 10^{-6}$. When the temperature rises, the exchange interaction degrades with thermal agitation, improving the sensitivity to the external field, and thus increasing the susceptibility. At a specific material temperature, called Néel temperature, the antiferromagnetic coupling disappears. Beyond this temperature, the behavior becomes comparable to that of paramagnetic materials.

Ferrimagnetism

1

Ferrimagnetism is another magnetism type where magnetic moments are this time antiparallel due to the exchange interaction, but of different amplitudes. In the simplest configuration of the crystal structure of these materials, two families of sites A and B can be distinguished, occupied by ions having magnetic moments m_A and m_B respectively. The number of sites A differs from the number of sites B, and usually m_A differs from m_B, such that they do not fully compensate each other and a spontaneous magnetization remains in the absence of an applied field. Subjected to an external magnetic field, magnetic moments tend to align in the direction of the field. When the temperature is lower than the Curie temperature, a behavior similar to ferromagnetic materials is observed with a saturation of the magnetization. Above Curie temperature, the material behaves similarly to paramagnetic materials.

Magnetic domains exist also in ferrimagnetic materials since these are formed in materials where the magnetic moments align spontaneously under the effect of the short-range exchange interaction, whose field of action is localized.

At the end, ferrimagnetism exhibits all the hallmarks of ferromagnetic behavior with spontaneous magnetization, Curie temperatures, saturation, magnetic domains and thus hysteresis. Ferromagnetic and ferrimagnetic materials are often referred as magnetic materials, justified by their susceptibility 10^3 to 10^{11} times higher than those resulting from other types of magnetism, which are said to be non-magnetic [185]. In this thesis, which deals with the macroscopic description of magnetic material, ferromagnetic and ferrimagnetic behaviors will not be further distinguished in the following. In this sense, the subsequent macroscopic results and conclusions drawn for ferromagnetism can also apply for ferrimagnetism. In the next section, special attention is given to ferromagnetism with a more detailed reminder of its microscopic origin in order to derive macroscopic observations before the so-called hysteresis behavior.

1.3. Multi-Scale Origin of Ferromagnetism

In magnetic materials, the derivation of the macroscopic result of the magnetization process from the microscopic level is divided into two steps. The first consists in the study of the alignment of the magnetic moments at the scale of a magnetic domain, which is said to be the microscopic scale. The second concerns the calculation of the polarization at the scale of the sample, resulting from the superposition of the polarizations specific to each magnetic domain. This intermediate scale which encompasses the magnetic domain structure is called the mesoscopic scale.

Ferromagnetism at the Microscopic Scale

At the microscopic scale, a magnetic material can be seen as a collection of atoms carrying permanent magnetic moments $\mathbf{m}_0$.

In the classical representation proposed by Langevin [135], each individual magnetic moment is supposed independent from the others, and thus free to rotate in any direction. Submitted to an external field $\mathbf{h}$, each moment acquires a potential energy,

$-\mu_0 \mathbf{m}_0 \cdot \mathbf{h}$, which favors their alignment in the field direction, fighting against the thermal agitation energy, $k_B T$, which tends to shake them in random orientations. The physical constant k_B is the Boltzmann constant, $k_B = 1.3807 \times 10^{-23}$ J/K, and T is the temperature expressed in kelvin (K). The Langevin theory, whose calculation details are given in Appendix A-Section 1, predicts that the net magnetization, m, of a medium containing N_m atoms per unit volume varies according to

$$m = N_m m_0 \left(\coth \alpha - \frac{1}{\alpha} \right) := N_m m_0 L(\alpha) \qquad \text{with } \alpha = \frac{\mu_0 m_0 h}{k_B T}, \tag{1.11}$$

where $L(\alpha)$ is the so-called Langevin function, illustrated in Fig. 1.2 (left), and α the dimensionless factor which weights the two competing energies.

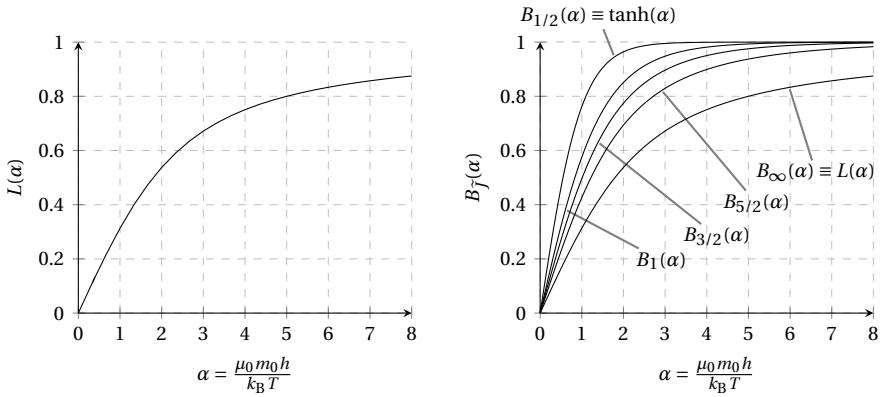

Figure 1.2: *(left): The Langevin function $L(\alpha)$. (right): The Brillouin functions $B_{\tilde{J}}(\alpha)$ for different $\tilde{J}$ values. For $\tilde{J} = 1/2$ and $\tilde{J} = \infty$, the Brillouin function degenerates into the hyperbolic tangent function* $\tanh(\alpha)$ *and the Langevin function $L(\alpha)$, respectively.*

Introducing in the description the quantum nature of the magnetic moment by restricting its orientation to certain discrete values brings a modification in the final expression of the net magnetization, which becomes, in quantum formalism [35, 129],

$$m = N_m m_0 \left(\frac{2\tilde{J}+1}{2\tilde{J}} \coth\left(\frac{2\tilde{J}+1}{2\tilde{J}} \alpha \right) - \frac{1}{2\tilde{J}} \coth\left(\frac{1}{2\tilde{J}} \alpha \right) \right) := N_m m_0 B_{\tilde{J}}(\alpha), \tag{1.12}$$

where the Langevin function from (1.11) is replaced by the Brillouin function, denoted by $B_{\tilde{J}}(\alpha)$, and $\tilde{J}$ is a quantum number having only integer or half-integer values which limits the number of discrete possible states of the magnetic moment. The derivation of (1.12) is presented with more depth in Appendix A-Section 2.

The Brillouin functions are drawn in Fig. 1.2 (right) for different $\tilde{J}$ values. They remain all qualitatively similar, exhibiting saturation when magnetic moments align mainly with the field, when $\alpha \to \infty$, and thus $m \to m_{sat} = N_m m_0$. In the limit $\tilde{J} \to \infty$, the Brillouin function reduces to the Langevin function since, in this situation, the magnetic moments are no more quantized and can take any direction, just like in the classical

framework. With the quantification of the orientation of $\mathbf{m}_0$, saturation actually occurs more rapidly than predicted by Langevin's classical theory. In the extreme case $\widetilde{J} = 1/2$, for which only two magnetic moment states are possible, the Brillouin function reduces to a hyperbolic tangent function.

A noticeable magnetization along the field can only be realized when the field energy becomes comparable to the amount of thermal energy, in other words when $\alpha \approx 1$. At room temperature, this requires an enormous field intensity, of about $h \approx 3 \times 10^8$ A/m, such that, in standard conditions, thermal agitation remains the predominant effect which destroys any preferred alignment. This description is thus satisfying for paramagnetism but not for ferromagnetism. Nonetheless, this theory allows to derive the Langevin and the hyperbolic tangent functions which appear to be suitable expressions to encompass the average magnetization of a system, from the microscopic scale to a higher scale. They are considered as a starting point for the description of spontaneous magnetization, one of the key ingredients of ferromagnetism.

Weiss extended the Langevin approach by proposing a simple phenomenological theory [209] to explain the spontaneous alignment of atomic magnetic moments within a ferromagnetic material, even at no field. This theory, which is discussed further in Appendix A-Section 3, assumes that each magnetic moment in the material is subjected to a strong internal magnetic field, $\mathbf{h}_\mathrm{W}$, due to the influence of its neighbors. This molecular field is supposed proportional to the net magnetization, $\mathbf{h}_\mathrm{W} \propto \mathbf{m}$, such that it self-reinforces the alignment of the moments in the field direction as soon as a nonzero magnetization exists. Therefore, at a given temperature below the critical Curie threshold, the material acquires a significant spontaneous magnetization, m_s, which can be close to the theoretical saturation value, $m_\mathrm{sat} = N_\mathrm{m} m_0$, even at zero field.

Ferromagnetism at the Mesoscopic Scale

Actually, all ferromagnetic materials do not present such permanent magnetic saturation at macroscopic scale, since they can exhibit small or null magnetization at no field, and be strongly magnetized under the application of a relatively small magnetic excitation.

This results from the fact that a sample of macroscopic size subdivides into many small regions, called magnetic domains. In each domain, the Weiss molecular field forces the alignment of the magnetic moments in a uniform direction, but the direction can be different from one domain to another because its action is localized in space. As the orientation of the spontaneous magnetization varies from region to region, the overall magnetization of a sample, including many domains, may well be very different from the spontaneous magnetization, and even be zero.

A subdivision in magnetic domains is illustrated on Fig. 1.3. The magnetic domain, or so-called Weiss domain, corresponds thus to a contiguous region in which all atomic magnetic moments are aligned parallel to each other. The spontaneous magnetization module m_s has the same value in all magnetic domains for a homogeneous medium at uniform temperature. Magnetic domains can have various shapes. In most materi-

als, they are microscopic in size, about 1 to 100 µm. Each domain is separated from a neighbor by a transition zone in which the orientation of the magnetic moments gradually changes from the magnetization direction in one domain to that in the other one. This interface between adjacent domains is called the domain wall.

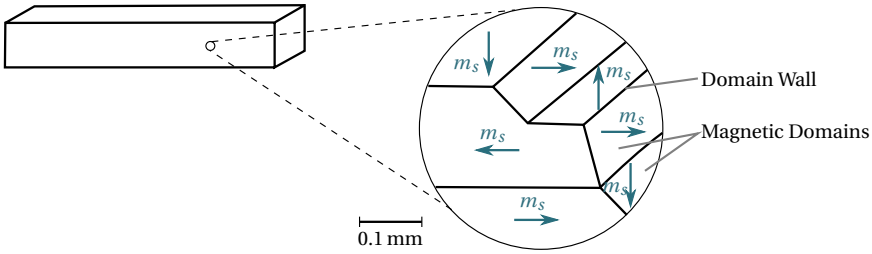

Figure 1.3: *Division of the magnetic material into magnetic domains at the mesoscopic scale [185].*

The average magnetization of the entire medium is necessarily between 0 and m_s. It can change from 0 to m_s under the application of a magnetic field, which implies a complete modification of the distribution of the Weiss domains. Their number, their shape, their size and the orientation of their local spontaneous magnetization can be largely altered.

In theory, the origin of the magnetic domains and their motion can be understood through micromagnetics. The magnetic domain structure comes from a complex and delicate balance between several competing energy terms, which are briefly presented and illustrated for the case of an ideal perfect monocrystalline sample in Appendix B-Section 1.

However, in practice, it seems impossible to apply micromagnetics to describe real materials, for which structural disorder dominates. Indeed, as sketched in Appendix B-Section 2, magnetic materials are generally polycrystalline materials, which means that they are composed of many crystalline grains, with the presence of relatively punctual defects, such as cavities, non-magnetic inclusions or dislocations in the crystallographic structure. This leads to random functions for the space-dependent parameters involved in the micromagnetics energy terms, such that a huge number of local minima, maxima and saddle points appear in the energy landscape, which makes the energy minimization problem of micromagnetics excessively complex and intractable for samples of size larger than microscopic scale. It is irrelevant to know all the fine details of the microstructure in order to extract macroscopic magnetic behavior, such that only general results of micromagnetics averaged over structural disorder are workable.

As a matter of fact, the magnetic domain pattern is strongly influenced by the presence of defects in the microstructure. A non-magnetic cavity in the material will tend to capture a domain wall because this situation corresponds to a local minimum in the magnetostatic energy, as presented in Appendix B-Section 2. A certain amount of energy is then needed to allow the domain wall to move again from its position. This

phenomenon is called the domain wall pinning effect and it has a direct influence on the macroscopic properties of a magnetic material.

Fig. 1.4 presents how the existence of specific crystal defects inside a simple single crystal modifies strongly, through the pinning effect, the movement dynamics of the domain walls and impacts the shape of the measured magnetization curve of the sample. In the initial unmagnetized state given by Fig. 1.4(a), with no applied field, a conventional domain pattern is formed, and the domain walls pass preferably through the nearby cavities, minimizing their magnetostatic energy. A small field as shown in Fig. 1.4(b), induces a reversible deformation of the walls which bend like elastic surfaces, but the pinning points do not change. The magnetization of the material is very little impacted. For a medium field associated to Fig. 1.4(c),(d), the energy brought to the domains becomes sufficient to unpin the domain walls. The walls move thus by a succession of jumps towards other pinning sites, favoring the expansion of the domains with a more **h**-oriented magnetization, and the shrinking of the others. These discrete changes of size of magnetic domains, corresponding to the Barkhausen effect, affect the magnetization which varies then, not continuously, but by tiny abrupt steps. These wall displacements are irreversible. Magnetization undergoes its maximal increase in this regime. At Fig. 1.4(e), the irreversible wall movements are finished, the domain structure has disappeared and only one domain occupying the entire sample remains. The magnetization within the domain stays parallel to the axis of easy magnetization, closest to the direction of **h**. By increasing further the applied field amplitude, as in Fig. 1.4(f), the energy supplied starts to overcome the magnetocrystalline energy, such that the magnetization deviates from the axis of easy magnetization to align with the direction of **h**, and the sample reaches its maximum spontaneous magnetization. This last effect is reversible again.

In a polycrystalline medium, a behavior similar to that described by Fig. 1.4 tends to occur in each grain, but the process is complicated by interactions between neighboring grains. The grain structure also has a strong influence as well.

In summary, the magnetic domain structure, which has microscopic origins, is responsible for all the magnetic properties exhibited by a material observed at larger scale. It is this multi-scale nature that makes the magnetization process in ferromagnetic material an extremely complicated phenomenon to tackle.

1.4. The Hysteresis Curve

The typical shape of the magnetization curve of a ferromagnetic material observed at a macroscopic scale in response to an external magnetic field can now be analyzed. This curve corresponds formally to the relation between the applied magnetic field h and the average magnetization m, averaged over a volume much larger than the domain size. Note that the term magnetization curve refers to the $m-h$ curve, but also to the $J-h$ curve or, more commonly, the $b-h$ curve, with J and b simply related to m through (1.5) or (1.2) respectively.

The $b(h)$ curve obtained by increasing the applied field on a sample that has never

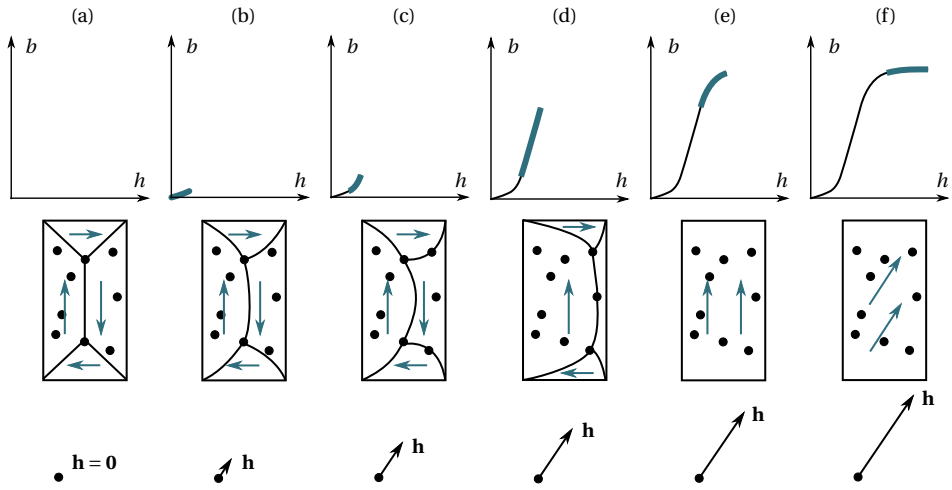

Figure 1.4: *Evolution of the magnetization of a single crystal with its magnetic domain structure in presence of pinning sites for an applied magnetic field* **h** *of increasing amplitude from (a) to (f). After reversible elastic bending of domain boundaries (a)-(b), the domain walls jump irreversibly between pinning sites (c)-(d), increasing sharply the magnetization, until the material is magnetized uniformly to saturation where reversible coherent rotation can ultimately take place (e)-(f) [185].*

been previously magnetized at macroscopic scale, as illustrated in Fig. 1.4, is called the first magnetization curve. When the field strength is then decreased, the magnetization tends to remain unchanged due to the pinning of the current domain structure. Therefore, the function $b(h)$ deviates from the first magnetization curve due to the irreversible processes involved in the magnetization. Cycling the magnetic field between opposite values makes the hysteresis form appear in the $b(h)$ curve. A typical hysteresis loop is represented at Fig. 1.5.

Because of hysteresis, the knowledge of h and b is not sufficient to completely describe the magnetization state, which depends fundamentally on the magnetic domain structure. Indeed, it has been shown that the evolution of the domain structure for further field changes differs according to the past history of the material. In that sense, the material exhibits a sort of memory of the magnetization it has undergone.

The saturation states are particular magnetization states because they correspond to situations where the domain structure is nearly deleted with only one domain left in uniform magnetization, such that subsequent magnetization changes are independent of the field history prior to saturation. Therefore, the major hysteresis loop that is the loop obtained by cycling the field between opposite saturated states, as represented on Fig. 1.5, is generally employed to characterize magnetic materials.

Only the magnetization and the magnetic polarization can reach actual saturation values, denoted by m_{sat} or J_{sat} respectively, when the temperature approaches 0 K or if $h \to \infty$. There is no saturation of the induction field b since in (1.2) or (1.4), the term

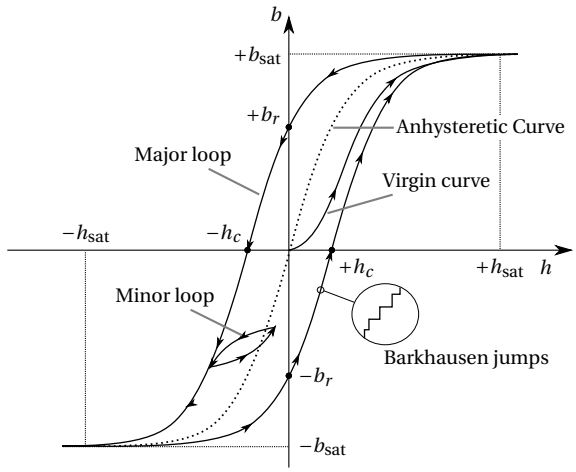

Figure 1.5: *Typical magnetic hysteresis curve.*

$\mu_0 h$ increases indefinitely. However, by abuse of language, the expression b_{sat} is also employed to denote the induction field at saturation that is defined as the saturation value of the magnetic polarization J_{sat}, which gives formally

$$b_{\text{sat}} = \lim_{h\to\infty} \left(b - \mu_0 h\right) = J_{\text{sat}} = \mu_0 m_{\text{sat}} \,. \tag{1.13}$$

Obvious practical limitations prevent the creation of infinitely large fields and the practical values m_{sat}, J_{sat} and b_{sat} are then defined associated to a feasible applied field h_{sat}, above which the hysteresis properties no longer change. The major hysteresis loop of the $b-h$ curve is then made of two different ascending and descending magnetization paths connecting the points $(+h_{\text{sat}}, +b_{\text{sat}})$ and $(-h_{\text{sat}}, -b_{\text{sat}})$, as in Fig. 1.5.

The Barkhausen effect, which causes discontinuous change in the magnetization process due to irreversible jumps of domain walls, is illustrated in Fig. 1.5. However, it is nearly impossible and mostly useless to try to give all details of the random nature of the Barkhausen signal, such that this effect is usually averaged out in the $b-h$ curve description.

A minor hysteresis loop is any other cycle between field peak values with lower intensity than the major loop. An example of asymmetric minor loop is shown in Fig. 1.5.

A return to the state of zero magnetization at zero field can be realized through thermal agitation, by increasing momentarily the temperature of the sample above the Curie point. The virgin curve depicted in Fig. 1.5 corresponds to the first magnetization curve traversed when increasing the applied field starting from that demagnetized state. Applying cycling field of variable amplitude centered to the demagnetized state allows to generate a set of symmetric minor loops as in Fig. 1.6 (left). The curve connecting the reversal points of these minor loops, coincides for all practical cases with the first magnetization curve or the so-called virgin curve.

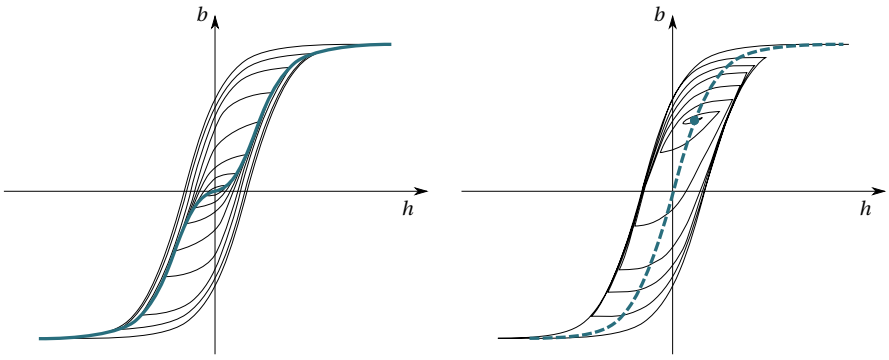

Figure 1.6: *(left): Set of symmetric minor hysteresis loops with the reversal points connections on the virgin curve, (right): Path history generated by a field with oscillating amplitude, slowly decreasing from infinity to zero, around a constant bias field value. Other final points can be reached by repeating the operation under different bias values. The locus of all these final points constitutes the anhysteretic curve (in dashed line).*

A return to the demagnetized state can also be realized by applying an oscillating field with an amplitude slowly decreasing from saturation to zero, in order to erase any memory of previous magnetization states. A spiraling path is thus followed in the $b-h$ diagram which ends up at the origin in the demagnetized state. The procedure can be extended by adding a constant field component to the slowly decreasing oscillating field, as in Fig. 1.6 (right). The final state reached by the so-built converging spiral is called an anhysteretic state, because it is a particular point in the $b-h$ diagram that is independent of prior history, and cleaned from hysteresis influence. The curve resulting from the connection of the anhysteretic states obtained with different constant bias field is called the anhysteretic curve. This curve, that should not be confused with the virgin curve, is also drawn in Fig. 1.5, and provides somehow the skeleton around which hysteresis establishes. In practice, the anhysteretic curve can be approximated by taking the average between the ascending and the descending branches of the major loop. The anhysteretic curve would be the magnetization curve followed by an ideal material if domain walls were free to move through reversible transformations only.

The remanent induction field, b_r, indicated for the major loop in Fig. 1.5, represents the induction that remains in the sample after h decreased to zero from a previous saturated state above h_{sat}. This characteristic parameter explains how a ferromagnet can present a spontaneous magnetization, even in the absence of external applied fields. The phenomenon of remanence also exists for maximum fields lower than h_{sat}, but then the induction which remains after disappearance of the field is lower than b_r, as it is visible with symmetric minor loops in Fig. 1.6 (left).

The coercive field, h_c, also shown in Fig. 1.5, is the magnetic field needed to cancel the remanent induction. This gives an information on the field strength that must be applied to a sample in order to reverse its magnetization. This value can be very different depending on the material internal structure.

Actually, the $b-h$ diagram, characterized by the major loop, the anhysteretic and the

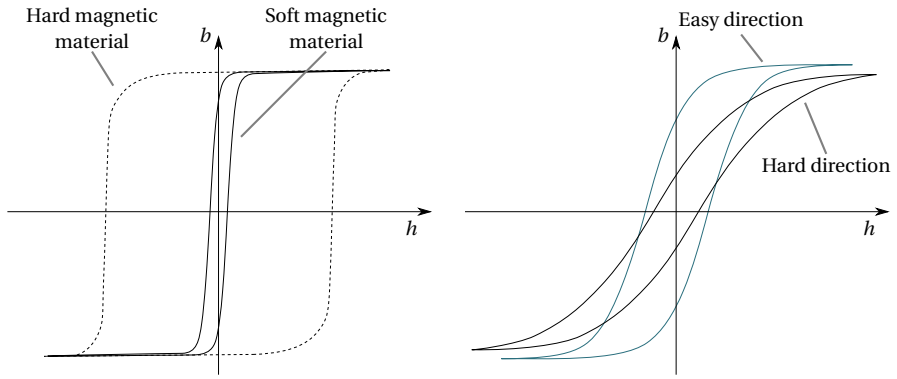

Figure 1.7: *(left): Typical $b-h$ loops for soft and hard magnetic materials. (right): Typical $b-h$ loops measured for easy and hard directions of magnetization on a sample having significant magnetic anisotropy.*

virgin curves, can vary greatly from one magnetic material to another. The materials are classified according to the values taken by the parameters that affect the $b-h$ diagram, such as the coercive field for example.

A qualitative representation of the difference between hysteresis loops for soft and hard magnetic materials is given in Fig. 1.7 (left).

Soft-magnetic materials are those materials that are easily magnetized or demagnetized, with a relatively low coercive field h_c of 1 to 100 A/m. Their major hysteresis cycle area is small. The iron-silicon alloys that are used in electrical motors or transformer cores, also known as electrical steels, are examples of such materials.

Conversely, hard-magnetic materials are those in which the coercive field is high, of the order $h_c \approx 50$ to 100 kA/m, with strong pinning of the domain walls. These materials present a stable permanent source of magnetic field, nearly unaffected by external actions. The area of their main hysteresis cycle is large. Permanent magnets are made of this category of magnetic materials.

At this point, it is important to remember that field and magnetization are basically vector quantities and that the scalar representation of hysteresis curve, based on field intensity, gives an incomplete information on the magnetic behavior.

Actually, the magnetic properties of bulk materials observed at the macroscopic scale are, in general, dependent on the direction in which they are measured, i.e. magnetic anisotropy. There are several sources of anisotropy, either intrinsic to the material or induced [47]. The magnetocrystalline anisotropy due to the crystal lattice configuration, discussed in Appendix B-Section 1, and illustrated by Fig. B.2, is the most intrinsic kind of anisotropy. The macroscopic anisotropy observed for a polycrystalline aggregate comes from the average orientation of each individual crystal grain. The disposition of these grains can be favored in a certain direction, through different treatments, such as magnetic annealing, plastic deformation or magnetic irradiation, that lead to induced magnetic anisotropy. The stress state and the shape of the sample also have

an impact on the overall anisotropy. At the end, the $b-h$ hysteresis curve of a given material can thus be very different according to the direction of magnetization considered, and one can identify axes where magnetization is either particularly easy or difficult, giving rise to different hysteresis curves measured for the same specimen as in Fig. 1.7 (right).

The anisotropy is an important characteristic in the manufacturing of most magnetic materials. Depending on the application, materials with various degree of anisotropy are employed.

For example, in transformers, the magnetization remains predominantly in a fixed direction with a core column. It is therefore beneficial to use grain-oriented (*GO*) steel sheets, based on Goss texture for example, which are produced by successive rolling and annealing processes in such a way to present highly anisotropic property with easy magnetization axis in their rolling direction (*RD*). The *GO* sheets are then used to the maximum of their possibilities when their *RD* is parallel to the main preponderant flux direction, improving the material permeability and its efficiency. The magnetization deteriorates in other directions, especially in the transverse direction (*TD*), which corresponds to a hard axis. *GO* sheets are thus characterized by different $b-h$ curves depending on the magnetization directions.

For rotating electrical machines, the field continually changes its orientation in the core, or part of it, during operation, such that there is no reason in having an easier axis than another in the sheet plane. As a consequence, non-grain-oriented (*NGO*) steel sheets are more appropriate in that case. These materials can more easily be considered as isotropic even if a small degree of anisotropy may still exist in practice.

More information on the type of magnetic materials that are used in various electrical engineering applications can be found in [54, 83, 127, 45].

1.5. Iron Losses

Any variation of the induction in a magnetic material is accompanied by energy dissipation inside the material. This energy appears in the form of heat and is not recoverable. The term magnetic losses, or iron losses, is used to designate this phenomenon.

The area of a closed hysteresis loop traversed during a magnetization cycle has an important physical meaning because it represents precisely the amount of energy per unit of volume that is irreversibly transformed into heat. This comes from the fact that the increment of magnetic work brought to the sample per unit volume during the process is given by

$$\delta W = \mathbf{h} \cdot \delta \mathbf{b} \tag{1.14}$$

with δW expressed in joule per unit volume ($\mathrm{J/m^3}$). Anticipating Chapter 2 where thermodynamics principles are reviewed, the net variation of the internal energy of the sample under a closed hysteresis loop, at constant temperature, is zero. Therefore, through the first thermodynamic law, the magnetic work supplied to the sample is totally dissipated as heat in one magnetization cycle. For each cycle, the energy that is

irreversibly lost is thus given by

$$W = \oint_{\text{cycle}} \mathbf{h} \cdot \delta \mathbf{b}, \tag{1.15}$$

which corresponds effectively to the area enclosed by the hysteresis loop. It is worth noting that through the second thermodynamic law, the loop area must always be positive, such that hysteresis loops must always be traversed counterclockwise in the $b-h$ diagram. The power loss density, P, related to (1.15), is deduced by expressing the dissipation per unit time instead of unit cycle, thus

$$P = f \oint_{\text{cycle}} \mathbf{h} \cdot \delta \mathbf{b}, \tag{1.16}$$

where f is the average frequency in hertz (Hz) at which the cycle is completed, and P is measured in watt per unit volume (W/m^3). The mass-specific power loss, p, is the term used when the power is expressed in watt per unit mass (W/kg), such that

$$p = \frac{1}{\rho_V} f \oint_{\text{cycle}} \mathbf{h} \cdot \delta \mathbf{b}, \tag{1.17}$$

with ρ_V the volumetric mass density of the sample in kg/m^3.

In the description given so far, the origin of hysteresis loops comes from the irreversible nature of the Barkhausen jumps of domain walls in the material. For metals, the dissipation mechanism can be fundamentally explained by the occurence of microscopic eddy currents, according to Faraday's law, by the local variation of the induction accompanying each domain wall jump. Consequently, from this perspective, the energy is dissipated in the magnetic material through eddy current losses around domain wall motion.

Hitherto, it was implicitly assumed that the rate at which the external field varied was sufficiently low so that the field did not change appreciably during the time needed for a Barkhausen jump to be made. The Barkhausen jumps were indeed considered as instantaneous events, and thus unaffected by the rate of the applied field. In this condition, the magnetization curve remains independent of the field rate, and the term rate-independent applies to this type of hysteresis.

However, in reality, magnetization processes are somehow impacted by the rate of change of the field, in particular when fast enough to produce a significant variation of the field during a Barkhausen jump. The transformations in the magnetic domain structure no longer result from a succession of spontaneous rearrangements only, but are also controlled by the sudden variation exerted by the external field. In these circumstances, the magnetization curves are affected by the field rate and the hysteresis is said to be rate-dependent.

Therefore, when the magnetization oscillates at frequency above the rate-independent frequency limit, the intensity of induced eddy currents also increases, which leads to additional energy dissipation and thus to an increase of loop area along with a modification in loop shape, as observed in Fig. 1.8.

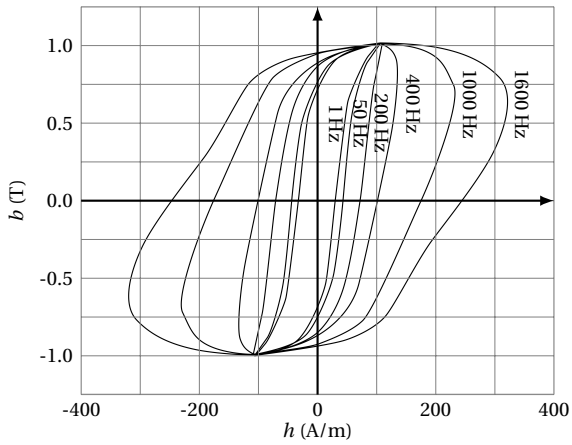

Figure 1.8: *Dynamic influence on the hysteresis loops measured on a specimen of a non-oriented iron-silicon alloy under sinusoidal induction of* 1 T *amplitude at different frequencies [26].*

The calculation and prediction of iron losses is a key factor in the design and optimization process of electrical machines. These losses have a significant influence on the energy efficiency of a machine. It is therefore desirable to have accurate, fast, and easily implementable iron loss models in order to take into account their effect in the preliminary simulation stages in the design process of new electrical machines, before their manufacturing.

An overview of the most used iron loss models is presented in [134] and a very brief summary is given hereafter. There exists a wide range of different iron loss models but they can be sorted into two families. The first family consists of simple models that neglect the hysteresis effect on the field distribution in the device and calculate the losses a posteriori from a simple application of theoretical or experimental formulas. The second family relies on hysteresis models that try to describe mathematically or empirically the hysteresis characteristics of magnetic materials directly within the constitutive law $b(h)$ during the simulation of the device or machine. The iron losses are then calculated by the enclosed area of the resulting hysteresis curves, through (1.17).

2. Simple Iron Loss Models

2.1. Approaches based on the Steinmetz Equation

The first group of models within the simple iron loss models family is based on the Steinmetz equation (*SE*) [200] which establishes in its foundation a power law dependence between the specific iron losses p, with the amplitude of the flux density $\hat{b}$, and the frequency f of a periodic signal,

$$p = C_{\mathrm{SE}} f^{\alpha} \hat{b}^{\beta}, \tag{1.18}$$

where C_{SE}, α and β are empirical material-dependent coefficients that have to be determined by fitting to measurement data. Strictly speaking, equation (1.18) is only

adapted for sinusoidal waveforms in a limited range of frequencies. Therefore, several adaptations of the formula have been studied to enlarge its scope of application to non-sinusoidal flux density waveforms, as caused by power electronics [161], for example. A modification of the *SE*, more suitable for arbitrary waveforms, is proposed with the so-called modified Steinmetz equation (*MSE*) [181], where an equivalent frequency deduced from the field change rate is defined and used instead of f in (1.18). The generalized Steinmetz equation (*GSE*) [143] is another variation, still based on a typical power law as in (1.18), but using an average over one time period of the instantaneous values $\frac{db(t)}{dt}$ and $b(t)$, which makes the formula sensitive to a direct current (*DC*)-component in the signal. Further extensions of *SE*, consistent with the power law (1.18), have been investigated since the early 2000s in an effort to respond to other limitations. These models bear names referring to Steinmetz, such as the improved generalized Steinmetz equation (*iGSE*) [206], or the natural Steinmetz extension (*NSE*) [32], and so on in different subsequent works [31, 192, 42, 164].

All these models offer a simple and fast way to evaluate iron losses, as soon as the empirical coefficients are identified from measurements, if not directly provided by manufacturer's data. Nevertheless, in any model, a given parameter set only works on a frequency-limited spectrum, and it remains difficult to identify suitable coefficients which give satisfactory results over a wide frequency range, as required for waveforms with high harmonic content, for example. Given their simplicity, it is not surprising that the prediction of iron losses from these models is generally tainted with significant errors when deviating slightly from the measurement framework.

2.2. Standard Loss Separation Approach

In the continuity of the original *SE* (1.18), Jordan separated the iron loss expression into two terms: the hysteresis losses p_{hyst}, and the eddy current losses p_{ec} [126]. Then, Pry and Bean went further by characterizing the so-called excess losses, appearing at high frequencies, by introducing a corrective empirical factor [178]. Finally, Bertotti identified excess losses more precisely using the Pry and Bean equations, and separated the iron losses into three terms, giving a full place to the excess losses p_{exc} [20], such that iron loss behavior is now often decomposed in

$$p = p_{\text{hyst}} + p_{\text{ec}} + p_{\text{exc}} = C_{\text{hyst}} f \hat{b}^{\beta} + C_{\text{ec}} f^2 \hat{b}^2 + C_{\text{exc}} f^{1.5} \hat{b}^{1.5}, \tag{1.19}$$

where β is a coefficient generally set at 2, and C_{hyst},C_{ec} and C_{exc} are the hysteresis, the eddy-current and the excess-loss coefficients respectively. The structure of (1.19) reflects the loss separation theory which splits the total iron losses in three categories. The separation has no straightforward significance because all the iron loss terms are technically due to eddy currents induced by magnetization changes in the sample at three different scales, as mentioned in Chapter 1-Section 1.5.

The scale associated with the hysteresis loss, p_{hyst}, is the microscopic scale where the Barkhausen effect takes place. This comes from the small spontaneous jumps of magnetic domain walls between pinning sites housed at lattice imperfections, which give rise to localized eddy currents around them. This dissipation is related to the rate-

independent, or static, energy loss contribution that corresponds to the hysteresis loop area at low frequencies ($f \to 0$Hz).

On the other hand, the scale corresponding to the classical eddy-current loss, p_{ec}, is linked to the macroscopic sample geometry, in which global induced currents are bound to develop under changes in magnetization. This is a rate-dependent, or dynamic, phenomenon which contributes to the widening of the hysteresis loop area when the frequency increases.

Lastly, the scale of the excess loss, p_{exc}, is connected to the mesoscopic scale, at the magnetic domain level. The associated eddy currents result from the movements of the domain walls in dynamic regime, under the driving action of the external field. This effect is significant at frequencies above the rate-independent limit discussed in Chapter 1-Section 1.5. The excess loss is thus again a rate-dependent contribution which enlarges also the hysteresis loop area with the frequency.

Unlike the static component, p_{hyst}, which is expressed empirically, the two dynamic losses components, p_{ec} and p_{exc}, can also be expressed, for simplified geometries by analytical formulae which have a physical meaning.

Hence, the classical loss contribution, p_{ec}, comes naturally from Maxwell's equations in the characterization of a completely uniform material, ignoring magnetic domain patterns. It depends mainly on the specimen shape and the boundary conditions of the problem. In the condition of a lamination sheet of infinite length, under sufficiently low excitation field dynamics such that a homogeneous field is assumed in the sheet, neglecting the skin effect, the expression of instantaneous specific power losses by induced currents is approximated by [20]

$$p_{\text{ec}} = \frac{\sigma d^2}{12\rho_V}\left(\frac{db(t)}{dt}\right)^2, \tag{1.20}$$

where $b(t)$ is the instantaneous induction field, d the thickness of the lamination sheet, σ the electrical conductivity and ρ_V the volumetric mass density of the lamination sheets, respectively.

Concerning the physical description of the excess losses, Bertotti developed a statistical model theory [18, 19, 25], which leads to an analytical expression of the loss factor C_{exc}, that reads, in the case of a laminated material [74],

$$C_{\text{exc}} = \frac{1}{\rho_V}\sqrt{SV_0\sigma G}, \tag{1.21}$$

where G is a dimensionless coefficient of friction between the magnetic domains, V_0 is a parameter, affected by the grain size, which characterizes the statistical distribution of the local coercive field, and S is the transverse surface of the lamination sample. Nevertheless, in practice, the material parameters σ, V_0, G are often difficult to obtain, and the global coefficients C_{ec},C_{exc} are preferably identified directly from measurements and used without details of their nature, as for C_{hyst}.

As with the standard *SE*, the equation (1.19) is in principle limited to the case of sinusoidal field waveform, at frequencies that do not give rise to the skin effect [20]. Through various attempts to improve Bertotti's model (1.19), some authors have chosen to make the coefficients dependent on the frequency and the peak induction values [212, 108, 175, 109], or decided to adapt the expression to take fields of arbitrary waveforms into account [211]. The properties of the coefficients of Bertotti's model are further investigated in [174].

2.3. Rotational Iron Loss Models

In electrical engineering, the magnetic field is not always unidirectional and oriented along the axis of easy magnetization, as assumed in the models presented so far. This is particularly true in the T-joint regions of three-phase transformer cores, where the combination of the fields associated with the different phases leads to the appearance of a locally rotating induction. Similarly, the cores of rotating electrical machines can also be subjected, in some regions, to rotating magnetic fields in the lamination sheets.

In practice, iron losses in the rotating field and in the unidirectional field differ. This difference finds its explanation in the complex mechanism involved during the magnetization. For weak fields, a similar power law behavior, as for alternating losses, applies also for rotating field losses [76], but the losses with rotating field may have values twice as high as those with unidirectional field [71, 162]. One can roughly approximate, at least for p_{ec}, the rotating field losses by the sum of the unidirectional field losses according to the rolling and the transverse directions. Conversely, for fields with very large amplitudes, while the losses in unidirectional field continue to grow as a function of the amplitude of $\mathbf{b}$, the losses with rotational field decrease as a function of b. This phenomenon is in agreement with the reversible nature of the rotating field observed for induction values close to saturation, as illustrated in Fig. 1.4(f).

Several iron loss models have been proposed to tackle the losses due to rotational magnetization in the lamination sheet [4, 75, 131, 201]. A review on rotational iron loss models and measurement techniques is presented in [190, 92]. The results of an international study that compares measurements with rotating iron losses are given in [194].

A common practical approach to estimate iron losses in electrical machines consists in separating losses according to the type of excitations behind the magnetization. The total iron loss can be seen, for example, as the sum of three terms originating from linear magnetization, rotational magnetization and higher harmonics magnetization [159]. In [111], the iron losses due to rotational magnetization are added to the standard loss separation model from Bertotti (1.19), via a particular rotational loss factor to the hysteresis loss term. Actually, the improved empirical loss model takes the form

$$p = a_2 \hat{b}^2 f + \left(a_1 + a_4 \hat{b}^{a_3}\right) \hat{b}^2 f^2 , \tag{1.22}$$

where $a_1 = C_{\mathrm{ec}}$ and $a_2 = C_{\mathrm{hyst}} \left(1 + \check{b}/\hat{b}\,(r-1)\right)$, with r the rotational hysteresis factor and with $\check{b}$ and $\hat{b}$ the minimum and maximum values of $|\mathbf{b}(t)|$ over one period. A higher

order term of the flux density b is introduced with the factor a_4 and the exponent a_3, in order to obtain an accurate representation of iron losses at large fields. This term is in fact called high order losses. The excess loss term C_{exc} turns out to be negligible compared to the other terms in this model and is not taken into account in (1.22).

3. Hysteresis Models

Compared to the previous iron loss expressions, hysteresis models give the most accurate representation of the phenomena involved in the magnetic energy dissipation process. These models approximate, more or less closely, the actual magnetization cycle, material behavior and associated losses, which can be obtained by calculating the surface of the cycle (1.17). They achieve better results in terms of accuracy compared to the simpler expressions (1.18) or (1.19), but at higher computational costs.

Among the hysteresis models existing in the literature, the most commonly used are the Preisach model [176, 157] and the Jiles-Atherton model [125]. Basically, the classical Preisach and Jiles-Atherton models describe the rate-independent hysteresis phenomenon and are scalar models in nature, which restricts their use to quasi-static unidirectional magnetization cases. Subsequently, some improvements have been made to use these models in dynamic operating ranges, taking into account eddy-current losses and, potentially, excess losses, depending on the degree of precision desired in the model development. For example, dynamic Preisach models and dynamic Jiles-Atherton models are considered in [21, 22, 66, 64, 69, 157] and [121, 124, 44], respectively. Furthermore, different extensions transforming the original scalar models into vector models, in order to deal with rotational magnetizing processes, have been proposed in several works, like in [81, 65, 94, 189, 157] for vector Preisach models and in [12, 95, 139, 137] for vector Jiles-Atherton models. All these adaptations remain, however, relatively artificial.

The following subsections recall, without going into much detail, the main foundations of the classical Preisach and the Jiles-Atherton models, while pointing out some of their advantages and disadvantages. Some other remarkable hysteresis models, partly derived from these two, are also presented, with a particular focus on the Bergqvist's vector friction-like hysteresis model, which constitutes the basis of the Energy-Based hysteresis model that is studied throughout this thesis.

3.1. Classical Preisach Hysteresis Model

The classical Preisach model [176] is presented as a purely mathematical model [157], whose application is actually not limited to magnetism. This model is based on a set of elementary hysteresis operators $\hat{m}_{(h_u,h_d)}$. Each of these operators can be represented by a rectangular cycle like in Fig. 1.9 (left). The values h_u and h_d correspond to values of the input magnetic field h for which the operator switches to "up" or "down" magnetization state respectively, with the assumption $h_d \leq h_u$. In other words, the operator can characterize a particle, or an elementary domain, whose local magnetization, or magnetic moment, changes between two values, $\hat{m}_{(h_u,h_d)}h = +m_s$ or

1

$\hat{m}_{(h_u,h_d)}h = -m_s$, through a simple rectangular hysteresis loop, that translates a local memory effect. The magnetic material is assumed to be composed of many such entities. The Preisach model is then built from a network of elementary operators connected as shown in Fig. 1.9 (right). The output of these operators is multiplied by a weight function $\phi(h_u, h_d)$, which depends on h_u and h_d. The final output of the Preisach model, i.e. the total magnetization $m(t)$ from the magnetic field input $h(t)$, is defined from the integral of each weighted elementary contribution

$$m(t) = \int\int_{h_u \geq h_d} \phi(h_u, h_d)\, \hat{m}_{(h_u,h_d)}\, h(t)\, dh_u dh_d\,. \tag{1.23}$$

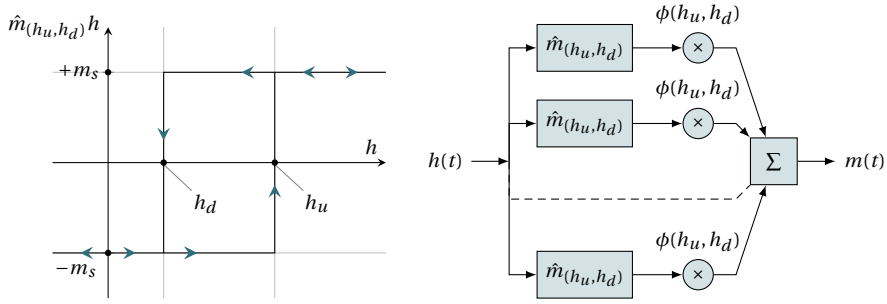

Figure 1.9: *(left): Elementary relay hysteron of the Preisach model. (right): Bloc diagram of the Preisach model that consists of many relay hysterons connected in parallel and summed with given weights.*

The local memory effect of each operator generates a global memory effect, perfectly adapted to describe magnetic materials. Preisach's model can indeed be very accurate and reflects well the magnetic hysteresis. In order to use the model in numerical simulations, the continuous form is changed to a discrete one by replacing the integrals in (1.23) with sums. Due to the contribution of several hysterons, it requires a very high computing power, because each state must be reevaluated if one of the operators changes state. Moreover, the Preisach model requires a relatively extensive measurement campaign to produce the characteristic distribution function $\phi(h_u, h_d)$ of a material. The statistical nature, usually assumed, of this weighting function has no rigorous justification or experimental validation. Consequently, since the model has no physical basis, it can only be used as a mathematical black-box, without any predictive skill for magnetization processes simulated outside the measurement range. Nevertheless, this is the first model that has allowed the reconstitution of hysteresis cycles, and it is at the base of many models that are among the most accurate today.

3.2. Play and Stop Models

A purely mathematical formalism has been developed to model the hysteresis phenomenon by assembling simple operators, called hysterons, in the same spirit as the Preisach decomposition. These elementary operators can be either play or stop hysteron types, and they correspond actually to the building blocks of the Prandtl-Ishlinskii

class of hysteresis models, derived from continuum mechanics [27]. More details on these abstract tools can be found in [151, 207].

For magnetism, a play operator P^k is more likely to be applied to the magnetic field h. It produces as output a state variable, whose evolution is defined, for an ordinary static scalar operator case, by

$$P^k[h] = \max\left[\min\left(P^k_{(p)}, h+\zeta^k\right), h-\zeta^k\right] = \begin{cases} P^k_{(p)}, & \text{if } \left|h-P^k_{(p)}\right| \le \zeta^k \\ h-\zeta^k \dfrac{h-P^k_{(p)}}{\left|h-P^k_{(p)}\right|}, & \text{otherwise,} \end{cases} \tag{1.24}$$

where $P^k_{(p)}$ is the state value of the hysteron P^k at a previous time, reflecting a local memory effect, and ζ^k is a constant threshold above which the internal state value P^k is allowed to change with h.

On the other hand, a stop operator S^k is more adapted to take the induction field b as input. The evolution of its internal variable is defined, in a way more or less complementary to P^k, by

$$S^k[b] = \max\left[\min\left(db+S^k_{(p)}, \eta^k\right), -\eta^k\right] = \begin{cases} db+S^k_{(p)}, & \text{if } \left|db+S^k_{(p)}\right| \le \eta^k \\ \eta^k \dfrac{db+S^k_{(p)}}{\left|db+S^k_{(p)}\right|}, & \text{otherwise,} \end{cases} \tag{1.25}$$

with $db = b - b_{(p)}$, and where $b_{(p)}$ and $S^k_{(p)}$ are the values taken by b and S^k at a previous time, and η^k is a constant limit. The changes with db of the internal value are stopped as soon as this limit η^k is reached.

The summation of a finite number N of play or stop hysterons leads to a play-type model (1.26) or a stop-type model (1.27), able to represent the constitutive relations $b(h)$ or $h(b)$ respectively, having global memory [27]:

$$b(t) = \sum_{k=1}^{N} f^k\left(P^k[h](t)\right), \qquad h(t) = \sum_{k=1}^{N} g^k\left(S^k[b](t)\right), \tag{1.26, 1.27}$$

where f^k and g^k are memoryless functions.

As noted in [1], these mathematical models can be extended to become vector models, either by integrating the final output of the scalar models (1.26)-(1.27), along different directions [155], or by vectorization of the elementary scalar operators (1.24)-(1.25) [138, 156, 153]. An example of dynamic extension of play-type model based on Bertotti's decomposition can further be found in [128]. Since there is no direct physical interpretation behind their derivation, the play-type and stop-type models can only be identified from a best fitting technique with experimental results, without guarantee of satisfactory agreement with measurements [3, 152, 154]. It is worth noting that the

Preisach model can also be represented thanks to a superposition of Prandtl-Ishilinskii play-type operators [27]. Generally speaking, play-type and stop-type models promise a lighter digital implementation than the Preisach model.

3.3. Notable Experimental Hysteresis Models

A multitude of other hysteresis models without a direct constructive link to the underlying physical phenomena but that rely on the fitting of experimental data, have been proposed over the years. Most notable amongst those are the Loss-Surface Model and the Zirka-Moroz Models.

The Loss Surface Model, introduced in [43], was initially designed as a purely experimental hysteresis model, built from $b(h)$ cycle measurements on an Epstein frame. The data related to a material are obtained by use of triangular controlled flux signals imposed at different rate $\frac{db}{dt}$ and for different maximum amplitudes $\hat{b}$. The material characterization is then carried out by scanning in frequency and amplitude to get the characteristic surface $h(b, \hat{b}, \frac{db}{dt})$. Then, based on these surfaces, it is possible to reconstruct, a posteriori, a cycle $b(h)$ from the knowledge of the couples $(b, \frac{db}{dt})$. However, this approach does not correctly approximate the hysteresis cycle when minor cycles are present. An improvement was made in [84], by decomposing the field h to obtain a static contribution $h_{\text{stat}}(b)$ and a dynamic contribution $h_{\text{dyn}}(b, \frac{db}{dt})$. A scalar hysteresis model is used to obtain the static field h_{stat} [80]. The surface $h_{\text{dyn}}(b, \frac{db}{dt})$ is then obtained from the measurements by subtracting the static part [144].

The Zirka-Moroz hysteresis model [214, 215] is another model based on direct use of experimental measurements. The material data needed for this model are experimental measurements of the static major loop and of first-order reversal curves only. Then, through the assumption of similarity between the trajectories of major and minor hysteresis loops, any second- or higher-order reversal curve can be obtained by transplanting (or copying) the segment, or a weighted sum of segments, from the first-order curves which present the same overall dimensions and are the nearest to the modeled curve. An extension to take the dynamic excess loss into account is investigated in [216] with the introduction of a viscosity term.

Nevertheless, since the loss surface or the Zirka-Moroz model have no physical basis and rely essentially on the direct use of experimental measurements, they may require substantial material data storage and there is no guarantee that these models provide satisfactory predictions in situations of field excitations relatively far from the measurement conditions.

3.4. Jiles-Atherton Model

Unlike previous models, Jiles-Atherton's model is inspired by the physics of the material and more particularly on the displacement of magnetic walls [125]. It is constructed on the basis of the decomposition of the total magnetization m into two com-

ponents, one reversible, m_{rev}, and the other irreversible, m_{irr}:

$$m = m_{\text{rev}} + m_{\text{irr}}\,, \quad \text{with}\, m_{\text{rev}} = c(m_{\text{an}} - m_{\text{irr}})\,, \tag{1.28}$$

where c is a parameter between 0 and 1 which reflects the proportion of reversibility in the wall displacements, and m_{an} is the anhysteretic magnetization. The anhysteretic curve is often described by the Langevin function, $m_{\text{an}} = m_s L\left(\frac{h_e}{a}\right)$, presented in Fig. 1.2 (left), where m_s and a are two parameters which control the saturation level and the slope of the curve, respectively. The field $h_e = h + \alpha m$, is introduced to account for the effective field seen by the magnetic domains, by analogy with the molecular field from the Weiss theory (A.18). The parameter α reflects the coupling between magnetic domain moments. The irreversible character of the material is given by

$$\frac{dm_{\text{irr}}}{dh_e} = \frac{m_{\text{an}} - m_{\text{irr}}}{\delta k}\,, \quad \text{with}\, \delta = \text{sign}\left(\frac{dh}{dt}\right), \tag{1.29}$$

where k is related to the irreversibility of wall movement, quantifying the importance of the pinning effect due to the presence of impurities and dislocations which impede the wall displacements. The number δ takes the value ± 1 according to the direction of change of h. Other definitions than (1.29) may be adopted [12] in order to avoid a pathologically negative value for $\frac{dm_{\text{irr}}}{dh_e}$. After development and derivation of the different terms, the following differential equation is obtained

$$\frac{dm}{dh} = \frac{c\dfrac{dm_{\text{an}}}{dh_e} + (1-c)\dfrac{dm_{\text{irr}}}{dh_e}}{1 - \alpha c\dfrac{dm_{\text{an}}}{dh_e} - \alpha(1-c)\dfrac{dm_{\text{irr}}}{dh_e}}\,, \tag{1.30}$$

from which it is possible to reconstruct the hysteresis cycle $m(h)$ by integration.

The five parameters c, m_s, a, α and k must be determined from experimental measurements. While the computer implementation of the Jiles-Atherton model (1.30) is relatively simple, the derivation of a set of material parameters capable of satisfactorily representing a wide variety of excitation types is however not straightforward, which often leads to inaccurate predictions, especially for complex hysteresis trajectories [11]. Different identification strategies have been investigated, either derived from global magnetic properties of the $b-h$ diagram [122] or through various optimization techniques by action on the five parameters in order to minimize the gap between measured and simulated major cycles [10, 8, 150]. Experience has shown that the model is unable to approximate minor loops with the same parameters as those deduced from the major loop. In order to get around this issue, it is possible to consider parameters that vary with magnetic field strength [210, 204], but the predictive skills of the model are questionable. More fundamentally, the Jiles-Atherton model sometimes results in unrealistic minor loops for which the closure is not guaranteed. Several model corrections were thus recommended [41, 123, 160, 9, 140], but these attempts rely on artificial and often awkward modifications to make the model stick to the measurements, with little justification. Moreover, the alleged physical foundations

of the original model have been criticized in [217]. In particular, the postulated decomposition of the magnetization in reversible and irreversible parts (1.28) has a doubtful physical interpretation. Nevertheless, this model remains easy to exploit, with a relatively low cost in computer resources, which certainly explains its huge popularity.

3.5. Bergqvist Model

Bergqvist developed a quasi-static magnetic vector hysteresis model relying strongly on thermodynamic principles and presenting features in common with both the Jiles-Atherton and the Preisach models [17]. From the former, it borrows the idea of modeling the domain wall pinning with dry friction force to explain the physical origin of the hysteresis phenomenon. From the latter, it considers the magnetization as the superposition of the contribution from a large number of pseudo-particles. Based on thermodynamic principles, the magnetic system is described by means of its Landau free energy density g_L whose local minima correspond to metastable magnetization states. For each independent particle with magnetization $\mathbf{m}^k$ constituting the system, this energy reads

$$g_L = f(\mathbf{m}^k) - \mu_0 \mathbf{h} \cdot \mathbf{m}^k \,, \tag{1.31}$$

where $f(\mathbf{m}^k)$ is the associated Helmholtz free energy density assumed to be the sum of two components

$$f(\mathbf{m}^k) = f_{\text{an}}(\mathbf{m}^k) + f_p(\mathbf{m}^k) \,. \tag{1.32}$$

The term $f_{\text{an}}(\mathbf{m}^k)$ is a convex energy function corresponding to the anhysteretic behavior. The presence of impurities responsible for the pinning effect of the domain walls manifests itself through small potential wells in the energy landscape of the system. A large number of these impurities introduces a periodic ripple in the energy expression, denoted by $f_p(\mathbf{m}^k)$ in (1.32). The effect of the ripple is described through a friction mechanism, which induces hysteresis behavior for each pseudo-particle forming the magnetic sample. This representation shows similarities with stress-strain hysteresis models encountered in plasticity with kinematic hardening [148]. At the end, the total magnetization is obtained by integrating the contributions of each particle. For a computer implementation, this integration is replaced by a weighted sum. The model parameters that characterize a material are those that define the shape of the anhysteretic curve, also with the weight and the friction coefficient associated with each pseudo-particle.

In addition to being naturally vectorial, the Bergqvist model benefits from the simplicity of the Jiles-Atherton model and, like the Preisach model, is characterized by an adjustable precision according to the number of pseudo-particles chosen to represent the magnetic material. Because of its true thermodynamical background, the model is predisposed to predict magnetic material responses in a more satisfactory way than with empirical or black-box type models, in particular when exploited outside the measurement configuration ranges used for the parameter identification. Moreover, as the magnetization state is based on an energy balance, the stored and dissipated energy can be calculated at any moment in time, not only at the end of closing hysteresis loops.

Actually, the so-called Energy-Based hysteresis model [103] which is developed in depth in this thesis is closely related to the Bergqvist model. It has all its advantages and all its features. Its derivation is the subject of a more detailed presentation in Chapter 2.

The Bergqvist model and the Energy-Based hysteresis model have been further studied and improved in several subsequent works. Various parameters identification techniques are presented and compared to measurements in [15, 132, 104]. The influence of temperature on the parameters is investigated in [14, 196]. There are original proposals for model extensions to anisotropic cases [198] or dynamic regime cases [102, 197]. In [145], an improvement of the core loss predictions is achieved by making the friction coefficient dependent on the magnetic field strength, and the model is finally integrated into finite element calculations.

Basically, Bergqvist employed an approximation in his model in order to deduce an explicit magnetization evolution rule instead of minimizing exactly the energy expression (1.31). This simplification has the effect of transforming his model into a vector play-type hysteresis model. This easier model approach has been used in almost all following works related to the Bergqvist model except in [79, 116, 113, 177], where the minimization problem is effectively tackled. The consequences of this choice will be discussed in Chapter 3.

CHAPTER

2 Energy-Based Hysteresis Model

THIS chapter presents the physical origin of the energy-based (*EB*) hysteresis model. The considered model is based on the first and second laws of thermodynamics to represent the hysteretic behavior of ferromagnetic materials. The basic thermodynamic principles will be particularized to the description of magnetic bodies. The presence of hysteresis complicates the analysis as it is a naturally out-of-equilibrium phenomenon, where irreversible processes take place, that can only be studied with non equilibrium thermodynamic features. To progress step by step, the hysteresis phenomena will be first neglected to derive thermodynamic relations valid only for systems that are always in equilibrium, for which constitutive laws are exclusively depicted by anhysteretic magnetization curves. The complexity of non equilibrium thermodynamics will be added later to finally take hysteresis behavior into account. At the end, the magnetic system is decomposed in an infinite number of subsystems, each with an irreversible nature of smoothly varying strength, in order to express the net magnetization of a more realistic composite material as the integral of every subsystems contributions.

1. Fundamentals in Thermodynamics

The first law of thermodynamics expresses the conservation of energy. For a generic system under constant mass density, this principle may be expressed in local form as

$$\dot{u} = \dot{W} - \operatorname{div}\mathbf{q}, \tag{2.1}$$

stating that the change in the internal energy $\dot{u}$, in watts per unit volume (W/m^3), is equal to the sum of the rate of work $\dot{W}$ performed on the system and the amount of heat flux $\mathbf{q}$ transferred to the system[1]. The rate of magnetic work, in watts per unit volume (W/m^3), is usually expressed as

$$\dot{W} = \mathbf{h} \cdot \dot{\mathbf{b}}, \tag{2.2}$$

[1] The dot above a symbol stands for a total time derivative.

where **h** corresponds to the applied magnetic field, in ampere per meter (A/m), and **b** to the magnetic flux density, in tesla (T). The magnetic flux density **b** is represented by the sum of the empty space magnetic polarization $\mathbf{J}^0 = \mu_0 \mathbf{h}$, with μ_0 the magnetic permeability of vacuum, and the material magnetic polarization **J**, from (1.4),

$$\mathbf{b} = \mathbf{J}^0 + \mathbf{J}. \tag{2.3}$$

The energy of empty space associated to $\mathbf{J}^0$ does not depend on the magnetization of the material and contributes to increase reversibly the internal energy of the system. Therefore, focusing only on the relevant magnetic energy contribution involved within a magnetic media, the work expression (2.2) reduces to

$$\dot{W} = \mathbf{h} \cdot \dot{\mathbf{J}}. \tag{2.4}$$

The second law of thermodynamics states that the change in entropy $\dot{s}$ of a given system comes from the entropy exchanges with the exterior $\dot{s}^{\text{ext}}$ and the internal entropy creation $\dot{s}^{\text{int}}$. The internal entropy production is due to irreversible processes like hysteresis and is always a nonnegative contribution. This principle can be written in local form as

$$\dot{s} = \dot{s}^{\text{ext}} + \dot{s}^{\text{int}} = -\text{div}\,(T^{-1}\mathbf{q}) + \dot{s}^{\text{int}}, \qquad \dot{s}^{\text{int}} \geq 0, \tag{2.5}$$

where T is the absolute temperature. The following divergence identity

$$\text{div}\,\mathbf{q} = \mathbf{grad}\,T \cdot (T^{-1}\mathbf{q}) + T\,\text{div}\,(T^{-1}\mathbf{q}), \tag{2.6}$$

is used to combine (2.1) and (2.5) including (2.4) to obtain

$$\dot{u} = \mathbf{h} \cdot \dot{\mathbf{J}} - \mathbf{grad}\,T \cdot (T^{-1}\mathbf{q}) + T(\dot{s} - \dot{s}^{\text{int}}), \qquad \dot{s}^{\text{int}} \geq 0. \tag{2.7}$$

Introducing now the Helmholtz free energy density $f(\mathbf{J}, T)$, defined as $f := u - Ts$, and using the relation $\dot{f} = \dot{u} - T\dot{s} - s\dot{T}$ in (2.7) allows to get after rearranging the terms

$$T\dot{s}^{\text{int}} = \mathbf{h} \cdot \dot{\mathbf{J}} - \mathbf{grad}\,T \cdot (T^{-1}\mathbf{q}) - (\dot{f} + s\dot{T}) \geq 0. \tag{2.8}$$

The relation (2.8) is also known as the Clausius-Duhem inequality. Neglecting spatial and temporal thermal variations ($\mathbf{grad}\,T = \mathbf{0}$, $\dot{T} = 0$), it reduces to

$$D = \mathbf{h} \cdot \dot{\mathbf{J}} - \dot{f} \geq 0, \tag{2.9}$$

where, from the rate of entropy production $\dot{s}^{\text{int}}$ and temperature T, the dissipation function $D := T\dot{s}^{\text{int}}$ is introduced. This positive quantity represents the power density that is lost and dissipated by irreversible processes, in watts per unit volume (W/m^3).

2. Reversible Part - Helmholtz Free Energy and Anhysteretic Curve

In case of a reversible transformation, the system is in thermodynamic equilibrium with its surroundings throughout the entire process such that there is no energy dissipated ($D = 0$) and the equality sign holds in (2.9), leading to

$$\dot{f} = \mathbf{h} \cdot \dot{\mathbf{J}}, \qquad \mathbf{h} = \left.\frac{\partial f}{\partial \mathbf{J}}\right|_T. \tag{2.10}$$

Equation (2.10) gives the possibility to derive the system constitutive law $\mathbf{h}(\mathbf{J})$ as soon as f is expressed as a function of its natural variables $f(\mathbf{J}, T)$. Indeed, based on (2.10), one can deduce the variation of the free energy Δf associated to reversible transformations at constant temperature with

$$\Delta f = \int \mathbf{h} \cdot d\mathbf{J}, \tag{2.11}$$

highlighting that the change in the potential, Δf, can be estimated based on a scalar plot of the material constitutive law linking the magnetization $\mathbf{J}$ and the field $\mathbf{h}$. It is important to recall that this result is only valid when the system is in thermodynamic equilibrium at each step of the transformation. In this reversible context, there is no dissipation due to hysteresis and the fields $\mathbf{J}$ and $\mathbf{h}$ are related by a one-to-one function that is said to be anhysteretic and that can be expressed, for a given temperature, by

$$\mathbf{J} = \mathbf{J}_{\text{an}}(\mathbf{h}) \longleftrightarrow \mathbf{h} = \mathbf{J}_{\text{an}}^{-1}(\mathbf{J}), \qquad \text{with} \quad \mathbf{J}_{\text{an}} = \left[\frac{\partial f}{\partial \mathbf{J}}\right]^{-1}. \tag{2.12}$$

For an anisotropic material, the vector constitutive law (2.12), as well as the Helmholtz free energy, varies in function of the field directions. Otherwise, in isotropic conditions, the vector fields $\mathbf{J}$ and $\mathbf{h}$ are assumed to be parallel, such that (2.12) is restricted to

$$\mathbf{J} = \mathscr{J}_{\text{an}}(|\mathbf{h}|)\frac{\mathbf{h}}{|\mathbf{h}|} \longleftrightarrow \mathbf{h} = \mathscr{J}_{\text{an}}^{-1}(|\mathbf{J}|)\frac{\mathbf{J}}{|\mathbf{J}|}, \qquad \text{with} \quad \mathscr{J}_{\text{an}} = \left[\frac{\partial f}{\partial |\mathbf{J}|}\right]^{-1}, \tag{2.13}$$

where $\mathscr{J}_{\text{an}}$ is a scalar-function depending only on the field magnitude. Fig. 2.1 illustrates the classical shape of a reversible magnetic polarization curve $J = J_{\text{an}}(h)$ where both $\mathbf{J}$ and $\mathbf{h}$ are in a parallel direction with magnitudes $J = |\mathbf{J}|$ and $h = |\mathbf{h}|$ respectively. The variation Δf corresponds to the area delimited by the polarization curve and the J axis.

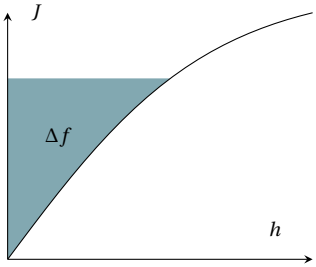

Figure 2.1: *Reversible anhysteretic magnetization curve with the Helmholtz free energy.*

In the following, the Helmholtz free energy density f is assumed to be only a function of $\mathbf{J}$ since temperature effects are neglected, and the reversible part of the magnetic field $\mathbf{h}_{\text{rev}}$ is defined in accordance with the observation (2.10), such that

$$f = f(\mathbf{J}), \qquad \dot{f} = \mathbf{h}_{\text{rev}} \cdot \dot{\mathbf{J}}, \qquad \mathbf{h}_{\text{rev}} := \frac{\partial f}{\partial \mathbf{J}}. \tag{2.14}$$

Adopting this expression also in the case of non-reversible transformations and introducing it in the general relation (2.9) give

$$D = (\mathbf{h} - \mathbf{h}_{\text{rev}}) \cdot \dot{\mathbf{J}} \geq 0 \,. \tag{2.15}$$

3. Irreversible Part - Pinning Force and Hysteresis Dissipation

Developing now the irreversible contribution, magnetic hysteresis is brought into the model via the dissipation function D. In the studied framework, the dissipation is supposed to be exclusively due to magnetic hysteresis losses that stem from the pinning of Bloch walls around defects in the ferromagnetic material structure. The pinning effect that opposes the motion of Bloch walls at microscopic scale can be reasonably represented by a dry-friction force that acts against to any change in magnetization at the macroscopic scale, such that the associated dissipative work D, per unit volume, reads

$$D = |\kappa \dot{\mathbf{J}}| \,, \tag{2.16}$$

with the introduction of the pinning field κ, a material parameter expressed in ampere per meter (A/m) that corresponds to the magnitude of the frictional force in the mechanical analogy. For an isotropic material, the coefficient κ is a positive scalar. Some anisotropy may be introduced by using a symmetric positive definite matrix for κ [177], but this case is not studied in this thesis.

The dissipation function depends on the rate-of-change of the internal variable and thus be expressed as $D = D(\dot{\mathbf{J}})$. By analogy with the definition of $\mathbf{h}_{\text{rev}}$, an irreversible magnetic field $\mathbf{h}_{\text{irr}}$ is here defined such that

$$D = \mathbf{h}_{\text{irr}} \cdot \dot{\mathbf{J}} \,. \tag{2.17}$$

The quantity D can thus be seen as the power delivered by the magnetic field $\mathbf{h}_{\text{irr}}$ as the magnetic polarization $\mathbf{J}$ varies in time. While it might be tempting to write $\mathbf{h}_{\text{irr}} = \partial_{\dot{\mathbf{J}}} D$ from (2.17) to deduce the algebraic expression of $\mathbf{h}_{\text{irr}}$, this result is not straightforward due to the non-differentiability of (2.16) at $\dot{\mathbf{J}} = \mathbf{0}$. However, since the defined functional (2.16) is convex, the notion of subgradient [193, 70], a generalization of the concept of gradient, can be used to write

$$\mathbf{h}_{\text{irr}} \in \partial D(\dot{\mathbf{J}}) \tag{2.18}$$

where the set is mathematically defined by

$$\partial D(\dot{\mathbf{J}}) := \left\{ \mathbf{h}_{\text{irr}} \in \mathbb{R}^3 : D(\mathbf{y}) \geq D(\dot{\mathbf{J}}) + \mathbf{h}_{\text{irr}} \cdot (\mathbf{y} - \dot{\mathbf{J}}) \,, \forall \mathbf{y} \in \mathbb{R}^3 \right\} \,, \tag{2.19}$$

and detailing with (2.16), it can be rewritten under the form

$$\partial D(\dot{\mathbf{J}}) = \begin{cases} \mathbf{h}_{\text{irr}} \,, |\mathbf{h}_{\text{irr}}| \leq \kappa \,, & \text{if } \dot{\mathbf{J}} = \mathbf{0} \\ \mathbf{h}_{\text{irr}} = \kappa \dfrac{\dot{\mathbf{J}}}{|\dot{\mathbf{J}}|} \,, & \text{otherwise} \end{cases} \,. \tag{2.20}$$

This set is called the subdifferential of D at the point $\dot{\mathbf{J}}$ and its elements $\mathbf{h}_{\text{irr}} \in \partial D(\dot{\mathbf{J}})$ are subgradients of D at $\dot{\mathbf{J}}$. This concept is illustrated in Fig. 2.2. The subgradient $\mathbf{h}_{\text{irr}}$

is non-univocally defined at $\dot{\mathbf{j}} = \mathbf{0}$ since a whole set of possible gradients exists in that case. It is from this non-univocity that the hysteresis effect originates. On the other hand, $\mathbf{h}_{\text{irr}}$ corresponds to the classical gradient definition on the rest of the domain where the functional D is differentiable.

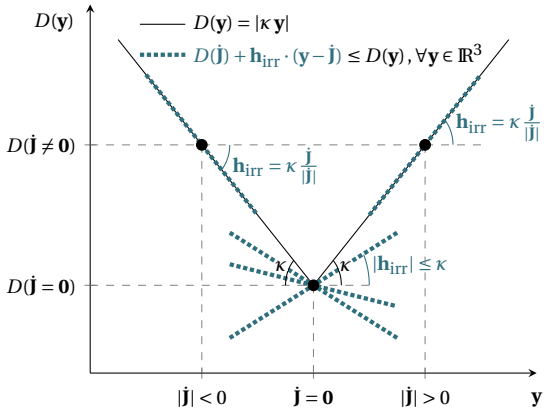

Figure 2.2: *Illustration of the subgradient concept for the convex function $D(\dot{\mathbf{j}}) = |\kappa \dot{\mathbf{j}}|$. This function is non-differentiable at the origin ($\dot{\mathbf{j}} = \mathbf{0}$). Several lines can be drawn through the origin and which are everywhere either touching or below the graph of $D(\mathbf{y})$. The slope of such lines is called a subgradient and it corresponds to the definition of $\mathbf{h}_{irr}$. The subdifferential at the origin is then the interval $[-\kappa, \kappa]$, since all $|\mathbf{h}_{irr}| \leq \kappa$ verifies the inequality (2.19). At any other point ($\dot{\mathbf{j}} \neq \mathbf{0}$), the function $D(\dot{\mathbf{j}})$ is differentiable. In this situation, the local tangent line is the only line that passes through the considered point and which remains everywhere on or below the graph of $D(\mathbf{y})$. Therefore, the subdifferential is the singleton set $\{\kappa \frac{\dot{\mathbf{j}}}{|\dot{\mathbf{j}}|}\}$, such that the value of $\mathbf{h}_{irr}$ is then equivalent to the classical gradient expression. in this case.*

4. Single-Cell Model

The equilibrium equation (2.15) can be rewritten, after factorisation of $\dot{\mathbf{j}}$, as

$$(\mathbf{h} - \mathbf{h}_{\text{rev}} - \mathbf{h}_{\text{irr}}) \cdot \dot{\mathbf{j}} = 0\,. \tag{2.21}$$

Considering that this should be true for any $\dot{\mathbf{j}}$, one generally writes that the term in parentheses must therefore be cancelled, such that

$$\mathbf{h} - \mathbf{h}_{\text{rev}} - \mathbf{h}_{\text{irr}} = \mathbf{0} \quad \rightarrow \quad \mathbf{h} - \frac{\partial f}{\partial \mathbf{j}} \in \partial D(\dot{\mathbf{j}}) = \begin{cases} \mathbf{h}_{\text{irr}}\,, |\mathbf{h}_{\text{irr}}| \leq \kappa\,, & \text{if} \dot{\mathbf{j}} = \mathbf{0} \\ \mathbf{h}_{\text{irr}} = \kappa \dfrac{\dot{\mathbf{j}}}{|\dot{\mathbf{j}}|}\,, & \text{otherwise} \end{cases}, \tag{2.22}$$

which gives the fundamental relation of the *EB* Hysteresis Model.

With a more detailed look, one must note that the original equation (2.21) actually only leads to the much weaker conclusion that $(\mathbf{h} - \mathbf{h}_{\text{rev}} - \mathbf{h}_{\text{irr}})$ is always orthogonal to $\dot{\mathbf{j}}$. Nevertheless, the stronger statement (2.22) is generally assumed and used to give realistic descriptions for many magnetic materials, regardless of the possible conditions

behind the passage from (2.21) to (2.22). This questioning also arises in thermomechanical frameworks [213] for constitutive models of dissipative materials, where it is believed that this type of simplification can also be made [105], as it is sufficient to provide satisfactory descriptions for a wide variety of materials.

The *EB* Hysteresis Model has a simple mechanical analogy formed by the parallel connection of a spring and a sliding frictional element, as illustrated in Fig. 2.3 (left).

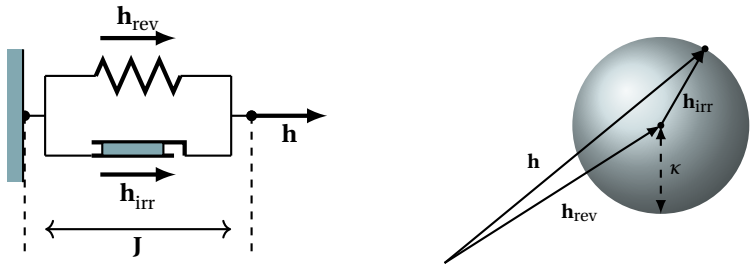

Figure 2.3: *1D Mechanical analogy (left) and 3D pictorial representation (right) of one cell of the EB Model.*

In this one-dimensional (*1D*) representation, the applied force corresponds to the applied magnetic field $\mathbf{h}$ while the elongation mimics the magnetic polarization $\mathbf{J}$ of the material. In this model, the reversible part $\mathbf{h}_{\text{rev}}$ and the irreversible part $\mathbf{h}_{\text{irr}}$ act respectively as spring force and friction force with their corresponding lumped element. The friction slider unlocks when the applied field exceeds the threshold κ, allowing the spring to elongate and thus the magnetization to change, impacting on the Helmholtz free energy f that is stored in the non-linear spring element.

Fig. 2.3 (right) gives another visual three-dimensional (*3D*) representation of the equation (2.22). The grey sphere of radius κ centred in $\mathbf{h}_{\text{rev}}$ is the representation of all the elements $\mathbf{h}_{\text{irr}}$ of the subdifferential (2.20). While the tip of the applied field $\mathbf{h}$ remains inside the sphere, one has $|\mathbf{h}_{\text{irr}}| = |\mathbf{h} - \mathbf{h}_{\text{rev}}| < \kappa$ such that the magnetization remains constant, $\dot{\mathbf{J}} = \mathbf{0}$, implying that the reversible field $\mathbf{h}_{\text{rev}}$ stays unmodified so that the sphere does not move. This situation illustrates the constancy of the magnetization at a given value $\mathbf{J}$ even if the applied field $\mathbf{h}$ is changing. As soon as the extremity of the vector $\mathbf{h}$ reaches the sphere, $\mathbf{h}_{\text{rev}}$ changes and the sphere moves along with it in order to verify condition (2.22). In this situation, the magnetization changes, $\dot{\mathbf{J}} \neq \mathbf{0}$, and verifies the evolution law

$$\mathbf{h} - \frac{\partial f}{\partial \mathbf{J}} - \kappa \frac{\dot{\mathbf{J}}}{|\dot{\mathbf{J}}|} = \mathbf{0}. \tag{2.23}$$

Fig. 2.4 displays the relation between magnetization and magnetic field with hysteresis behaviour in the scalar case, i.e. when the fields are assumed to vary in the same direction. The evolution equation (2.23) simplifies to $h = \partial_J f \pm \kappa$ respectively along the ascending ($\dot{J} > 0$) and descending ($\dot{J} < 0$) branches of the magnetic polarization curve. Minor loops and first magnetization curve are unrealistic horizontal lines ($\dot{J} = 0$) linking the branches of the major loop.

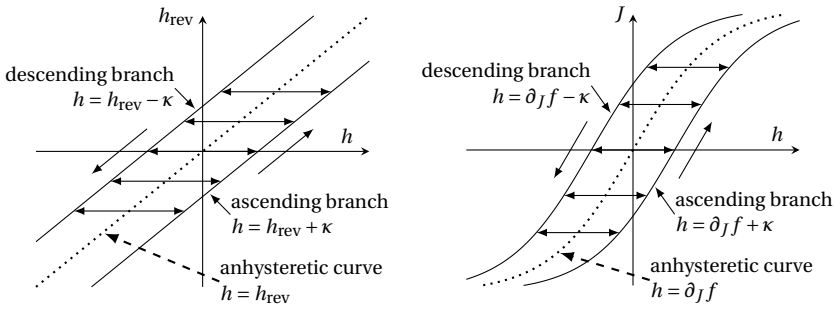

Figure 2.4: *Magnetic polarization curve with hysteresis in one spatial direction.*

The elementary $\mathbf{J}-\mathbf{h}$ curve in Fig. 2.4 (right), is non-differentiable at specific angular points, when there is a brutal change in the derivative $\frac{\partial \mathbf{J}}{\partial \mathbf{h}}$ induced by (2.20), at the moment where the magnetization process switches between a constant ($\dot{\mathbf{J}} = \mathbf{0}$) and a varying regime ($|\mathbf{h} - \mathbf{h}_{rev}| = |\mathbf{h}_{irr}| = \kappa$). These changes in the derivative occurring at reversal or turnaround points are intrinsic of the hysteresis phenomenon and appear in every hysteresis model description. Such discontinuities are responsible for numerical problems in hysteresis model implementation. These difficulties and practical solutions leading to efficient computer implementations will be presented in Chapter 3 and Chapter 4.

5. Multi-Cells Model

The single cell model prediction for the major hysteresis loops can already agree with experimental measurements. However, this is not true for minor loops which are far from realistic as shown in Fig. 2.4. This highly simplistic behaviour comes from the fact that the state of the material is only predicted from the net magnetization and that the considered pinning strength is a single quantity. To give a more realistic picture, the complex influence of the pinning sites characterized by different and rapidly varying strengths at the microscopic scale has to be integrated somehow. Because a complete description of the microscopic structure remains inconceivable, the approach followed here and already presented in [17, 15, 104] considers that, instead of a single value κ, the pinning field obeys a distribution law to represent better the statistical distribution of the pinning strengths in the ferromagnetic microstructure. The idea consists in decomposing the media into independent regions, all subjected to the magnetic field $\mathbf{h}$, but each with its own pinning strength, $\kappa^*(\lambda) = \lambda\kappa$, where λ is a dimensionless value characteristic of the region, which scales the width of the hysteresis loop. A magnetic moment then belongs to the region associated to the pinning field $\kappa^*(\lambda)$ with a given probability $\zeta(\lambda)$. By definition, the distribution $\zeta(\lambda)$ verifies the normalization condition $\int_0^\infty \zeta(\lambda)d\lambda = 1$. The magnetic state of a λ-region is defined by a magnetic polarization $\mathbf{J}^*(\lambda)$ that is related to a reversible magnetic field $\mathbf{h}^*_{rev}(\lambda)$ by

$$\mathbf{J}^*(\lambda) = \zeta(\lambda)\mathbf{J}_{an}\left(\mathbf{h}^*_{rev}(\lambda)\right) \longleftrightarrow \mathbf{h}^*_{rev}(\lambda) = \mathbf{J}^{-1}_{an}\left(\frac{\mathbf{J}^*(\lambda)}{\zeta(\lambda)}\right), \tag{2.24}$$

where the probability $\zeta(\lambda)$ weights the constitutive law to balance the relative importance of the λ-region contribution. The associated free-energy density stored in the λ-region, $f^*(\mathbf{J}^*(\lambda))$, can be expressed in terms of the known free-energy function $f(\mathbf{J})$, deducing the weighted relation

$$f^*(\mathbf{J}^*(\lambda)) = \zeta(\lambda) f\left(\frac{\mathbf{J}^*(\lambda)}{\zeta(\lambda)}\right), \tag{2.25}$$

such that $\dot{f}^*(\mathbf{J}^*(\lambda)) = \mathbf{h}^*_{\text{rev}}(\lambda)\cdot\dot{\mathbf{J}}^*(\lambda)$. Likewise, a region-dependent dissipation function $D^*(\lambda)$ with a related irreversible field $\mathbf{h}^*_{\text{irr}}(\lambda)$ is introduced

$$D^*(\lambda) = |\kappa^*(\lambda)\dot{\mathbf{J}}^*(\lambda)| = \mathbf{h}^*_{\text{irr}}(\lambda)\cdot\dot{\mathbf{J}}^*(\lambda), \tag{2.26}$$

such that, in each λ-subsystem, the energy conservation (2.9) writes

$$D^*(\lambda) = \mathbf{h}\cdot\dot{\mathbf{J}}^*(\lambda) - \dot{f}^*(\mathbf{J}^*(\lambda)) \tag{2.27}$$

or, after factorizing $\dot{\mathbf{J}}^*(\lambda)$ as in (2.21), one deduces

$$\left(\mathbf{h} - \mathbf{h}^*_{\text{rev}}(\lambda) - \mathbf{h}^*_{\text{irr}}(\lambda)\right)\cdot\dot{\mathbf{J}}^*(\lambda) = 0. \tag{2.28}$$

As the state variables $\dot{\mathbf{J}}^*(\lambda)$ are arbitrary, the expression between the parentheses must vanish. Therefore, each of the λ-region is governed by a fundamental evolution law similar to (2.22),

$$\begin{aligned} &\mathbf{h} - \mathbf{h}^*_{\text{rev}}(\lambda) - \mathbf{h}^*_{\text{irr}}(\lambda) = \mathbf{0} \\ \Leftrightarrow\ &\mathbf{h} - \frac{\partial f^*}{\partial \mathbf{J}^*} \in \partial D^*(\dot{\mathbf{J}}^*(\lambda)) = \begin{cases} \mathbf{h}^*_{\text{irr}}(\lambda)\,, |\mathbf{h}^*_{\text{irr}}(\lambda)| \le \kappa^*(\lambda), & \text{if} \dot{\mathbf{J}}^*(\lambda) = \mathbf{0} \\ \mathbf{h}^*_{\text{irr}}(\lambda) = \kappa^*(\lambda)\dfrac{\dot{\mathbf{J}}^*(\lambda)}{|\dot{\mathbf{J}}^*(\lambda)|}, & \text{otherwise} \end{cases}. \end{aligned} \tag{2.29}$$

In this simplified approach, it is supposed that the pseudo-regions are all independent of one another such that the equations (2.29) can be handeld separately in each λ-region, for a given magnetic field $\mathbf{h}$. In addition with (2.24), the model is thus perfectly defined at the mesocopic scale. Finally, all the region-dependent quantities have to be averaged out into the homogenized macroscopic quantities. There are at least two ways to homogenize the model in order to bring the information up to the macroscopic scale.

5.1. Homogenization of the Energy Balance

In this strategy, the total homogenized magnetic polarization is expressed as the sum of all contributions from an infinite number of λ-regions

$$\mathbf{J} = \int_0^\infty \mathbf{J}^*(\lambda)\,d\lambda = \int_0^\infty \zeta(\lambda)\mathbf{J}_{\text{an}}\left(\mathbf{h}^*_{\text{rev}}(\lambda)\right)d\lambda. \tag{2.30}$$

Integrating (2.28) over all λ, allows to get the homogenized energy balance

$$\mathbf{h}\cdot\dot{\mathbf{J}} = \int_0^\infty \left(\mathbf{h}^*_{\text{rev}}(\lambda)\cdot\dot{\mathbf{J}}^*(\lambda)\right)d\lambda + \int_0^\infty \left(\mathbf{h}^*_{\text{irr}}(\lambda)\cdot\dot{\mathbf{J}}^*(\lambda)\right)d\lambda, \tag{2.31}$$

where the first and second integrals correspond to the homogenized quantities of the rate-of-change of the Helmholtz free energy density and the dissipation function, respectively. The former integral may also be expressed with

$$\int_0^\infty \left(\mathbf{h}^*_{\text{rev}}(\lambda)\cdot\dot{\mathbf{J}}^*(\lambda)\right)d\lambda = \int_0^\infty \dot{f}^*(\mathbf{J}^*(\lambda))d\lambda = \int_0^\infty \zeta(\lambda)\dot{f}\left(\frac{\mathbf{J}^*(\lambda)}{\zeta(\lambda)}\right)d\lambda := \frac{d}{dt}\langle f\rangle. \quad (2.32)$$

The global equilibrium (2.31) is verified exactly provided the local equations (2.29) are resolved.

This homogenization technique, that remains in accordance with the energy balance and defines the net magnetization as an infinite sum of elementary contributions, represents the most natural way to express the *EB* model at macroscopic scale. Moreover, to the author knowledge, all the *EB* hysteresis model studied in the literature rely exclusively on this way of homogenizing.

5.2. Homogenization of the Magnetic Field

It is worth mentioning an interesting alternative homogenization method based, this time, on the averaging of the magnetic fields. According to this approach, the homogenized reversible and irreversible magnetic fields are simply defined by taking the weighted average from every λ-component

$$\mathbf{h}_{\text{rev}} := \int_0^\infty \zeta(\lambda)\mathbf{h}^*_{\text{rev}}(\lambda)d\lambda, \qquad \mathbf{h}_{\text{irr}} := \int_0^\infty \zeta(\lambda)\mathbf{h}^*_{\text{irr}}(\lambda)d\lambda. \quad (2.33, 2.34)$$

The anhysteretic one-to-one relation between the homogenized quantities $\mathbf{J}$ and $\mathbf{h}_{\text{rev}}$ is no more guaranteed from the postulates (2.30) and (2.33). Therefore, from (2.33), it is possible to investigate an alternative macroscopic vector $\check{\mathbf{J}}$ directly linked through the anhysteretic function law to the averaged quantity $\mathbf{h}_{\text{rev}}$ by

$$\check{\mathbf{J}} := \mathbf{J}_{\text{an}}(\mathbf{h}_{\text{rev}}) = \mathbf{J}_{\text{an}}\left(\int_0^\infty \zeta(\lambda)\mathbf{h}^*_{\text{rev}}(\lambda)d\lambda\right), \quad (2.35)$$

where the symbol $\check{}$ is used to distinguish this definition from the previous homogenized value $\mathbf{J}$, obtained by the other homogenization strategy (2.30). Actually, comparing both expressions (2.30) and (2.35), it appears that only the position of the application of the anhysteretic function, that is either inside or outside the integral operator, differs between these two definitions.

Exploiting these new homogenized values $\mathbf{h}_{\text{rev}}, \mathbf{h}_{\text{irr}}$ and $\check{\mathbf{J}}$, a thermodynamic balance in the same idea as (2.31), can also be expressed at the macroscopic level with

$$\mathbf{h}\cdot\dot{\check{\mathbf{J}}} = \mathbf{h}_{\text{rev}}\cdot\dot{\check{\mathbf{J}}} + \mathbf{h}_{\text{irr}}\cdot\dot{\check{\mathbf{J}}}, \quad (2.36)$$

which is also satisfied as soon as all the local energy balances (2.29) are equilibrated. The first and second terms of the right hand side in (2.36) can be assimilated to a variation of Helmholtz free energy density and to a dissipation function respectively. For

the former, this may seem to be a proper way to homogenize the rate-of-change of the Helmholtz energy, with

$$\mathbf{h}_{\text{rev}} \cdot \check{\dot{\mathbf{J}}} = \mathbf{J}_{\text{an}}^{-1}\left(\check{\mathbf{J}}\right) \cdot \check{\dot{\mathbf{J}}} = \dot{f}\left(\check{\mathbf{J}}\right) := \frac{d}{dt}\langle \check{f} \rangle, \tag{2.37}$$

having regard to the definition of $\check{\mathbf{J}}$ (2.35) and (2.14), although the value obtained for $\langle \check{f} \rangle$ is then obviously slightly different from the one defined for $\langle f \rangle$ in (2.32). On the other hand, the last term in (2.36) is a rather artificial term of dissipation. There is actually no real sense to consider a globally averaged irreversible magnetic field in the dissipation description. As a result, the equation (2.36) only reflects, at the end, a pseudo balance of energies involving unnatural global terms, that only tend to approximate the more appropriate homogenized energy definitions proposed with the general thermodynamic balance in (2.31).

This illustrates the paradox of choosing one or the other homogenization strategy, that cannot escape some form of approximation at some point. Thus, by making the choice to preserve the characteristics of the anhysteretic law at the macroscopic scale with (2.35), the homogenization continuity is necessarily accompanied by a loss of representability of the thermodynamic balance for the macroscopic scale.

Therefore, since, as its name indicates, the emphasis is mainly on energy, the choice of a homogenization based on the energy balance is preferentially used in practice for the *EB* hysteresis model. However, homogenization by the magnetic field must not be neglected for the cause. Indeed, it will be shown that it also has a role to play in the model parameter identification strategy discussed in Chapter 6.

CHAPTER

3 Discrete Energy-Based Hysteresis Model Implementations

AFTER discretization of the pinning field distribution, this chapter introduces three numerical implementations of the energy-based (*EB*) hysteresis model, all driven by the magnetic field $\mathbf{h}$. The first one, which is similar to a Vector Play Model, is rigorous in the one-dimensional (*1D*) case but contains a small approximation when used in two-dimensional (*2D*) or three-dimensional (*3D*) cases. The second implementation, of the variational approach type, has been undertaken more recently. It is based on a visco-plasticity model in solid mechanics and avoids the approximation mentioned above. Finally, an original third approach, called differential approach, is implemented and consists in directly solving the non-linear differential equation which reflects the energy balance of the ferromagnetic material, without minimizing an energy functional. The latter approach exploits the fact that the solution of the equation is necessarily located on a circle (in *2D*) or a sphere (in *3D*) in the space of the variables that define the state of magnetization, when it changes. These three implementations are then verified with illustrative examples and intensely compared with respect to each other on the basis of efficiency and accuracy.

1. Discretization

For numerical implementations, the continuous distribution $\zeta(\lambda)$ is approximated by a mixture of N types of pseudo-particles. It is obtained by partitioning the λ range into N parts, $\lambda^0 = 0 < \lambda^1 < \cdots < \lambda^{N-1} < \lambda^N = \infty$, each part, $k = 1, \ldots, N$, being associated with a specific weight, ω^k, and a distinct pinning strength, κ^k, given respectively by

$$\omega^k = \int_{\lambda^{k-1}}^{\lambda^k} \zeta(\lambda)\, d\lambda\,, \qquad \kappa^k = \frac{\displaystyle\int_{\lambda^{k-1}}^{\lambda^k} \zeta(\lambda)\kappa^*(\lambda)\, d\lambda}{\omega^k}\,. \tag{3.1, 3.2}$$

Therefore, the integrals from the previous chapter are replaced by sums and the homogenization relation (2.30) becomes

$$\mathbf{J} = \sum_{k=1}^{N} \mathbf{J}^k = \sum_{k=1}^{N} \omega^k \mathbf{J}_{\text{an}}\left(\mathbf{h}_{\text{rev}}^k\right), \tag{3.3}$$

with $\mathbf{J}^k$ and $\mathbf{h}_{\text{rev}}^k$, the magnetic polarization and the reversible magnetic field of region k, respectively. The global energy balance (2.31), in this discretized context, becomes

$$\mathbf{h}\cdot\dot{\mathbf{j}} = \sum_{k=1}^{N} \mathbf{h}_{\text{rev}}^k \cdot \dot{\mathbf{J}}^k + \sum_{k=1}^{N} \mathbf{h}_{\text{irr}}^k \cdot \dot{\mathbf{J}}^k, \tag{3.4}$$

with $\mathbf{h}_{\text{irr}}^k$, the irreversible magnetic field of region k. In the mechanical analogy, this comes down to connecting in series N cells like Fig. 2.3 (left) resulting in Fig. 3.1.

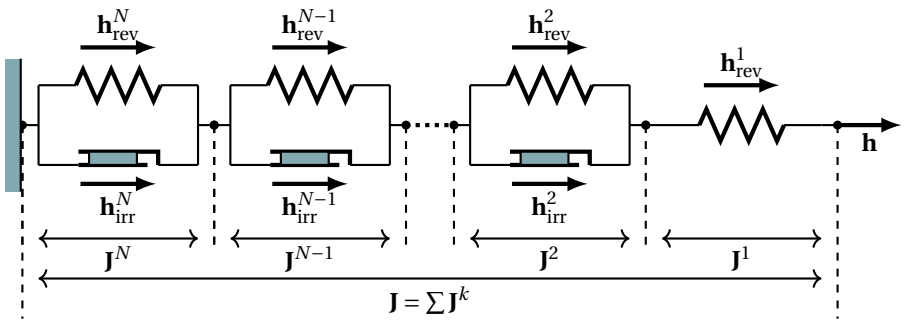

Figure 3.1: *Mechanical analogy of the hysteresis model with N cells.*

Like previously, the individual cell energy balances can be solved separately, such that each region k is governed by an analogue of the local fundamental evolution law (2.29) of the *EB* hysteresis model

$$\mathbf{h} - \mathbf{h}_{\text{rev}}^k - \mathbf{h}_{\text{irr}}^k = \mathbf{0}, \tag{3.5}$$

each characterized by a specific pinning strength κ^k, one of them, e.g. $k = 1$, being zero, $\kappa^1 = 0$, in order to incorporate local reversibility. The reversible magnetization $\mathbf{h}_{\text{rev}}^1$ associated with this fraction represents the bending of the Bloch walls. Pursuing the analogy with the continuous case, the N subsystems have their own free-energy density $f^k(\mathbf{J}^k)$ and dissipation function $D^k(\dot{\mathbf{J}}^k)$, likewise (2.25) and (2.26) after substituting $\zeta(\lambda)$ with ω^k and $\kappa^*(\lambda)$ with κ^k. Eventually, the *EB* hysteresis model (3.5) can be expressed in terms of $\mathbf{J}^k$

$$\mathbf{h} - \frac{\partial f^k}{\partial \mathbf{J}^k} \in \partial D^k(\dot{\mathbf{J}}^k) = \begin{cases} \mathbf{h}_{\text{irr}}^k, |\mathbf{h}_{\text{irr}}^k| \le \kappa^k, & \text{if} \dot{\mathbf{J}}^k = \mathbf{0} \\ \mathbf{h}_{\text{irr}}^k = \kappa^k \dfrac{\dot{\mathbf{J}}^k}{|\dot{\mathbf{J}}^k|}, & \text{otherwise} \end{cases}. \tag{3.6}$$

The output induction field $\mathbf{b}$ of the *EB* Hysteresis model is represented as a sum of the empty space magnetic polarization $\mathbf{J}^0$, and the total material magnetic polarization $\mathbf{J}$

$$\mathbf{b} = \mathbf{J}^0 + \mathbf{J} = \mu_0 \mathbf{h} + \sum_{k=1}^{N} \mathbf{J}^k = \mu_0 \mathbf{h} + \sum_{k=1}^{N} \omega^k \mathbf{J}_{\text{an}} \left(\mathbf{h}_{\text{rev}}^k \right). \tag{3.7}$$

Three implementations of the hysteresis model are considered hereafter. The first one is an approximate explicit solution of the non-linear differential equation in terms of $\mathbf{h}_{\text{rev}}^k$. The second one exploits a variational formulation of (3.6) in function of $\mathbf{J}^k$, derived from the theory of plasticity, to deduce the exact solution from an optimization problem. Finally, the third one solves the non-linear equation implicitly, expressed in terms of $\mathbf{h}_{\text{rev}}^k$, to provide an alternative exact resolution method. These three implementations are called: the Vector Play Model, the variational approach and the differential approach, respectively. They are presented in more detail in the three following dedicated sections.

For their numerical implementation, the update equations have to be discretized in time. Accordingly, the vector quantities $\mathbf{J}^k$ for the variational approach or $\mathbf{h}_{\text{rev}}^k$ for the two other ones must be recorded in each pinning domain, $k = 1, \ldots, N$, to account for the memory effect at a given time step. In the following, the subscript (p) is used to denote a saved value from the previous time instant so that the derivative of an arbitrary quantity $\dot{x}$ is approximated by $(x - x_{(p)})/\Delta t$, with Δt the time increment between two time steps.

2. Simplified Differential Approach - Vector Play Model

The resolution of the differential equation in terms of $\mathbf{h}_{\text{rev}}^k$, for given k, is not straightforward, namely because the direction of the irreversible field $\mathbf{h}_{\text{irr}}^k = \mathbf{h} - \mathbf{h}_{\text{rev}}^k$ from (3.5) depends on the unknown vector $\mathbf{h}_{\text{rev}}^k$. The unit vector indicating the direction of the irreversible field is indeed

$$\mathbf{e}_{\mathbf{h}_{\text{irr}}^k} = \frac{\mathbf{h}_{\text{irr}}^k}{|\mathbf{h}_{\text{irr}}^k|} = \frac{\mathbf{h} - \mathbf{h}_{\text{rev}}^k}{|\mathbf{h} - \mathbf{h}_{\text{rev}}^k|}. \tag{3.8}$$

Therefore, a simplification already presented in [104] has been considered as a first approach where it is assumed that $\mathbf{h}_{\text{irr}}^k$ is parallel to $\mathbf{h} - \mathbf{h}_{\text{rev}(p)}^k$ instead of $\mathbf{h} - \mathbf{h}_{\text{rev}}^k$ (see Fig. 3.2), with $\mathbf{h}_{\text{rev}(p)}^k$ the value of $\mathbf{h}_{\text{rev}}^k$ at the previous time instant, such that the unit vector of the irreversible fields (3.8) can now be expressed based only on known vector quantities $\mathbf{h}$ and $\mathbf{h}_{\text{rev}(p)}^k$

$$\mathbf{e}_{\mathbf{h}_{\text{irr}}^k} \approx \frac{\mathbf{h} - \mathbf{h}_{\text{rev}(p)}^k}{|\mathbf{h} - \mathbf{h}_{\text{rev}(p)}^k|}. \tag{3.9}$$

Using this simplification (3.9) in the differential equation (3.6) expressed in terms of $\mathbf{h}_{\text{rev}}^k$ allows to derive an approximate solution that verifies the following explicit update

rule

$$\mathbf{h}^k_{\text{rev}} = \mathscr{U}^k(\mathbf{h}, \mathbf{h}^k_{\text{rev}(p)}) := \begin{cases} \mathbf{h}^k_{\text{rev}(p)}\,, & \text{if } |\mathbf{h} - \mathbf{h}^k_{\text{rev}(p)}| \leq \kappa^k\,, \\ \mathbf{h} - \kappa^k \dfrac{\mathbf{h} - \mathbf{h}^k_{\text{rev}(p)}}{|\mathbf{h} - \mathbf{h}^k_{\text{rev}(p)}|}\,, & \text{otherwise} \end{cases}, \tag{3.10}$$

turning the hysteresis model into a Vector Play Model (*vpm*) where the whole implementation of the hysteresis delay relies on the conditional statement, similar to (1.24). By construction, the *vpm* approach (3.10) ensures $|\mathbf{h}^k_{\text{irr}}| = \kappa^k$ when $\dot{\mathbf{h}}^k_{\text{rev}} \neq \mathbf{0}$, but with $\mathbf{h}^k_{\text{irr}}$ pointing in the approximated direction (3.9). Actually, the assumed parallelism between $\mathbf{h}^k_{\text{irr}}$ and $\mathbf{h} - \mathbf{h}^k_{\text{rev}(p)}$, can be expressed as follows

$$\mathbf{h}^k_{\text{irr}} \approx r(\mathbf{h} - \mathbf{h}^k_{\text{rev}(p)})\,, \tag{3.11}$$

with r a positive constant scalar value. Moreover, as $\mathbf{h}^k_{\text{rev}(p)} \approx \mathbf{h}^k_{\text{rev}} - \Delta t \dot{\mathbf{h}}^k_{\text{rev}}$ due to the time discretization and as $\mathbf{h}^k_{\text{irr}} = \mathbf{h} - \mathbf{h}^k_{\text{rev}}$ from (3.5), the relation (3.11) can be rewritten as

$$\mathbf{h}^k_{\text{irr}} \approx \frac{r}{1-r} \Delta t \dot{\mathbf{h}}^k_{\text{rev}}\,. \tag{3.12}$$

This new link of proportionality shows that with the approximation (3.9), $\mathbf{h}^k_{\text{irr}}$ is supposed parallel to $\dot{\mathbf{h}}^k_{\text{rev}}$ instead of $\dot{\mathbf{J}}^k$. As a consequence, the explicit rule (3.10) is theoretically exact only for situations where $\dot{\mathbf{J}}^k = r' \dot{\mathbf{h}}^k_{\text{rev}}$, with r' a coefficient of proportionality. Therefore, this is valid for unidirectional and purely rotational hysteresis problems, or in situations where $\mathbf{J}^k$ depends linearly on $\mathbf{h}^k_{\text{rev}}$. In other cases, the *vpm* approach remains an approximation that can introduce a small error [113], that does not reduce even if the increment of $\mathbf{h}$ between two time steps tends to zero [177].

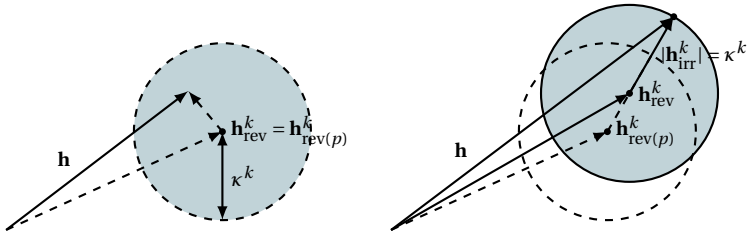

Figure 3.2: *Illustration of the vpm approach when* $\dot{\mathbf{h}}^k_{rev} = \mathbf{0}$ *(left) and* $\dot{\mathbf{h}}^k_{rev} \neq \mathbf{0}$ *(right).*

From the known values $\mathbf{h}^k_{\text{rev}(p)}$ corresponding to the magnetic state $\mathbf{J}^k_{(p)}$ at time $t - \Delta t$, the explicit rule (3.10) determines the new values $\mathbf{h}^k_{\text{rev}}$ after a slight field change to a new value $\mathbf{h}$ at time t. The induction field $\mathbf{b}$ deduced from the *vpm* approach for the current instant t is obtained with

$$\mathbf{b} = \mathscr{B}^{vpm}(\mathbf{h}, \mathbf{h}^k_{\text{rev}(p)}) = \mu_0 \mathbf{h} + \sum_{k=1}^{N} \omega^k \mathbf{J}_{\text{an}} \left(\mathscr{U}^k(\mathbf{h}, \mathbf{h}^k_{\text{rev}(p)}) \right). \tag{3.13}$$

This constitutes a direct, explicit, implementation of the *EB* hysteresis model.

3. Variational Approach - Functional Minimization

The second approach investigated in [79] and used in [116, 113], consists in solving exactly the non-linear equations (3.6) in terms of $\mathbf{J}^k$ through a variational formulation inspired from the theory of plasticity, due to the similarity between the magnetic hysteresis model and the stress-strain model with kinematic hardening of Saint-Venant [179], the fields $\mathbf{h}$ and $\mathbf{J}^k$ being analoguous to the stress and strain tensors respectively. The idea consists in building for each cell a functional Ω^k of the state variable $\mathbf{J}^k$ such that the evolution of the magnetic polarization $\mathbf{J}^k$ can only proceed in the sense of minimizing these functionals Ω^k. Each of them is determined in two steps. First, for each cell k, the Landau free energy $g_L^k(\mathbf{h},\mathbf{J}^k)$, that is linked to the Helmholtz potential f^k by

$$g_L^k(\mathbf{h},\mathbf{J}^k) = f^k(\mathbf{J}^k) - \mathbf{h}\cdot\mathbf{J}^k\,, \tag{3.14}$$

is introduced, and one verifies that

$$\frac{\partial g_L^k}{\partial \mathbf{J}^k} = \frac{\partial f^k}{\partial \mathbf{J}^k} - \mathbf{h} \qquad , \qquad \frac{\partial g_L^k}{\partial \mathbf{h}} = -\mathbf{J}^k\,. \tag{3.15}$$

Second, due to a disagreement between the natural argument of the dissipation function D^k, i.e. $\dot{\mathbf{J}}^k$, and the desired functional Ω^k that should be a function of $\mathbf{J}^k$, it is convenient to define pseudo-potentials, i.e. alternative dissipation functions,

$$\tilde{D}^k(\mathbf{J}^k,\mathbf{J}^k_{(p)}) = \kappa^k|\mathbf{J}^k - \mathbf{J}^k_{(p)}|\,, \tag{3.16}$$

expressed in joule per unit volume (J/m^3), whose related subgradients,

$$\partial_{\mathbf{J}^k}\tilde{D}^k(\mathbf{J}^k,\mathbf{J}^k_{(p)}) = \begin{cases} \mathbf{h}^k_{\text{irr}}\,, |\mathbf{h}^k_{\text{irr}}| \le \kappa^k\,, & \text{if} \mathbf{J}^k = \mathbf{J}^k_{(p)} \\ \mathbf{h}^k_{\text{irr}} = \kappa^k \dfrac{\mathbf{J}^k - \mathbf{J}^k_{(p)}}{|\mathbf{J}^k - \mathbf{J}^k_{(p)}|}\,, & \text{otherwise} \end{cases}\,, \tag{3.17}$$

correspond to discrete approximations of the subdifferentials of $\partial D^k(\dot{\mathbf{J}}^k)$, like with (2.20). These functions are now expressed in terms of the magnetic polarization field $\mathbf{J}^k$, as desired, with, as additional argument, the value from the previous time step $\mathbf{J}^k_{(p)}$, that contains the magnetic history of the material response. Thanks to (3.14) and (3.16), the problem (3.6) can be restated as

$$\frac{\partial}{\partial \mathbf{J}^k}\left(g_L^k + \tilde{D}^k\right) = \mathbf{0}\,, \tag{3.18}$$

that results in the functional to minimize:

$$\Omega^k(\mathbf{h},\mathbf{J}^k,\mathbf{J}^k_{(p)}) := g_L^k(\mathbf{h},\mathbf{J}^k) + \tilde{D}^k(\mathbf{J}^k,\mathbf{J}^k_{(p)})\,. \tag{3.19}$$

It is worth noting that the functional (3.19) has the unit of an energy density (J/m^3) while its gradient with respect to $\mathbf{J}^k$ (3.18) has the unit of a magnetic field (A/m). The typical shape of a functional Ω^k is illustrated in Fig. 3.3. It consists of a strictly convex

function with the presence of an angulous point in $\mathbf{J}^k_{(p)}$. The updated values $\mathbf{J}^k$, at each time step, follow from minimizing separately each independent Ω^k

$$\mathbf{J}^k = \mathscr{J}^k(\mathbf{h}, \mathbf{J}^k_{(p)}) = \underset{\mathbf{J}^k}{\operatorname{argmin}}\, \Omega^k(\mathbf{h}, \mathbf{J}^k, \mathbf{J}^k_{(p)})\,. \tag{3.20}$$

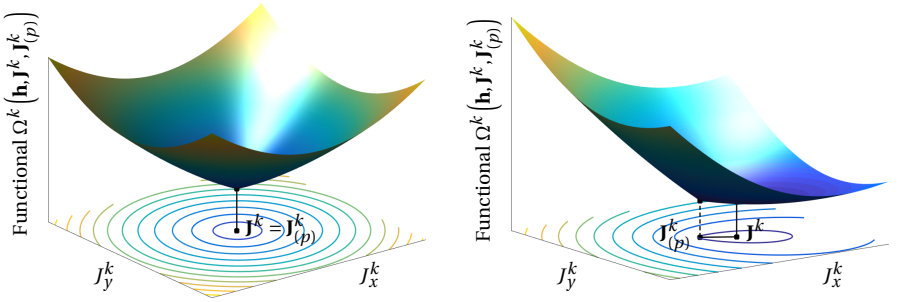

Figure 3.3: *Illustration of the var approach when $\dot{\mathbf{J}}^k = \mathbf{0}$ (left) and $\dot{\mathbf{J}}^k \neq \mathbf{0}$ (right).*

At the end, the so-called variational approach (*var*) computes the magnetic induction field $\mathbf{b}$, knowing the magnetic field $\mathbf{h}$ and the state variables from the previous instant $\mathbf{J}^k_{(p)}$ with

$$\mathbf{b} = \mathscr{B}^{var}(\mathbf{h}, \mathbf{J}^k_{(p)}) = \mu_0 \mathbf{h} + \sum_{k=1}^{N} \mathscr{J}^k(\mathbf{h}, \mathbf{J}^k_{(p)})\,. \tag{3.21}$$

It is important to mention that the minimization procedure should in reality only be carried out when the magnetization of a cell is about to change, i.e. when $\dot{\mathbf{J}}^k \neq \mathbf{0}$, and that a new magnetization state $\mathbf{J}^k$ has to be calculated. Therefore, when $|\mathbf{h} - \mathbf{h}^k_{\text{rev}(p)}| \leq \kappa^k$, a condition for which magnetization is frozen, it is known that the magnetization value of minimum energy is necessarily $\mathbf{J}^k = \mathbf{J}^k_{(p)}$, and this can be exploited without any additional computational effort being required. On the other hand, as soon as $|\mathbf{h} - \mathbf{h}^k_{\text{rev}(p)}| > \kappa^k$, the minimum of the energy functional moves towards another point that must be determined through the resolution of an optimization problem (3.20) in order to update accordingly the cell state.

The minimization of the functional can be performed using a collection of different techniques for the descent direction and the step size selections.

As a matter of fact, the followed descent direction updated at each iteration can either be along the steepest descent (*sd*) or along a conjugate gradient (*cg*) direction. The former is based only on the local gradient of the functional while the latter builds the new direction from the knowledge of the previous ones, thanks to the nonlinear conjugate gradient algorithm by Polak and Ribiere described in [172] (pp. 120-122). For a given time step of a simulation, an example of functional minimization accomplished by both of these descent strategies is shown on Fig. 3.4 and Fig. 3.5, respectively. It

appears through this example that the *cg* method approaches much more quickly the solution $\mathbf{J}_{\min}$ than the *sd* method. The latter may require many iterations to converge to the minimum of the potential, especially if the curvature changes significantly in different directions, as seen in this example.

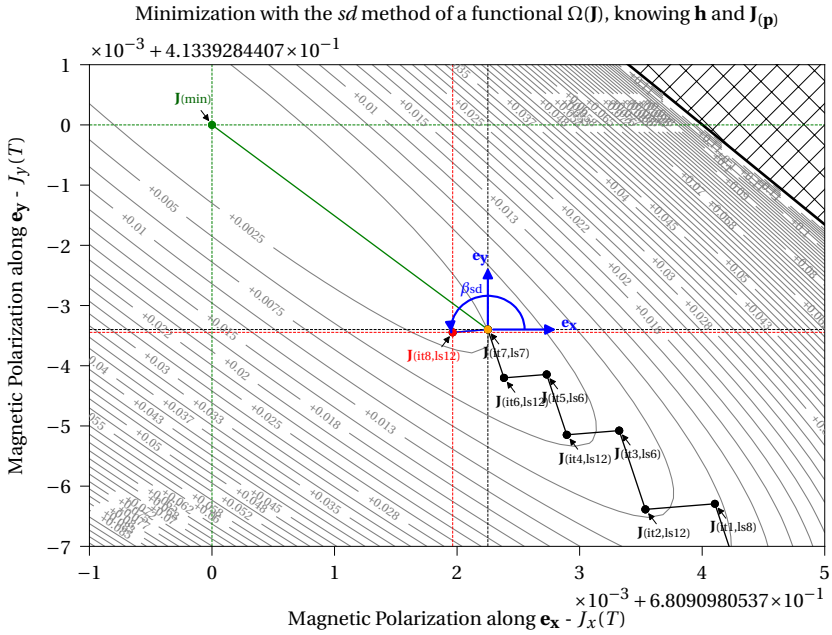

Figure 3.4: *Example of a functional minimization at a given time step using a steepest descent algorithm.* $\mathbf{J}_{(itI,lsL)}$ *indicates the point obtained at iteration* I*, after a line search of* L *steps.* $\mathbf{J}_{(min)}$ *represents the solution.* β_{sd} *indicates the steepest descent direction, here followed at iteration* $I = 8$*. The process requires a lot of direction search steps and converges rather slowly to* $\mathbf{J}_{(min)} \approx (0.68, 0.41)\,(\mathrm{T})$.

Moreover, concerning the step length selection, a line search needs to be applied in order to identify an approximate minimum of the nonlinear functional along the search direction. Here, three line search methods are considered. The first one, referred to as naive (*naive*), consists simply in dividing by two the step length at each line search iteration until the functional becomes smaller than the current value, which is ensured to happen given the convexity of the functional (see Fig. 3.6 (left)). The second method (wolfe (*wolfe*)) probes the functional at different subsequent step lengths in the search direction, until satisfying the strong Wolfe conditions [172]. The functional verifies thus, at the end, a sufficient decrease condition combined with a curvature condition such that the updated slope becomes slightly larger than initially, without being too positive. The *wolfe* conditions lead therefore to a point in a region not far from the stationary point (see Fig. 3.6 (right)). The last studied technique (brent (*brent*)) relies on Brent's method [34] to find the step length that minimizes exactly the functional in the search direction. This algorithm minimizes a function of one variable without use of derivatives, based on a smart combination of inverse parabolic interpolation and improved bisection methods. The *brent* method is thus very robust but also more costly

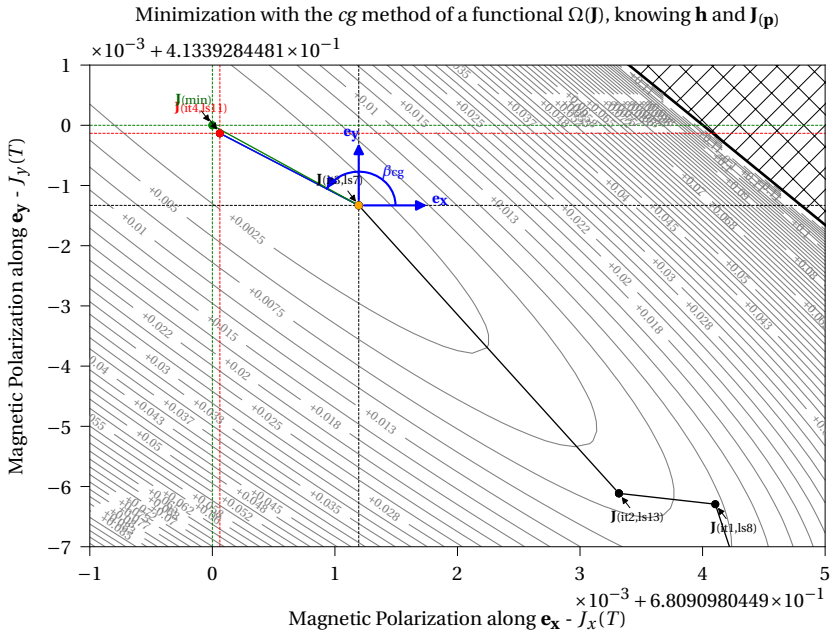

Figure 3.5: *Example of a functional minimization at a given time step using a conjugate gradient algorithm.* $\mathbf{J}_{(itI,lsL)}$ *indicates the point obtained at iteration* I*, after a line search of* L *steps.* $\mathbf{J}_{(min)}$ *represents the solution.* β_{cg} *indicates the conjugate gradient direction, here followed at iteration* $I = 4$*. Compared to the sd method applied in the same condition in Fig. 3.4, the cg process converges more directly to* $\mathbf{J}_{(min)} \approx (0.68, 0.41)(\mathrm{T})$.

compared to the *naive* or the *wolfe* techniques as it converges to the exact minimum rather than an approximation that may be sufficient to continue to the next direction search iteration. In the example of Fig. 3.6, the *brent* method allows hence to find the step length that gives the true minimum of the functional profile in the direction studied.

Eventually, six *var* approach derivations are considered resulting from the combination of each direction choice (*sd* or *cg*) with each line search technique (*naive*, *wolfe* or *brent*).

The choice of the starting point $\mathbf{J}_0^k$ in the minimization procedure also affects greatly the performance of the algorithms. A natural choice is to start the minimization of the functional from the previous time step magnetization state $\mathbf{J}_0^k = \mathbf{J}_{(p)}^k$. This choice is however not the most judicious since this point corresponds precisely to an angular point in the energy functional, as illustrated in Fig. 3.3, which is clearly not ideal for gradient-based descent search methods such as the *sd* and the *cg* methods. Nevertheless, once passed the first iteration by following an initial approximated descent direction, the algorithms can then continue their routine in a more conventional way since the gradient is defined everywhere else. Besides this, a second, more effective starting choice consists to take the result of the *vpm* approach, to initiate the algorithms with

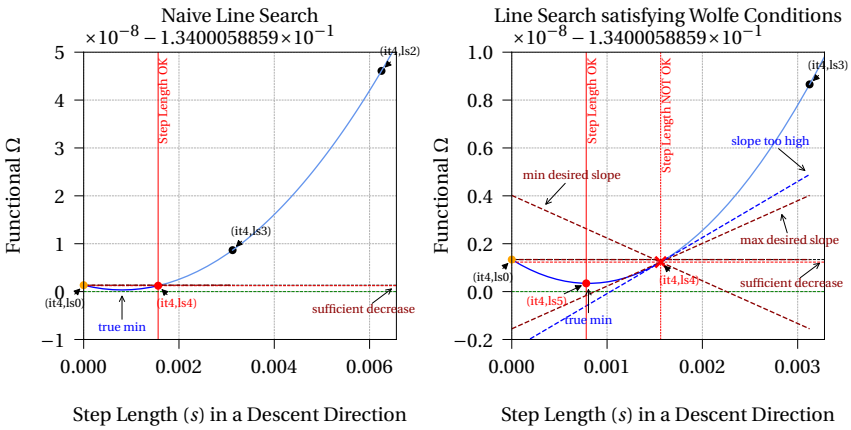

Figure 3.6: *Example of Line Search techniques applied at a given time step, for a given descent direction. The potential profile is shown as a function of the step length in the current descent direction. The notation* (itI, lsL) *indicates the iteration number* I *of the direction search algorithm, which is at* $I = 4$ *here, and the step number* L *of the line search process used in this same direction. From the current position* $(it4, ls0)$*, a naive line search technique (left) tries to find a step length that allows simply to reduce the functional value. After a first guess at* $(it4, ls1)$*, that is possibly taken too far, successive steps are then tested by dividing by two the step length until the corresponding functional value becomes smaller than that of* $(it4, ls0)$*, which happens for* $(it4, ls4)$ *in this example (left). A line search for a step length satisfying the wolfe conditions (right) requires in addition that the slope of the functional lies between minimal and maximal limits in order to come closer to the functional minimizer associated to the current direction. In these conditions,* $(it4, ls4)$ *is no more valid, such that the line search continues and ends at* $(it4, ls5)$*, approaching more the stationary point of the considered direction in this example (right). Note that the search for a step satisfying the wolfe criteria may sometimes require more advanced probing mechanisms than a simple division by two between two successive stages, although that is sufficient for the naive research given the convexity of the energy functional.*

$\mathbf{J}_0^k = \mathbf{J}_{(vpm)}^k = \omega^k \mathbf{J}_{\text{an}}\left(\mathscr{U}^k(\mathbf{h}, \mathbf{h}_{\text{rev}(p)}^k)\right)$, given that it constitutes a fast to compute, good initial approximation of the minimum location. Naturally, the better the initial estimate, the faster the algorithm converges.

The minimization algorithms are supposed to have converged to the solution as soon as the gradient norm of the functional at the current iteration is smaller than an absolute tolerance fixed at $\epsilon = 10^{-11}\,\text{A/m}$. However, in practice, this academic level of accuracy is difficult to reach due to limitation in the number representation using finite-precision arithmetic. Indeed, the line search becomes irrelevant when the step size becomes too small and has no impact on the significant digits of the functional value. Actually, for conventional test cases and more particularly for the examples considered in Chapter 3-Section 5, it can be shown that a modification of the functional value in the order of the machine epsilon, that is the minimal sensitivity for the number representation of the functional, corresponds to a deviation of the solution point $\mathbf{J}^k$ of about $10^{-8}\,\text{T}$ in average, so that it is difficult in view of round-off error to get a better precision than that to the optimal solution. A visualization of this phenomenon encountered during a functional minimization procedure is shown in Fig. 3.7. The numerical pollution manifests clearly with the introduction of parasitic oscillations in

the energy landscape, appearing already for sensitivity scales in the order of 10^{-8} T for $\mathbf{J}^k$. The precision loss is therefore a real limiting factor for the *var* approach accuracy. In order to avoid or limit this undesirable effect, as soon as the step size becomes too small during the search process, the functional is approximated around the current iteration point value by a second-order Taylor polynomial, from which the minimum is thus directly known and can be used as a new starting point for the next direction search iteration if the stop criterion is still not satisfied. Eventually, when the loss of significance is detected, the algorithm is stopped prematurely.

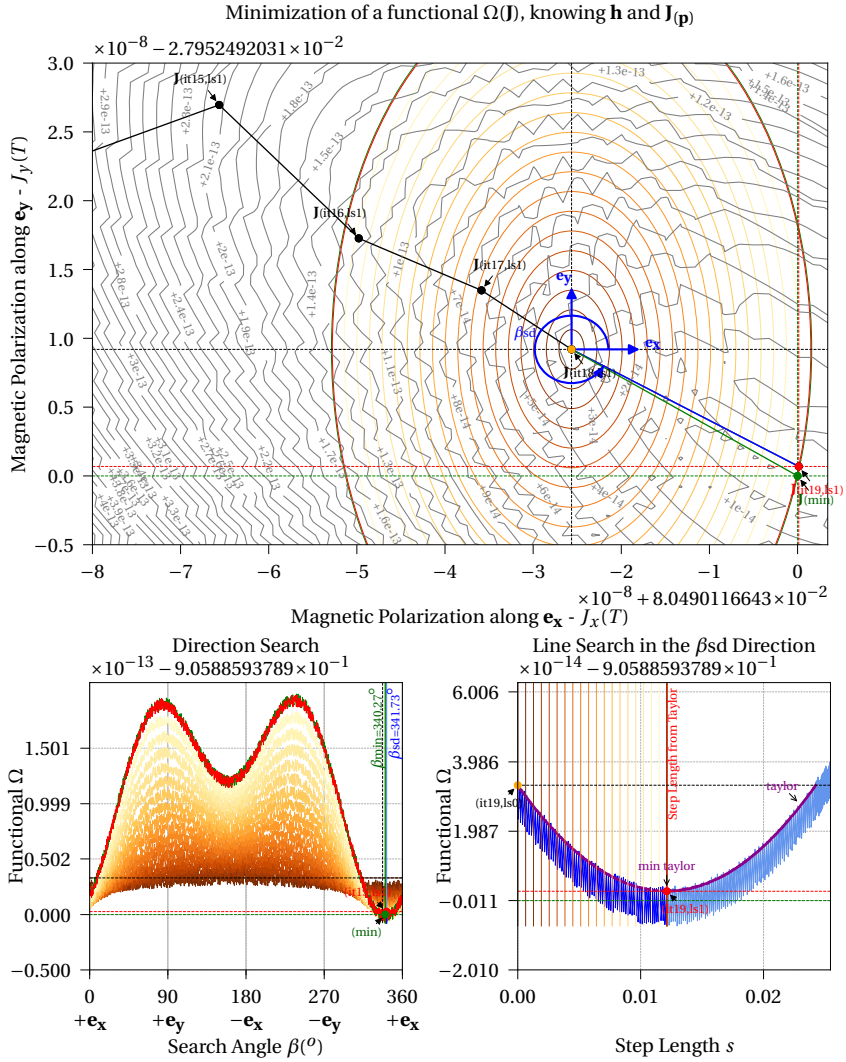

Figure 3.7: *Example of numerical loss of significance effect occurring during a functional minimization at a given time step using a sd algorithm. (top):* $\boldsymbol{J}_{(itI,lsL)}$ *indicates the point obtained at iteration* I*, after a line search of* L *steps.* $\boldsymbol{J}_{(min)} \approx (0.08, -0.03)(\mathrm{T})$ *represents the solution.* β_{sd} *indicates the sd direction, here followed at iteration* $I = 19$*. (bottow left): Energy profiles in function of the search angle* β *are drawn for concentric circles centered on* $\boldsymbol{J}_{(it18,ls1)}$ *(see top) with increasingly larger radii, up to* $\approx 2.7 \times 10^{-8}\,\mathrm{T}$ *(in red), which corresponds to the distance between the value* $\boldsymbol{J}(it18, ls1)$ *and the next iterate* $\boldsymbol{J}(it19, ls1)$*, that is very close to the solution* $\boldsymbol{J}_{(min)}$*. (bottow right): Energy profile along the steepest descent direction, in function of the step length* s*, from* $\boldsymbol{J}(it18, ls1)$*, also denoted by* $\boldsymbol{J}(it19, ls0)$*, towards* $\boldsymbol{J}(it19, ls1)$*, associated to a step length* $s \approx 0.012$*, which coincides hence with a jump of* $\approx 2.7 \times 10^{-8}\,\mathrm{T}$*. In (top), the contour lines are non-smooth and show very tiny suspitious variations. In (bottow left) and (bottow right), energy profiles fluctuate between very low values, in the orders of* 10^{-13} *and* $10^{-14}\,\mathrm{J/m^3}$*, which start to become close to the epsilon machine precision. They are characterized by high frequency digital noise which complicates the continuation of the optimization process. In (bottow right), the line search can be facilitated thanks to a second-order Taylor approximation of the one-dimensional function that smoothes out the parasitic fluctuations. The step length that minimizes the Taylor approximation can then be deduced analytically. This strategy works up to a certain point beyond which the energy sensitivity deteriorates such that there is no longer any hope to continue the minimization.*

4. Full Differential Approach - Angle Searching

The full differential approach aims to solve the non-linear equation (3.6) in terms of $\mathbf{h}_{\text{rev}}^k$ implicitly without any additional approximation other than the time discretization. First, notice that at each time point instant, the solution of (3.6) is $\mathbf{J}^k = \mathbf{J}_{(p)}^k$, i.e. $\mathbf{h}_{\text{rev}}^k = \mathbf{h}_{\text{rev}(p)}^k$, if $|\mathbf{h} - \mathbf{h}_{\text{rev}(p)}^k| \leq \kappa^k$. If this inequality is not verified, the resulting $\mathbf{h}_{\text{rev}}^k$ should necessarily ensure $|\mathbf{h} - \mathbf{h}_{\text{rev}}^k| = \kappa^k$ such that the solution lies on the surface of a sphere of radius κ^k centered in $\mathbf{h}$. For *2D* problems in particular, as illustrated by Fig. 3.8, the tip of the solution $\mathbf{h}_{\text{rev}}^k$ is somewhere on a circle and one establishes

$$\mathbf{h}_{\text{rev}}^k(\alpha^k) = \mathbf{h} - \kappa^k \mathbf{e}_{\mathbf{h}_{\text{irr}}^k}(\alpha^k), \tag{3.22}$$

with

$$\mathbf{e}_{\mathbf{h}_{\text{irr}}^k}(\alpha^k) = (\cos\alpha^k, \sin\alpha^k), \tag{3.23}$$

a unit vector in the direction of the irreversible magnetic field, i.e. angle α^k in the $\mathbf{e}_x$-$\mathbf{e}_y$ plane. For a *3D* problem, the direction is determined by two angles but this case is not discussed further.

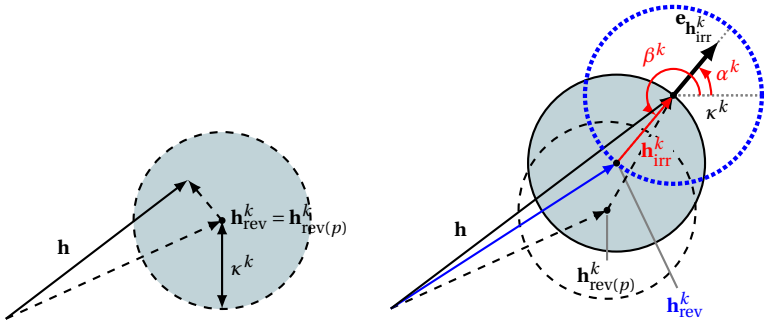

Figure 3.8: *Illustration of the diff approach when* $\dot{\mathbf{h}}_{rev}^k = \mathbf{0}$ *(left) and* $\dot{\mathbf{h}}_{rev}^k \neq \mathbf{0}$ *(right).*

Therefore, the problem now reduces to finding the angle α^k ensuring that the direction of the irreversible field (3.23) is parallel to the time derivative of the polarization $\dot{\mathbf{J}}^k$. For its numerical implementation, this unit direction is approximated after time discretization by,

$$\mathbf{e}_{\dot{\mathbf{J}}^k} = \frac{\dot{\mathbf{J}}^k}{|\dot{\mathbf{J}}^k|} \approx \frac{\mathbf{J}_{\text{an}}(\mathbf{h}_{\text{rev}}^k) - \mathbf{J}_{\text{an}}(\mathbf{h}_{\text{rev}(p)}^k)}{\left|\mathbf{J}_{\text{an}}(\mathbf{h}_{\text{rev}}^k) - \mathbf{J}_{\text{an}}(\mathbf{h}_{\text{rev}(p)}^k)\right|}, \tag{3.24}$$

since the one-to-one relations $\mathbf{J}^k = \omega^k \mathbf{J}_{\text{an}}(\mathbf{h}_{\text{rev}}^k)$ are always valid and the weights ω^k with the time increments Δt cancel in the ratio in (3.24). Substituting (3.22) in (3.24) highlights the dependence of $\mathbf{e}_{\dot{\mathbf{J}}^k}$ in terms of the angle α^k

$$\mathbf{e}_{\dot{\mathbf{J}}^k}(\alpha^k) \approx \frac{\mathbf{J}_{\text{an}}\left(\mathbf{h} - \kappa^k \mathbf{e}_{\mathbf{h}_{\text{irr}}^k}(\alpha^k)\right) - \mathbf{J}_{\text{an}}(\mathbf{h}_{\text{rev}(p)}^k)}{\left|\mathbf{J}_{\text{an}}\left(\mathbf{h} - \kappa^k \mathbf{e}_{\mathbf{h}_{\text{irr}}^k}(\alpha^k)\right) - \mathbf{J}_{\text{an}}(\mathbf{h}_{\text{rev}(p)}^k)\right|}. \tag{3.25}$$

The parallelism, and thus the equality, between the unit vectors $\mathbf{e}_{\mathbf{h}^k_{\text{irr}}}$ (3.23) and $\mathbf{e}_{\mathbf{j}^k}$ (3.25) is ensured if α^k verifies

$$\mathbf{e}_{\mathbf{j}^k}(\alpha^k) \times \mathbf{e}_{\mathbf{h}^k_{\text{irr}}}(\alpha^k) = \mathbf{0} \quad \longleftrightarrow \quad \mathbf{e}_{\mathbf{j}^k}(\alpha^k) = \mathbf{e}_{\mathbf{h}^k_{\text{irr}}}(\alpha^k), \tag{3.26}$$

or, using the notation $\Delta\mathbf{J}^k(\alpha^k) = \omega^k \mathbf{J}_{\text{an}}\left(\mathbf{h} - \kappa^k \mathbf{e}_{\mathbf{h}^k_{\text{irr}}}(\alpha^k)\right) - \omega^k \mathbf{J}_{\text{an}}(\mathbf{h}^k_{\text{rev}(p)})$, the vector relation (3.26) is guaranteed, for *2D* cases, as soon as the following α^k-dependent scalar function $\mathscr{S}^k(\alpha^k)$ cancels

$$\mathscr{S}^k(\alpha^k) = \left(\Delta\mathbf{J}^k(\alpha^k) \cdot \mathbf{e}_x\right) \sin\alpha^k - \left(\Delta\mathbf{J}^k(\alpha^k) \cdot \mathbf{e}_y\right) \cos\alpha^k. \tag{3.27}$$

Note that $\mathscr{S}^k(\alpha^k)$, as well as $\Delta\mathbf{J}^k(\alpha^k)$, are also functions of the vector quantities $\mathbf{h}$ and $\mathbf{h}^k_{\text{rev}(p)}$, but this dependence is not reported in the function's arguments for the sake of brevity here. In summary, in the case when $|\mathbf{h} - \mathbf{h}^k_{\text{rev}(p)}| > \kappa^k$, for given $\mathbf{h}$ and $\mathbf{h}^k_{\text{rev}(p)}$, the problem consists in finding the root α^k_* for which $\mathscr{S}^k(\alpha^k_*, \mathbf{h}, \mathbf{h}^k_{\text{rev}(p)}) = 0$. This can be solved with a one-dimensional bracketing root finding method. Once the correct angles α^k are found, the corresponding updated states $\mathbf{h}^k_{\text{rev}}$ are easily computed with (3.22). Therefore, the update law of the differential approach (*diff*) writes for each cell

$$\mathbf{h}^k_{\text{rev}} = \mathscr{H}^k_{\text{rev}}(\mathbf{h}, \mathbf{h}^k_{\text{rev}(p)}) := \begin{cases} \mathbf{h}^k_{\text{rev}(p)}, & \text{if } |\mathbf{h} - \mathbf{h}^k_{\text{rev}(p)}| \leq \kappa^k, \\ \mathbf{h} - \kappa^k \mathbf{e}_{\mathbf{h}^k_{\text{irr}}}(\alpha^k_*), & \text{otherwise} \end{cases}, \tag{3.28}$$

where α^k_* is such that $\mathscr{S}^k(\alpha^k_*, \mathbf{h}, \mathbf{h}^k_{\text{rev}(p)}) = 0$, which ensures that $\mathbf{e}_{\mathbf{h}^k_{\text{irr}}}(\alpha^k_*) = \mathbf{e}_{\mathbf{j}^k}(\alpha^k_*)$, with the vector identity (3.26). The induction field $\mathbf{b}$ is then calculated by

$$\mathbf{b} = \mathscr{B}^{diff}(\mathbf{h}, \mathbf{h}^k_{\text{rev}(p)}) = \mu_0 \mathbf{h} + \sum_{k=1}^{N} \omega^k \mathbf{J}_{\text{an}}\left(\mathscr{H}^k_{\text{rev}}(\mathbf{h}, \mathbf{h}^k_{\text{rev}(p)})\right). \tag{3.29}$$

An example of cell-update performed by the differential approach for a time step where $|\mathbf{h} - \mathbf{h}^k_{\text{rev}(p)}| > \kappa^k$ is shown in Fig. 3.9. Actually, the function $\mathscr{S}^k(\alpha^k)$ is preferably written in terms of the angle β^k, also visible in Fig. 3.8, which corresponds simply to the angle indicating the opposite searched direction of the irreversible field, such that $\alpha^k = \beta^k + \pi$. The shape of the function $\mathscr{S}^k(\beta^k + \pi)$ is represented in Fig. 3.9 (right). The direction angle β^k_* that cancels $\mathscr{S}^k$ can be found thanks to a one-dimensional bracketing root finding *brent* algorithm. As a starting bracketing interval for the algorithm, one can give the angles $\beta^k_a = \beta^k_{vpm} - \beta^k_\Delta$ and $\beta^k_b = \beta^k_{vpm} + \beta^k_\Delta$, with

$$\beta^k_{vpm} = \text{atan}\left(\frac{\left(\mathbf{h}^k_{\text{rev}(p)} - \mathbf{h}\right) \cdot \mathbf{e}_y}{\left(\mathbf{h}^k_{\text{rev}(p)} - \mathbf{h}\right) \cdot \mathbf{e}_x}\right), \qquad \beta^k_\Delta = \text{acos}\left(\frac{\kappa^k}{\left|\mathbf{h}^k_{\text{rev}(p)} - \mathbf{h}\right|}\right), \tag{3.30, 3.31}$$

where β^k_{vpm} is the angle associated to the direction given by the *vpm* approach. The *brent* algorithm finds then subsequent smaller intervals until the searched angle root

is known to lie within a sufficiently narrow region. In the numerical tests presented in the following section, a strong stopping criterion is adopted such that the value returned is ensured to be as close as 10^{-11} rad to the exact angle. It can be observed that, in this example, the angle β_*^k that cancels $\mathscr{S}^k$ does not correspond to the initial approximation angle β_{vpm}^k.

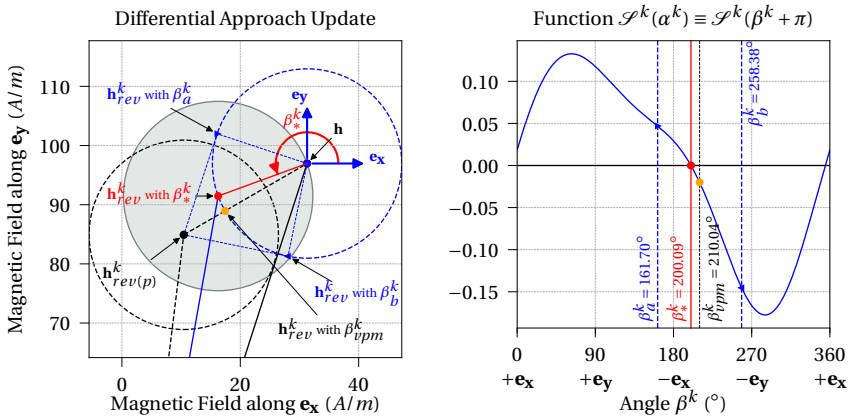

Figure 3.9: *Example of a diff approach update at a time step where* $|\mathbf{h} - \mathbf{h}_{rev(p)}^k| > \kappa^k$ *(left), with* β_*^k *satisfying the cancellation of the function* $\mathscr{S}^k(\alpha^k)$ *with* $\alpha^k = \beta^k + \pi$ *(right).*

5. Numerical Comparison

This section aims to present the behavior of the different implementations of the *EB* Hysteresis Model and to compare them numerically using illustrative examples. The simulations with the *vpm*, the *var* and the *diff* approaches, are quantitatively compared in terms of speed and accuracy.

For speed comparison, the ratio of central processing unit (*CPU*) times with respect to the *vpm* approach time is used as indicator. The *vpm* approach is taken as reference because it is obviously the fastest one since the result at each time step is immediate and requires no optimization process. Furthermore, attention is paid to the mean and maximum number of direction search iterations per cell per time step (*ts*) for the *var* and *diff* approaches. More particularly for the *var* approach, the mean and maximal number of line search steps per direction search iteration is also recorded.

In order to quantify the accuracy between each approach, a root mean square deviation norm (*RMSDN*) between the model output field and a reference field is introduced. This factor is calculated as follows. At each time point of a simulation $t_n = n\Delta t$, and $n = 1, \ldots, N_t$; the model, either using (3.13), (3.21) or (3.29), produces an induction field vector $\mathbf{b}(t_n) = (b_{x,n}, b_{y,n}, b_{z,n})$. At the end of the simulation, for each component $i = x, y, z$, of $\mathbf{b}$, one can evaluate a root mean square deviation $(RMSD)_i$ by taking the root of the average of the squared difference between the i-th component of the output field $b_{i,n}$ and a reference field $b_{i,n}^{\text{ref}}$ over all the N_t time steps of the simulation. One

has mathematically,

$$(\mathrm{RMSD})_i = \sqrt{\frac{1}{N_t}\sum_{n=1}^{N_t}\left(b_{i,n} - b_{i,n}^{\mathrm{ref}}\right)^2} \quad , \forall\, i = x, y, z. \tag{3.32}$$

The *RMSDN*, expressed in tesla (T), is then defined by taking the L^2-norm of the vector made by these three components (3.32). The output produced by the *diff* approach is chosen as the reference field for the definition of the *RMSDN* because it does not rely on an approximation like for the *vpm* approach and because unlike the *var* approach, there is no additional line search method within each direction search iteration that could reduce the reachable numerical precision, as already mentioned previously.

These useful comparison tools are exploited in the following with different illustrative simulation cases, where the various model approaches are fed by input fields $\mathbf{h}$ of increasing complexity, from unidirectional to rotational field excitations of increasing amplitudes.

Concerning the model parameters selection, the anhysteretic saturation law is approximated by a hyperbolic tangent function, as in [17, 177, 79],

$$J_{\mathrm{an}}(x) = J_a \tanh\left(\frac{x}{h_a}\right), \tag{3.33}$$

with J_a the saturation magnetic polarization in tesla (T), and h_a a parameter, expressed in ampere per meter (A/m), that affects the initial slope of the curve. Other functions than (3.33) able to represent the saturation law could be used as well [103]. For example, the Langevin function $J_{\mathrm{an}}(x) = J_a\big(\coth(x/h_a) - (h_a/x)\big)$ is another suitable curve, popular because it can fit quite remarkably measurements [103, 102, 2], and it has a physical origin from theory of magnetic dipole orientations. Practically, the function can also be deduced from interpolation between measured database points [15, 177]. Nevertheless, the choice of the expression (3.33) is motivated here because it presents the advantage to be analytically invertible, allowing to derive analytical expressions for the reversible field and the Helmholtz free energy. Assuming furthermore isotropic material, the vector generalization of the saturation law reads

$$\mathbf{J}_{\mathrm{an}}(\mathbf{x}) = J_{\mathrm{an}}(|\mathbf{x}|)\frac{\mathbf{x}}{|\mathbf{x}|}, \tag{3.34}$$

where $|\mathbf{x}|$ denotes the magnitude of the input vector field $\mathbf{x}$. The same parameters as in previous works [79, 116, 113], $J_a = 1.22\,\mathrm{T}$ and $h_a = 65\,\mathrm{A/m}$, with a 3-cell discretized representation of the pinning effect $[\omega^1 = 0.1; \kappa^1 = 0\,\mathrm{A/m}][\omega^2 = 0.65; \kappa^2 = 16\,\mathrm{A/m}][\omega^3 = 0.25; \kappa^3 = 47\,\mathrm{A/m}]$, deduced from a fitting on a standard non-oriented electrical steel grade M250-50A are picked up again here.

5.1. Unidirectional Excitation Field Source

First, the model is excited through $\mathbf{h}(t) = (h_{\max}\sin(2\pi f t), 0, 0)$ where $h_{\max} = 150\,\mathrm{A/m}$ is the amplitude, and f the frequency, make that the latter has no impact on the result

due to the rate-independence of the hysteresis model. The problem stated in the *diff* and *var* approaches have a direct analytical solution that corresponds to the *vpm* result as the latter does not introduce any approximation in this one-dimensional configuration. Still, this test case remains fruitful to analyze the minimization and root finding algorithms involved in the *var* and *diff* approaches. Starting from the demagnetized state $\mathbf{b}(0) = \mathbf{0}$ with $\mathbf{J}^k(0) = \mathbf{0}$ and $\mathbf{h}^k_{\text{rev}}(0) = \mathbf{0}$, $\forall k$, the simulation is performed on two periods, each of them including 200 *ts*. The last period of the simulation is shown in Fig. 3.10 (left), where the main hysteresis loop $b_x - h_x$ is visible.

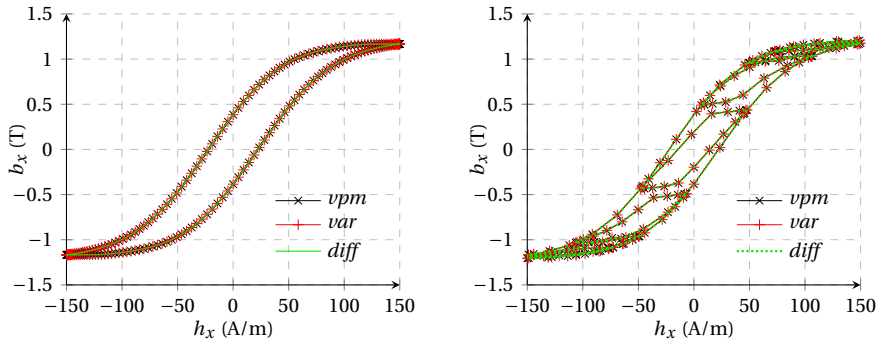

Figure 3.10: *Unidirectional (left) and Multi-harmonic (right) excitations with the three implementations of a 3-cell EB hysteresis model.*

As expected, the three approaches provide the same output field **b** in this simple case. The two branches of the major loop correspond approximately to the anhysteretic curve horizontally shifted over $\pm h_c = \sum \omega^k \kappa^k$, that is $h_c = 22.43\,\text{A/m}$ in this example, in agreement with Fig. 2.4 (right) but complicated in addition with the action of three weighted cells, even if the multi-cell aspect is not much visible here on the main loop of Fig. 3.10 (left). The total polarization field already comes close to its maximal value of $J_a = 1.22\,\text{T}$ for $|h_x| = 150\,\text{A/m}$.

Table 3.1 gathers all the information to compare the different simulated approaches. As can be seen, besides the *vpm* and *diff* approaches, the *var* approach is declined with the variety of possible techniques combinations discussed in Chapter 3-Section 3. The six *var* approach derivations result from the composition of each direction choice (*sd* or *cg*) with each line search technique (*naive*, *wolfe* or *brent*). Moreover, a first set of six *var* approach versions is obtained by choosing as initial point for the minimization the value from the previous time step $\mathbf{J}^k_0 = \mathbf{J}^k_{(p)}$, while the second set of *var* approach variants takes the result from the *vpm* approach as starting point $\mathbf{J}^k_0 = \mathbf{J}^k_{(vpm)}$, since it offers in general a rather good initial guess, readily accessible to begin the minimization. The comparative tools mentioned in the preamble of this section are all listed in Table 3.1, for each approach. The ratio of computational times with respect to the *vpm* approach time is reported in the second column. The third column gives the mean and maximal number of direction search iterations per cell per *ts*. The fourth column, that is only relevant for the *var* approaches, displays the mean and maximal number of

Table 3.1: *Direct model using 3 cells - Unidirectional Excitation.*

approach	*CPU* time ratio (*vpm* as ref.)	iter / cell / ts mean (max)	line search / iter mean (max)	RMSDN (T) (*diff* as ref.)
vpm	1.0	1.00 (1)	–	$1.6 \cdot 10^{-16}$
diff	8.6	2.58 (3)	–	0.0
var-sd-naive	79.1	13.25 (21)	2.05 (11)	$7.7 \cdot 10^{-16}$
var-sd-wolfe	97.6	15.05 (81)	2.09 (11)	$1.6 \cdot 10^{-14}$
var-sd-brent	54.7	3.43 (4)	5.04 (16)	$1.2 \cdot 10^{-14}$
var-cg-naive	109.3	24.68 (48)	1.53 (11)	$7.6 \cdot 10^{-16}$
var-cg-wolfe	75.1	10.74 (26)	2.31 (12)	$1.7 \cdot 10^{-14}$
var-cg-brent	57.3	4.45 (6)	4.20 (16)	$1.2 \cdot 10^{-14}$
var-sd-naive-(vpm)	6.9	1.00 (1)	0.00 (0)	$1.6 \cdot 10^{-16}$
var-sd-wolfe-(vpm)	6.8	1.00 (1)	0.00 (0)	$1.6 \cdot 10^{-16}$
var-sd-brent-(vpm)	6.9	1.00 (1)	0.00 (0)	$1.6 \cdot 10^{-16}$
var-cg-naive-(vpm)	6.9	1.00 (1)	0.00 (0)	$1.6 \cdot 10^{-16}$
var-cg-wolfe-(vpm)	6.9	1.00 (1)	0.00 (0)	$1.6 \cdot 10^{-16}$
var-cg-brent-(vpm)	7.0	1.00 (1)	0.00 (0)	$1.6 \cdot 10^{-16}$

line search steps per direction search iteration. The last column outlines the so-called *RMSDN* factor in order to quantify the average **b**-field output deviations between each model approach and the *diff* approach, that is taken as reference.

In Table 3.1 resulting from the *1D* excitation test case, all the methods end up to the same solution because each *RMSDN* from the reference field is negligible. Concerning the *diff* approach, less than 3 iterations are needed to satisfy the stopping criterion and the *CPU* time is a little bit lower than the *vpm* approach but still relatively short. The longest *CPU* times are for the subset of *var* methods which start the minimization from the previous time solution. There is no real improvement between the *cg* or the *sd* direction search algorithms because the test case is unidirectional. Despite being more costly, the *brent* line search algorithm allows to reduce significantly the number of direction search iterations, and so the computational time, compared to the *naive* and *wolfe* methods. The *wolfe* line search seems more interesting only with the *cg* than with the *sd* routine for which the *naive* approach is even preferable. Naturally, all the subsets of *var* methods which start from the *vpm* solution are exactly at the minimum of the functional at the beginning thus satisfying immediately the stopping criterion. There is no iteration needed and no possible comparison between the *var* algorithms in this case.

Another excitation mode with the additional presence of an 8th harmonic is shown in Fig. 3.10 (right). As before, the same conclusion about the performance of the algorithms can be drawn for this case because the excitation is still in a single direction and the *vpm* approach already gives the exact solution.

5.2. Purely Circular Rotational Excitation Field Source

In the next example, a pure two-dimensional rotational excitation is considered. From the demagnetized state, the rotating source field $\mathbf{h}(t)$ is smoothly increased in length during the first period until reaching the steady state $\mathbf{h}(t) = h_{\max}\big[\sin(2\pi f t), \cos(2\pi f t), 0\big]$ established for the four next periods. As in the first example, $h_{\max} = 150$ A/m and each period is decomposed in 200 *ts*. The $b_x - h_x$ curve and the b locus drawn at the last period of the simulation are shown in Fig. 3.11 while information on the algorithms is given in Table 3.2.

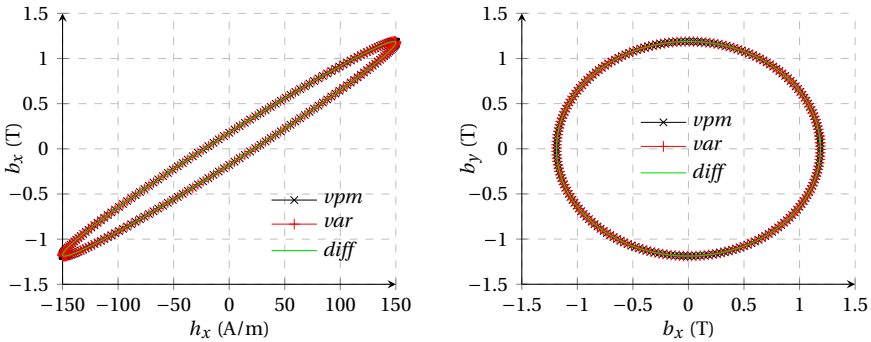

Figure 3.11: *2D Purely rotational excitation with the three implementations of a 3-cell EB hysteresis model; $b_x - h_x$ curve (left) and **b** loci (right).*

Table 3.2: *Direct model using 3 cells - 2D purely rotational Excitation.*

approach	*CPU* time ratio (*vpm* as ref.)	iter / cell / ts mean (max)	line search / iter mean (max)	RMSDN (T) (*diff* as ref.)
vpm	1.0	1.00 (1)	–	$1.6 \cdot 10^{-16}$
diff	15.8	6.33 (8)	–	0.0
var-sd-naive	649.1	105.46 (121)	1.13 (6)	$8.2 \cdot 10^{-15}$
var-sd-wolfe	648.8	88.66 (121)	1.15 (6)	$4.4 \cdot 10^{-14}$
var-sd-brent	294.7	23.17 (26)	2.13 (13)	$8.9 \cdot 10^{-15}$
var-cg-naive	464.4	80.85 (103)	1.17 (6)	$2.8 \cdot 10^{-15}$
var-cg-wolfe	186.3	17.33 (22)	2.32 (6)	$2.2 \cdot 10^{-16}$
var-cg-brent	113.2	5.00 (6)	5.26 (13)	$8.8 \cdot 10^{-16}$
var-sd-naive-(vpm)	8.6	1.00 (1)	0.00 (0)	$2.1 \cdot 10^{-16}$
var-sd-wolfe-(vpm)	8.6	1.00 (1)	0.00 (0)	$2.1 \cdot 10^{-16}$
var-sd-brent-(vpm)	8.6	1.00 (1)	0.00 (0)	$2.1 \cdot 10^{-16}$
var-cg-naive-(vpm)	8.7	1.00 (1)	0.00 (0)	$2.1 \cdot 10^{-16}$
var-cg-wolfe-(vpm)	8.6	1.00 (1)	0.00 (0)	$2.1 \cdot 10^{-16}$
var-cg-brent-(vpm)	8.6	1.00 (1)	0.00 (0)	$2.1 \cdot 10^{-16}$

Once again, the *vpm* approach is not an approximation in this example and gives the

exact solution. The output fields from the three implementations are overlapping in Fig. 3.11 and the *RMSDN* are insignificant in Table 3.2 for every case. The *diff* approach needs about 6 iterations in average to find a satisfactory root angle for this *2D* test case simulation, that is a little bit more than with the previous *1D* excitation source. Concerning the subset of *var* approaches that start the minimization from the previous time solution, an appreciable decrease of about a factor 3 on the *CPU* time can be observed between the *cg* and the *sd* methods, as the former converges in less direction search iterations. This reduction is less pronounced when the *naive* line search technique is adopted. The *wolfe* technique gives intermediate performance results while the *brent* routine remains the best choice to minimize the computational time in this subset of *var* approaches. However, all the *var* versions based on the previous time solution remain at best more than 100 times as long as the *vpm* approach. Using the *vpm* solution as first guess for the *var* approaches automatically satisfies the stopping criterion, with no iterations needed. All the *var* versions based on *vpm* are thus fast and equivalent in terms of efficiency for this purely rotational test case.

5.3. Growing Spiral Excitation Field Source

A test case is investigated with a *2D* spiral excitation field. The magnetic field rotates, $\mathbf{h}(t) = h_{\max}(t)\big[\cos(2\pi f t), \cos(2\pi f t - \Phi), 0\big]$, with an amplitude $h_{\max}(t) = 200\, t/t_f$ growing until reaching its maximal value 200 A/m at the final time t_f and with a phase shift $\Phi = 20°$ between $h_x - h_y$ perpendicular excitation directions. Three periods of 200 *ts* each are simulated, i.e. $t_f = 3/f$. The applied magnetic field is represented in Fig. 3.12 (left) while the output induction fields from each approach is shown in Fig. 3.12 (right) with the information gathered in Table 3.3. The *diff* and all the *var* approaches converge to the same exact result, the former faster than the latter. The *vpm* approach remains about 14 times faster than the *diff* approach but no longer provides the exact solution here. The *RMSDN* value of about 50 mT for the *vpm* approach cannot be reduced even by refining the time discretization. Nevertheless, the difference is relatively small in this example, and it can be shown that the *vpm* approach is usually a good approximation saving a significant amount of calculation time for such kind of excitation [113]. The approximation may be less accurate if anisotropy is taken into account [177], because the *vpm* error, which comes from the direction field inaccuracy (3.9), may be larger if the material law varies also with the direction, but this consideration is no further discussed here. About the *var* approaches, the exploitation of the *vpm* approximation to start the minimization allows to decrease the computation time. The use of the *cg* directions requires much less iterations compared to the *sd* method. In this way, the maximal number of iterations per cell per *ts* varies from more than 20000 in the worst situation with the *sd*-*naive* association starting minimization from the previous time step result, to only 11 with the better *cg*-*brent* combination using the *vpm* approximation as starting point. Nevertheless, in this example, the *var* approaches are at best around 7 times as long as the *diff* approach or 100 times as long as the *vpm* approach.

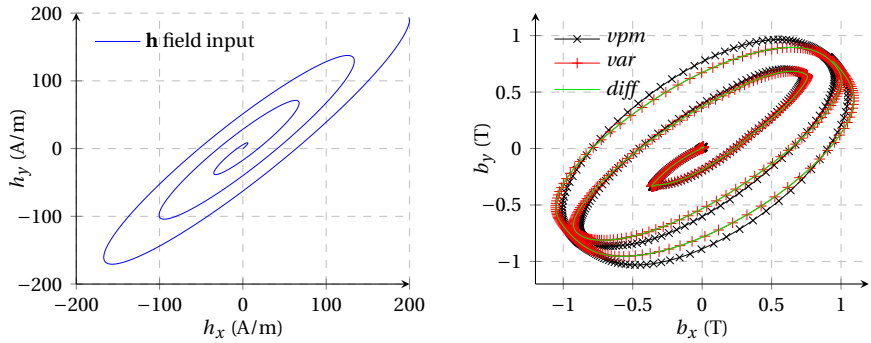

Figure 3.12: *2D Spiral excitation with the three implementations of a 3-cell EB hysteresis model; applied $h_x - h_y$ curve (left) and produced **b** loci (right).*

Table 3.3: *Direct model using 3 cells - 2D Spiral Excitation.*

approach	*CPU* time ratio (*vpm* as ref.)	iter / cell / ts mean (max)	line search / iter mean (max)	RMSDN (T) (*diff* as ref.)
vpm	1.0	1.00 (1)	–	$4.8 \cdot 10^{-2}$
diff	13.7	7.05 (11)	–	0.0
var-sd-naive	966.6	156.13 (20715)	1.38 (17)	$5.8 \cdot 10^{-13}$
var-sd-wolfe	1412.8	195.27 (19853)	1.33 (16)	$5.2 \cdot 10^{-13}$
var-sd-brent	1180.8	60.56 (2680)	4.45 (17)	$5.7 \cdot 10^{-13}$
var-cg-naive	323.3	64.30 (1614)	1.34 (18)	$5.4 \cdot 10^{-13}$
var-cg-wolfe	129.6	14.37 (30)	2.43 (15)	$5.3 \cdot 10^{-13}$
var-cg-brent	142.3	7.37 (12)	5.00 (17)	$5.3 \cdot 10^{-13}$
var-sd-naive-(vpm)	607.5	100.56 (14469)	0.67 (16)	$5.0 \cdot 10^{-13}$
var-sd-wolfe-(vpm)	838.9	110.30 (2911)	0.68 (16)	$4.9 \cdot 10^{-13}$
var-sd-brent-(vpm)	429.5	24.21 (6203)	2.41 (16)	$4.9 \cdot 10^{-13}$
var-cg-naive-(vpm)	224.1	39.20 (871)	0.72 (16)	$5.3 \cdot 10^{-13}$
var-cg-wolfe-(vpm)	84.8	8.03 (25)	1.39 (15)	$5.3 \cdot 10^{-13}$
var-cg-brent-(vpm)	102.6	4.63 (11)	3.25 (17)	$5.3 \cdot 10^{-13}$

5.4. Scanning of Excitation Fields from Unidirectional to Rotational Sources

Finally, the three direct approaches, *vpm*, *diff*, and *var*, with more precisely the most promising *var*-*cg*-*brent*-(*vpm*) version for the latter, are all compared in a general way by being subjected to a serie of varied excitation fields to cover a maximum of possible magnetization paths. Sinusoidal **h**-field excitations with different phase shifting Φ between $h_x - h_y$ perpendicular excitation directions and with different maximal amplitudes, compose the set of input sources that feed the direct models. The imposed **h**-field sources describe paths of ellipsoidal shape in the $h_x - h_y$ plane, as shown in Fig. 3.13 (left) and Fig. 3.14 (left) for maximal component fields $h_{\max} = 50\,\mathrm{A/m}$ and $h_{\max} = 200\,\mathrm{A/m}$ respectively, with gradually varying phase shifting Φ, from unidirec-

tional degenerated case ($\Phi = 0°$) to purely circular rotational excitation ($\Phi = 90°$). Each cycle is discretized in 500 *ts*. From each of these input fields, the direct *vpm*, *diff* and *var* approaches produce the corresponding induction field responses, whose trajectories in the $b_x - b_y$ plane are shown in Fig. 3.13 (right) and Fig. 3.14 (right), from the sets of source fields having $h_{\max} = 50\,\mathrm{A/m}$ or $h_{\max} = 200\,\mathrm{A/m}$ respectively.

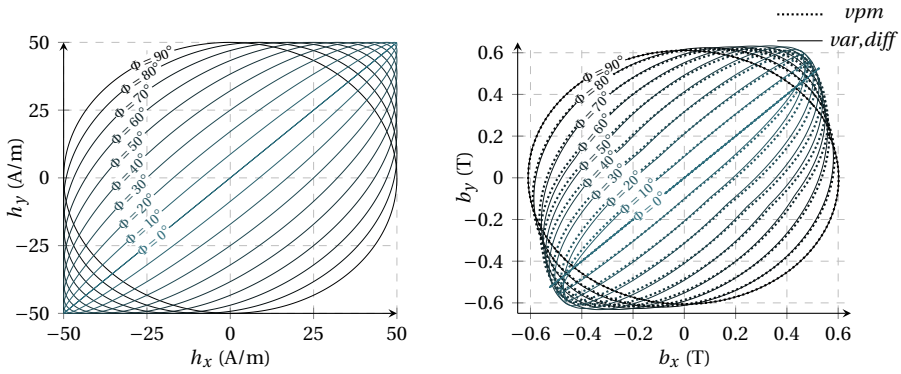

Figure 3.13: *Input magnetic field sources with $h_{\max} = 50\,\mathrm{A/m}$, with various phase shifting Φ between h_x and h_y components (left); and corresponding output induction fields obtained with each direct model approach, vpm, var, diff (right).*

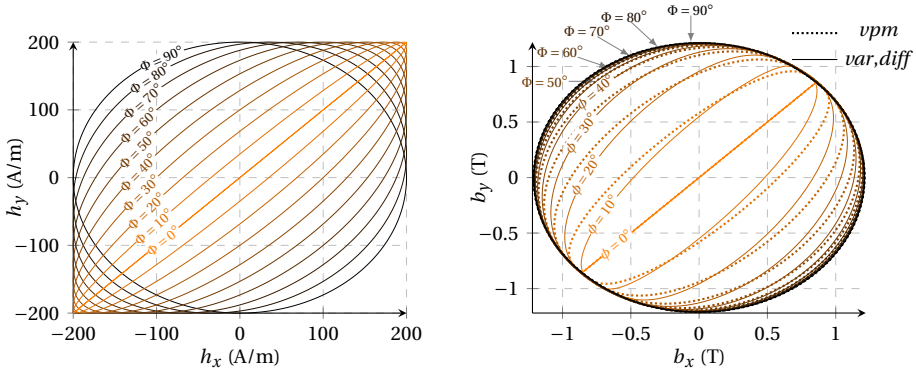

Figure 3.14: *Input magnetic field sources with $h_{\max} = 200\,\mathrm{A/m}$, with various phase shifting Φ between h_x and h_y components (left); and corresponding output induction fields obtained with each direct model approach, vpm, var, diff (right).*

With imposed fields of $h_{\max} = 50\,\mathrm{A/m}$, the induction fields do not reach the saturation region, and a regular enlargement of the loop area formed in the $b_x - b_y$ plane happens from $\Phi = 0°$ to $\Phi = 90°$ in Fig. 3.13 (right). On the contrary, with excitations of $h_{\max} = 200\,\mathrm{A/m}$ as in Fig. 3.14 (right), the saturation region is visited, and the loop in the $b_x - b_y$ plane grows with Φ, sharply at first, but then more and more slowly as soon as $|\mathbf{b}|$ becomes close to $b_{sat} = 1.22\,\mathrm{T}$. Hence, the paths describe by $\mathbf{b}$ for increasing Φ are closer to each other and tend to a circular saturation limit. This manifests clearly when

$\Phi \geq 50°$ in the example of Fig. 3.14 (right), that is when the amplitude of the imposed rotating **h** remains high enough during a complete cycle to stay mostly in saturation.

It can be expressed that, from every excitation cases, the *var* and the *diff* approaches converge to the same result **b**. Actually, there is still some tiny numerical differences between their outputs due to the convergence criteria in the algorithms which leaves some flexibility in approximating the final result, but they would be indistinguishable in Fig. 3.13 (right) and Fig. 3.14 (right), such that both approaches are identified by a same single line here. On the other hand, the approximations behind the *vpm* approach introduce more or less significant deviations compared to the other approaches, depending on the phase shift angle Φ or the maximum amplitude $h_{\max}$.

As already demonstrated, there is no deviation due to *vpm* in unidirectional ($\Phi = 0°$) or in purely circular ($\Phi = 90°$) situations, regardless of the $h_{\max}$ value. This is also verified by looking at Fig. 3.13 (right) and Fig. 3.14 (right). For the fields with intermediate Φ values ($0° < \Phi < 90°$), it is interesting to note that these deviations are visually the most important when, during the rotation of the induction field **b**, its amplitude, $|\mathbf{b}|$, varies strongly from small values in one direction to saturated values in other one. In the examples, this situation is encountered with the case $h_{\max} = 200\,\mathrm{A/m}$ in Fig. 3.14 (right), for small Φ values. Then, as Φ increases, the **b** fields rotate more and more mainly in saturation mode, and the *vpm* deviations become smaller. On the other hand, with the examples based on $h_{\max} = 50\,\mathrm{A/m}$ in Fig. 3.13 (right), the imposed rotating field **h** has always small amplitudes that do not induce saturation, such that the differences brought by the *vpm* approach in the **b**-field responses are less visible compared to *var* and *diff* approaches. Indeed, the variations of the magnetic polarization fields remain essentially linear at low magnetic fields, and the *vpm* approximation is rather appropriate to describe this scenario, as noted in Chapter 3-Section 2.

The quantitative information about the deviations introduced by the *vpm* approach is summarized in Fig. 3.15 (left), where the *RMSDN* of the **b**-fields from *vpm* with respect to the results from the *diff* approach are represented in function of Φ, for different $h_{\max}$ values. The value of *RMSDN* naturally drops for degenerated cases $\Phi = 0°$ and $\Phi = 90°$, and this for all sets of $h_{\max}$ considered. For small imposed fields, such as $h_{\max} = 50\,\mathrm{A/m}$, the *RMSDN* present values more or less independent of Φ between the two dropping extremities. These *RMSDN* values are among the smallest over the entire phase angle Φ spectrum in Fig. 3.15 (left), of about $10^{-2}\,\mathrm{T}$ in average. For more intense fields, as large as $h_{\max} = 300\,\mathrm{A/m}$, it appears that the deviations are more important for Φ slightly larger than 0°, with a peak around $\Phi = 10°$, and then decrease with the increase of Φ until the final drop at $\Phi = 90°$. This is consistent with the trend observed in Fig. 3.14 (right) with the saturating fields $h_{\max} = 200\,\mathrm{A/m}$. Nevertheless, among all the covered situations, the maximum *RMSDN* value remains smaller than 0.08 T, even for the worst case, which corresponds to a deviation smaller than 7 % when viewed with respect to the saturation value of 1.22 T. Therefore, the *vpm* approach appears as a rather good approximation in general, even for arbitrary excitations.

The same comparison is made in Fig. 3.15 (right) with the *RMSDN* between the *var* and the *diff* approaches, the latter still being taken as reference. Despite both meth-

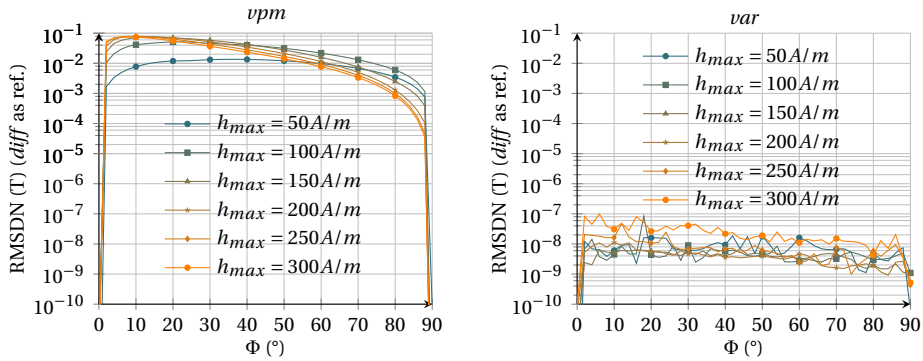

Figure 3.15: *RMSDN between the vpm and the diff* ***b****-field outputs (left), and RMSDN between the var and the diff* ***b****-field outputs (right), in function of* Φ *from different excitation modes having various* h_{max}.

3

ods should give the same result in theory, there are still remaining tiny deviations in the solutions. These differences are due to the numerical implementations of the algorithms which only find the solutions within one convergence criterion. Given the finite-precision arithmetic and the loss of significant figures that is more likely to affect the minimization process in the *var* approach, it is impossible to satisfy an infinitely exact tolerance criterion. In Fig. 3.15 (right), both approaches have been pushed to satisfy the strictest tolerance criterion that can be met on the basis of floating-point arithmetic. The *var* approach is much more limited in the maximum level of precision that can be achieved to reach the exact solution. Globally, it appears that there is always a *RMSDN* value of the order of 10^{-8} T averaged over all simulation cases. It also seems that the minimization with the *var* approach encounters more numerical difficulties when the solutions lie in saturation regime. Indeed in Fig. 3.15 (right), the *RMSDN* is often greater for simulations with $h_{\text{max}} = 300\,\text{A/m}$, with an average value closer to 10^{-7} T over all Φ. Moreover, the *RMSDN* is actually not really affected by the Φ value, except that it is minimal in degenerated cases $\Phi = 0°$ and $\Phi = 90°$.

The *CPU* times ratios for the *diff* and the *var* approaches with respect to the time taken with the fastest *vpm* approach are given in Fig. 3.16 (left) and Fig. 3.16 (right) respectively, for each excitation cases. These figures show that the *diff* approach is about 10 times as long as the *vpm* approach, while it is even worse for the *var* approach which is about 100 times as long as with the *vpm* way. These orders of magnitude are true for virtually all the simulations that have been performed, for any field amplitudes h_{max} and any phase shifting angles Φ.

Until now, the *EB* model has always consisted of 3 cells. Changing the number of cells does not really have an impact on the conclusions drawn on the *RMSDN* factors or on the time ratios compared to the *vpm* approach. However, if the number of cells is changed, the number of internal variables change, and each of them requires a processing time to describe its evolution during the simulation. The Fig. 3.17 shows, for each approach, how the calculation time to perform a simulation in average, increases in function of the number of cells chosen, compared to the case of a single cell that is

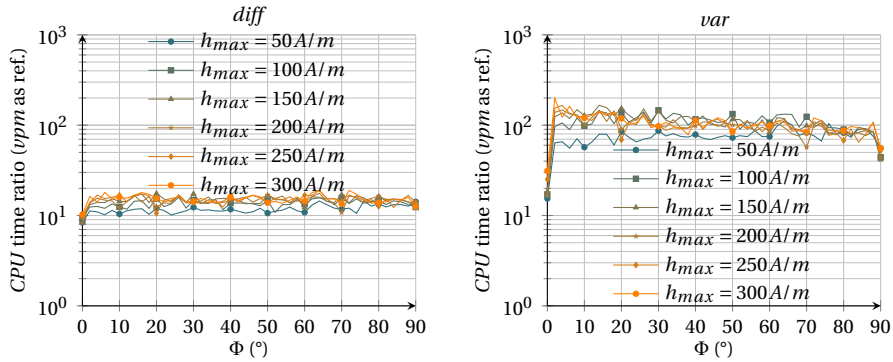

Figure 3.16: *CPU times ratios with respect to the vpm, for the diff (left) and for the var approaches (right).*

taken as reference. Each point in Fig. 3.17 results from the average of the simulation times from an entire test campaign covering all the different $h_{\max}$ and Φ spectra. It appears that the complexity grows sublinearly with the number of cells. The curves are below the linear growth in Fig. 3.17 because all the variables constituting a multi-cell model are not necessarily updated at each time step since the magnetic field strength is not always sufficient to overcome the pinning force associated to the cell.

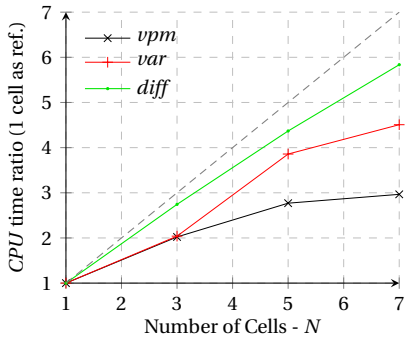

Figure 3.17: *Evolution for the vpm, var and diff approaches of the averaged CPU times in function of the number of cells chosen, taking the ratio with their single-cell case, being their own reference times.*

In general, one may conclude that the *vpm* approximation is a remarkable trade-off between accuracy and calculation time performance, at least in the isotropic case. The elegant *var* formulation allows to keep directly the link with the energy potential minimization concept from the thermodynamic background of the hysteresis model. However, this approach appears to be more likely subjected to undesirable numerical effects, due to the loss of significance in the functional evaluation that occurs sometimes during the minimization. Despite numerous attempts to improve the *var* performances, the new proposed *diff* approach seems preferable in practice to find efficiently the exact solution when more complicated sources than unidirectional or purely rotational cases appear.

CHAPTER

4 Inversion of the Energy-Based Hysteresis Model

HITHERTO, the energy-based (*EB*) hysteresis model takes the magnetic field $\mathbf{h}$ as an input variable in the three direct implementations which can all be written under the same generic format $\mathbf{b} = \mathscr{B}^{dir}\left(\mathbf{h}, \mathbf{X}^k_{(p)}\right)$, where $\mathbf{X}^k$ correspond to $\mathbf{h}^k_{\text{rev}}$ for the Vector Play Model (*vpm*) (3.13) and the differential approach (*diff*) (3.29); or to $\mathbf{J}^k$ for the variational approach (*var*) (3.21). However, in order to include it in finite element (*FE*) formulations where the magnetic induction field $\mathbf{b}$ is the unknown field, it is required to have a $\mathbf{b}$-based hysteresis model to express $\mathbf{h}$ as function of the actual induction $\mathbf{b}$ and the past values of the magnetic state $\mathbf{X}^k_{(p)}$. The aim of this chapter is to present several techniques to perform such inversion for the *EB* model and to compare the numerical performance of various implementations on an illustrative set of test cases.

1. Preliminary Remarks

Basically, the *var* approach offers an opportunity to perform such an inversion. Thus, a first attempt at inversion was made by trying to adjust the expression of the energy potential, by means of Legendre transformations, so that the model always consists of minimizing a functional, but expressed in terms of the induction field instead of the magnetic field. However, when several cells are considered, the decoupled treatment in several part for each magnetization vector is no longer possible, which requires considering a global functional, grouping each cell elements in a global magnetization vector, and minimizing it in a larger space to simultaneously search all the components of this global vector. The search for the minimum according to this strategy is then much more complicated than in the direct case and simple algorithms of steepest descent or conjugate gradient are no longer sufficient. The Nelder-Mead minimization algorithm has also been tested without any further success. In addition, the existence of a single minimum of this global functional has not been proven and the attempt to invert from this perspective has therefore been suspended.

Furthermore, the concept of inverse of a given hysteresis operator has been tackled in several works [151, 207, 36, 133], and further discussed for the class of magnetic hysteresis models based on Play and Stop hysterons [27], to which the *vpm* approach belongs. Despite the fact that the inversion of a single play hysteron seems to be feasible by turning it into a stop operator, the procedure to find the inverse operator does not seem available analytically when models are built up by the superposition of several cells.

Therefore, at the end, more general inversion techniques derived from the classical Newton-Raphson method have been mostly investigated and studied for the inversion of the *EB* hysteresis model in this work. It is worth noting that arc methods, inspired from Riks-Crisfield techniques [184, 46, 72] to overcome strong non-linearities have also been considered but to a lesser extent and with less success. The most promising techniques that have been used in this thesis are presented in the following sections.

2. Newton-Raphson Method

2.1. Classical Newton-Raphson Method

In its simplest application, the Newton-Raphson (*NR*) method is an efficient algorithm to find numerically a precise approximation of a root of a real function $r(x)$ of one variable x. The procedure is illustrated graphically on Fig. 4.1, where, from an initial guess x^0 reasonably close to the true root, the function $r(x)$ is approximated by its tangent line of slope $r'(x^0)$, where r' denotes the derivative of the function r. The intersection of the tangent line with the x-axis gives a new point x^1, which results from the linear equation

$$r\left(x^0\right) + r'\left(x^0\right)\left(x^1 - x^0\right) = 0 \longleftrightarrow x^1 = x^0 - \frac{r\left(x^0\right)}{r'\left(x^0\right)}.$$

The point x^1 may typically be a better approximation to the function's root than the starting point x^0. This scheme can be iterated by applying successively

$$x^l = x^{l-1} - \frac{r\left(x^{l-1}\right)}{r'\left(x^{l-1}\right)}, \tag{4.1}$$

to produce a sequence $x^2, x^3, \ldots$ that converges to the root x^* as can be seen with the examples on Fig. 4.1.

Although it is more complicated to visualize it graphically, the same *NR* method can also be used to solve systems of M nonlinear equations with M variables, which amounts to finding the zeroes of functions $\mathbf{r}(\mathbf{x}) : \mathbb{R}^M \to \mathbb{R}^M$. The generalization of (4.1) consists then, instead of dividing by $r'(x^{l-1})$, to left multiply with the inverse of the $M \times M$ Jacobian matrix $\frac{\partial \mathbf{r}}{\partial \mathbf{x}}\Big|^{l-1}$ evaluated at $\mathbf{x}^{l-1}$, such that the iterative formulation writes

$$\mathbf{x}^l = \mathbf{x}^{l-1} - \left[\frac{\partial \mathbf{r}}{\partial \mathbf{x}}\Big|^{l-1}\right]^{-1} \cdot \mathbf{r}\left(\mathbf{x}^{l-1}\right). \tag{4.2}$$

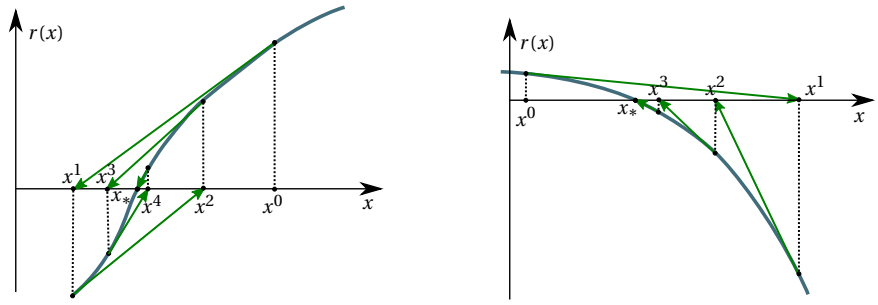

Figure 4.1: *Graphical Illustrations of the convergence of the NR Method for simple univariate functions.*

On that basis, the inversion problem of the *EB* hysteresis model can be overcome by explicitly inverting the direct implementation form by means of the *NR* method. For a known magnetic state $(\mathbf{h}_{(p)}, \mathbf{b}_{(p)}, \mathbf{X}^k_{(p)})$ at previous time instant (p) and a given induction $\mathbf{b}^*$ at the current time instant, the sought magnetic field $\mathbf{h}^*$ is the solution of the nonlinear vector equation $\mathbf{r}(\mathbf{h}) = \mathscr{B}^{dir}(\mathbf{h}, \mathbf{X}^k_{(p)}) - \mathbf{b}^* = \mathbf{0}$, involving the direct *EB* model. Starting from the initial estimate $\mathbf{h}^0 = \mathbf{h}_{(p)}$, the *NR* process builds subsequent approximations $\mathbf{h}^l$, $l = 1, 2, \ldots$, of the magnetic field by solving

$$\mathbf{h}^l = \mathbf{h}^{l-1} - \left[\frac{\partial \mathscr{B}^{dir}}{\partial \mathbf{h}} \bigg|^{l-1} \right]^{-1} \cdot \left[\mathscr{B}^{dir}(\mathbf{h}^{l-1}, \mathbf{X}^k_{(p)}) - \mathbf{b}^* \right], \tag{4.3}$$

which comes from the linearization of $\mathbf{r}(\mathbf{h}^l)$ around the previous estimate $\mathbf{h}^{l-1}$, as simple application of (4.2). The iteration process is repeated until the vector equation $\mathbf{r}(\mathbf{h}^l) = \mathbf{0}$ is verified within a certain tolerance, for example,

$$\left\| \mathscr{B}^{dir}(\mathbf{h}^l, \mathbf{X}^k_{(p)}) - \mathbf{b}^* \right\| < \epsilon, \tag{4.4}$$

with ϵ, a small number expressed in tesla (T) here.

The differential permeability tensors $\frac{\partial \mathscr{B}^{dir}}{\partial \mathbf{h}}$ appearing in (4.3) are obtained by differentiating with respect to $\mathbf{h}$ the direct hysteresis model $\mathscr{B}^{dir}(\mathbf{h}, \mathbf{X}^k_{(p)})$, either supplied by the *vpm* (3.13), the *var* (3.21) or the *diff* (3.29) approaches, evaluated with the field $\mathbf{h}^{l-1}$, obtained at the previous iteration.

Actually, it is possible to derive analytical expressions for the tensors $\frac{\partial \mathscr{B}^{dir}}{\partial \mathbf{h}}$, from each approach, as partially presented in [113]. In this work, this type of inversion technique for the *EB* model is then denoted by the shorthand: Newton-Raphson with Jacobian matrix evaluated analytically (NR_{ana}). The derivations of these analytical expressions is the subject of the following section.

2.2. Analytical Expressions of the Differential Permeability Tensor

As already mentioned, depending on the chosen approach, the state variables that are considered are either the polarization vectors $\mathbf{X}^k = \mathbf{J}^k$, or the reversible magnetic fields

$\mathbf{X}^k = \mathbf{h}_{\text{rev}}^k$, leading to two general expressions for the differential permeability tensor expressed either in terms of $\mathbf{J}^k$

$$\frac{\partial \mathscr{B}^{dir}}{\partial \mathbf{h}}(\mathbf{h}, \mathbf{J}^k) = \mu_0 \underline{\boldsymbol{I}} + \sum_{k=1}^{N} \frac{\partial \mathbf{J}^k}{\partial \mathbf{h}}, \tag{4.5}$$

or in terms of $\mathbf{h}_{\text{rev}}^k$

$$\frac{\partial \mathscr{B}^{dir}}{\partial \mathbf{h}}(\mathbf{h}, \mathbf{h}_{\text{rev}}^k) = \mu_0 \underline{\boldsymbol{I}} + \sum_{k=1}^{N} \underline{\boldsymbol{\chi}_\partial}^k \left(\mathbf{h}_{\text{rev}}^k\right) \frac{\partial \mathbf{h}_{\text{rev}}^k}{\partial \mathbf{h}}, \tag{4.6}$$

thanks to the introduction of the differential magnetic susceptibility tensors $\underline{\boldsymbol{\chi}_\partial}^k(\mathbf{h}_{\text{rev}}^k)$, that come from vector-by-vector derivatives $\frac{\partial \mathbf{J}^k}{\partial \mathbf{h}_{\text{rev}}^k}$, which have the same units as an absolute magnetic permeability, in henry per meter (H/m). For isotropic materials, vectors $\mathbf{J}^k$ and $\mathbf{h}_{\text{rev}}^k$ are colinear (2.13) and related by a scalar anhysteretic law, $\mathbf{J}^k = \omega^k \mathscr{J}_{\text{an}}(|\mathbf{h}_{\text{rev}}^k|) \frac{\mathbf{h}_{\text{rev}}^k}{|\mathbf{h}_{\text{rev}}^k|}$, from where an analytical expression for the derivative with respect to the vector $\mathbf{h}_{\text{rev}}^k$ can be calculated

$$\underline{\boldsymbol{\chi}_\partial}^k(\mathbf{h}_{\text{rev}}^k) = \frac{\partial \mathbf{J}^k}{\partial \mathbf{h}_{\text{rev}}^k} = \omega^k \left(\chi_{\text{an}}(|\mathbf{h}_{\text{rev}}^k|) \underline{\boldsymbol{I}} + \frac{\chi_{\text{an}\partial}(|\mathbf{h}_{\text{rev}}^k|) - \chi_{\text{an}}(|\mathbf{h}_{\text{rev}}^k|)}{|\mathbf{h}_{\text{rev}}^k|^2} \mathbf{h}_{\text{rev}}^k {\mathbf{h}_{\text{rev}}^k}^T \right). \tag{4.7}$$

In this last relation, the factor $\mathbf{h}_{\text{rev}}^k {\mathbf{h}_{\text{rev}}^k}^T$ denotes a tensor resulting from the dyadic product between the two vectors, where the transpose of the second one is indicated by a superscript T. The scalar quantities, χ_{an} and $\chi_{\text{an}\partial}$, correspond to the apparent and the differential scalar magnetic susceptibilities respectively. They are defined by

$$\chi_{\text{an}}(|\mathbf{h}_{\text{rev}}^k|) = \frac{\mathscr{J}_{\text{an}}(|\mathbf{h}_{\text{rev}}^k|)}{|\mathbf{h}_{\text{rev}}^k|}, \qquad \chi_{\text{an}\partial}(|\mathbf{h}_{\text{rev}}^k|) = \frac{\partial \mathscr{J}_{\text{an}}(|\mathbf{h}_{\text{rev}}^k|)}{\partial |\mathbf{h}_{\text{rev}}^k|}. \tag{4.8, 4.9}$$

Their analytical derivations are straightforward from the anhysteretic law $\mathscr{J}_{\text{an}}$, if this one is represented by a simple function, such as a hyperbolic tangent or a Langevin function, for example.

In order to complete the analytical determination of $\frac{\partial \mathscr{B}^{dir}}{\partial \mathbf{h}}$, it remains to deduce analytical expressions for the tensors $\frac{\partial \mathbf{J}^k}{\partial \mathbf{h}}$ according to (4.5), or $\frac{\partial \mathbf{h}_{\text{rev}}^k}{\partial \mathbf{h}}$ under (4.6). In the following, these developments are particularized for the different model approaches that have been discussed in the previous chapter, ie. *vpm*, *var* and *diff*.

Vector Play Model

With the *vpm* approach, the state variables $\mathbf{h}_{\text{rev}}^k$ are updated by a simple law $\mathscr{U}^k(\mathbf{h}, \mathbf{h}_{\text{rev}(p)}^k)$ given by (3.10). The tensors $\frac{\partial \mathbf{h}_{\text{rev}}^k}{\partial \mathbf{h}}$ can thus be deduced by derivating this update rule with respect to $\mathbf{h}$, such that when $|\mathbf{h} - \mathbf{h}_{\text{rev}(p)}^k| > \kappa^k$,

$$\frac{\partial \mathbf{h}_{\text{rev}}^k}{\partial \mathbf{h}} = \frac{\partial \mathscr{U}^k}{\partial \mathbf{h}}(\mathbf{h}, \mathbf{h}_{\text{rev}(p)}^k) = \underline{\boldsymbol{I}} - \frac{\kappa^k}{|\mathbf{h} - \mathbf{h}_{\text{rev}(p)}^k|} \left(\underline{\boldsymbol{I}} - \frac{\left(\mathbf{h} - \mathbf{h}_{\text{rev}(p)}^k\right)\left(\mathbf{h} - \mathbf{h}_{\text{rev}(p)}^k\right)^T}{|\mathbf{h} - \mathbf{h}_{\text{rev}(p)}^k|^2} \right), \tag{4.10}$$

whereas $\frac{\partial \mathbf{h}_{\text{rev}}^k}{\partial \mathbf{h}} = \frac{\partial \mathscr{U}^k}{\partial \mathbf{h}} = \underline{\mathbf{0}}$ in the other case, when the magnetization is frozen. Introducing this result (4.10) in (4.6) in addition with the tensor expression (4.7) evaluated with the updated fields $\mathbf{h}_{\text{rev}}^k = \mathscr{U}^k$ allows to end up with an analytical expression for the differential permeability tensor specific to the *vpm* approach

$$\frac{\partial \mathscr{B}^{vpm}}{\partial \mathbf{h}}(\mathbf{h}, \mathbf{h}_{\text{rev}(p)}^k) = \mu_0 \underline{\boldsymbol{I}} + \sum_{k=1}^{N} \underline{\boldsymbol{\chi}_\partial}^k(\mathscr{U}^k) \frac{\partial \mathscr{U}^k}{\partial \mathbf{h}}. \tag{4.11}$$

It is important to note that, despite the fact that both the differential magnetic susceptibility $\underline{\boldsymbol{\chi}_\partial}^k(\mathscr{U}^k)$ and the derivative of the update rule $\frac{\partial \mathscr{U}^k}{\partial \mathbf{h}}$ are always symmetric tensors by definition, this is not the case for the tensor resulting from their matrix multiplication, such that the differential permeability tensor $\frac{\partial \mathscr{B}^{vpm}}{\partial \mathbf{h}}$ is not necessary symmetric. Indeed, by detailing this matrix multiplication in the case when $|\mathbf{h} - \mathbf{h}_{\text{rev}(p)}^k| > \kappa^k$, one has

$$\underline{\boldsymbol{\chi}_\partial}^k(\mathscr{U}^k) \frac{\partial \mathscr{U}^k}{\partial \mathbf{h}} = \underline{\boldsymbol{A}} + \underline{\boldsymbol{B}} + \underline{\boldsymbol{C}}, \qquad \text{with}$$

$$\underline{\boldsymbol{A}} = \left(1 - \frac{\kappa^k}{|\mathbf{h} - \mathbf{h}_{\text{rev}(p)}^k|}\right) \underline{\boldsymbol{\chi}_\partial}^k(\mathscr{U}^k), \qquad \boxed{\text{sym.}}$$

$$\underline{\boldsymbol{B}} = \frac{\kappa^k \omega^k \chi_{\text{an}}(|\mathbf{h}_{\text{rev}}^k|)}{|\mathbf{h} - \mathbf{h}_{\text{rev}(p)}^k|^3} \left(\mathbf{h} - \mathbf{h}_{\text{rev}(p)}^k\right) \left(\mathbf{h} - \mathbf{h}_{\text{rev}(p)}^k\right)^T, \qquad \boxed{\text{sym.}}$$

$$\underline{\boldsymbol{C}} = \frac{\kappa^k \omega^k \left(\chi_{\text{an}\partial}(|\mathbf{h}_{\text{rev}}^k|) - \chi_{\text{an}}(|\mathbf{h}_{\text{rev}}^k|)\right)}{|\mathbf{h} - \mathbf{h}_{\text{rev}(p)}^k|^3 |\mathbf{h}_{\text{rev}}^k|^2} \mathbf{h}_{\text{rev}}^k \mathbf{h}_{\text{rev}}^{k\,T} \left(\mathbf{h} - \mathbf{h}_{\text{rev}(p)}^k\right) \left(\mathbf{h} - \mathbf{h}_{\text{rev}(p)}^k\right)^T,$$

where the product is decomposed under the sum of three tensorial terms $\underline{\boldsymbol{A}}, \underline{\boldsymbol{B}}$ and $\underline{\boldsymbol{C}}$. While the symmetry of the two first is obvious, this property is not guaranteed for the last one. Therefore, the resulting sum, and consequently the tensor $\frac{\partial \mathscr{B}^{vpm}}{\partial \mathbf{h}}$, is not necessary symmetric. Actually, the symmetry is ensured only in situations where $\mathbf{h}_{\text{rev}}^k$ is parallel to $\mathbf{h} - \mathbf{h}_{\text{rev}(p)}^k$. In this case, these two vectors are related by a proportionality relation $\mathbf{h}_{\text{rev}}^k = r\left(\mathbf{h} - \mathbf{h}_{\text{rev}(p)}^k\right)$, with r a scalar factor, such that the last tensor term $\underline{\boldsymbol{C}}$ can be simplified to the following one, which is symmetric this time:

$$\underline{\boldsymbol{C}} = \frac{\kappa^k \omega^k \left(\chi_{\text{an}\partial}(|\mathbf{h}_{\text{rev}}^k|) - \chi_{\text{an}}(|\mathbf{h}_{\text{rev}}^k|)\right)}{|\mathbf{h} - \mathbf{h}_{\text{rev}(p)}^k|^3} \left(\mathbf{h} - \mathbf{h}_{\text{rev}(p)}^k\right) \left(\mathbf{h} - \mathbf{h}_{\text{rev}(p)}^k\right)^T. \qquad \boxed{\text{sym.}}$$

This simplification is valid only in unidirectional loadings and in case of purely rotational hysteresis, which corresponds, not surprisingly, to situations where the *vpm* verifies exactly the physical equation behind the *EB* model.

The symmetry of the differential permeability tensor with the *vpm* approach in the particular case of a purely rotational excitation is illustrated by means of an example in Fig. 4.2. However, in general, this symmetry is not guaranteed with the *vpm* approach as shown through another example in Fig. 4.3, where a rotating distorted signal

in presence of harmonics is now considered. It is obvious that the non-diagonal components of the tensors calculated by (4.11) are different from each other at almost each time step in this simulation.

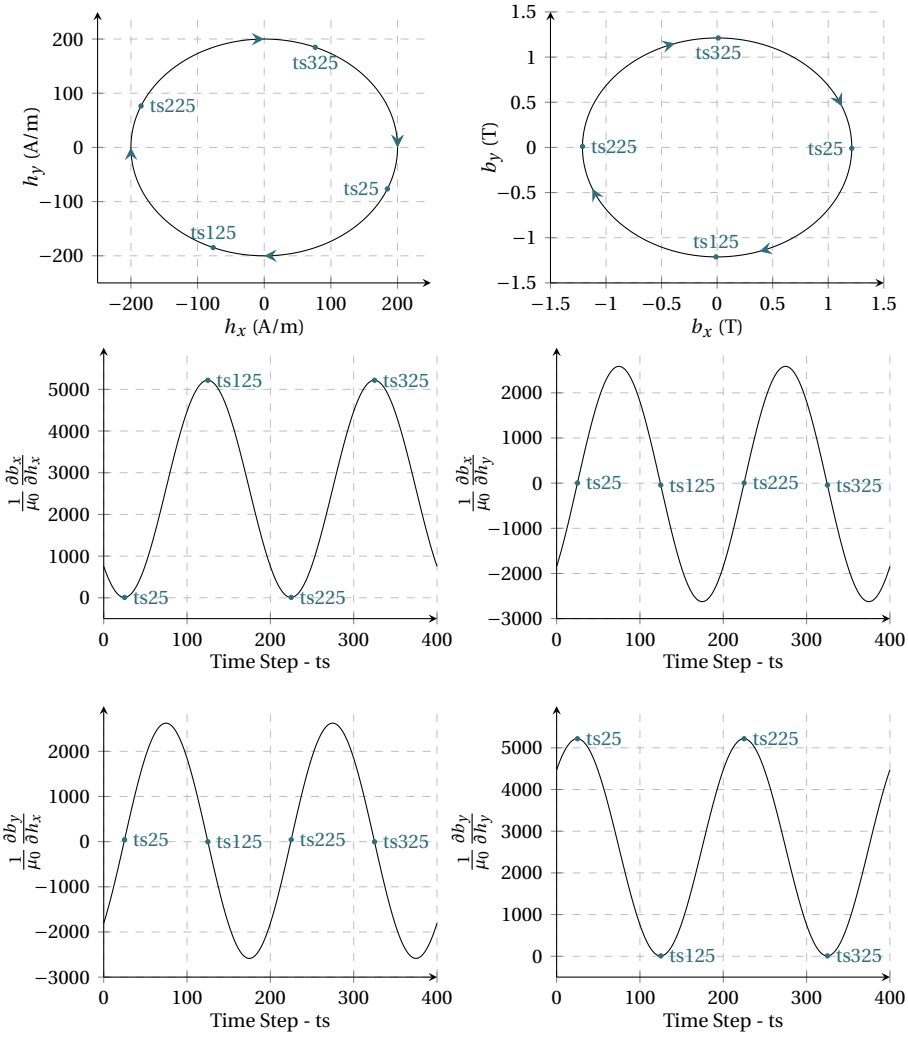

Figure 4.2: *Simulation with a direct vpm hysteresis model made up of* 1 *cell [*$\omega^1 = 1; \kappa^1 = 75\,\mathrm{A/m}$*] and with a hyperbolic tangent function as anhysteretic curve (*$J_a = 1.22\,\mathrm{T}$, $h_a = 65\,\mathrm{A/m}$*), subjected to a purely rotational magnetic field excitation of* $h_{max} = 200\,\mathrm{A/m}$*, with* 400 *time steps per period. (top left):* $\boldsymbol{h}$ *locus imposed as input, (top right):* $\boldsymbol{b}$ *locus calculated as output. Note that* $\boldsymbol{b}$ *rotates clock-wise with a slight phase lag behind* $\boldsymbol{h}$ *due to hysteresis, as indicated by the time step (ts) markers, ts*25*,ts*125*,ts*225*,ts*325*. (bottom): Evolution of the* xx*,* xy*,* yx *and* yy *components of the differential permeability tensor* $\frac{\partial \boldsymbol{b}}{\partial \boldsymbol{h}}$ *(divided by* μ_0*) calculated analytically with* (4.11) *at each time step. This tensor remains symmetric throughout the period since* $\frac{\partial b_x}{\partial h_y} = \frac{\partial b_y}{\partial h_x}$ *for all time steps in this purely rotational example.*

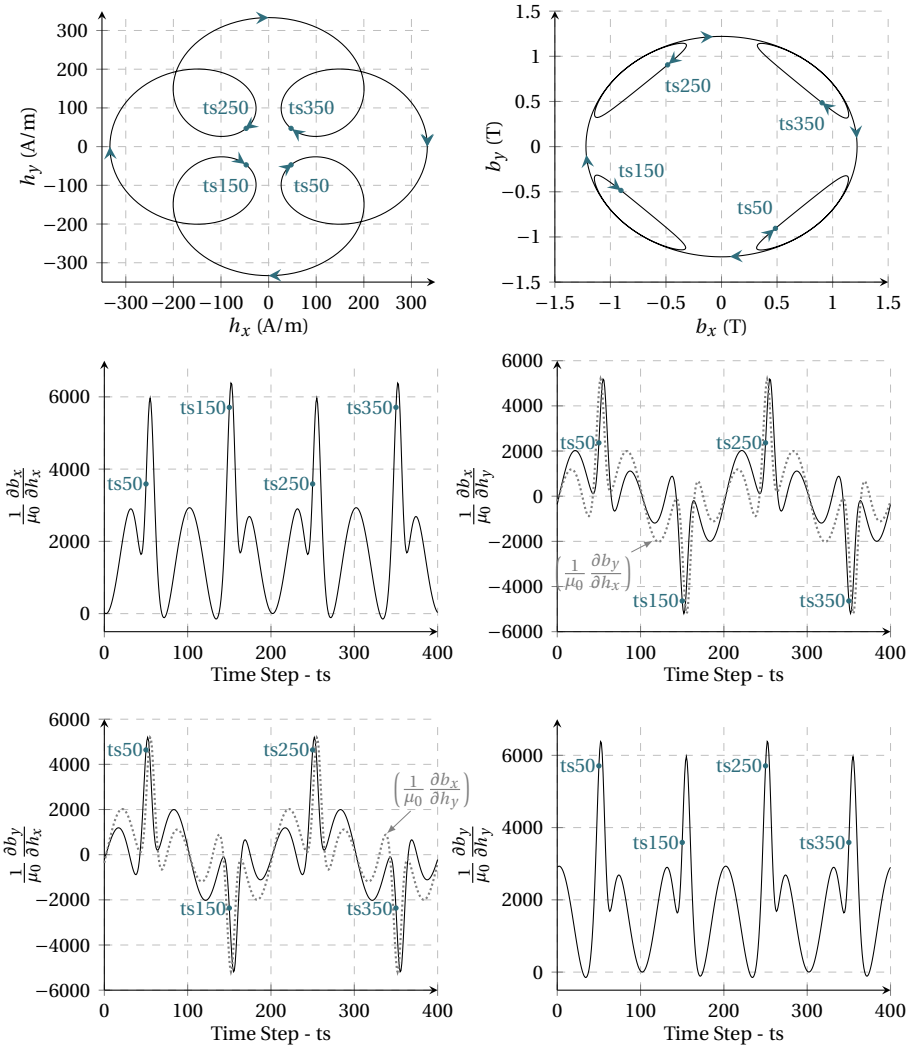

Figure 4.3: *Simulation with a direct vpm hysteresis model made up of* 1 *cell* [$\omega^1 = 1; \kappa^1 = 25\,\mathrm{A/m}$] *and with a hyperbolic tangent function as anhysteretic curve* ($J_a = 1.22\,\mathrm{T}$, $h_a = 65\,\mathrm{A/m}$), *subjected to a rotational magnetic field excitation with a fundamental of* $h_{max} = 200\,\mathrm{A/m}$, *in presence of a fifth higher harmonic of magnitude* $h_{harm} = (2/3)h_{max}$, *with* 400 *time steps per fundamental period. (top left):* $\mathbf{h}$ *locus imposed as input, (top right):* $\mathbf{b}$ *locus calculated as output. Note that* $\mathbf{b}$ *rotates with a slight phase lag behind* $\mathbf{h}$ *due to hysteresis, as indicated by the time step (ts) markers, ts*50,*ts*150,*ts*250,*ts*350. *(bottom): Evolution of the* xx, xy, yx *and* yy *components of the differential permeability tensor* $\frac{\partial \mathbf{b}}{\partial \mathbf{h}}$ *(divided by* μ_0*) calculated analytically with* (4.11) *at each time step. This tensor is not symmetric throughout the period since* $\frac{\partial b_x}{\partial h_y} \neq \frac{\partial b_y}{\partial h_x}$ *for all time steps in this example. The evolution of the two non-diagonal components are superimposed on each other to facilitate the comparison and make the differences more striking.*

Thanks to thermodynamical considerations, it can be shown that the differential permeability tensor $\frac{\partial \mathscr{B}}{\partial \mathbf{h}}$ should be symmetric in theory. However, it has been highlighted

that the *vpm* approach does not always guarantee this property with $\frac{\partial \mathscr{B}^{vpm}}{\partial \mathbf{h}}$ and hence suffers from a lack of consistency with basic thermodynamic laws. This limitation comes from the approximation used behind the construction of the *vpm* approach. Moreover, by anticipating Chapter 5 which focuses on the inclusion of the *EB* model in *FE* formulations, the *vpm* approach prevents the possibility to exploit symmetric Jacobian methods for the resolution of *FE* systems of equations, if the global assembled matrix associated to the *FE* model relies on local asymmetric tensors. Nonetheless, the symmetry of the Jacobian matrix does not constitute the fundamental basis of the theory and, more to the point, that property is not exploited fundamentally in the numerical methods employed in this thesis.

Variational Approach

Concerning the *var* approach, the state variables $\mathbf{J}^k$ are calculated by minimizing the potentials $\Omega^k(\mathbf{h},\mathbf{J}^k,\mathbf{J}^k_{(p)})$ evaluated by (3.19). Once again, it is possible to deduce an analytical expression for the tensors $\frac{\partial \mathbf{J}^k}{\partial \mathbf{h}}$ by exploiting the annulation of the functionals gradients at the potentials minima (3.18). Derivating this equality (3.18) with respect to $\mathbf{J}^k$ leads to the new relation

$$\frac{\partial^2}{\partial \mathbf{J}^{k2}}\left(g_L^k + \tilde{D}^k\right) = \mathbf{0}, \tag{4.12}$$

that involves the second derivatives with respect to $\mathbf{J}^k$ of the Landau free energy $g_L^k(\mathbf{h},\mathbf{J}^k)$, defined by (3.14), and of the pseudo-dissipation functions $\tilde{D}^k(\mathbf{J}^k,\mathbf{J}^k_{(p)})$, provided by (3.16). Starting then by breaking down the first term, that writes

$$\frac{\partial^2}{\partial \mathbf{J}^{k2}} g_L^k = \frac{\partial^2 f^k}{\partial \mathbf{J}^{k2}} - \frac{\partial \mathbf{h}}{\partial \mathbf{J}^k}, \tag{4.13}$$

reveals the tensor $\frac{\partial \mathbf{h}}{\partial \mathbf{J}^k}$, that corresponds exactly to the inverse of the tensor $\frac{\partial \mathbf{J}^k}{\partial \mathbf{h}}$ for which it is desired to determinate an analytical expression. The other term that appears in (4.13) comes from the second derivative of the Helmholtz potential $f^k(\mathbf{J}^k)$. This contribution can be rewritten thanks to the definition of the reversible field (2.14), in order to highlight that $\frac{\partial^2 f^k}{\partial \mathbf{J}^{k2}}$ has the characteristics of an inverse of a differential magnetic susceptibility tensor, with the units of an absolute magnetic reluctivity, in meter per henry (m/H),

$$\frac{\partial^2 f^k}{\partial \mathbf{J}^{k2}} = \frac{\partial}{\partial \mathbf{J}^k}\left(\frac{\partial f^k}{\partial \mathbf{J}^k}\right) = \frac{\partial}{\partial \mathbf{J}^k}\left(\mathbf{h}^k_{\text{rev}}\right) = \frac{\partial \mathbf{h}^k_{\text{rev}}}{\partial \mathbf{J}^k} = \underline{\boldsymbol{\chi}_{\partial}^{-1}}^k(\mathbf{J}^k). \tag{4.14}$$

Furthemore, this tensor can be expressed analytically based on the assumption that there exists a suitable analytical relation to describe the anhysteretic curve connecting $\mathbf{h}^k_{\text{rev}}$ and $\mathbf{J}^k$. In isotropic conditions, the vectors $\mathbf{h}^k_{\text{rev}}$ and $\mathbf{J}^k$ are parallel and related by a scalar anhysteretic function, $\mathbf{h}^k_{\text{rev}} = \mathscr{J}_{\text{an}}^{-1}\left(\frac{|\mathbf{J}^k|}{\omega^k}\right)\frac{\mathbf{J}^k}{|\mathbf{J}^k|}$, such that the tensor expression

$\underline{\boldsymbol{\chi}_{\partial}^{-1\,k}}(\mathbf{J}^k)$ can be calculated by derivation:

$$\underline{\boldsymbol{\chi}_{\partial}^{-1\,k}}(\mathbf{J}^k) = \frac{\partial \mathbf{h}_{\text{rev}}^k}{\partial \mathbf{J}^k} = \frac{1}{\omega^k}\left(\chi_{\text{an}}^{-1}\left(\frac{|\mathbf{J}^k|}{\omega^k}\right)\underline{\boldsymbol{I}} + \frac{\chi_{\text{an}\,\partial}^{-1}\left(\frac{|\mathbf{J}^k|}{\omega^k}\right) - \chi_{\text{an}}^{-1}\left(\frac{|\mathbf{J}^k|}{\omega^k}\right)}{|\mathbf{J}^k|^2}\mathbf{J}^k\mathbf{J}^{k\,T}\right). \tag{4.15}$$

Like previously, the factor $\mathbf{J}^k\mathbf{J}^{k\,T}$ denotes a tensor resulting from the dyadic product between the two vectors, and the transpose of the second one is indicated by a superscript T. The scalar quantities, χ_{an}^{-1} and $\chi_{\text{an}\,\partial}^{-1}$, correspond to the inverse of the apparent and the differential scalar magnetic susceptibilities respectively, defined by

$$\chi_{\text{an}}^{-1}\left(\frac{|\mathbf{J}^k|}{\omega^k}\right) = \frac{\mathscr{J}_{\text{an}}^{-1}\left(\frac{|\mathbf{J}^k|}{\omega^k}\right)}{\frac{|\mathbf{J}^k|}{\omega^k}}, \qquad \chi_{\text{an}\,\partial}^{-1}\left(\frac{|\mathbf{J}^k|}{\omega^k}\right) = \frac{\partial\,\mathscr{J}_{\text{an}}^{-1}\left(\frac{|\mathbf{J}^k|}{\omega^k}\right)}{\partial\left(\frac{|\mathbf{J}^k|}{\omega^k}\right)}. \tag{4.16, 4.17}$$

The analytical derivations of (4.16) and (4.17), may not be possible if the anhysteretic law, $\mathscr{J}_{\text{an}}$, is not invertible analytically, as for example with the Langevin function, for which $\mathscr{J}_{\text{an}}^{-1}$ is not defined.

The analogy between the tensors $\underline{\boldsymbol{\chi}_{\partial}^{\,k}}(\mathbf{h}_{\text{rev}}^k)$ (4.7) and $\underline{\boldsymbol{\chi}_{\partial}^{-1\,k}}(\mathbf{J}^k)$ (4.15) is obvious. Actually, they are reciprocal by definition, as a direct consequence of the chain rule:

$$\underline{\boldsymbol{\chi}_{\partial}^{-1\,k}}(\mathbf{J}^k)\,\underline{\boldsymbol{\chi}_{\partial}^{\,k}}(\mathbf{h}_{\text{rev}}^k) = \frac{\partial \mathbf{h}_{\text{rev}}^k}{\partial \mathbf{J}^k}\frac{\partial \mathbf{J}^k}{\partial \mathbf{h}_{\text{rev}}^k} = \underline{\boldsymbol{I}} \quad \longleftrightarrow \quad \underline{\boldsymbol{\chi}_{\partial}^{-1\,k}}(\mathbf{J}^k) = \left[\underline{\boldsymbol{\chi}_{\partial}^{\,k}}(\mathbf{h}_{\text{rev}}^k)\right]^{-1}. \tag{4.18}$$

Similarly for the scalar quantities $\chi_{\text{an}}(|\mathbf{h}_{\text{rev}}^k|)$ (4.8) and $\chi_{\text{an}\,\partial}(|\mathbf{h}_{\text{rev}}^k|)$ (4.9) which are the multiplicative inverses for $\chi_{\text{an}}^{-1}(|\mathbf{J}^k|/\omega^k)$ (4.16) and $\chi_{\text{an}\,\partial}^{-1}(|\mathbf{J}^k|/\omega^k)$ (4.17) respectively:

$$\chi_{\text{an}}^{-1}\left(\frac{|\mathbf{J}^k|}{\omega^k}\right) = \frac{1}{\chi_{\text{an}}(|\mathbf{h}_{\text{rev}}^k|)}, \qquad \chi_{\text{an}\,\partial}^{-1}\left(\frac{|\mathbf{J}^k|}{\omega^k}\right) = \frac{1}{\chi_{\text{an}\,\partial}(|\mathbf{h}_{\text{rev}}^k|)}. \tag{4.19, 4.20}$$

Therefore, the direct analytical functions of the apparent (4.8) and differential (4.9) scalar magnetic susceptibilities, and more generally, the direct differential magnetic susceptibility tensor expression (4.7), can be exploited instead of their inverse analogues (4.16), (4.17) or (4.15). That is of particular interest when the anhysteretic function has no analytical inverse $\mathscr{J}_{\text{an}}^{-1}$, and thus no analytical functions for χ_{an}^{-1} or $\chi_{\text{an}\,\partial}^{-1}$. Nevertheless, to follow this path, it remains necessary to deduce the $\mathbf{h}_{\text{rev}}^k$ corresponding to the $\mathbf{J}^k$, as $\mathbf{h}_{\text{rev}}^k$ is the natural input for the direct analytical versions (4.8), (4.9) and (4.7). From this perspective, it can be considered to build a database of pairs $(\mathbf{h}_{\text{rev}}^k, \mathbf{J}^k)$ based on the direct one-to-one anhysteretic curve for a wide range of discreetly spaced $\mathbf{h}_{\text{rev}}^k$ values. Any $\mathbf{h}_{\text{rev}}^k$ corresponding to a specific $\mathbf{J}^k$ can then be retrieved by interpolation between the database points. Another way to determinate $\mathbf{h}_{\text{rev}}^k$ from $\mathbf{J}^k$ when the anhysteretic curve does not have an analytical inverse $\mathscr{J}_{\text{an}}^{-1}$ consists in reversing the anhysteretic law $\mathscr{J}_{\text{an}}$ numerically. Anticipating the discussion of Chapter 4-Section 2.3, a *NR* iterative scheme is well suited to perform the inversion at this stage

because the anhysteretic curve is usually a twice continuously differentiable function, ensuring a quadratic convergence in the neighborhood of the solution.

In short, there is always a way out to calculate the tensor expression $\underline{\boldsymbol{\chi}_{\partial}^{-1}}^{k}(\mathbf{J}^k)$, and thus $\frac{\partial^2 f^k}{\partial \mathbf{J}^{k^2}}$ from (4.14), even if the anhysteretic law $\mathscr{J}_{\text{an}}$ is not analytically invertible.

Finally, it remains to characterize the expression of the second derivative with respect to $\mathbf{J}^k$ of the pseudo-dissipation functions, the last term of (4.12). This is achieved by taking the derivative with respect to $\mathbf{J}^k$ of the subgradients expression (3.17):

$$\partial^2_{\mathbf{J}^{k^2}} \tilde{D}^k(\mathbf{J}^k, \mathbf{J}^k_{(p)}) = \begin{cases} \dfrac{\partial \mathbf{h}^k_{\text{irr}}}{\partial \mathbf{J}^k}, |\mathbf{h}^k_{\text{irr}}| \leq \kappa^k, & \text{if} \mathbf{J}^k = \mathbf{J}^k_{(p)} \\ \dfrac{\partial \mathbf{h}^k_{\text{irr}}}{\partial \mathbf{J}^k} = \dfrac{\kappa^k}{|\mathbf{J}^k - \mathbf{J}^k_{(p)}|} \left(\underline{\boldsymbol{I}} - \dfrac{\left(\mathbf{J}^k - \mathbf{J}^k_{(p)}\right)\left(\mathbf{J}^k - \mathbf{J}^k_{(p)}\right)^T}{|\mathbf{J}^k - \mathbf{J}^k_{(p)}|^2} \right), & \text{otherwise} \end{cases} . \tag{4.21}$$

After reassembling the expressions (4.21) with (4.13) and (4.14), the equality (4.12) becomes in the case when $\mathbf{J}^k \neq \mathbf{J}^k_{(p)}$:

$$\frac{\partial \mathbf{h}}{\partial \mathbf{J}^k} = \underline{\boldsymbol{\chi}_{\partial}^{-1}}^{k}(\mathbf{J}^k) + \frac{\kappa^k}{|\mathbf{J}^k - \mathbf{J}^k_{(p)}|} \left(\underline{\boldsymbol{I}} - \frac{\left(\mathbf{J}^k - \mathbf{J}^k_{(p)}\right)\left(\mathbf{J}^k - \mathbf{J}^k_{(p)}\right)^T}{|\mathbf{J}^k - \mathbf{J}^k_{(p)}|^2} \right). \tag{4.22}$$

Taking the inverse of (4.22) leads finally to the analytical expression for the tensors $\frac{\partial \mathbf{J}^k}{\partial \mathbf{h}}$:

$$\frac{\partial \mathbf{J}^k}{\partial \mathbf{h}} = \frac{\partial \mathscr{J}^k}{\partial \mathbf{h}}(\mathbf{h}, \mathbf{J}^k_{(p)}) = \left[\underline{\boldsymbol{\chi}_{\partial}^{-1}}^{k}(\mathbf{J}^k) + \frac{\kappa^k}{|\mathbf{J}^k - \mathbf{J}^k_{(p)}|} \left(\underline{\boldsymbol{I}} - \frac{\left(\mathbf{J}^k - \mathbf{J}^k_{(p)}\right)\left(\mathbf{J}^k - \mathbf{J}^k_{(p)}\right)^T}{|\mathbf{J}^k - \mathbf{J}^k_{(p)}|^2} \right) \right]^{-1}, \tag{4.23}$$

which is valid only when the magnetization is changing, $\mathbf{J}^k \neq \mathbf{J}^k_{(p)}$. On the other hand, these tensors cancel, $\frac{\partial \mathbf{J}^k}{\partial \mathbf{h}} = \frac{\partial \mathscr{J}^k}{\partial \mathbf{h}} = \underline{\mathbf{0}}$, when the magnetization does not change with respect to a variation of the magnetic field $\mathbf{h}$, as $\mathbf{J}^k = \mathbf{J}^k_{(p)}$.

At the end, as soon as the updated $\mathbf{J}^k$ has been calculated through the minimization process (3.20), $\mathbf{J}^k = \mathscr{J}^k(\mathbf{h}, \mathbf{J}^k_{(p)})$, that depends only on $\mathbf{h}$ and $\mathbf{J}^k_{(p)}$, the tensors $\frac{\partial \mathbf{J}^k}{\partial \mathbf{h}}$ can be evaluated analytically from (4.23), and used to build the differential permeability tensor associated to the *var* approach with (4.5),

$$\frac{\partial \mathscr{B}^{var}}{\partial \mathbf{h}}(\mathbf{h}, \mathbf{J}^k_{(p)}) = \mu_0 \underline{\boldsymbol{I}} + \sum_{k=1}^{N} \frac{\partial \mathscr{J}^k}{\partial \mathbf{h}}. \tag{4.24}$$

Contrary to the *vpm* approach, the differential permeability tensor $\frac{\partial \mathscr{B}^{var}}{\partial \mathbf{h}}$ is always symmetric, considering the symmetry of the terms $\frac{\partial \mathscr{J}^k}{\partial \mathbf{h}}$, as verified analytically with (4.23), since $\underline{\boldsymbol{\chi}_{\partial}^{-1}}^{k}$ verifies also this property. With the *var* approach, the permeability is therefore in accordance with thermodynamic principles in all situations.

Differential Approach

By construction, the *diff* approach solves the same partial differential equations than the *var* approach (3.6), but in terms of the reversible field $\mathbf{h}_{\text{rev}}^k$ instead of the polarization field $\mathbf{J}^k$. Therefore, it is expected to reach the same analytical expression for the differential permeability tensor $\frac{\partial \mathscr{B}^{diff}}{\partial \mathbf{h}}$, formulated in terms of $\mathbf{h}_{\text{rev}}^k$.

The development can be replicated following the same idea, by starting from the update law $\mathscr{H}_{\text{rev}}(\mathbf{h}, \mathbf{h}_{\text{rev}(p)}^k)$ (3.28), which translates the energy equilibrium that can be written as

$$\mathbf{h}_{\text{rev}}^k = \mathbf{h} - \kappa^k \frac{\Delta \mathbf{J}^k}{|\Delta \mathbf{J}^k|}, \tag{4.25}$$

for the case when $|\mathbf{h} - \mathbf{h}_{\text{rev}(p)}^k| > \kappa^k$. The notation $\Delta \mathbf{J}^k = \omega^k \mathbf{J}_{\text{an}}(\mathbf{h}_{\text{rev}}^k) - \omega^k \mathbf{J}_{\text{an}}(\mathbf{h}_{\text{rev}(p)}^k)$ is used to express the direction of the irreversible field $\mathbf{e}_{\mathbf{h}_{\text{irr}}^k} = \mathbf{e}_{\dot{\mathbf{J}}^k} \approx \frac{\Delta \mathbf{J}^k}{|\Delta \mathbf{J}^k|}$, in accordance with (3.24) and (3.26). The dependence of $\Delta \mathbf{J}^k$ with respect to $\mathbf{h}_{\text{rev}}^k$ and $\mathbf{h}_{\text{rev}(p)}^k$ is not reported for the sake of brevity in the following. Taking the derivative with respect to $\mathbf{h}$ of (4.25) leads to

$$\frac{\partial \mathbf{h}_{\text{rev}}^k}{\partial \mathbf{h}} = \underline{\boldsymbol{I}} - \frac{\kappa^k}{|\Delta \mathbf{J}^k|} \left(\underline{\boldsymbol{I}} - \frac{\Delta \mathbf{J}^k \Delta \mathbf{J}^{k\,T}}{|\Delta \mathbf{J}^k|^2} \right) \frac{\partial \Delta \mathbf{J}^k}{\partial \mathbf{h}}. \tag{4.26}$$

The tensor $\frac{\partial \Delta \mathbf{J}^k}{\partial \mathbf{h}}$ can be broken down into the product of the differential susceptibility tensor $\underline{\boldsymbol{\chi}_\partial}^k(\mathbf{h}_{\text{rev}}^k)$ (4.7) with the vector-by-vector derivative factor $\frac{\partial \mathbf{h}_{\text{rev}}^k}{\partial \mathbf{h}}$, after application of the chain rule

$$\frac{\partial \Delta \mathbf{J}^k}{\partial \mathbf{h}} = \frac{\partial \mathbf{J}^k}{\partial \mathbf{h}} = \frac{\partial \mathbf{J}^k}{\partial \mathbf{h}_{\text{rev}}^k} \frac{\partial \mathbf{h}_{\text{rev}}^k}{\partial \mathbf{h}} = \underline{\boldsymbol{\chi}_\partial}^k(\mathbf{h}_{\text{rev}}^k) \frac{\partial \mathbf{h}_{\text{rev}}^k}{\partial \mathbf{h}}, \tag{4.27}$$

such that the tensor $\frac{\partial \mathbf{h}_{\text{rev}}^k}{\partial \mathbf{h}}$ can be highlighted in (4.26)

$$\underline{\boldsymbol{I}} = \left[\underline{\boldsymbol{I}} + \frac{\kappa^k}{|\Delta \mathbf{J}^k|} \left(\underline{\boldsymbol{I}} - \frac{\Delta \mathbf{J}^k \Delta \mathbf{J}^{k\,T}}{|\Delta \mathbf{J}^k|^2} \right) \underline{\boldsymbol{\chi}_\partial}^k(\mathbf{h}_{\text{rev}}^k) \right] \frac{\partial \mathbf{h}_{\text{rev}}^k}{\partial \mathbf{h}}. \tag{4.28}$$

An analytical expression for the tensor $\frac{\partial \mathbf{h}_{\text{rev}}^k}{\partial \mathbf{h}}$ can then be deduced after applying an inverse multiplication:

$$\frac{\partial \mathbf{h}_{\text{rev}}^k}{\partial \mathbf{h}} = \frac{\partial \mathscr{H}_{\text{rev}}^k}{\partial \mathbf{h}}(\mathbf{h}, \mathbf{h}_{\text{rev}(p)}^k) = \left[\underline{\boldsymbol{I}} + \frac{\kappa^k}{|\Delta \mathbf{J}^k|} \left(\underline{\boldsymbol{I}} - \frac{\Delta \mathbf{J}^k \Delta \mathbf{J}^{k\,T}}{|\Delta \mathbf{J}^k|^2} \right) \underline{\boldsymbol{\chi}_\partial}^k(\mathbf{h}_{\text{rev}}^k) \right]^{-1}, \tag{4.29}$$

This result (4.29) is only valid when $|\mathbf{h} - \mathbf{h}_{\text{rev}(p)}^k| > \kappa^k$. In the other case, when the magnetization does not change, the reversible field is also frozen and $\frac{\partial \mathbf{h}_{\text{rev}}^k}{\partial \mathbf{h}} = \frac{\partial \mathscr{H}_{\text{rev}}^k}{\partial \mathbf{h}} = \underline{\mathbf{0}}$. In summary, once the $\mathbf{h}_{\text{rev}}^k$ is calculated from the update law $\mathscr{H}_{\text{rev}}^k(\mathbf{h}, \mathbf{h}_{\text{rev}(p)})$ (3.28), that depends on $\mathbf{h}$ and $\mathbf{h}_{\text{rev}(p)}$, the differential permeability tensor associated to the *diff* approach can be expressed analytically from (4.6), combining (4.29) and (4.7), evaluated

with the updated fields $\mathbf{h}_{\text{rev}}^k = \mathscr{H}_{\text{rev}}^k$:

$$\frac{\partial \mathscr{B}^{diff}}{\partial \mathbf{h}}(\mathbf{h}, \mathbf{h}_{\text{rev}(p)}^k) = \mu_0 \underline{\boldsymbol{I}} + \sum_{k=1}^{N} \underline{\boldsymbol{\chi}_\partial}^k(\mathscr{H}_{\text{rev}}^k) \frac{\partial \mathscr{H}_{\text{rev}}^k}{\partial \mathbf{h}}. \tag{4.30}$$

Not surprisingly, the mathematical development behind the magnetic differential permeability tensor of the *diff* approach (4.30) leads to the same analytical form that for the *var* approach (4.24). Indeed, the tensor products $\underline{\boldsymbol{\chi}_\partial}^k(\mathscr{H}_{\text{rev}}^k) \frac{\partial \mathscr{H}_{\text{rev}}^k}{\partial \mathbf{h}}$ from (4.30) are, at the end, equivalent to the tensors $\frac{\partial \mathscr{J}^k}{\partial \mathbf{h}}$ from (4.24), but written in terms of $\mathbf{h}_{\text{rev}}^k$. This correspondence can be established clearly regarding the reciprocal property given by (4.18), and the matrix arithmetic rule for the inverse product, $\left[\underline{\boldsymbol{AB}}\right]^{-1} = \underline{\boldsymbol{B}}^{-1}\underline{\boldsymbol{A}}^{-1}$, so that, for the case when $|\mathbf{h} - \mathbf{h}_{\text{rev}(p)}^k| > \kappa^k$, or equivalently when $\mathbf{J}^k \neq \mathbf{J}_{(p)}^k$, one has

$$\begin{aligned}
\underline{\boldsymbol{\chi}_\partial}^k(\mathscr{H}_{\text{rev}}^k) \frac{\partial \mathscr{H}_{\text{rev}}^k}{\partial \mathbf{h}} &= \underline{\boldsymbol{\chi}_\partial}^k(\mathbf{h}_{\text{rev}}^k) \left[\underline{\boldsymbol{I}} + \frac{\kappa^k}{|\Delta \mathbf{J}^k|} \left(\underline{\boldsymbol{I}} - \frac{\Delta \mathbf{J}^k \Delta \mathbf{J}^{k\,T}}{|\Delta \mathbf{J}^k|^2} \right) \underline{\boldsymbol{\chi}_\partial}^k(\mathbf{h}_{\text{rev}}^k) \right]^{-1} \\
&= \left[\underline{\boldsymbol{\chi}_\partial^{-1}}^k(\mathbf{J}^k) \right]^{-1} \left[\underline{\boldsymbol{I}} + \frac{\kappa^k}{|\Delta \mathbf{J}^k|} \left(\underline{\boldsymbol{I}} - \frac{\Delta \mathbf{J}^k \Delta \mathbf{J}^{k\,T}}{|\Delta \mathbf{J}^k|^2} \right) \underline{\boldsymbol{\chi}_\partial}^k(\mathbf{h}_{\text{rev}}^k) \right]^{-1} \\
&= \left[\underline{\boldsymbol{\chi}_\partial^{-1}}^k(\mathbf{J}^k) + \frac{\kappa^k}{|\Delta \mathbf{J}^k|} \left(\underline{\boldsymbol{I}} - \frac{\Delta \mathbf{J}^k \Delta \mathbf{J}^{k\,T}}{|\Delta \mathbf{J}^k|^2} \right) \underline{\boldsymbol{\chi}_\partial}^k(\mathbf{h}_{\text{rev}}^k) \underline{\boldsymbol{\chi}_\partial^{-1}}^k(\mathbf{J}^k) \right]^{-1} \\
&= \left[\underline{\boldsymbol{\chi}_\partial^{-1}}^k(\mathbf{J}^k) + \frac{\kappa^k}{|\Delta \mathbf{J}^k|} \left(\underline{\boldsymbol{I}} - \frac{\Delta \mathbf{J}^k \Delta \mathbf{J}^{k\,T}}{|\Delta \mathbf{J}^k|^2} \right) \right]^{-1} = \frac{\partial \mathscr{J}^k}{\partial \mathbf{h}},
\end{aligned}$$

retrieving the expression from the *var* approach (4.23), considering that $\Delta \mathbf{J}^k = \mathbf{J}^k - \mathbf{J}_{(p)}^k$.

Therefore, just like for the *var* approach, the differential permeability tensor $\frac{\partial \mathscr{B}^{diff}}{\partial \mathbf{h}}$ is also symmetric in all circumstances, which is in agreement with thermodynamic considerations.

This property is illustrated by means of the example shown in Fig. 4.4, where the same distorted excitation source as in Fig. 4.3 is used again, but applied here to the *diff* model approach. This time, there is no difference between the non-diagonal components of the differential permeability tensor, calculated through (4.30) at each time step, meaning that the tensor remains well symmetric throughout the simulation. The same result can be produced with the *var* approach.

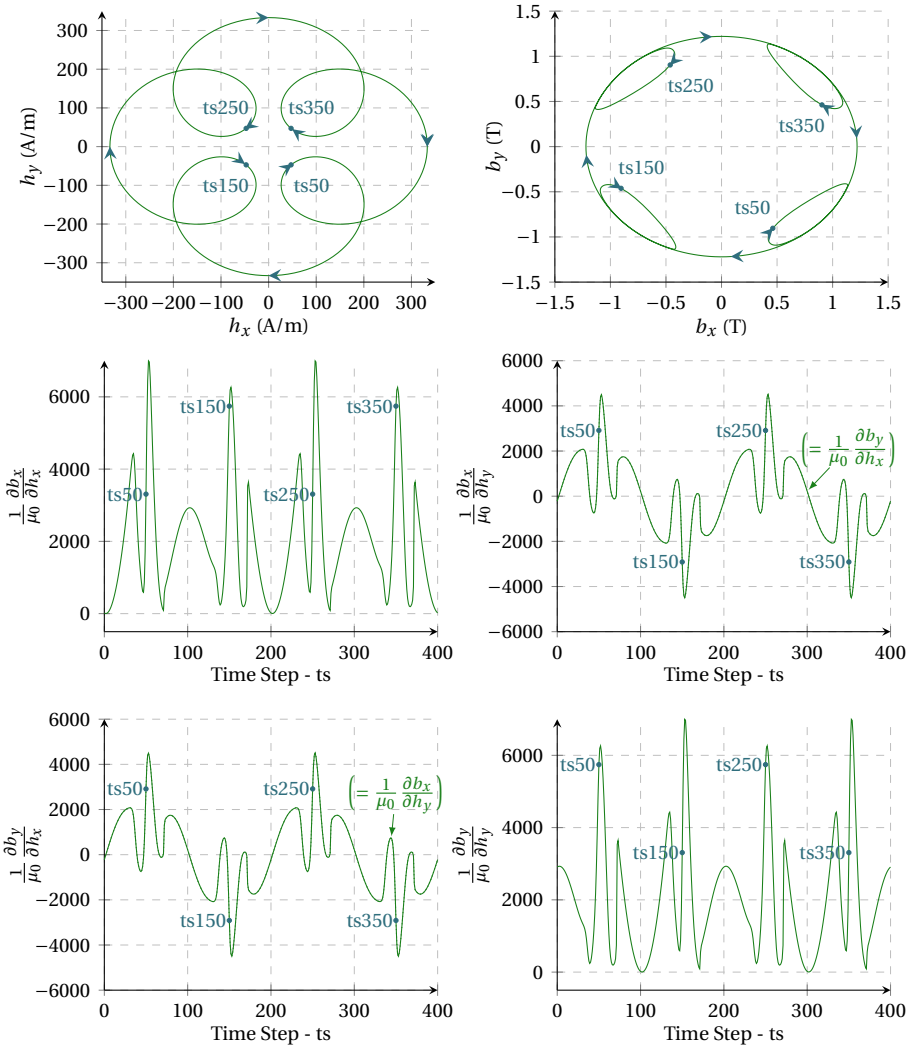

Figure 4.4: *Simulation with a direct diff hysteresis model made up of* 1 *cell* $[\omega^1 = 1; \kappa^1 = 25\,\mathrm{A/m}]$ *and with a hyperbolic tangent function as anhysteretic curve* ($J_a = 1.22\,\mathrm{T}$, $h_a = 65\,\mathrm{A/m}$)*, subjected to the same excitation as in Fig. 4.3, i.e. a rotational magnetic field excitation with a fundamental of* $h_{max} = 200\,\mathrm{A/m}$*, in presence of a fifth higher harmonic of magnitude* $h_{harm} = (2/3)h_{max}$*, with* 400 *time steps per fundamental period (top left):* $\boldsymbol{h}$ *locus imposed as input, (top right):* $\boldsymbol{b}$ *locus calculated as output. Note that* $\boldsymbol{b}$ *rotates with a slight phase lag behind* $\boldsymbol{h}$ *due to hysteresis, as indicated by the time step (ts) markers,* $ts50, ts150, ts250, ts350$*. (bottom): Evolution of the* xx*,* xy*,* yx *and* yy *components of the differential permeability tensor* $\frac{\partial \boldsymbol{b}}{\partial \boldsymbol{h}}$ *(divided by* μ_0*) calculated analytically with (4.30) at each time step. This tensor is symmetric throughout the period since* $\frac{\partial b_x}{\partial h_y} = \frac{\partial b_y}{\partial h_x}$ *for all time steps. The evolution of the two non-diagonal components are superimposed on each other to facilitate the comparison and they are in perfect agreement.*

2.3. Practical Considerations about the Convergence

Before discussing the ability of the *NR* method to perform the inversion of the *EB* model, it is worth recalling the general requirements under which the convergence of the *NR* method is ensured. This is easily sketched by considering again the simpler application of the *NR* algorithm on the root-finding of a univariate function $r(x)$, for which a direct geometrical interpretation of the update (4.1) exists, as shown with Fig. 4.1.

This illustrative description indicates that at least two conditions are required for the algorithm to work properly: the function must be differentiable at each points x^l that are visited in order to linearize the function there; and the derivatives must not cancel at these points so that the linearized function has a zero. In addition to these conditions, there is the strong constraint of having the initial guess x^0 close enough to the unknown zero x^* of the function so that the convergence is ensured. Mathematically, it can be proved that the sequence produced by the *NR* method is a very powerful technique which may exhibit a local quadratic convergence in the conditions where the function $\mathbf{r}(\mathbf{x})$ is continuously differentiable with a zero $\mathbf{r}(\mathbf{x}^*) = \mathbf{0}$, if (i) the Jacobian $\frac{\partial \mathbf{r}(\mathbf{x})}{\partial \mathbf{x}}$ is non singular at $\mathbf{x}^*$, and (ii) the Jacobian is Lipschitz continuous on a neighborhood of $\mathbf{x}^*$, and that the initial point is close to $\mathbf{x}^*$ [87, 165].

Nevertheless, they are many situations in which the required criteria are not met, so that the *NR* method can fail to converge. Some of these complications are illustrated with several non-converging examples in Fig. 4.5. The non-smoothness and/or the non-differentiability of the function in a neighborhood of the root are a first obvious violation of the *NR* method. An example of divergence due to an angular point, where a discontinuous change in the derivative happens, is presented on Fig. 4.5(a). Fig. 4.5(b) exposes the failure of the method when a stationary iteration point is encountered. The zero derivative produces a tangent line parallel to the x-axis which shoots off the solution. Actually, even if the derivative is small but does not cancel, the next iteration point will be found very far away horizontally and be a poor approximation of the root.

The behaviour of the *NR* method may be highly dependent on the choice of the initial point x^0. Fig. 4.5(c-d) shows how an initial guess, relatively close to one root, with a rather small slope, can jump away to another location, possibly converging to another unwanted root that may exist there (Fig. 4.5(c)), or reaching a region where the method simply does not converge, which can arise, for example, if the function approaches zero asymptotically as x goes to $\pm\infty$ (Fig. 4.5(d)). If the initial iteration is not taken close enough to a zero and that the function presents an inflection point with a rather brutal curvature change in the vicinity of a root, iterations may progressively diverge from the root as illustrated by Fig. 4.5(e). For some functions, the visited points may enter an infinite cycle, preventing convergence, as illustrated with Fig. 4.5(f-g), where oscillations caused by an inflection point or by a local minimum are presented, respectively. The behavior of the sequence can be more complicated than an alternation between two points, as depicted with a wandering example of the method caused by a local minimum at Fig. 4.5(h). In other word, when the initial iteration is taken too far away from a local root, the iterated sequence generated by the algorithm has an

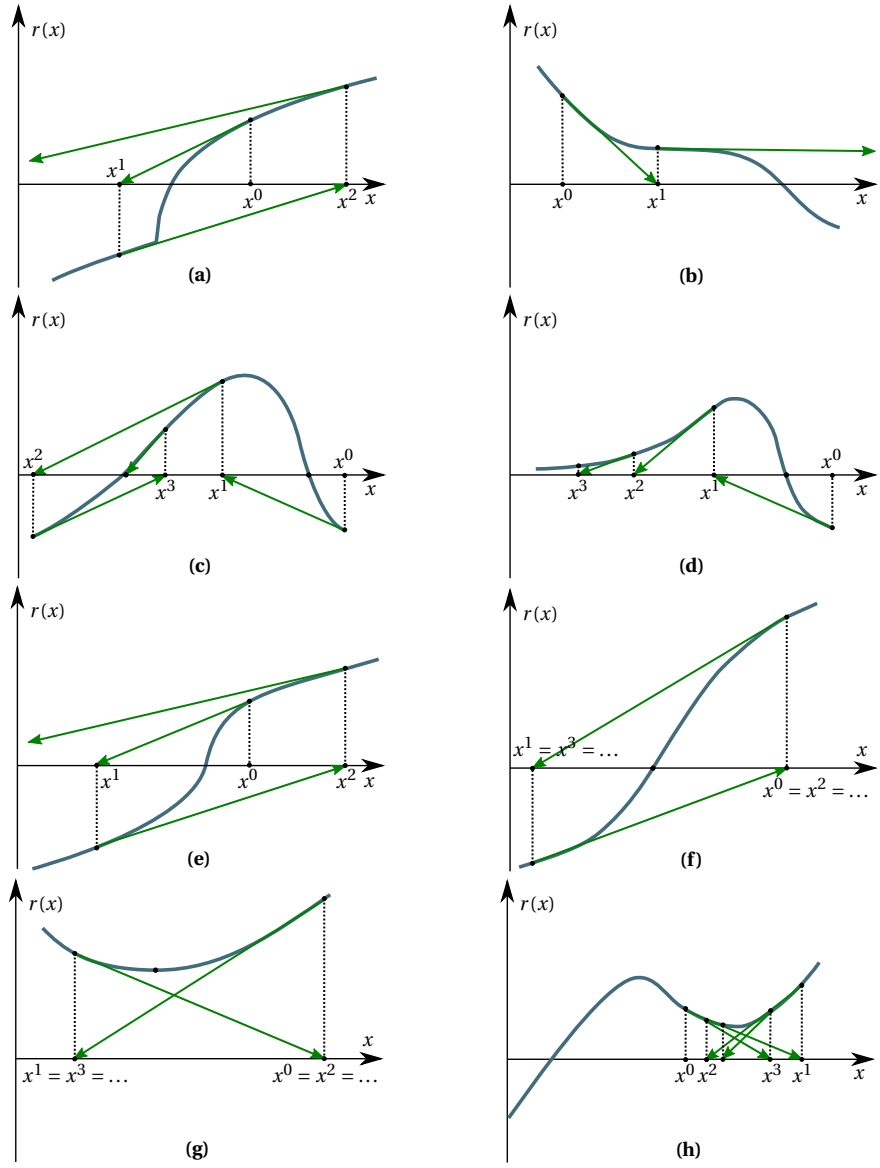

Figure 4.5: *Failures of the classical NR Method:* ***(a)*** *Divergence due to an angular point;* ***(b)*** *Shoots-off of the solution due to a near zero slope;* ***(c-d)*** *Jumps away from the solution due to a poor initial guess;* ***(e)*** *Divergence due to a poor initial guess and the influence of an inflection point near the root;* ***(f-g)*** *Cycling behabiours;* ***(h)*** *Non-converging wandering sequence.*

erratic behavior, whose possible convergence can only be the fruit of chance if one of the iterates is fortunately close to a zero.

In the light of the various general limitations of the *NR* method listed above, the atten-

tion is now paid on the specific application of this method for the inversion of the *EB* model through (4.3). It is clear that the function, $\mathbf{r}(\mathbf{h}) = \mathscr{B}^{dir}(\mathbf{h}, \mathbf{X}^k_{(p)}) - \mathbf{b}^*$, does not meet all the criteria required to the proper functioning of the classical *NR* iterative scheme.

Indeed, whatever the approach behind the *EB* model, the relation $\mathscr{B}^{dir}(\mathbf{h}, \mathbf{X}^k_{(p)})$ is obviously not continuously differentiable at each magnetic field value due to the presence of angular points, which are associated to brutal changes in the magnetization regime for specific values of the magnetic field $\mathbf{h}$, that reflect the transition between the cases $|\mathbf{h} - \mathbf{h}^k_{r(p)}| \leq \kappa^k$ and $|\mathbf{h} - \mathbf{h}^k_{r(p)}| > \kappa^k$ in the *vpm* and the *diff* approaches, which corresponds to the turning situation between $|\mathbf{J}^k - \mathbf{J}^k_{(p)}| = 0$ and $|\mathbf{J}^k - \mathbf{J}^k_{(p)}| > 0$ in the *var* approach. The components of the differential permeability tensors are modified by jumps between these two frozen or unfrozen magnetization behaviors, and are actually undefined analytically at these transition points.

This situation can be easily illustrated by means of a simple 1-cell *EB* model subjected to unidirectional ramp excitation starting from the demagnetized state, with an imposed magnetic field increasing monotonously at each time step, as in Fig. 4.6(top left). The response of the direct model, shown in Fig. 4.6(top right), gives an induction field that increases first linearly with a slope of μ_0, as long as the magnetic field magnitude remains smaller than the cell pinning field κ^1, until the magnetization changes suddenly at the moment where this threshold is reached, and evolves then according to the anhysteretic function for the following time steps. The xx-component of the differential permeability tensor presents thus a brutal increase at the instant where the cell becomes activated, as shown in Fig. 4.6(bottom left), and decreases then smoothly towards the value μ_0 in the saturation limit.

An effective inverse form of the *EB* model must be able to produce the magnetic field $\mathbf{h}$ from an imposed induction field $\mathbf{b}$, which amounts to retrieving the signal of Fig. 4.6(top left), based on the data of Fig. 4.6(top right), taken as input. For each time step n, the current value $\mathbf{b}^*_n$ is thus known, and the classical *NR* method (4.3) may be applied to determine the corresponding magnetic field $\mathbf{h}_n$, starting each iteration from the field obtained at the previous time step, i.e. $\mathbf{h}^0_n = \mathbf{h}_{(p)} = \mathbf{h}_{n-1}$. In this example, the *NR* method works properly for the first time steps where the induction field increases with a constant slope μ_0 between subsequent time instants. Actually, the *NR* method requires only 1 iteration to converge for these time steps since the function is linear in that region. However, the classical *NR* method cannot work for the time step just beyond the angular point. The zoom around this zone in Fig. 4.6(bottom right) shows hence the points that can be retrieved by the inverse form, superimposed over the result from the direct form that serves as reference.

The detail on the failure of the classical *NR* method in finding the solution for this specific time step, just after the angular point, is illustrated graphically by Fig. 4.7. In these figures, the function $\mathscr{B}^{dir}(\mathbf{h}, \mathbf{X}^k_{(p)})$ associated to the considered time step is represented. The subsequent values $\mathbf{h}^l$ found by the application of the *NR* update (4.3) are depicted. Only the composition along the excitation direction, thus along $\mathbf{x}$, is given. The algorithm is initialized at (h^0_x, b^0_x) based on the previous time step solution with

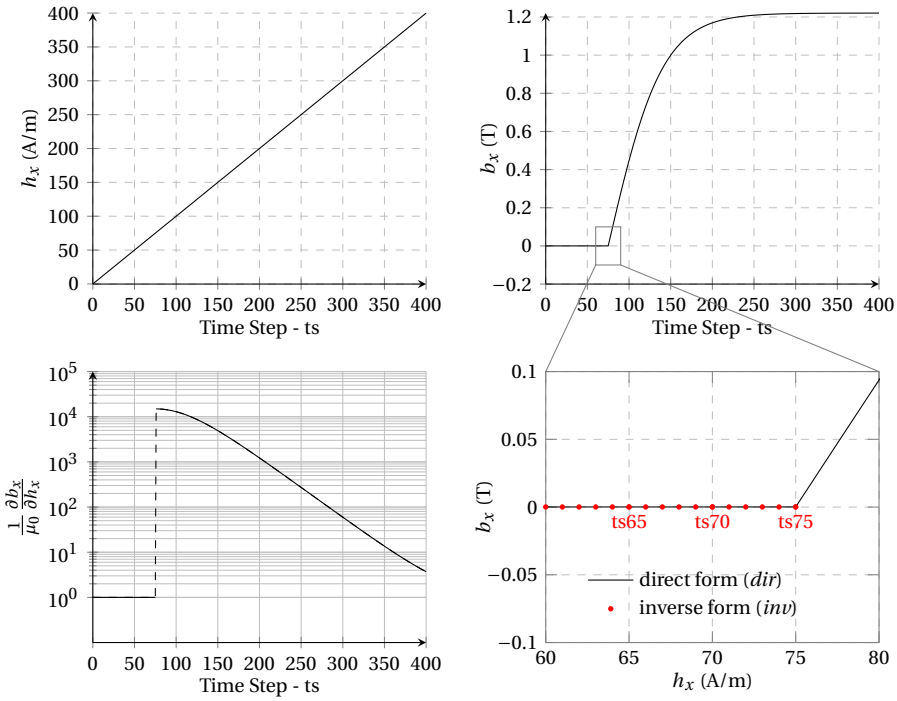

Figure 4.6: *Simulation with a direct vpm hysteresis model made up of* 1 *cell* $[\omega^1 = 1; \kappa^1 = 75\,\mathrm{A/m}]$ *and with a hyperbolic tangent function as anhysteretic curve* ($J_a = 1.22\,\mathrm{T}$, $h_a = 65\,\mathrm{A/m}$)*, subjected to a ramp magnetic field excitation (top left), which produces an induction field response with an angular point at time step* 75 *(top right). (bottom left): Evolution of the xx component of the differential permeability tensor* $\frac{\partial \boldsymbol{b}}{\partial \boldsymbol{h}}$ *(divided by* μ_0*) calculated analytically with* (4.11) *at each time step. (bottom right): Inversion of the direct vpm hysteresis model with the classical NR method. The induction field* $\boldsymbol{b}$ *in (top right) is used as input for the inverse form with the aim to retrieve as output the magnetic field in (top left) originally imposed for the direct form. The inversion works until time step* 76 *where the presence of the angular point causes the method to fail.*

the aim to find the solution h_x^*, associated to the known value b_x^*. Unfortunately, the near zero slope μ_0 at the starting point leads to a value h_x^1 far away in the saturation range, where a slope as equally low as μ_0 produce a next estimate h_x^2 that far in the opposite saturated region. The algorithm determines then subsequent iterates $h_x^3, h_x^4, \ldots$ that enter in a cycling behavior, oscillating between very distant values in opposite saturation, where the differential permeability tensors, i.e. the slopes, remain unchanged, not allowing any progress in converging to the solution h_x^*.

In summary, due to the discontinuities displayed by the differential permeability tensor, the classical *NR* process may exhibit a cycling behavior when successive iterates lie from one side to another around the derivative discontinuity, preventing the algorithm to converge. Furthermore, some stability problems may be encountered when the *NR* iterations lead to values far from the solution and near magnetic saturation where $|\mathbf{h}_{\mathrm{rev}}^k|$ values are high and $|\mathbf{J}^k|$ are close to their maximum values, since the ten-

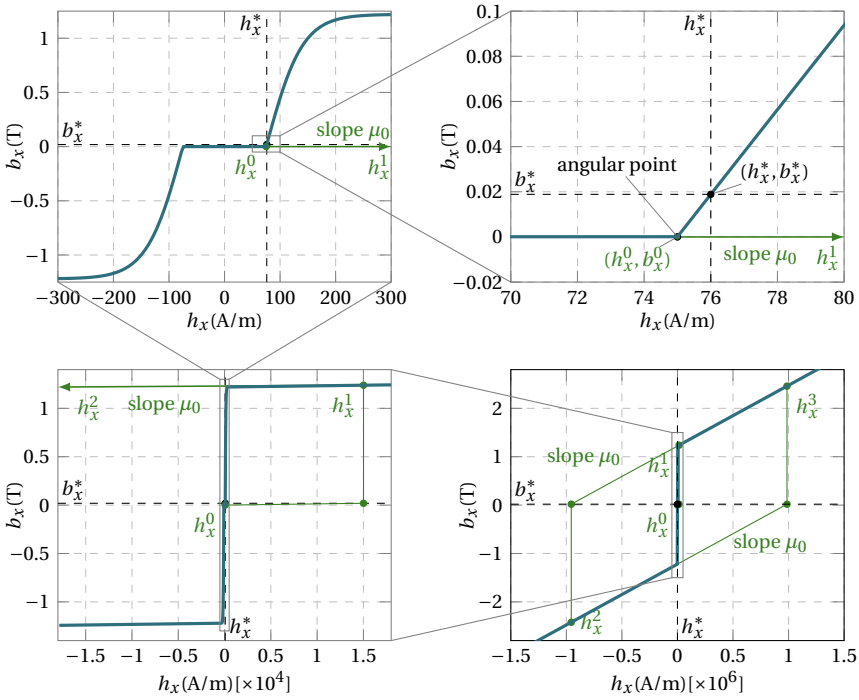

Figure 4.7: *Failure of the classical NR method to determine the solution $\mathbf{h}^*$ associated to the known value $\mathbf{b}^*$, at time step 76 in the example of Fig. 4.6. The function $\mathscr{B}^{dir}(\mathbf{h}, \mathbf{X}^k_{(p)})$ associated to this time step is represented, focusing on its composition along the direction $\mathbf{x}$. Starting from the previous time step solution (h_x^0, b_x^0), the algorithm generates subsequent iterate values $h_x^1, h_x^2, h_x^3, \ldots$ which move further away from the solution h_x^*, before cycling indefinitely between two iterate states in opposite saturation.*

sors $\frac{\partial \mathbf{J}^k}{\partial \mathbf{h}}$ of each cell tend to become singular in that region. Therefore, the tensor $\frac{\partial \mathscr{B}}{\partial \mathbf{h}}$ may become ill-conditioned, with small diagonal component values, almost equal to the vacuum permeability value μ_0, such that the update (4.3) may probably determine a value $\mathbf{h}^l$ very far away from the previous one $\mathbf{h}^{l-1}$, thus with large increments between two *NR* iterations, $\Delta\mathbf{h}^l = \mathbf{h}^l - \mathbf{h}^{l-1}$, that may lead to divergence.

2.4. Relaxation Technique

It is well known that the complications encountered with the classical *NR* method may be alleviated by using a relaxation factor $\gamma \in]0,1]$, to reduce the increment towards the next iterate and avoid proceeding into a region where the convergence is compomised. In the preliminary *NR* scheme (4.1) for the root-finding of univariate function $r(x)$, it comes down to consider

$$x^l_{\text{relaxed}} = x^{l-1} + \gamma\,(x^l - x^{l-1}) = x^{l-1} + \gamma\,\Delta x^l\,, \tag{4.31}$$

where x^l_{relaxed} is then the next iterate used in the *NR* scheme, instead of x^l. The value of the relaxation factor can be fixed a priori to a constant value γ. A value $\gamma = 1$ means that

the scheme is non-relaxed, as in the classical scheme. As γ is selected closer to zero, the relaxation is accentuated. If the factor γ is chosen very small, this may increase the number of *NR* iterations needed, and so the computation time, but may guarantee the convergence by progressing by tiny increments.

More wisely, the relaxation factor can be adapted at each *NR* iteration, in such a way that the next iterate is forced to be a better approximation of the root than the previous point. At a given *NR* iteration l, several factors $\gamma^l_{[m]}$ may be tested before finding a value that satisfies, for instance

$$\left|r(x^l_{[m]})\right| < \left|r(x^{l-1})\right|, \tag{4.32}$$

where $x^l_{[m]} = x^{l-1} + \gamma^l_{[m]}\,\Delta x^l$, from (4.31). The search can start from $\gamma^l_{[0]} = 1$, and then probe smaller values following, for example, a geometric sequence

$$\gamma^l_{[m]} = \frac{1}{\varphi^m}, \tag{4.33}$$

with $m = 0, 1, 2, \ldots$, where φ is a common ratio generally chosen equal to the golden ratio or to 2. The search is stopped as soon as the criterium (4.32) is verified. For each tested relaxation factor $\gamma^l_{[m]}$, there is thus one additional function evaluation $r(x^l_{[m]})$.

Considering again the earlier illustration from Fig. 4.1 (right), one can see that the *NR* method takes too large a first step with the standard approach. Introduction an adaptive relaxation mechanism in this example allows to improve significantly the determination of the increment, as shown on Fig. 4.8. The relaxation process is here highly attractive since it requires less *NR* iterations than in the non-relaxed situation to approach faster the function root. Each relaxation factor search needs only to evaluate $r(x^l_{[m]})$ such that its computational cost is rather low as compared to applying the left multiplication by the inverted derivative, $[r'(x^{l-1})]^{-1}\cdot$, as needed in each *NR* update (4.1), especially in the multi-dimensional case (4.2). It is therefore always preferable to have fewer *NR* iterations at the cost of a greater number of relaxation factor processing.

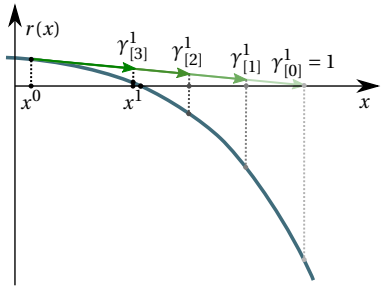

Figure 4.8: *Illustration of a relaxed NR method applied on the same example as Fig. 4.1 (right).*

More importantly, the relaxation mechanism makes it possible to converge for situations where the classical *NR* method fails. This is illustrated on Fig. 4.9, which includes

two previous non-converging examples from Fig. 4.5(a),(e) respectively, but the convergence is achieved here thanks to the relaxation on the increments.

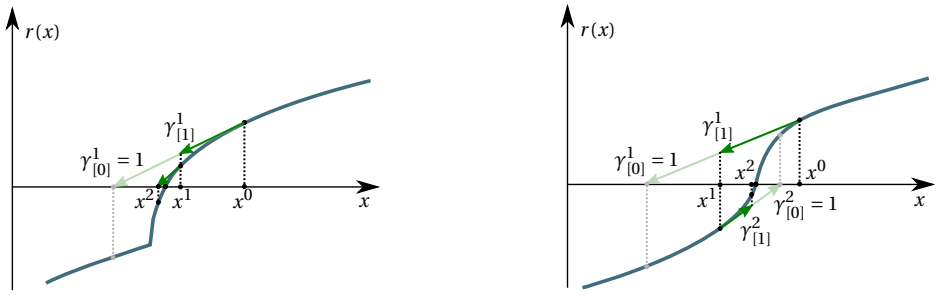

Figure 4.9: *Convergence of the relaxed NR method where the classical NR method fails, illustrated around an angular point (left), or an inflection point (right), taken from the illustrations in Fig. 4.5(a),(e), respectively.*

In the same way, the relaxation method can be applied on the *NR* method used for the inversion of the *EB* model, whose update scheme is (4.3). Particularizing the relaxation technique (4.31) and the relaxation factor search criterium (4.32), for this application consists in searching the factor $\gamma^l_{[m]}$ that gives

$$\mathbf{h}^l_{[m]} = \mathbf{h}^{l-1} + \gamma^l_{[m]}\left(\mathbf{h}^l - \mathbf{h}^{l-1}\right) = \mathbf{h}^{l-1} + \gamma^l_{[m]}\Delta\mathbf{h}^l\,, \tag{4.34}$$

such that

$$\left\| \mathscr{B}^{diff}\left(\mathbf{h}^l_{[m]}, \mathbf{X}^k_{(p)}\right) - \mathbf{b}^* \right\| < \left\| \mathscr{B}^{diff}\left(\mathbf{h}^{l-1}, \mathbf{X}^k_{(p)}\right) - \mathbf{b}^* \right\|\,. \tag{4.35}$$

Thanks to the relaxed scheme, the *EB* model can now be inverted successfully for each time step of the ramp excitation from Fig. 4.6. This is shown on Fig. 4.10, where the direct form and the inverse form are superimposed. This solution cannot be obtained with a standard non-relaxed NR_{ana} technique, as discussed before.

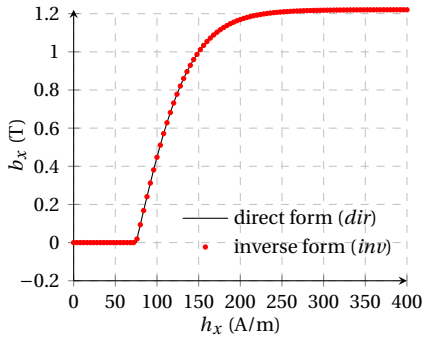

Figure 4.10: *Comparison between $b_x - h_x$ curves of a direct form ($\mathbf{h} \rightarrow \mathbf{b}$) and an inverse form ($\mathbf{b} \rightarrow \mathbf{h}$) of an EB hysteresis model on the example of Fig. 4.6. The inversion is performed with a relaxed NRana technique.*

The same agreement can be observed with rotational excitation, such as those considered in Fig. 4.2 and Fig. 4.3. The corresponding h-loci, imposed as input for the direct

form and produced as output with the inverse form, are drawn in Fig. 4.11 (left) and Fig. 4.11 (right), for each of these test cases. Once again, such results are not feasible under the influence of angular points without relying on the relaxation procedure for the inversion with the NR_{ana} technique.

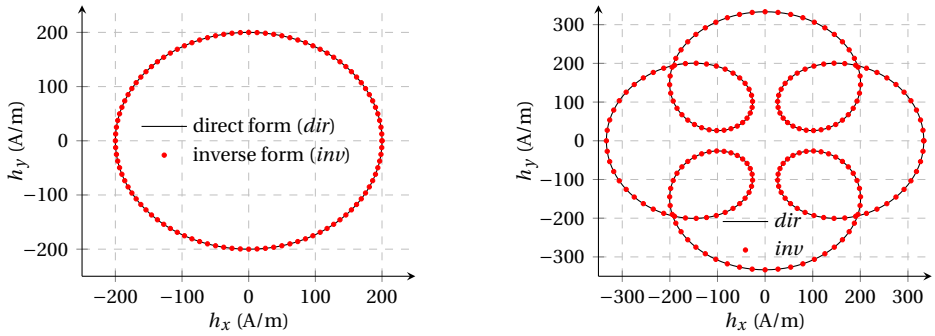

Figure 4.11: *Comparison between the* $\mathbf{h}$ *loci of a direct form (*$\mathbf{h} \rightarrow \mathbf{b}$*) and an inverse form (*$\mathbf{b} \rightarrow \mathbf{h}$*) of an EB hysteresis model on the examples of Fig. 4.2 for (left) and Fig. 4.3 for (right). The inversion is performed with a relaxed NRana technique.*

3. Approximated Newton-Raphson Methods

It is also interesting to investigate alternative approximated *NR* methods to perform the inversion of the *EB* hysteresis model (4.3), by replacing the exact Jacobian matrix, $\frac{\partial \mathscr{B}^{dir}}{\partial \mathbf{h}}$, by an approximated matrix, denoted here under $\underline{\boldsymbol{B}_{\partial}}$. In this context, the update scheme (4.3) becomes thus

$$\mathbf{h}^{l} = \mathbf{h}^{l-1} - \left[\underline{\boldsymbol{B}_{\partial}}^{l-1}\right]^{-1} \cdot \left[\mathscr{B}^{dir}(\mathbf{h}^{l-1}, \mathbf{X}^{k}_{(p)}) - \mathbf{b}^{*}\right]. \tag{4.36}$$

At least two reasons can motivate to do so.

First, it has been assumed so far that the differential permeability tensors can be calculated analytically. However, strictly speaking, this is only possible if the anhysteretic curve is adequately described by a smooth analytical function, for which the inverse exists also mathematically. In practice, this is not necessarily the case since the selected function can be non-invertible, such as with the Langevin function, or approximated by interpolation between database points, for instance. In this context, the differential permeability tensor can still be expressed in a kind of NR_{ana} approach, by exploiting the analytical formula given in Chapter 4-Section 2.2, but knowing that each elementary relation, such as $\mathscr{J}_{\text{an}}(|h_{\text{rev}}|)$, $\chi_{\text{an}}(|h_{\text{rev}}|)$, $\chi_{\text{an}\partial}(|h_{\text{rev}}|)$, or $\mathscr{J}^{-1}_{\text{an}}(|J|)$, $\chi^{-1}_{\text{an}}(|J|)$ $\chi^{-1}_{\text{an}\partial}(|J|)$, that appear inside have actually no analytical expressions behind them, and should rather be seen as numerical mapping between two sets of quantities, which is already a semi-analytical - semi-numerical (or semi-experimental) approximation of the Jacobian matrix. Moreover, if one decides to make the *EB* model more complicated by describing the pinning field as a function of the magnetic field, or by introducing other dependencies for the anisotropic case for example, there is no guarantee

that an exact analytical expression for the differential permeabilities will still exist in the end. In anticipation of this, it is thus natural to study approximated approaches for the determination of the Jacobian matrix.

Secondly, in some circumstances, it is sometimes interesting to use an approximated Jacobian matrix instead of the exact one in a *NR* scheme in order to improve the convergence. Actually, this is somehow the idea behind the relaxation procedure, recalled in Chapter 4-Section 2.4, since the relaxation factor can be seen as a factor which weights the Jacobian matrix in the classical *NR* update. Indeed, by introducing (4.34) in (4.3), one ends up with

$$\mathbf{h}^{l}_{[m]} = \mathbf{h}^{l-1} - \left[\frac{1}{\gamma^{l}_{[m]}} \frac{\partial \mathscr{B}^{dir}}{\partial \mathbf{h}} \Big|^{l-1} \right]^{-1} \cdot \left[\mathscr{B}^{dir}(\mathbf{h}^{l-1}, \mathbf{X}^{k}_{(p)}) - \mathbf{b}^{*} \right], \tag{4.37}$$

which, when compared with (4.36), gives the corresponding approximated form behind $\underline{\boldsymbol{B}_{\partial}}^{l-1}$, associated to the relaxation process of the NR_{ana} technique.

The following subsections investigate two other families of techniques which propose other strategies to approximate the Jacobian matrix $\underline{\boldsymbol{B}_{\partial}}$.

3.1. Numerical Newton-Raphson Method

One possibility consists for example in evaluating the differential permeability tensor purely numerically by finite differences. The inversion technique according to that approach is then simply denoted as the Newton-Raphson with Jacobian matrix evaluated numerically (NR_{num}), in the following.

In the general three-dimensional (*3D*) case, the Jacobian matrix $\underline{\boldsymbol{B}_{\partial}}^{l}$ is a 3×3 matrix,

$$\underline{\boldsymbol{B}_{\partial}}^{l} = \begin{pmatrix} (B_{\partial}{}^{l})_{xx} & (B_{\partial}{}^{l})_{xy} & (B_{\partial}{}^{l})_{xz} \\ (B_{\partial}{}^{l})_{yx} & (B_{\partial}{}^{l})_{yy} & (B_{\partial}{}^{l})_{yz} \\ (B_{\partial}{}^{l})_{zx} & (B_{\partial}{}^{l})_{zy} & (B_{\partial}{}^{l})_{zz} \end{pmatrix}, \tag{4.38}$$

where each component $(B_{\partial}{}^{l})_{\alpha\beta}$ corresponds thus formally to the differential permeability tensor component $\frac{\partial \mathscr{B}^{dir}_{\alpha}}{\partial h_{\beta}} \Big|^{l}$, with α,β=x,y,z. Numerical differentiations techniques can then be exploited for each component to approximate the derivatives based on forward differences:

$$(B_{\partial}{}^{l})_{\alpha\beta} = \frac{\left(\mathscr{B}^{dir}(\mathbf{h}^{l} + \delta_{\beta} \cdot \mathbf{e}_{\beta}, \mathbf{X}^{k}_{(p)}) - \mathscr{B}^{dir}(\mathbf{h}^{l}, \mathbf{X}^{k}_{(p)}) \right) . \mathbf{e}_{\alpha}}{\delta_{\beta}}, \tag{4.39}$$

or central differences:

$$(B_{\partial}{}^{l})_{\alpha\beta} = \frac{\left(\mathscr{B}^{dir}(\mathbf{h}^{l} + \delta_{\beta} \cdot \mathbf{e}_{\beta}, \mathbf{X}^{k}_{(p)}) - \mathscr{B}^{dir}(\mathbf{h}^{l} - \delta_{\beta} \cdot \mathbf{e}_{\beta}, \mathbf{X}^{k}_{(p)}) \right) . \mathbf{e}_{\alpha}}{2\delta_{\beta}}, \tag{4.40}$$

where $\mathbf{e}_{\alpha}$ refers to a unit vector in the direction α, and δ_{α} represents a small perturbation of the magnetic field along that direction, measured in A/m.

The selection of the step sizes $\delta_x, \delta_y, \delta_z$ is rather delicate. The derivative is better approximated when the perturbation step is small, but too small values may lead to subtractive cancellation errors when the differentiated quantities are numerically very close in (4.39) or (4.40). More to the point, the idea is not necessarily to get the accurate derivative since it has been shown in Chapter 4-Section 2.3 that the exact differential permeability tensor does not allow the *NR* method to converge in all situations. Therefore, one can decide voluntarily to make a rough approximation of the derivative by choosing a larger step δ_α, increasing intentionally the truncation error. In particular, with the presence of angular point around the solution, as in the example from Fig. 4.7, choosing a rather large perturbation δ_α in order to probe points situated around the discontinuity for the finite differences calculation may allow to smooth out the brutal local change of the derivatives. An approximated Jacobian matrix can thus be constructed with a better knowledge of the average slope change in the neighborhood of the angular point, being possibly more conductive to convergence.

Nevertheless, the determination of optimal values for the finite difference steps, δ_x, δ_y, δ_z, is a difficult problem. In a pragmatic approach, theses values can be fixed to constant sizes and be determied a priori by trial and error, since it depends on the material and on the problem characteristics. For instances, different constant step values δ_α, ranging between 10^1 A/m and 10^{-3} A/m, have been experienced in several applications during this thesis, and different efficiencies have been observed in function of the simulation context.

In practice, the same perturbation step δ has been finally adopted for each direction, such that $\delta_x = \delta_y = \delta_z = \delta$. Moreover, its has been observed in the course of numerous tests that satisfying results can be obtained by considering perturbation steps δ^l, that change dynamically at each *NR* iteration l, according to

$$\delta^l = c\,|\Delta\mathbf{h}^l| = c\,|\mathbf{h}^l - \mathbf{h}^{l-1}|\,, \tag{4.41}$$

where $\Delta\mathbf{h}^l$ is thus the *NR* increment step calculated at iteration l, and c is a constant weighting factor, which can be modified if needed, but with a typical value set at $c = 0.1$ in the simulations here. This gives thus an automatic way that adjusts the perturbation step at each *NR* iteration in function of the increment step. It remains yet a flexibility in chosing the value δ^0 used in the first *NR* iteration.

The construction of the numerical approximation for the Jacobian matrix requires 4 evaluations of the direct *EB* model with the forward-difference formula (4.39), including the central one that is actually already evaluated by default per each iteration, and 6 evaluations with the central-difference case (4.39). Note that the number of direct model evaluations needed to build the Jacobian matrix remains the same whether the matrix is symmetric or not.

In purely two-dimensional (*2D*) excitation case, the components with respect to z can be discarded

$$({B_\partial}^l)_{xz} = ({B_\partial}^l)_{yz} = ({B_\partial}^l)_{zx} = ({B_\partial}^l)_{zy} = 0\,, \qquad ({B_\partial}^l)_{zz} = 1\,, \tag{4.42}$$

and the Jacobian matrix reduces eventually to a 2×2 matrix if the vector fields $\mathbf{h}, \mathbf{b}, \mathbf{X}^k$ are expressed with two components only. At the end, the Jacobian matrix determination requires then now 3 or 4 evaluations of the direct *EB* model with the forward- or the central- difference formulae, respectively.

Forward differences are thus less costly compared to central differences. However, in practice, better results have been obtained with the central difference approach such that this is always the corresponding formula (4.39) that is used behind the NR_{num} technique in all cases presented in this thesis. In light of this, one can already anticipate that the preparation of the Jacobian matrix at each NR_{num} iteration will be all the more costly in terms of computation time as the direct *EB* model is time-consuming.

3.2. Quasi Newton-Raphson Methods

Finally, quasi Newton-Raphson methods are other alternative of the *NR* method, that are able to find roots of multivariate functions, without relying on an exact Jacobian determination. Contrary to the NR_{num} technique, the Jacobian matrix is here updated based on the knowledge from the previous iterations, without needing additional evaluation of the functions. This is an important advantage for the inversion of the *EB* hysteresis model since the direct model can some sometimes be laborious to compute, in particular with the *var* approach.

Basically, quasi Newton-Raphson methods can be seen as generalizations of the secant method, but for multidimensional problems. The secant method for finding the root of a single-variable function $r(x)$ relies on a process similar to the *NR* method (4.1), but where the derivative $r'(x^{l-1})$ is substituted by the slope of the line that joins the two last visited points, x^{l-1},x^{l-2}, such that the recurrence relation becomes

$$x^l = x^{l-1} - \frac{x^{l-1} - x^{l-2}}{r(x^{l-1}) - r(x^{l-2})} r(x^{l-1}) . \tag{4.43}$$

The graphical illustration of this update scheme is shown in Fig. 4.12 on the same examples as in Fig. 4.1. Actually, the secant method can sometimes converge in situations where the classical *NR* method fails, as illustrated in Fig. 4.13. The previous non-converged examples in presence of angular point and inflection point of the non-relaxed NR_{ana} technique from Fig. 4.5(a),(e), are here solved without problem based on the update scheme from (4.43). Since such delicate situations with angular and inflection points are typically encountered in the direct *EB* model functions, this further motivates the need to investigate generalization of the secant method for the inversion of the hysteresis model.

Actually, there exist a number of different techniques to generalize the secant method to multivariable functions. Inspired by the secant equation (4.43), all quasi-Newton methods satisfy the condition

$$\underline{\boldsymbol{B}_{\partial}}^{l+1} \Delta \mathbf{h}^l = \Delta \mathbf{b}^l , \tag{4.44}$$

where the following vectors are defined to simplify the notation,

$$\Delta \mathbf{h}^l = \mathbf{h}^l - \mathbf{h}^{l-1} , \qquad \Delta \mathbf{b}^l = \mathscr{B}^{dir}(\mathbf{h}^l, \mathbf{X}^k_{(p)}) - \mathscr{B}^{dir}(\mathbf{h}^{l-1}, \mathbf{X}^k_{(p)}) , \tag{4.45, 4.46}$$

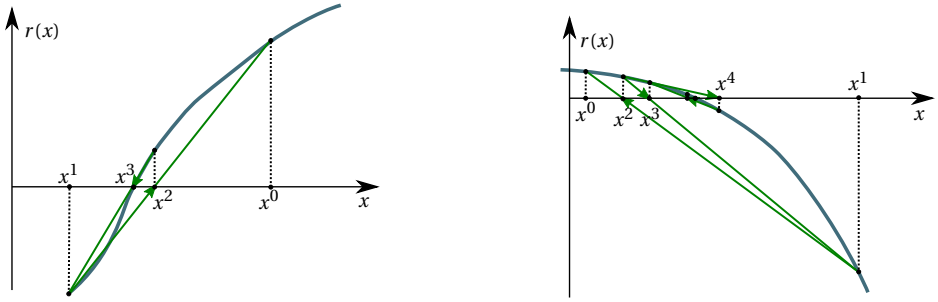

Figure 4.12: *Graphical illustrations of the secant method applied on the same examples as Fig. 4.1.*

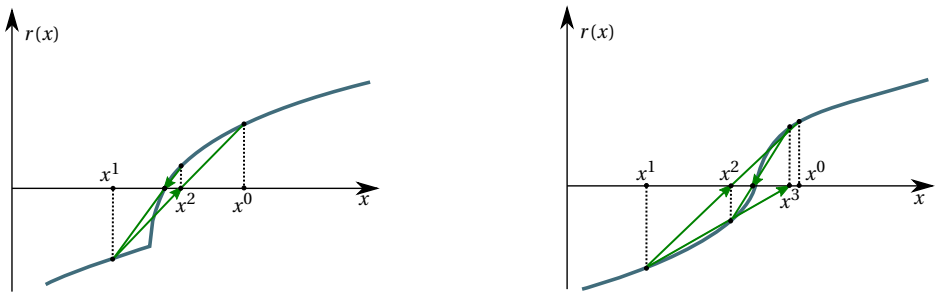

Figure 4.13: *Convergence of the secant method where classical NR method failed, illustrated around an angular point (left), or an inflection point (right), taken from the examples in Fig. 4.5(a),(e), respectively.*

where the adaptation for the *EB* hysteresis model application is already considered. Nevertheless, the relation (4.44) is underdetermined when there is more than one variable, such that it does not define a unique matrix $\underline{\boldsymbol{B}_\partial}^{l+1}$, but a class of matrices. Some freedom remains to make further assumptions about the matrix properties in order to completely determined $\underline{\boldsymbol{B}_\partial}^{l+1}$. Different formulae have been developed to update the Jacobian matrix, or its inverse, different in the rank of the update matrix and in the properties that are maintained through this update [172]. Some of them are recalled hereafter.

The simplest quasi-Newton approach is the Broyden formula [37], where the update minimizes the change to the Jacobian, between $\underline{\boldsymbol{B}_\partial}^{l+1}$ and $\underline{\boldsymbol{B}_\partial}^{l}$.

The Davidon-Fletcher-Powell Formula (*DFP*) [50, 78] is another quasi-Newton method where the update formula for the Jacobian is determined in such a way to preserve symmetry and positive definiteness, whose solution is

$$\underline{\boldsymbol{B}_\partial}^{l+1} = \left(\underline{\boldsymbol{I}} - \frac{\Delta\mathbf{b}^l \Delta\mathbf{h}^{l\,T}}{\Delta\mathbf{b}^{l\,T} \Delta\mathbf{h}^l}\right) \underline{\boldsymbol{B}_\partial}^{l} \left(\underline{\boldsymbol{I}} - \frac{\Delta\mathbf{h}^l \Delta\mathbf{b}^{l\,T}}{\Delta\mathbf{b}^{l\,T} \Delta\mathbf{h}^l}\right) + \frac{\Delta\mathbf{b}^l \Delta\mathbf{b}^{l\,T}}{\Delta\mathbf{b}^{l\,T} \Delta\mathbf{h}^l}, \tag{4.47}$$

The inverse of $\underline{\boldsymbol{B}_\partial}^{k}$, denoted by

$$\underline{\boldsymbol{H}_\partial}^{l} = \left[\underline{\boldsymbol{B}_\partial}^{l}\right]^{-1}, \tag{4.48}$$

is useful in the implementation of the algorithm, since the next search point (4.36) can then be computed as a simple matrix-vector multiplication

$$\mathbf{h}^l = \mathbf{h}^{l-1} - \underline{\boldsymbol{H}_\partial}^{l-1} \cdot \left[\mathscr{B}^{dir}(\mathbf{h}^{l-1}, \mathbf{X}^k_{(p)}) - \mathbf{b}^* \right] . \tag{4.49}$$

By using the Sherman-Morrison-Woodbury relation, that is

$$\left(\underline{\boldsymbol{A}} + \mathbf{x}\mathbf{y}^T\right)^{-1} = \underline{\boldsymbol{A}}^{-1} - \frac{\underline{\boldsymbol{A}}^{-1}\mathbf{x}\mathbf{y}^T\underline{\boldsymbol{A}}^{-1}}{1 + \mathbf{y}^T\underline{\boldsymbol{A}}^{-1}\mathbf{x}} , \tag{4.50}$$

the *DFP* update (4.47) can be explicitely expressed in terms of the inverse of the Jacobian approximation $\underline{\boldsymbol{H}_\partial}^l$, to get

$$\underline{\boldsymbol{H}_\partial}^{l+1} = \underline{\boldsymbol{H}_\partial}^l - \frac{\underline{\boldsymbol{H}_\partial}^l \Delta\mathbf{b}^l \Delta\mathbf{b}^{l\,T} \underline{\boldsymbol{H}_\partial}^l}{\Delta\mathbf{b}^{l\,T} \underline{\boldsymbol{H}_\partial}^l \Delta\mathbf{b}^l} + \frac{\Delta\mathbf{h}^l \Delta\mathbf{h}^{l\,T}}{\Delta\mathbf{h}^{l\,T} \Delta\mathbf{b}^l} , \tag{4.51}$$

saving thus the effort of having to inverse the Jacobian matrix at each iteration.

The most popular of the quasi-Newton method is the Broyden–Fletcher–Goldfarb–Shanno (*BFGS*) method [38, 77, 88, 191], which is generally considered as the most effective of all quasi-Newton updating formulae [172]. The *BFGS* update can be derived as being the dual of the *DFP* approach (4.47). Instead of considering the Jacobian matrix $\underline{\boldsymbol{B}_\partial}^l$, similar conditions can be imposed on their inverse $\underline{\boldsymbol{H}_\partial}^l$, to preserve the symmetry and positive definiteness of the matrices at each iteration, giving thus the dual formula:

$$\underline{\boldsymbol{H}_\partial}^{l+1} = \left(\underline{\boldsymbol{I}} - \frac{\Delta\mathbf{h}^l \Delta\mathbf{b}^{l\,T}}{\Delta\mathbf{h}^{l\,T} \Delta\mathbf{b}^l} \right) \underline{\boldsymbol{H}_\partial}^l \left(\underline{\boldsymbol{I}} - \frac{\Delta\mathbf{b}^l \Delta\mathbf{h}^{l\,T}}{\Delta\mathbf{h}^{l\,T} \Delta\mathbf{b}^l} \right) + \frac{\Delta\mathbf{h}^l \Delta\mathbf{h}^{l\,T}}{\Delta\mathbf{h}^{l\,T} \Delta\mathbf{b}^l} , \tag{4.52}$$

or equivalently, written efficiently without matrix multiplications:

$$\underline{\boldsymbol{H}_\partial}^{l+1} = \underline{\boldsymbol{H}_\partial}^l + \frac{\left(\Delta\mathbf{h}^{l\,T} \Delta\mathbf{b}^l + \Delta\mathbf{b}^{l\,T} \underline{\boldsymbol{H}_\partial}^l \Delta\mathbf{b}^l\right)\left(\Delta\mathbf{h}^l \Delta\mathbf{h}^{l\,T}\right)}{\left(\Delta\mathbf{h}^{l\,T} \Delta\mathbf{b}^l\right)^2} - \frac{\underline{\boldsymbol{H}_\partial}^l \Delta\mathbf{b}^l \Delta\mathbf{h}^{l\,T} + \Delta\mathbf{h}^l \Delta\mathbf{b}^{l\,T} \underline{\boldsymbol{H}_\partial}^l}{\Delta\mathbf{h}^{l\,T} \Delta\mathbf{b}^l} . \tag{4.53}$$

This is this last expansion (4.53), called the Good Broyden–Fletcher–Goldfarb–Shanno algorithm (*GoodBFGS*), that has been chosen to approximate the inverse of the Jacobian matrix used in the iterative scheme (4.49) to find the next estimate of the magnetic field for the inversion of the *EB* hysteresis model. For the first iterate, the inverse Jacobian matrix is calculated analytically $\underline{\boldsymbol{H}_\partial}^0 = \left[\frac{\partial \mathscr{B}^{dir}}{\partial \mathbf{h}} \Big|^0 \right]^{-1}$.

The *GoodBFGS* technique has the reputation to be rather robust and has proven to have good performance even for non-smooth systems in [141, 142]. A superlinear rate of convergence has been observed on practical problems, which has to be compared with the one of the *NR* method, that is quadratic. In general, a quasi-Newton algorithm usually needs more iterations than a classical *NR* method, but its costs per iteration is usually lower, since the Jacobian matrices update are very light, even more if the update is directly applied on the inverse Jacobian.

4. Numerical Comparison

In this section, the proposed inversion techniques, namely the NR_{ana}, the NR_{num} and the *GoodBFGS* algorithms, are extensively tested, with or without the relaxation process, and compared on their ability to reverse each of the direct *EB* hysteresis model approaches, i.e. the *vpm*, the *var* and the *diff* methods. For that purpose, the battery of test cases used in the previous Chapter 3-Section 5 for the comparison of the direct models is here used again. Furthermore, the analysis is also realized with the same 3-cell hysteresis model parameters as in Chapter 3-Section 5.

Therefore, a set of 40 excitation sources of similar type as in the previous chapter, i.e. $\mathbf{h}^{dir}(t) = h_{\max}\big[\cos(2\pi f t), \cos(2\pi f t - \Phi), 0\big]$, is made-up with various maximum field value components, $h_{\max} = 50, 100, 150, 200\,\mathrm{A/m}$, and various phase shifting angles Φ, from 0° to 90° by step of 10°, such as to cover a large panel of possible excitation source types, from unidirectional to purely circular cases, as shown by the illustrations of Fig. 3.13 and Fig. 3.14. Preliminary, the direct forms of the *EB* model are fed by these excitation sources $\mathbf{h}^{dir}(t)$ to produce the flux density responses $\mathbf{b}(t)$. Then, in a second stage, the generated fields $\mathbf{b}(t)$ are used as input sources for the corresponding inverse forms of the *EB* model in order to retrieve, at the end, magnetic fields $\mathbf{h}^{inv}(t)$, that should in theory be the same as those imposed at the beginning. Each periodic signal is here discretized by 500 evenly spaced time steps in each simulation. In general, the smaller the time step, the better the convergence of the inversion methods since the approximation from the previous time step is then closer to the current solution. But this influence is not discussed here and a fixed time increment is considered. At each time step n, the inversion technique is assumed to have converged at an iteration l when the stopping criterion $\left|\mathscr{B}^{dir}(\mathbf{h}_n^l, \mathbf{X}_{(p)}^k) - \mathbf{b}_n^*\right| < 10^{-7}\,\mathrm{T}$ is verified.

At the end of a simulation, the accuracy of the inversion technique can be measured by comparing the input magnetic field $\mathbf{h}_n^{dir}$ and the corresponding output $\mathbf{h}_n^{inv}$ that results from the serial application of the direct and the inverse forms of the *EB* model. To this end, a root mean square deviation norm (*RMSDN*), analogous to (3.32), is calculated from the mean-square differences between these fields over all the time step (*ts*), $n = 1, \ldots, N_t$, used in the simulation, thus based on the composition

$$(\mathrm{RMSD})_i = \sqrt{\frac{1}{N_t}\sum_{n=1}^{N_t}\left(h_{i,n}^{inv} - h_{i,n}^{dir}\right)^2} \quad , \forall\, i = x, y, z, \tag{4.54}$$

from which the *RMSDN* is derived by taking the L^2-norm. Naturally, this factor is measured in ampere per meter (A/m) this time.

Here, the three model approaches are tested with each of the three inversion techniques, each of which being combined with a relaxation process, or not, making a total of 18 different implementations that can be submitted to the set of 40 excitation sources. The various implementations performances are summarized in Table 4.1 and Table 4.2, which group the inversions without, or with, the relaxation mechanism, respectively. Each line in these tables corresponds thus to an association of an *EB* model approach with an inversion technique, as specified on the first two columns.

The third column indicates, for a given implementation choice, the number of simulations among the 40 tested ones for which a convergence issue arises during the inversion, when the maximum number of iterations, set at $l_{\max} = 200$, is reached for some time step. The values in the following columns give additional characteristics of the inversion technique, such as the central processing unit (*CPU*) time needed per simulation with the inverse form, the *CPU* time ratio of the inverse form with respect to the direct form, the mean and maximal number of iterations per time step for the inversion, and the *RMSDN* factor calculated with (4.54). All the indicated values are determined exclusively from the average over the test cases that have converged for all time steps. The simulations which have not worked properly among the 40 tested ones for a given implementation choice are discarded, such that a reduced number of valid values are then taken into account to calculate the average quantities. These situations are identified on Table 4.1 and Table 4.2, by increasing the shading of the rows in function of the number of simulations that have not been successfully inverted for the given implementation.

Table 4.1: *Simulations without relaxation in the inversion techniques applied on each model approach.*

approach	inversion method (without relaxation)	non-converged simulations	*CPU* time per simulation (s)	*CPU* time ratio per simulation (*dir* as ref.)	iter / time step mean (max)	RMSDN (A/m) (*dir* as ref.)
vpm	*NRnum*	2/40 (◆)	1.65 (◆)	24.3	3.33 (5)	$2.8 \cdot 10^{-4}$
	NRana	30/40	1.1	16.9	3.60 (5)	$1.5 \cdot 10^{-5}$
	GoodBFGS	17/40	0.87	13.4	6.58 (118)	$4.8 \cdot 10^{-4}$
var	*NRnum*	0/40	152.51 (▲)	33.1	3.23 (6)	$2.8 \cdot 10^{-4}$
	NRana	30/40	35.01	7.0	3.08 (5)	$1.4 \cdot 10^{-5}$
	GoodBFGS	0/40	45.98 (✓)	8.2	5.32 (16)	$3.3 \cdot 10^{-4}$
diff	*NRnum*	0/40	27.27 (▲)	22.3	3.23 (6)	$2.7 \cdot 10^{-4}$
	NRana	30/40	8.29	8.3	3.71 (5)	$1.3 \cdot 10^{-5}$
	GoodBFGS	0/40	10.54 (✓)	8.8	7.45 (19)	$3.4 \cdot 10^{-4}$

Table 4.2: *Simulations with relaxation in the inversion techniques applied on each model approach.*

approach	inversion method (with relaxation)	non-converged simulations	*CPU* time per simulation(s)	*CPU* time ratio per simulation (*dir* as ref.)	iter / time step mean (max)	RMSDN (A/m) (*dir* as ref.)
vpm	*NRnum (Relax)*	2/40 (◆)	1.77 (◆)	28.6	3.33 (6)	$2.8 \cdot 10^{-4}$
	NRana (Relax)	5/40	1.62	24.3	3.56 (61)	$3.3 \cdot 10^{-4}$
	GoodBFGS (Relax)	23/40	1.32	20.8	5.26 (32)	$5.5 \cdot 10^{-4}$
var	*NRnum (Relax)*	0/40	165.8 (▲)	35.8	3.23 (6)	$2.8 \cdot 10^{-4}$
	NRana (Relax)	0/40	79.31 (▼)	12.5	3.21 (6)	$2.7 \cdot 10^{-4}$
	GoodBFGS (Relax)	0/40	89.25	16.1	4.76 (10)	$3.4 \cdot 10^{-4}$
diff	*NRnum (Relax)*	0/40	28.49 (▲)	25.8	3.23 (6)	$2.7 \cdot 10^{-4}$
	NRana (Relax)	0/40	18.95 (▼)	15.7	3.52 (5)	$2.4 \cdot 10^{-4}$
	GoodBFGS (Relax)	0/40	22.23	18.6	5.69 (13)	$3.1 \cdot 10^{-4}$

By comparing the shaded rows between Table 4.1 and Table 4.2, it is clear that the NR_{ana} inversion technique must absolutely be combined with a relaxation process. Indeed, a large number of the NR_{ana} simulations (75 %) do not converge without this mechanism, whatever the underlying *EB* model approach chosen, as seen in Table 4.1,

whereas the use of the relaxation allows all the NR_{ana} simulations with the *var* and the *diff* approaches to converge, according to Table 4.2. Furthermore, among the relaxed inversion methods tested for the *var* and the *diff* approaches in Table 4.2, the NR_{ana} method requires the least *CPU* time (indicated by ▼), compared to NR_{num} and *GoodBFGS* techniques.

On the other hand, with the *vpm* approach, despite the fact that the relaxation of the NR_{ana} does improve the algorithm by reducing the number of non-converged simulations from 30 to 5, there are still some test cases which remain problematic (12.5 %). Generally speaking, the *vpm* approach is numerically more difficult to invert than the two other approaches. Indeed, for the *vpm* approach, there are none of the three inversion techniques, whether relaxed or not, that are able to converge for all the 40 test cases, as there is never zero non-converged simulations with each of the *vpm*-based implementations in Table 4.1 and Table 4.2. In the best situation, which corresponds to the inversion with NR_{num} for the *vpm* approach (marked by ◆), there are still 2 test cases (5 %) for which the inversion fails for some time step, with or without relaxation.

While the relaxation is essential for the NR_{ana} method, it is not recommended for the NR_{num} and the *GoodBFGS* inversion techniques in the light of the presented examples. Indeed, when applied to *var* and *diff* approaches, these inversion techniques are already fully capable of converging without relying on a relaxation process for the 40 test cases, with 0% failure, as seen in Table 4.1. Introducing relaxation is therefore unnecessary in this situation since it only slows down the convergence, without making any improvements, as checked in Table 4.2. In the same way, when applied to the *vpm* approach, the relaxation of the NR_{num} and the *GoodBFGS* techniques is useless since it does not allow here to reduce the number of non-converged simulations, and the situation is even worse for the *GoodBFGS* because this number increases in the relaxed configuration.

The *GoodBFGS* technique is clearly not adapted for the *vpm* approach since this association leads to an important number of non-converged simulations, either with or without the relaxation. Actually, this observation seems consistent with the fact that the *GoodBFGS* update formula (4.53) aims to conserve the symmetry and the positive-definiteness of the Jacobian matrix approximations, whereas these properties are not always guaranteed by nature with the *vpm* approach, as demonstrated mathematically in Chapter 4-Section 2.2. Conversely, the differential permeability tensors associated to the *var* and the *diff* approaches are symmetric and positive-definite in all circumstances, such that their inversion by the *GoodBFGS* method is therefore more appropriate to this context. By comparing the *CPU* time in Table 4.1, one can see that *GoodBFGS* is in fact the most effective non-relaxed inversion technique for each of the *var* and *diff* approaches, as it does not raise any convergence problems for the 40 excitation sources (indicated by ✓). Hence, the inverse form of the *var* and *diff* approaches are at best about 8.2 and 8.8 times slower than their dual direct form, respectively, thanks to the non-relaxed *GoodBFGS* inversion technique. The number of iterations required by the *GoodBFGS* algorithm is higher than with NR_{ana} or NR_{num} methods, but, since the inverse Jacobian matrix is straightforwardly updated through (4.53), the *CPU* time cost per *GoodBFGS* iteration is lower. Therefore, the average *CPU*

time per simulation with *GoodBFGS* is at the end, of the same order of magnitude as with NR_{ana} (discarding unconverged NR_{ana} simulations in the non-relaxed configuration), and remains significantly lower than with NR_{num}.

By contrast, the NR_{num} inversion technique is the most costly in terms of *CPU* time per iteration, because it requires additional evaluations of the direct *EB* model in order to construct the Jacobian matrix by finite differences. Therefore, the numerical calculations of the Jacobian approximations take all the more time as the resolution of the selected model approach is time-consuming. As discussed in Chapter 3, the *vpm* is naturally the fastest approach, with almost instantaneous resolution, whereas the *diff* and *var* approaches involve heavier numerical optimization algorithms in their update functions, and even more so for the *var* approach, which is an order of magnitude slower than *diff*. Consequently, the use of the NR_{num} inversion technique for the *var* and *diff* approaches takes a significant amount of time, as obvious in Table 4.1 and Table 4.2, where the NR_{num} method is by far the slowest inversion technique proposed for each of them (identified by ▲). Even in the fastest of these NR_{num}-based configurations, i.e. without relaxation and applied on the *diff* approach, the inverse form still takes about 22.3 times as long as the direct form. It goes up to be 35.8 times as long as in the slowest case, i.e. under relaxation and applied on the *var* approach. However, for the reasons given above, the NR_{num} inversion technique is the most suitable for the *vpm* approach since on the one hand, it is not too time-consuming to make several calls to the *vpm* update function per iteration to determine the finite differences used in the Jacobian approximations and, on the other hand, this is the most robust inversion method that provides the least number of non-converged test cases for the *vpm* approach.

Finally, it can be observed by looking at the last column in Table 4.1 and Table 4.2 that all implementation varieties end up with similar level of accuracy of equivalent order of magnitude for the *RMSDN* factors, of about 10^{-4} A/m. This value obviously depends on the tolerance chosen for the stopping criterion of the inversion method, which has been set at 10^{-7} T as maximum deviation on the flux density field values.

Lastly, the detailed characteristics of each of the 40 test cases, simulated with the 18 implementation varieties, is exposed from Fig. 4.14 to Fig. 4.19. They illustrate the content of the averaged values displayed on Table 4.1 and Table 4.2, with the specification of each simulation result. Each column of subplots in the figures is dedicated to one of the 18 implementations, which is associated to a row in the tables, and thus to a choice of an *EB* model approach, with an inversion technique, with or without the relaxation mechanism. For each implementation configuration, these figures provide some insight for each test case by plotting the evolution of the mean iteration per time step, the *CPU* time and the *RMSDN* values, in function of the phase shifting angles and for different maximum field values of the imposed sources. Each point in these graphics is thus associated to a simulation of one of the 40 test cases.

It appears that problems linked to non-convergence tend to be more common for excitation sources with high fields that reach saturation ($h_{\max} \to 200\,\mathrm{A/m}$) and with small non-zero phase shifting angles ($0° < \Phi < 50°$), which correspond to elongated ellip-

soidal shaped signals, where magnetization changes strongly in magnitude, while rotating.

In summary, several inversion techniques (*NR*$_{ana}$, *NR*$_{num}$, *GoodBFGS*) have been tested on the different hysteresis model approaches (*vpm*, *var*, *diff*). It has been shown that the approximation behind the construction of the *vpm* approach no longer guarantees that its differential permeability tensor remains a symmetric positive-definite tensor in all circumstances, whereas this property is always verified with the *var* and the *diff* approaches. This asymmetry may explain the significant numerical complications encountered for the inversion of the *vpm* approach compared to the two others. Moreover, the *NR*$_{ana}$ inversion technique must necessarily be combined with a relaxation process to ensure convergence, whereas this is not necessary for the two other investigated techniques. The *GoodBFGS* technique generally requires the most iterations before converging, but each iteration needs less *CPU* time because the Jacobian matrix is approximated on the basis of the previous iteration result. Thus, the *GoodBFGS* method is the fastest inversion technique, unlike *NR*$_{num}$, which is the slowest. However, *NR*$_{num}$ is interesting for the inversion of the fast *vpm* approach. Nevertheless, the *NR*$_{ana}$ technique combined with a controlled relaxation generally remains the most robust technique to ensure convergence compared to *GoodBFGS*, even if it has not been directly illustrated by the set of examples presented in this section. A relaxed *NR*$_{ana}$ is thus generally preferred in practice.

Based on this experience, the different *EB* hysteresis model approaches, namely the *vpm*, *var* and *diff*, can now be successfully inverted so as to be driven by the magnetic induction field **b**, instead of the magnetic field **h**. In the following, the inverse *EB* hysteresis model is expressed under a single generic form that can be associated with any of the three implementation approaches:

$$\mathbf{h} = \mathscr{H}^{inv}(\mathbf{b}, \mathbf{X}^k_{(p)}) = \arg\min_{\mathbf{h}} \left| \mathscr{B}^{dir}(\mathbf{h}, \mathbf{X}^k_{(p)}) - \mathbf{b} \right| . \tag{4.55}$$

These inverse forms can further be integrated into a *FE* computation code and tested in magnetic vector potential formulations where the induction field **b** constitutes then the variable of interest. This is the purpose of the following Chapter 5.

Inversion (without relaxation) of the *vpm* approach.

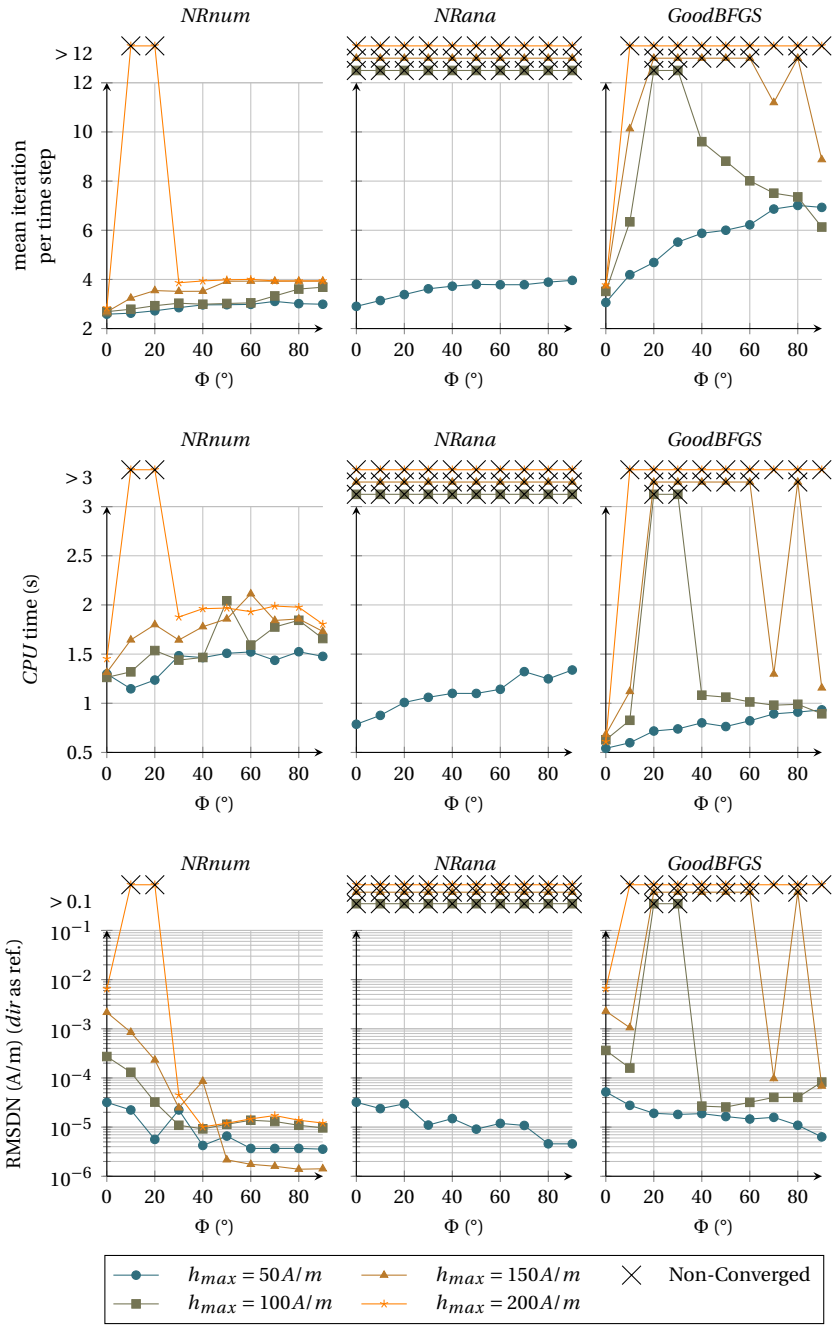

Figure 4.14: *Details on performances of different inversion techniques (without relaxation) for the vpm approach over* 40 *simulation test cases.*

Inversion (with relaxation) of the *vpm* approach.

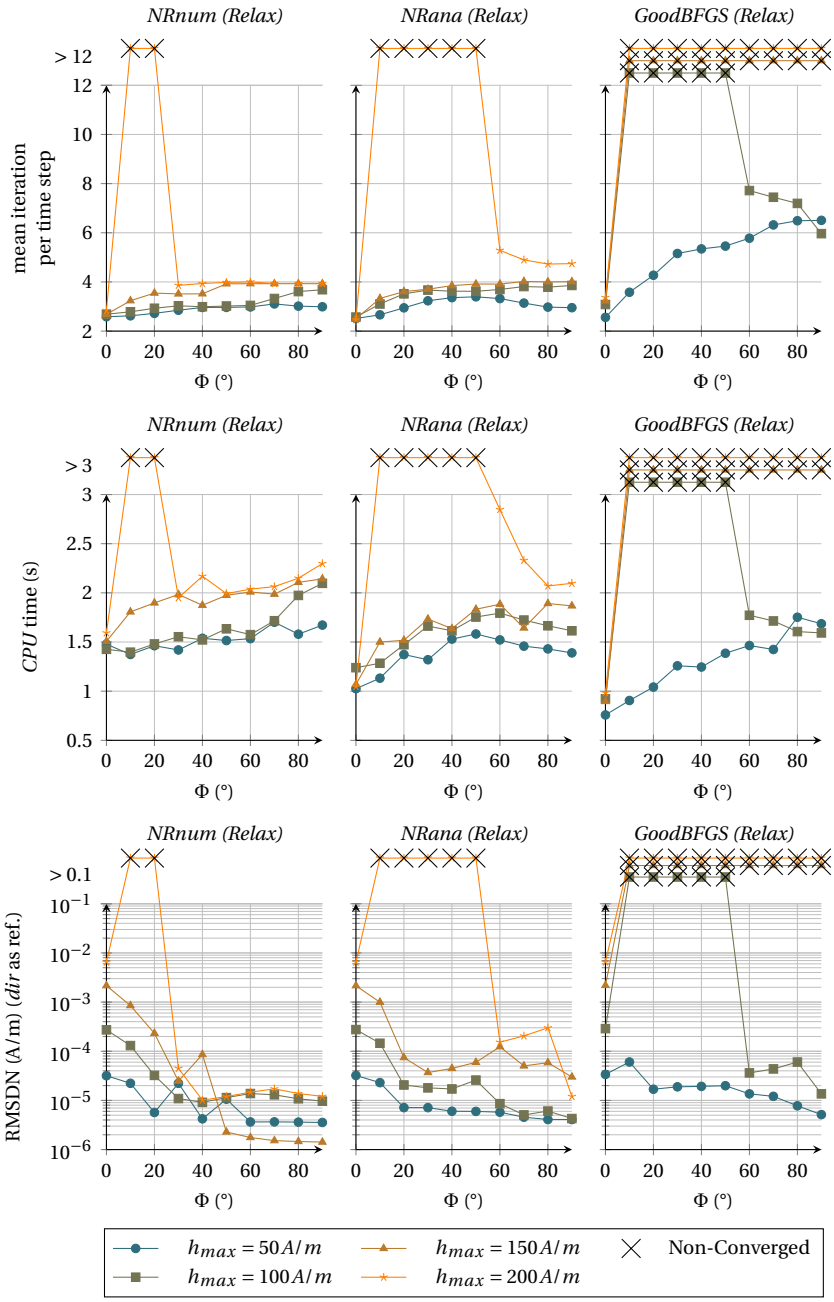

Figure 4.15: *Details on performances of different inversion techniques (with relaxation) for the vpm approach over* 40 *simulation test cases.*

Inversion (without relaxation) of the *var* approach.

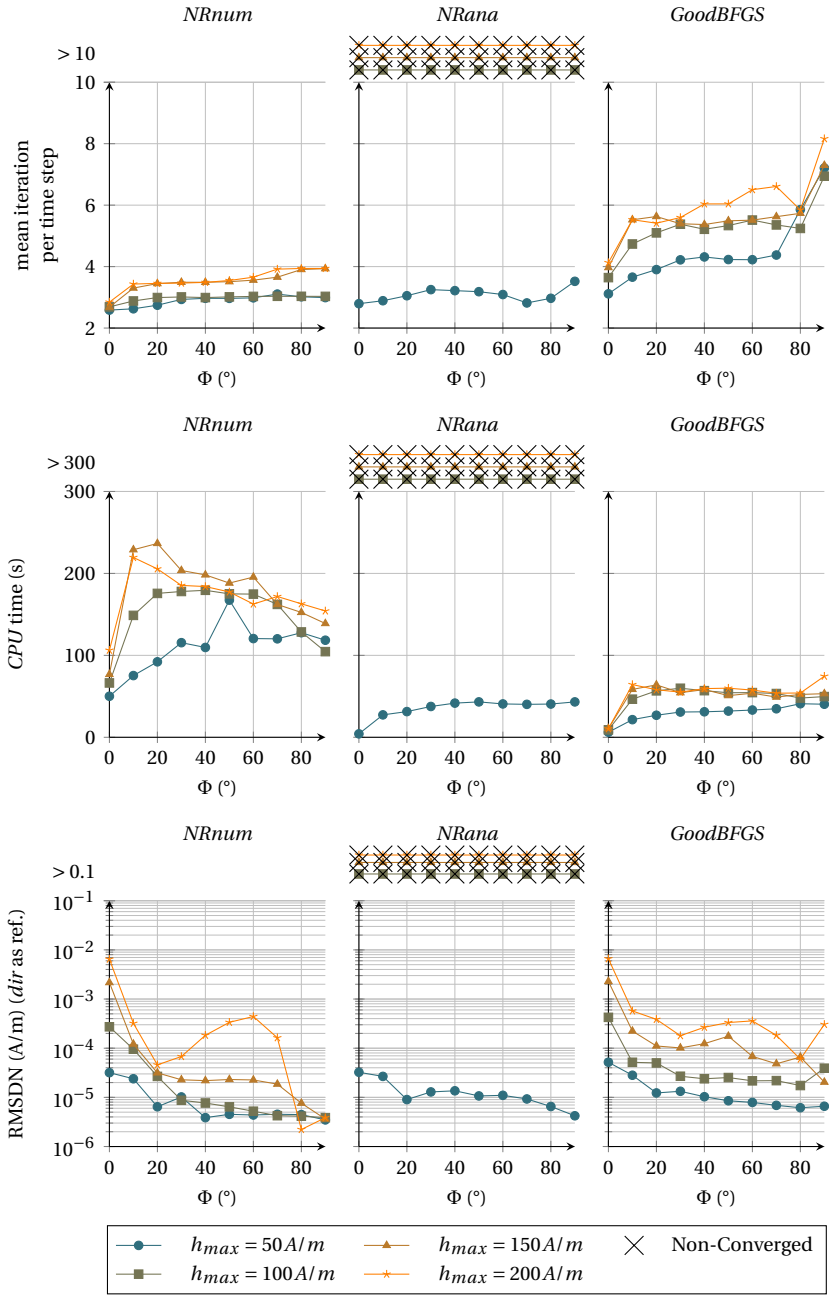

Figure 4.16: *Details on performances of different inversion techniques (with relaxation) for the var approach over 40 simulation test cases.*

Inversion (with relaxation) of the *var* approach.

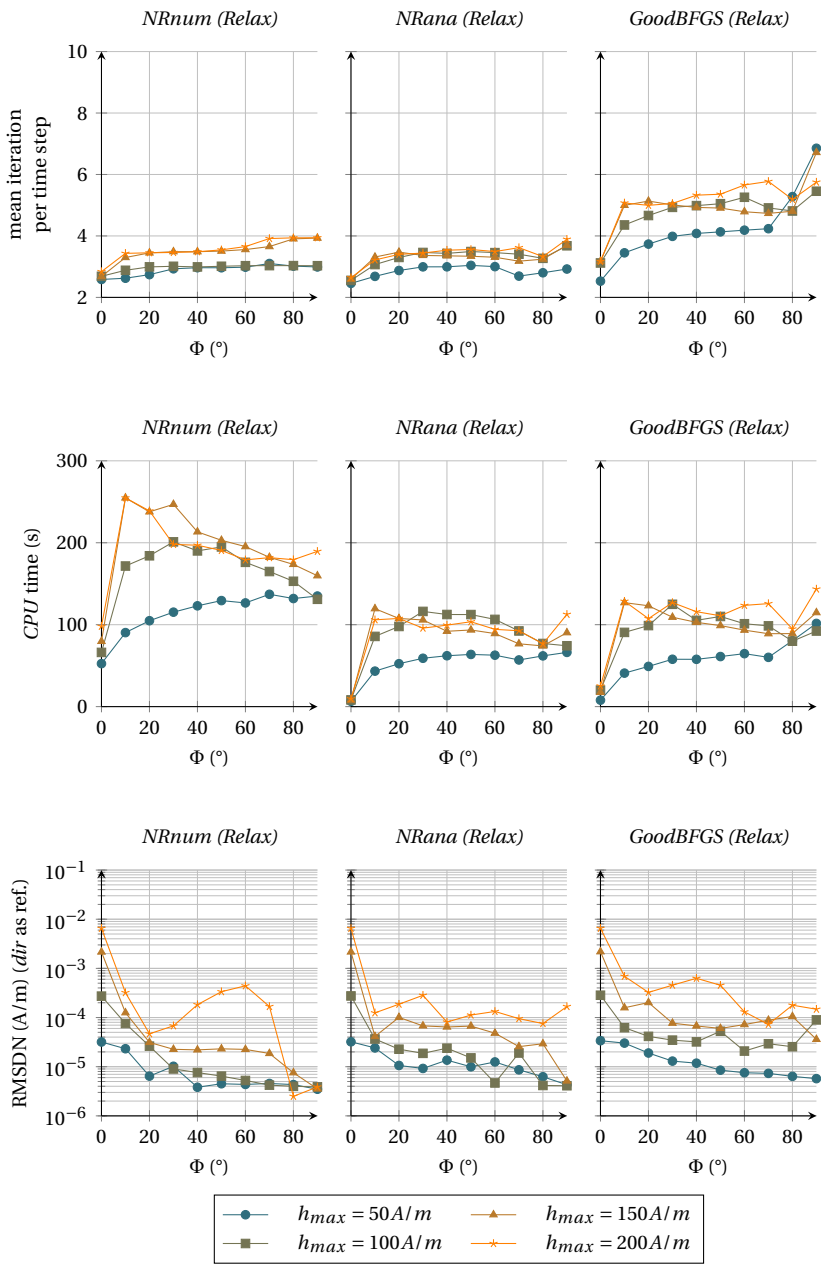

Figure 4.17: *Details on performances of different inversion techniques (with relaxation) for the var approach over 40 simulation test cases.*

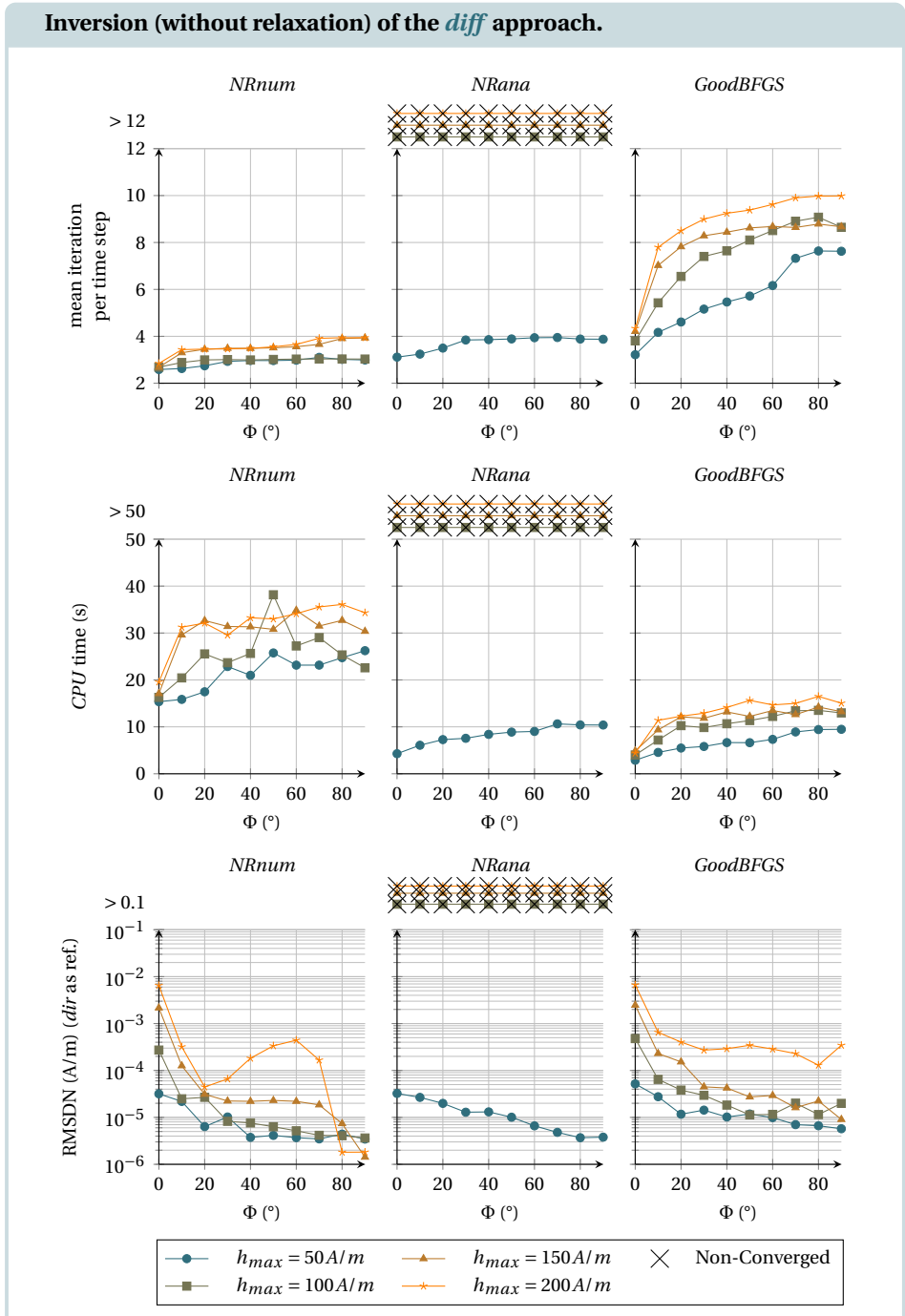

Figure 4.18: *Details on performances of different inversion techniques (without relaxation) for the diff approach over* 40 *simulation test cases.*

Inversion (with relaxation) of the *diff* approach.

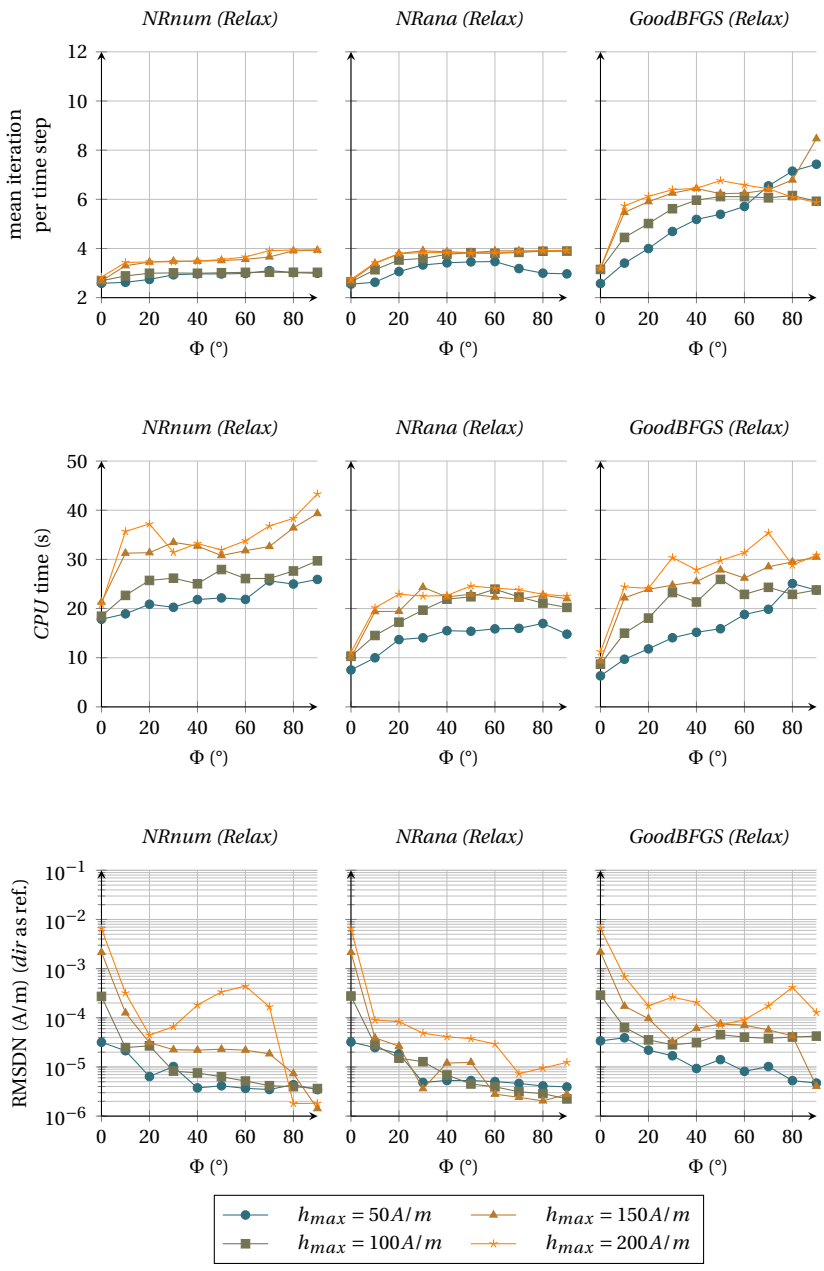

Figure 4.19: *Details on performances of different inversion techniques (with relaxation) for the diff approach over 40 simulation test cases.*

CHAPTER

5 Finite Element Formulations

In this chapter, the inclusions in the magnetic constitutive law of the energy-based (*EB*) Hysteresis Model for two complementary magnetic field conforming or magnetic flux density conforming formulations for finite element (*FE*) time stepping analysis are presented. The investigated *FE* formulations are the magnetodynamic $\mathbf{h}-\phi$ and $\mathbf{a}-\upsilon$ formulations, as well as their corresponding magnetostatic simplification, namely the $\mathbf{a}$ and the ϕ formulations, respectively. Similar inclusion of Preisach or Jiles-Atherton hysteresis models in complementary *FE* formulations can be found in [65, 67, 97] for the magnetostatic case, for example.

1. Electromagnetic Models

1.1. General Description

In classical electromagnetic theory, electromagnetism is described by the following general Maxwell's equations [202, 101]

$$\mathbf{curl}\,\mathbf{h}-\partial_t\mathbf{d}=\mathbf{j}\,,\qquad \mathbf{curl}\,\mathbf{e}=-\partial_t\mathbf{b}\,,\qquad \mathrm{div}\,\mathbf{b}=0\,,\qquad \mathrm{div}\,\mathbf{d}=q\,,\qquad (5.1, 5.2, 5.3, 5.4)$$

which are the generalized Ampere law, Faraday's law, the magnetic Gauss law and the electric Gauss law respectively. They involve the vector fields $\mathbf{h}$, $\mathbf{e}$, $\mathbf{b}$, $\mathbf{d}$ that are the magnetic field (A/m), the electric field (V/m), the magnetic flux density (T) and the electric flux density (C/m^2), respectively. The electric charge density q (C/m^3) and the electric current density $\mathbf{j}$ (A/m^2) are source terms in these equations. This system of equations is closed with the addition of constitutive laws [52, 124, 110], establishing some relations between the vector fields $\mathbf{h}$, $\mathbf{e}$, $\mathbf{b}$, $\mathbf{d}$ and $\mathbf{j}$ that are specific to a medium and can be written, with their main typical two-by-two coupling, as

$$\mathbf{b}=\mathscr{B}(\mathbf{h})\,,\qquad \mathbf{d}=\mathscr{D}(\mathbf{e})\,,\qquad \mathbf{j}=\mathscr{J}(\mathbf{e})\,.\qquad (5.5, 5.6, 5.7)$$

These connections are not necessarily simple, as they may be nonlinear, anisotropic, influenced by other physical quantities such as temperature, or may depend on past values of the fields, with some memory effect leading to hysteresis.

Namely, the study of the first one (5.5), the magnetic constitutive law, has been the central topic of this thesis since Chapter 1-Section 1.1, leading to the development of the *EB* hysteresis model in the subsequent chapters to describe hysteretic ferromagnetic material. The history-dependencies are hidden here for the sake of generality at this stage.

The second constitutive law (5.6) describes the behavior of dielectric materials. In its simplest expression, it states a proportionality relation between the electric flux density $\mathbf{d}$ and the electric field $\mathbf{e}$ through a material characteristic factor ϵ, the electric permittivity (F/m). Of course, material laws more complicated than a linear relation do exist, as example for ferroelectric materials, which can be seen as electric equivalent of ferromagnetic materials, characterized by saturation and hysteresis phenomenon as well. However, the electric behavior is not the topic of this work.

The third constitutive law (5.7) relates the current density $\mathbf{j}$ to the electric field $\mathbf{e}$. In this thesis, the simple Ohm's law is adopted, valid for conductors where $\mathbf{j}$ is proportional to $\mathbf{e}$, and thus linked linearly by a field-independent electric conductivity σ (S/m).

At the end, the analysis in this work is restricted to constitutive laws of the type

$$\mathbf{b} = \mathscr{B}(\mathbf{h}) \leftrightarrow \mathbf{h} = \mathscr{H}(\mathbf{b}), \quad \mathbf{d} = \epsilon\mathbf{e} \leftrightarrow \mathbf{e} = \epsilon^{-1}\mathbf{d}, \quad \mathbf{j} = \sigma\mathbf{e} \leftrightarrow \mathbf{e} = \sigma^{-1}\mathbf{j}, \qquad (5.8, 5.9, 5.10)$$

where only the magnetic law (5.8) can possibly describe nonlinear behaviors. As shown by (5.8), it is furthermore assumed that the nonlinear mapping $\mathscr{B}$ has an inverse $\mathscr{B}^{-1} := \mathscr{H}$. It has been shown in Chapter 4 that such inversion can be performed with the *EB* hysteresis model, while it is all the more trivial for linear laws such as (5.9) and (5.10).

All the set of partial differential equations from Maxwell, combined with the constitutive laws, defines a mathematical framework able to determine the evolution of the electromagnetic fields, locally at each point in space and time [49, 29], provided that appropriate initial and boundary conditions are given. The general goal consists in solving this system in a bounded open set Ω of the three-dimensional oriented Euclidean space ($\mathbb{E}^3$). On the boundary Γ of the domain Ω are defined complementary parts Γ_h and Γ_e on which the tangential trace of $\mathbf{h}$ (the normal trace of $\mathbf{j}$) or the tangential trace of $\mathbf{e}$ (the normal trace of $\mathbf{b}$) are imposed respectively, with $\mathbf{n}$ the unit normal vector exterior to Ω.

It is convenient to divide the domain Ω in subregions having specific characteristics. For instance, the considered domain Ω can be split in a conducting region Ω_c and a nonconducting one Ω_c^C, with $\Omega = \Omega_c \cup \Omega_c^C$. With this picture, the general framework is able to model eddy currents in massive inductors, which belongs to Ω_c and to take into account external sources from stranded conductors, where the current density $\mathbf{j}_s$ is imposed in the region $\Omega_s \subset \Omega_c^C$, as well as from boundary terms. Additional details on the coupling between inductors with external circuit equations to access directly the current or the voltage values thanks to electric global quantities can be found in [60, 62], but will not be reminded here. These contributions intervene in the set of source domains Ω_g, also called generators, which can be either a subset of Ω_c or Ω_c^C. For example, these generators can be connected to massive or stranded inductors, be-

longing thus to $\Omega_m \subset \Omega_c$ or $\Omega_s \subset \Omega_c^C$, respectively.

1.2. Magnetodynamics

The term $\partial_t \mathbf{d}$ in (5.1), also called the displacement current, is responsible for wave phenomena in electromagnetism. However, in the electrotechnical applications of interest, this contribution can be neglected, because the frequencies considered lead to much greater wavelength than the characteristic size of the devices studied [180, 166]. This leads to a decoupling between electrical and magnetic phenomena. This thesis focuses essentially on the latter, the description of magnetism.

In the magnetodynamic approximation [186], Maxwell's equations reduce to

$$\mathbf{curl}\,\mathbf{h} = \mathbf{j}\,, \qquad \mathbf{curl}\,\mathbf{e} = -\partial_t \mathbf{b}\,, \qquad \mathrm{div}\,\mathbf{b} = 0\,, \tag{5.11, 5.12, 5.13}$$

from which it is appropriate to provide the local magnetic and electric constitutive laws

$$\mathbf{b} = \mathscr{B}(\mathbf{h}) \longleftrightarrow \mathbf{h} = \mathscr{H}(\mathbf{b})\,, \qquad \mathbf{j} = \sigma\mathbf{e} \longleftrightarrow \mathbf{e} = \sigma^{-1}\mathbf{j}\,. \tag{5.14, 5.16}$$

This formalism allows to take the dynamic influence of eddy currents into account. The fields **h**, **b**, **e** and **j** are sufficient to characterize an electromagnetic state in space. Formulations can be expressed directly according to these fields. Nevertheless, as it will be reminded in the following sections, the introduction of precious potential definitions allows to reduce the computational cost associated with the resolutions of the magnetodynamic problem, leading to different formulations.

1.3. Magnetostatics

The magnetostatic approximation considers only magnetic phenomena independent of time. It assumes that the currents have slow enough variations so that the associated skin depth is much greater than the characteristic length of the domain. In this circumstances, eddy currents can no longer exist. Neglecting both the $\partial_t \mathbf{d}$ and $\partial_t \mathbf{b}$ terms, the Maxwell system evolves into

$$\mathbf{curl}\,\mathbf{h} = \mathbf{j}\,, \qquad \mathrm{div}\,\mathbf{b} = 0\,, \tag{5.17, 5.18}$$

for which only the local magnetic constitutive law remains required

$$\mathbf{b} = \mathscr{B}(\mathbf{h}) \longleftrightarrow \mathbf{h} = \mathscr{H}(\mathbf{b})\,. \tag{5.19}$$

The current density **j** is given and constitutes a source of magnetic field. The concepts of magnetic field **h** or induction **b** are of course sufficient to characterize a magnetic state in space. Nevertheless, once again, the concept of auxiliary potentials proves its interests and gives rise to various formulations depending on the potential adopted.

2. Magnetic Field Conforming Formulations

2.1. Magnetodynamic h − ϕ Formulation

Introduction of the Magnetic Scalar Potential

The magnetic field **h** can take the general expression

$$\mathbf{h} = \mathbf{h}_s + \mathbf{h}_r - \mathbf{grad}\,\phi\,, \tag{5.20}$$

involving three complementary fields $\mathbf{h}_s$,$\mathbf{h}_r$ and ϕ. The field $\mathbf{h}_s$ is a source magnetic field related to the imposed current density $\mathbf{j}_s$ in stranded conductor Ω_s through

$$\mathbf{curl}\,\mathbf{h}_s = \mathbf{j}_s\,. \tag{5.21}$$

The source magnetic field obeying (5.21) is not unique and several ways exist to define it [60]. One technique consists in building non physical generalized source fields chosen equal to zero everywhere outside the conductors Ω_s, except in a transition layer along their associated cuts [58]. This can be easily defined a priori, i.e. before the time stepping, which is a key feature of the method. The field $\mathbf{h}_r$ is the corresponding reaction field in conducting regions Ω_c, while ϕ is the associated reaction magnetic scalar potential derived in nonconducting regions Ω_c^C. When the domain Ω_c^C is multiply connected, the scalar potential ϕ is a priori multivalued, in which case cuts must be introduced to make this domain simply connected and avoid the multiplicity of ϕ.

5

Weak Formulation

Satisfying (5.11) in a strong sense through (5.20), the **h**−ϕ formulation is obtained from the weak form of (5.12) in combination with the constitutive laws (5.14) and (5.16):

$$\partial_t \left(\mathscr{B}(\mathbf{h}), \mathbf{h}'\right)_\Omega + \left(\sigma^{-1}\mathbf{curl}\,\mathbf{h}, \mathbf{curl}\,\mathbf{h}'\right)_{\Omega_c} + \left(\sigma^{-1}\mathbf{j}_s, \mathbf{curl}\,\mathbf{h}'\right)_{\Omega_s} + \langle \mathbf{n}\times\mathbf{e}_s, \mathbf{h}'\rangle_{\Gamma_e} = 0\,, \tag{5.22}$$

for all $\mathbf{h}' \in F_{h\phi}(\Omega)$, where $F_{h\phi}(\Omega)$ is an appropriate function space defined on Ω enclosing basis functions for **h**, coupled with ϕ, as well as for the test functions $\mathbf{h}'$. The notations $(\cdot,\cdot)_\Omega$ and $\langle\cdot,\cdot\rangle_\Gamma$, denote the integral of the scalar product of the two arguments over a domain Ω and on a boundary Γ respectively.

Spatial Discretization

Nevertheless in a computational context, only a restricted function space for the **h** − ϕ discretization may be considered. In order to satisfy (5.22), the magnetic field **h** is therefore interpolated with edge elements [28, 167, 59, 61, 55], generating the discrete function space defined on a mesh of Ω. Each degree of freedom related to each basis function is the circulation of **h** along its associated edge. The function space is also enriched with additional basis functions associated with the nodes of the mesh included in the Ω_c^C regions. Indeed, the circulation of **h** along an edge in Ω_c^C is actually the difference of the scalar potentials ϕ at both extremities of the edge. Exploiting the scalar potential helps to reduce the computational cost. In case Ω_c^C is multiply connected,

the discretization of $\mathbf{h}$, and more particularly of ϕ, needs the introduction of vector basis functions associated with cuts making Ω_c^C simply connected. The test functions $\mathbf{h}'$ are restricted to the same function space. Applying this discretization to the problem (5.22) leads it to become a system of differential equations, with one equation for each degree of freedom [158].

Time Discretization

Furthermore, a finite difference time-stepping algorithm based on the standard $\theta-$method is used to discretize the problem in time [208, 99]. This approach covers in particular the Euler implicit method ($\theta = 1$) and the Crank-Nicolson method ($\theta = 1/2$). Thanks to this scheme, the solution at time t_n, is built from the known solution at the previous instant t_{n-1}. The time derivative of a variable is thus approximated by

$$\theta \partial_t \mathscr{B}(\mathbf{h})\Big|_{t_n} + (1-\theta)\partial_t \mathscr{B}(\mathbf{h})\Big|_{t_{n-1}} = \frac{\mathscr{B}(\mathbf{h})\big|_n - \mathscr{B}(\mathbf{h})\big|_{n-1}}{\Delta t_n}\,, \tag{5.23}$$

with $\Delta t_n = t_n - t_{n-1}$ the time increment at step n. Exploiting this, the system of differential equations previously mentioned becomes a system of algebraic equations. In this thesis, the backward Euler method is adopted ($\theta = 1$), and applying this numerical scheme to (5.22) requires to cancel the following functional at each time step n

$$\begin{aligned}\mathscr{F}_{h\phi}(\mathbf{h}_n) := &\left(\frac{\mathscr{B}(\mathbf{h})\big|_n - \mathscr{B}(\mathbf{h})\big|_{n-1}}{\Delta t_n}, \mathbf{h}'\right)_\Omega + \left(\sigma^{-1}\mathbf{curl}\,\mathbf{h}_n, \mathbf{curl}\,\mathbf{h}'\right)_{\Omega_c} \\ &+ \left(\sigma^{-1}(\mathbf{j}_s)_n, \mathbf{curl}\,\mathbf{h}'\right)_{\Omega_s} + \langle \mathbf{n}\times(\mathbf{e}_s)_n, \mathbf{h}'\rangle_{\Gamma_e}\,.\end{aligned} \tag{5.24}$$

5

System Resolution

In case the constitutive magnetic law is linear, i.e. $\mathscr{B}(\mathbf{h})\big|_n = \mu \mathbf{h}_n$ with μ the constant magnetic permeability[1], the corresponding systems of algebraic equations in the discrete level are also linear and produce directly the fields $\mathbf{h}_n$ for each successive time instant.

Considering now a reversible anhysteretic constitutive relation, $\mathscr{B}(\mathbf{h})\big|_n = \mathscr{B}_{\text{an}}(\mathbf{h}_n)$, that depends nonlinearly on $\mathbf{h}_n$, the systems of algebraic equations are then nonlinear and have to be solved iteratively for each time step, usually by means of a Newton-Raphson (*NR*) method.

The same applies for irreversible hysteretic media. Here, the *EB* hysteresis model is included under its direct form $\mathscr{B}(\mathbf{h})\big|_n = \mathscr{B}^{dir}\left(\mathbf{h}_n, (\mathbf{X}^k)_{n-1}\right)$ where the variables $(\mathbf{X}^k)_{n-1}$ stand for $\mathbf{h}^k_{\text{rev}(p)}$ for the Vector Play Model (*vpm*) and the differential approach (*diff*), or $\mathbf{J}^k_{(p)}$ for the variational approach (*var*). These values are known from the previous instant $(p) = n-1$. Hence, the update magnetic field $\mathbf{b}_n$ depends only explicitly on the unknown $\mathbf{h}_n$ at a given time step. Therefore, the generic constitutive relation

[1] either a scalar if the medium is isotropic or a tensor for an anisotropic medium.

$\mathbf{b}_n = \mathscr{B}(\mathbf{h})\big|_n$ at each time step, is also adopted in the following for the hysteresis model because other possible dependencies, like $(\mathbf{X}^k)_{n-1}$, can be handled parametrically.

The term $\mathbf{b}_{n-1} = \mathscr{B}(\mathbf{h})\big|_{n-1}$ in (5.24) can be directly reused from the previous time step without calling again the magnetic constitutive law. This implies an additional data storage cost that may be worthwhile when the application of the constitutive law is computationally time consuming.

The *NR* method approximates the exact solution of (5.24) by a sequence $\mathbf{h}_n^i = \mathbf{h}_n^{i-1} + \Delta\mathbf{h}_n^i$, with $i = 1, 2, \ldots$ the iteration index in the nonlinear resolution, starting from an initial estimate $\mathbf{h}_n^0$ that could be, for example, the known value $\mathbf{h}_{n-1}$ from the previous time step. At each nonlinear iteration, the nonlinear system coming from (5.24) at the discrete level is linearised around the $(i-1)$-th known solution $\mathbf{h}_n^{i-1}$ and solved with respect to the increment $\Delta\mathbf{h}_n^i = \mathbf{h}_n^i - \mathbf{h}_n^{i-1}$ to find the new solution $\mathbf{h}_n^i$, as summarized in (5.25), until a given convergence criterion is satisfied.

Magnetodynamic $\mathbf{h}-\phi$ Formulation

At iteration i of the *NR* resolution, at time step n, find $\mathbf{h}_n^i \in F_{h\phi}(\Omega)$ such that

$$\left.\frac{\partial \mathscr{F}_{h\phi}}{\partial \mathbf{h}}\right|_{\mathbf{h}_n^{i-1}} \cdot \Delta\mathbf{h}_n^i = -\mathscr{F}_{h\phi}(\mathbf{h}_n^{i-1}), \tag{5.25}$$

holds for suitable test functions $\mathbf{h}' \in F_{h\phi}(\Omega)$; with $\Delta\mathbf{h}_n^i = \mathbf{h}_n^i - \mathbf{h}_n^{i-1}$ and where

$$\left.\frac{\partial \mathscr{F}_{h\phi}}{\partial \mathbf{h}}\right|_{\mathbf{h}_n^{i-1}} \cdot \Delta\mathbf{h}_n^i = \left(\frac{1}{\Delta t_n}\left.\frac{\partial \mathscr{B}}{\partial \mathbf{h}}\right|_n^{i-1} \Delta\mathbf{h}_n^i, \mathbf{h}'\right)_\Omega + \left(\sigma^{-1}\mathbf{curl}\,\Delta\mathbf{h}_n^i, \mathbf{curl}\,\mathbf{h}'\right)_{\Omega_c},$$

$$\mathscr{F}_{h\phi}(\mathbf{h}_n^{i-1}) = \left(\frac{\mathscr{B}(\mathbf{h})\big|_n^{i-1} - \mathscr{B}(\mathbf{h})\big|_{n-1}}{\Delta t_n}, \mathbf{h}'\right)_\Omega + \left(\sigma^{-1}\mathbf{curl}\,\mathbf{h}_n^{i-1}, \mathbf{curl}\,\mathbf{h}'\right)_{\Omega_c} + \left(\sigma^{-1}(\mathbf{j}_s)_n, \mathbf{curl}\,\mathbf{h}'\right)_{\Omega_s} + \langle \mathbf{n} \times (\mathbf{e}_s)_n, \mathbf{h}'\rangle_{\Gamma_e}.$$

At the discrete level, it comes down to solving, at each iteration i, a linear system in terms of the increments $\Delta\mathbf{h}_n^i$ to find the next $\mathbf{h}_n^i$. The tensor $\frac{\partial \mathscr{B}}{\partial \mathbf{h}}$ appears through the linearization in (5.25) and is computed with the known values from the $(i-1)$-th *NR* iteration.

When dealing with hysteretic media, the notation $\mathscr{B}(\mathbf{h})\big|_n^{i-1} = \mathscr{B}^{dir}\left(\mathbf{h}_n^{i-1}, (\mathbf{X}^k)_{n-1}\right)$ represents the induction field updated by the direct *EB* hysteresis model based on the known values $\mathbf{h}_n^{i-1}$ from the $(i-1)$-th iteration in the *NR* process, and the known material state from the previous time step $(\mathbf{X}^k)_{n-1}$. If saved, the computed induction fields from the previous time step $\mathbf{b}_{n-1} = \mathscr{B}(\mathbf{h})\big|_{n-1}$ can be reused as such.

With the *EB* model, the differential permeability tensor $\frac{\partial \mathscr{B}}{\partial \mathbf{h}}$ is the tensor already detailed in the *NR* process (4.3) used for the inversion of the hysteresis constitutive law at material level. It is worth noting that discontinuities on the differential permeability

are thus also likely to happen between subsequent iterations. Therefore, relaxation is in general mandatory with factor $\gamma \in]0,1]$, so that $\mathbf{h}_n^i = \mathbf{h}_n^{i-1} + \gamma \Delta \mathbf{h}_n^i$, to palliate stability problems in the *NR* scheme.

Finally, when the new solution field $\mathbf{h}_n$ is determined after convergence, the magnetic material variable states $(\mathbf{X}^k)_n$ are updated thanks to (3.10), (3.20) or (3.28), depending on the chosen implementation approach. The new material state characterization is thus completed and the next time step can start.

2.2. Magnetostatic ϕ Formulation

Based on the same developments that were made previously for the magnetodynamic problem, the simplified case of magnetostatics is now addressed. Similarly as in (5.20), the magnetic field $\mathbf{h}$ takes the general expression

$$\mathbf{h} = \mathbf{h}_s - \mathbf{grad}\,\phi\,, \tag{5.26}$$

with $\mathbf{h}_s$, the source term still related to $\mathbf{j}_s$ through (5.21) as before, and where all the reaction field can now be derived from a scalar potential, $-\mathbf{grad}\,\phi$, everywhere in Ω. Of course, once again, this derivation is only correct if appropriate cuts are introduced in Ω to make it simply connected [61, 188]. Compared to (5.20), there is no conducting regions where a reaction field $\mathbf{h}_r$ can develop in the magnetostatic case. This decomposition of $\mathbf{h}$ is sufficient to satisfy (5.17) in a strong sense.

In addition with the constitutive law (5.19), the weak form of the magnetic Gauss equation (5.18) then reads

$$\left(\mathscr{B}\left(\mathbf{h}_s - \mathbf{grad}\,\phi\right), -\mathbf{grad}\,\phi'\right)_\Omega + \langle \mathbf{n}\cdot\mathbf{b}_s, \phi' \rangle_{\Gamma_e} = 0, \tag{5.27}$$

for all test functions $\phi' \in F_\phi(\Omega)$, where $F_\phi(\Omega)$ is an appropriate function space, both for ϕ and ϕ', the gradient of which is actually included in $F_{h\phi}(\Omega)$.

Of course, in a *FE* context, the scalar field values ϕ and ϕ' are represented by nodal elements spanning discrete subspace of $F_\phi(\Omega)$. The degree of freedom associated to each nodal values in the mesh of Ω corresponds to the unknown of the *FE* problem. As before, the discrete equivalent of (5.27) consists then in a set of differential equations, with one equation for each node, such that the problem can eventually be written under a system in matrix form, in terms of the vector of unknown components that discretize spatially the scalar potential field ϕ.

Limiting once again this presentation to the continuous domain, the discretized ϕ formulation aims to cancel the functional

$$\mathscr{F}_\phi(\phi_n) := \left(\mathscr{B}\left(\mathbf{h}_s - \mathbf{grad}\,\phi\right)\Big|_n, -\mathbf{grad}\,\phi'\right)_\Omega + \langle \mathbf{n}\cdot(\mathbf{b}_s)_n, \phi' \rangle_{\Gamma_e}\,, \tag{5.28}$$

in order to determine the scalar potential field ϕ_n corresponding to the inner sources $(\mathbf{j}_s)_n$ and boundary sources $(\mathbf{b}_s)_n$ of a given time step n.

The remarks in the magnetodynamic case about the system resolution and the discussion on the type of magnetic law hidden behind the expression $\mathscr{B}(\mathbf{h})$, remains also

valid here. Namely, for a nonlinear constitutive law, with or without hysteresis, an iterative process has to be used to cancel (5.28). Adopting a *NR* scheme, the magnetostatic ϕ formulation can be summarized by the resolution of (5.29), at each *NR* iteration until convergence for a given time step.

Magnetostatic ϕ Formulation

At iteration i of the *NR* resolution, at time step n, find $\phi_n^i \in F_\phi(\Omega)$ such that

$$\left.\frac{\partial \mathscr{F}_\phi}{\partial \phi}\right|_{\phi_n^{i-1}} \cdot \Delta\phi_n^i = -\mathscr{F}_\phi(\phi_n^{i-1}), \tag{5.29}$$

holds for suitable test functions $\phi' \in F_\phi(\Omega)$; with $\Delta\phi_n^i = \phi_n^i - \phi_n^{i-1}$ and where

$$\left.\frac{\partial \mathscr{F}_\phi}{\partial \phi}\right|_{\phi_n^{i-1}} \cdot \Delta\phi_n^i = \left(-\left.\frac{\partial \mathscr{B}}{\partial \mathbf{h}}\right|_n^{i-1} \mathbf{grad}\,\Delta\phi_n^i, -\mathbf{grad}\,\phi'\right)_\Omega,$$
$$\mathscr{F}_\phi(\phi_n^{i-1}) = \left(\mathscr{B}\left(\mathbf{h}_s - \mathbf{grad}\,\phi\right)\Big|_n^{i-1}, -\mathbf{grad}\,\phi'\right)_\Omega + \langle \mathbf{n}\cdot(\mathbf{b}_s)_n, \phi'\rangle_{\Gamma_e}.$$

As for the $\mathbf{h}-\phi$ formulation, the direct form $\mathscr{B}^{dir}\left((\mathbf{h}_s)_n - \mathbf{grad}\,\phi_n^{i-1}, (\mathbf{X}^k)_{n-1}\right)$, and the differential permeability tensors $\frac{\partial \mathscr{B}}{\partial \mathbf{h}}$ are required for the inclusion of the *EB* hysteresis model in the magnetostatic ϕ formulation. The magnetic states $(\mathbf{X}^k)_n$ have to be updated at least at the end of each time step.

3. Magnetic Flux Density Conforming Formulations

3.1. Magnetodynamic $\mathbf{a}-v$ Formulation

Introduction of the Magnetic Vector Potential

The $\mathbf{a}-v$ formulation satisfies strongly (5.12) and (5.13) by expressing the fields $\mathbf{b}$ and $\mathbf{e}$ in terms of a magnetic vector potential $\mathbf{a}$ and an electric scalar potential v:

$$\mathbf{b} = \mathbf{curl}\,\mathbf{a}, \qquad \mathbf{e} = -\partial_t \mathbf{a} - \mathbf{grad}\,v. \tag{5.30, 5.31}$$

Weak Formulation

Based on these two potentials, the $\mathbf{a}-v$ formulation is deduced from the weak form of (5.11), in combination with (5.14) and (5.16) [30]:

$$\left(\mathscr{H}(\mathbf{curl}\,\mathbf{a}), \mathbf{curl}\,\mathbf{a}'\right)_\Omega + \left(\sigma\partial_t \mathbf{a}, \mathbf{a}'\right)_{\Omega_c} + \left(\sigma\,\mathbf{grad}\,v, \mathbf{a}'\right)_{\Omega_c} + \langle \mathbf{n}\times\mathbf{h}_s, \mathbf{a}'\rangle_{\Gamma_h} = \left(\mathbf{j}_s, \mathbf{a}'\right)_{\Omega_s}, \tag{5.32}$$

for all $\mathbf{a}' \in F_a(\Omega)$, where $F_a(\Omega)$ is an appropriate function space defined on Ω. Considering test functions $\mathbf{a}' = \mathbf{grad}\,v'$ in (5.32) gives

$$\left(\sigma\partial_t \mathbf{a}, \mathbf{grad}\,v'\right)_{\Omega_c} + \left(\sigma\,\mathbf{grad}\,v, \mathbf{grad}\,v'\right)_{\Omega_c} = \langle \mathbf{n}\cdot\mathbf{j}_s, v'\rangle_{\Gamma_j}, \tag{5.33}$$

for all $v' \in F_v(\Omega_c)$, another suitable function space for v and v'. Note that (5.33) is also the weak form of $\mathrm{div}\mathbf{j} = 0$ in Ω_c. The boundary Γ_j is the part of the boundary of Ω_c which is crossed by an electric current. The vector potential $\mathbf{a}$ is uniquely defined in Ω_c and a gauge condition must be defined in Ω_c^C. The electric scalar potential v is only defined in the conducting regions Ω_c and it can usually be fixed to zero in passive conductors.

In order to simplify the presentation in the following, it will be supposed that there is no active conductor in Ω_c, i.e. $v = 0$. Nevertheless, the extension with this additional contribution can be handled without difficulty. In order to keep track of this simplification, a modified vector potential $\overset{\star}{\mathbf{a}}$ can be introduced, verifying $\partial_t \overset{\star}{\mathbf{a}} = \partial_t \mathbf{a} + \mathbf{grad}\, v$, such that $\mathbf{e} = -\partial_t \overset{\star}{\mathbf{a}}$ from (5.31), and $\overset{\star}{\mathbf{a}}$ belongs formally to the space $F_e(\Omega) = F_a(\Omega) \cup F_v(\Omega_c)$. In the case where $v = 0$, one can then simply replace $\mathbf{a}$ by $\overset{\star}{\mathbf{a}}$ in (5.32), whereas the relation (5.33) is unnecessary [57].

Spatial Discretization

In practice, the continuous function spaces $F_a(\Omega)$ and $F_v(\Omega_c)$ are approximated by discrete equivalents. Therefore, a general choice to represent $\mathbf{a}'$ and v', and thus $\mathbf{a}$ and v, consists to use respectively an edge *FE* function space built on a mesh of Ω and an associated nodal *FE* function space, satisfying $\mathbf{grad}\, F_v(\Omega_c) \subset F_a(\Omega)$, formulation (5.32) including (5.33) in this case [28, 167, 59, 61, 55].

In that way, the potentials $\mathbf{a}$ and v can be expressed under their discrete form as linear combination of basis functions from their respective function space converting the problem into a system of differential equations. The coefficients weighting each basis function may be grouped in a vector of unknowns which have to be determined in order to satisfy (5.32) and so (5.33) within the restricted function spaces.

Time Discretization

A finite difference time-stepping algorithm using the θ-method is also used. The time derivative in (5.32) is approximated by

$$\theta(\partial_t \overset{\star}{\mathbf{a}})_{t_n} + (1-\theta)(\partial_t \overset{\star}{\mathbf{a}})_{t_{n-1}} = \frac{\overset{\star}{\mathbf{a}}_n - \overset{\star}{\mathbf{a}}_{n-1}}{\Delta t_n}, \tag{5.34}$$

where, as before, the subscripts n and $n-1$ refer to the current time step and the previous known one respectively. The results hereafter are all presented with the Euler implicit method ($\theta = 1$). In that way, the time discretized approximation of the problem (5.32) takes the form of a functional of $\overset{\star}{\mathbf{a}}_n$ that has to be canceled for each time step n, to find the current field $\overset{\star}{\mathbf{a}}_n$:

$$\begin{aligned} \mathscr{F}_{\overset{\star}{a}}(\overset{\star}{\mathbf{a}}_n) := &\left(\mathscr{H}(\mathbf{curl}\,\overset{\star}{\mathbf{a}})\big|_n, \mathbf{curl}\,\mathbf{a}'\right)_\Omega + \left(\sigma \frac{\overset{\star}{\mathbf{a}}_n - \overset{\star}{\mathbf{a}}_{n-1}}{\Delta t_n}, \mathbf{a}'\right)_{\Omega_c} \\ &+ \langle \mathbf{n} \times (\mathbf{h}_s)_n, \mathbf{a}' \rangle_{\Gamma_h} - \left((\mathbf{j}_s)_n, \mathbf{a}'\right)_{\Omega_s}. \end{aligned} \tag{5.35}$$

System Resolution

After translation to the restricted function space, the formulation (5.35) becomes a system of algebraic equations. Once again, depending on the linear or nonlinear nature of the magnetic constitutive law $\mathscr{H}(\mathbf{curl}\,\overset{\star}{\mathbf{a}})$, the corresponding systems of algebraic equations at the discrete stage are then either linear or nonlinear, with a *NR* scheme needed to find the solution field $\overset{\star}{\mathbf{a}}_n$ in the latter case, for each time step. In the linear case, one has $\mathscr{H}(\mathbf{curl}\,\overset{\star}{\mathbf{a}})\big|_n = \nu\,\mathbf{curl}\,\overset{\star}{\mathbf{a}}_n$ with ν a constant magnetic reluctivity[2], that is the inverse of the magnetic permeability μ. The fields $\mathbf{h}_n$ are then obtained directly by solving the corresponding linear system at each successive time step. Conversely, with a nonlinear anhysteretic law, written as $\mathscr{H}(\mathbf{curl}\,\overset{\star}{\mathbf{a}})\big|_n = \mathscr{H}_{\text{an}}(\mathbf{curl}\,\overset{\star}{\mathbf{a}}_n)$, an iterative process has to be used for the resolution within each time step.

For the hysteretic case, it is the inverse form of the *EB* hysteresis model that must be taken through $\mathscr{H}(\mathbf{curl}\,\overset{\star}{\mathbf{a}})\big|_n = \mathscr{H}^{inv}\left(\mathbf{curl}\,\overset{\star}{\mathbf{a}}_n, (\mathbf{X}^k)_{n-1}\right)$, where the variables $(\mathbf{X}^k)_{n-1}$, stand for $\mathbf{h}^k_{\text{rev}(p)}$ for the *vpm* and *diff* approaches, or $\mathbf{J}^k_{(p)}$ for the *var* approach. As the values $(\mathbf{X}^k)_{n-1}$ are known from the previous time step $(p) = n-1$, they can be treated as parametric at a given time step, such that the generic constitutive relation $\mathbf{h}_n = \mathscr{H}(\mathbf{curl}\,\overset{\star}{\mathbf{a}})\big|_n$, that depends only on the field $\overset{\star}{\mathbf{a}}_n$, is also considered for the hysteresis case in the following.

For nonlinear cases in general, at each time step n, the *NR* method approximates the exact solution of (5.35) by a sequence $\overset{\star}{\mathbf{a}}{}^i_n = \overset{\star}{\mathbf{a}}{}^{i-1}_n + \Delta\overset{\star}{\mathbf{a}}{}^i_n$, obtained by linearization of (5.35) around the $(i-1)$-th solutions $\overset{\star}{\mathbf{a}}{}^{i-1}_n$, with $i = 1, 2, \ldots$ denoting the iterate number in the nonlinear resolution, starting from an initial estimate $\overset{\star}{\mathbf{a}}{}^0_n$, being possibly the known field $\overset{\star}{\mathbf{a}}_{n-1}$ from the previous time step. Iteratively, the *NR* scheme satisfies the problem (5.36) until the verification of a stopping criterion.

[2] either a scalar if the medium is isotropic or a tensor for an anisotropic medium.

Magnetodynamic a – ν Formulation

At iteration i of the *NR* resolution, at time step n, find $\overset{\star}{\mathbf{a}}{}_n^i \in F_e(\Omega)$ such that

$$\left.\frac{\partial \mathscr{F}_{a}^{\star}}{\partial \overset{\star}{\mathbf{a}}}\right|_{\overset{\star}{\mathbf{a}}{}_n^{i-1}} \cdot \Delta \overset{\star}{\mathbf{a}}{}_n^i = -\mathscr{F}_{a}^{\star}(\overset{\star}{\mathbf{a}}{}_n^{i-1}), \tag{5.36}$$

holds for suitable test functions $\mathbf{a}' \in F_a(\Omega)$; with $\Delta \overset{\star}{\mathbf{a}}{}_n^i = \overset{\star}{\mathbf{a}}{}_n^i - \overset{\star}{\mathbf{a}}{}_n^{i-1}$ and where

$$\left.\frac{\partial \mathscr{F}_{a}^{\star}}{\partial \overset{\star}{\mathbf{a}}}\right|_{\overset{\star}{\mathbf{a}}{}_n^{i-1}} \cdot \Delta \overset{\star}{\mathbf{a}}{}_n^i = \left(\left.\frac{\partial \mathscr{H}}{\partial \mathbf{b}}\right|_n^{i-1} \mathbf{curl}\, \Delta \overset{\star}{\mathbf{a}}{}_n^i, \mathbf{curl}\, \mathbf{a}'\right)_{\Omega} + \left(\sigma \frac{\Delta \overset{\star}{\mathbf{a}}{}_n^i}{\Delta t_n}, \mathbf{a}'\right)_{\Omega_c},$$

$$\mathscr{F}_{a}^{\star}(\overset{\star}{\mathbf{a}}{}_n^{i-1}) = \left(\mathscr{H}(\mathbf{curl}\, \overset{\star}{\mathbf{a}})\big|_n^{i-1}, \mathbf{curl}\, \mathbf{a}'\right)_{\Omega} + \left(\sigma \frac{\overset{\star}{\mathbf{a}}{}_n^{i-1} - \overset{\star}{\mathbf{a}}{}_{n-1}}{\Delta t_n}, \mathbf{a}'\right)_{\Omega_c}$$
$$+ \langle \mathbf{n} \times (\mathbf{h}_s)_n, \mathbf{a}' \rangle_{\Gamma_h} - \left((\mathbf{j}_s)_n, \mathbf{a}'\right)_{\Omega_s}.$$

As can be seen with (5.36), the linearisation of (5.35) requires the evaluation of its derivative with respect to the degrees of freedom $\overset{\star}{\mathbf{a}}$, which gives the matrix of the linearized system written in terms of the differential reluctivity tensor $\frac{\partial \mathscr{H}}{\partial \mathbf{b}}$ evaluated at the known values from the $(i-1)$-th iteration in the *NR* process.

For the hysteresis case, the magnetic fields $\mathscr{H}(\mathbf{curl}\, \overset{\star}{\mathbf{a}})\big|_n^{i-1} = \mathscr{H}^{inv}\left(\mathbf{curl}\, \overset{\star}{\mathbf{a}}{}_n^{i-1}, (\mathbf{X}^k)_{n-1}\right)$ are built thanks to the inverse *EB* hysteresis model with the known values $\overset{\star}{\mathbf{a}}{}_n^{i-1}$ from the $(i-1)$-th iteration in the *NR* process, and the known material state from the previous time step $(\mathbf{X}^k)_{n-1}$.

Once again, due to the presence of the discontinuous differential reluctivity tensor $\frac{\partial \mathscr{H}}{\partial \mathbf{b}}$, which is, this time, the inverse of the tensor $\frac{\partial \mathscr{B}}{\partial \mathbf{h}}$ already encountered in the inversion at material level of the *EB* hysteresis model (4.3), relaxation formula between two iterates $\overset{\star}{\mathbf{a}}{}_n^i = \overset{\star}{\mathbf{a}}{}_n^{i-1} + \gamma \Delta \overset{\star}{\mathbf{a}}{}_n^i$, with $\gamma \in]0,1]$, is also recommended to improve the *NR* scheme.

At the end, if the *NR* method converges, the new solution $\overset{\star}{\mathbf{a}}{}_n$ is determined, and thus also $\mathbf{b}_n$. Knowing also the magnetic field $\mathbf{h}_n$ from $\mathscr{H}(\mathbf{curl}\, \overset{\star}{\mathbf{a}})_n$, the magnetic material variable states $(\mathbf{X}^k)_n$ are then updated thanks to (3.10), (3.20) or (3.28), depending on the chosen approach, to conclude the current material state characterization before starting the next time step.

3.2. Magnetostatic a Formulation

As in Chapter 5-Section 2, the magnetostatic problem can be derived as a particular case of the magnetodynamic problem where all time dependent variations are neglected such that there is no domain Ω_c where eddy current can develop.

This formulation still relies on the magnetic vector potential $\mathbf{a}$ definition

$$\mathbf{b} = \mathbf{curl}\,\mathbf{a}\,, \tag{5.37}$$

which thus satisfies directly (5.18). The weak form of (5.17) with the constitutive law (5.19) gives

$$\left(\mathscr{H}(\mathbf{curl}\,\mathbf{a}), \mathbf{curl}\,\mathbf{a}'\right)_\Omega + \langle \mathbf{n}\times\mathbf{h}_s, \mathbf{a}'\rangle_{\Gamma_h} = \left(\mathbf{j}_s, \mathbf{a}'\right)_{\Omega_s}\,, \tag{5.38}$$

for all $\mathbf{a}' \in F_a(\Omega)$, which is, as expected, similar to (5.32), but without the dynamic contributions from domain Ω_c. As before, it should be noted that the vector potential is still not uniquelly defined in the domain Ω, in which the conductivity has now no effect, and it requires in general the imposition of a gauge condition to ensure its unicity. The function space $F_a(\Omega)$ defined on Ω is the same as in the previous formulation, still suitable for $\mathbf{a}$ and $\mathbf{a}'$ in the magnetostatic case.

The spatial discretization for a *FE* implementation is thus based on edge elements as before, which approximate the vector field $\mathbf{a}$ and $\mathbf{a}'$ within the *FE* mesh.

In the continuous level, the following functional has to be cancelled at a given time step n to calculate the magnetic vector potential $\mathbf{a}_n$

$$\mathscr{F}_a(\mathbf{a}_n) := \left(\mathscr{H}(\mathbf{curl}\,\mathbf{a})\big|_n, \mathbf{curl}\,\mathbf{a}'\right)_\Omega + \langle \mathbf{n}\times(\mathbf{h}_s)_n, \mathbf{a}'\rangle_{\Gamma_h} - \left((\mathbf{j}_s)_n, \mathbf{a}'\right)_{\Omega_s}\,, \tag{5.39}$$

where $(\mathbf{h}_s)_n$ and $(\mathbf{j}_s)_n$ intervene in surface and volume source terms respectively.

The treatment of the problem (5.39) with linear, nonlinear, hysteretic or not, constitutive laws $\mathscr{H}(\mathbf{curl}\,\mathbf{a})$ is similar to the treatment presented for the dynamic case. With nonlinear behavior, an iterative *NR* method can be adopted to find subsequent fields $\mathbf{a}_n^i$, as described by (5.40), until convergence.

Magnetostatic a Formulation

At iteration i of the *NR* resolution, at time step n, find $\mathbf{a}_n^i \in F_a(\Omega)$ such that

$$\left.\frac{\partial \mathscr{F}_a}{\partial \mathbf{a}}\right|_{\mathbf{a}_n^{i-1}} \cdot \Delta\mathbf{a}_n^i = -\mathscr{F}_a(\mathbf{a}_n^{i-1})\,, \tag{5.40}$$

holds for suitable test functions $\mathbf{a}' \in F_a(\Omega)$; with $\Delta\mathbf{a}_n^i = \mathbf{a}_n^i - \mathbf{a}_n^{i-1}$ and where

$$\left.\frac{\partial \mathscr{F}_a}{\partial \mathbf{a}}\right|_{\mathbf{a}_n^{i-1}} \cdot \Delta\mathbf{a}_n^i = \left(\left.\frac{\partial \mathscr{H}}{\partial \mathbf{b}}\right|_n^{i-1} \mathbf{curl}\,\Delta\mathbf{a}_n^i, \mathbf{curl}\,\mathbf{a}'\right)_\Omega\,,$$
$$\mathscr{F}_a(\mathbf{a}_n^{i-1}) = \left(\mathscr{H}(\mathbf{curl}\,\mathbf{a})\big|_n^{i-1}, \mathbf{curl}\,\mathbf{a}'\right)_\Omega + \langle \mathbf{n}\times(\mathbf{h}_s)_n, \mathbf{a}'\rangle_{\Gamma_h} - \left((\mathbf{j}_s)_n, \mathbf{a}'\right)_{\Omega_s}\,.$$

As for the $\mathbf{a}-\nu$ formulation, this is the inverse form $\mathscr{H}^{inv}\left(\mathbf{curl}\,\mathbf{a}_n^{i-1}, (\mathbf{X}^k)_{n-1}\right)$, and the differential reluctivity tensors $\frac{\partial \mathscr{H}}{\partial \mathbf{b}}$ that are required for the inclusion of the *EB* hysteresis model in the magnetostatic $\mathbf{a}$ formulation. Moreover, the magnetic states $(\mathbf{X}^k)_n$ have to be updated at least at the end of each time step.

4. Improvements of the Nonlinear Resolution

4.1. About the Nonlinear Resolution

As already mentioned, after the spatial discretization of the *FE* method, which is not further detailed in this thesis, all the *NR* iterations used to solve the nonlinear problem associated to each investigated formulation (5.25), (5.29), (5.36), or (5.40), can be written under a generic form of a linear system to be solved in terms of the unknowns $\Delta\mathbf{x}_n^i = \mathbf{x}_n^i - \mathbf{x}_n^{i-1}$, such as

$$\underline{\boldsymbol{J}_{\mathbf{F}}}(\mathbf{x}_n^{i-1}) \cdot \Delta\mathbf{x}_n^i = -\mathbf{F}(\mathbf{x}_n^{i-1}), \tag{5.41}$$

where i and n, still indicating the *NR* iteration and the time step indices, and with

$$\mathbf{x} = \begin{pmatrix} x_{\text{dof1}} \\ \vdots \\ x_{\text{dof}M} \end{pmatrix}, \qquad \mathbf{F}(\mathbf{x}) = \begin{pmatrix} \mathbf{F}(\mathbf{x})|_{\text{dof1}} \\ \vdots \\ \mathbf{F}(\mathbf{x})|_{\text{dof}M} \end{pmatrix}, \qquad \underline{\boldsymbol{J}_{\mathbf{F}}}(\mathbf{x}) = \begin{pmatrix} \frac{\partial \mathbf{F}(\mathbf{x})|_{\text{dof1}}}{\partial x_{\text{dof1}}} & \cdots & \frac{\partial \mathbf{F}(\mathbf{x})|_{\text{dof1}}}{\partial x_{\text{dof}M}} \\ \vdots & \ddots & \vdots \\ \frac{\partial \mathbf{F}(\mathbf{x})|_{\text{dof}M}}{\partial x_{\text{dof1}}} & \cdots & \frac{\partial \mathbf{F}(\mathbf{x})|_{\text{dof}M}}{\partial x_{\text{dof}M}} \end{pmatrix},$$

where $\mathbf{x}$ is the vector of unknowns to be computed, of size M, which corresponds to the total number of degrees of freedom (*DOF*s) employed in the *FE* representation. The vector $\mathbf{x}$ thus gathers the coefficients associated to each *FE* basics function that allows to suitably construct the field of interest in the discretized space. In this generic representation, these coefficients can be related to the spatial representation of the fields $\mathbf{h}$, ϕ, $\overset{\star}{\mathbf{a}}$ or $\mathbf{a}$, depending on the magnetic formulation that is adopted. The vector $\mathbf{F}(\mathbf{x})$ is a nonlinear function from $\mathbb{R}^M$ to $\mathbb{R}^M$, that comes from the discretized representation in the *FE* basis functions of the defined functional $\mathcal{F}_h(\mathbf{h}), \mathcal{F}_\phi(\phi), \mathcal{F}_{\underset{a}{\star}}(\overset{\star}{\mathbf{a}})$ or $\mathcal{F}_a(\mathbf{a})$, according to the formulation that is used, either (5.24),(5.28),(5.35) or (5.39), from the continuous domain. It should be noted that these functions $\mathbf{F}$ include the source terms which change generally with time, such that, stricktly speaking, a subscript n should be added to $\mathbf{F}$, but this is not done for readibility concerns here. Lastly, $\underline{\boldsymbol{J}_{\mathbf{F}}}(\mathbf{x})$ is the Jacobian matrix of square size $M \times M$, associated to the *FE* system. It refers directly to the translation of the terms $\frac{\partial \mathcal{F}_h(\mathbf{h})}{\partial \mathbf{h}}$, $\frac{\partial \mathcal{F}_\phi(\phi)}{\partial \phi}$, $\frac{\partial \mathcal{F}_{\underset{a}{\star}}(\overset{\star}{\mathbf{a}})}{\partial \overset{\star}{\mathbf{a}}}$ or $\frac{\partial \mathcal{F}_a(\mathbf{a})}{\partial \mathbf{a}}$, depending on the formulation (5.25), (5.29), (5.36), or (5.40), in a *FE* context.

For a given time step n, the *NR* resolution (5.41) tries to approach the solution $\mathbf{x}_n^*$, which verifies $\mathbf{F}(\mathbf{x}_n^*) = \mathbf{0}$, through a succession of approximations $\mathbf{x}_n^i$. However, the convergence of this iterative process is by no means guaranteed. In case of strong nonlinearity or poor regularity of $\mathbf{F}(\mathbf{x})$, divergence is not unlikely, as already discussed in Chapter 4 for the inversion of the hysteresis material law.

Several factors affect strongly the behavior of the *NR* method for the resolution of the *FE* system and must be chosen wisely to improve convergence. The convergence criterion, the relaxation factor γ, the Jacobian matrix $\underline{\boldsymbol{J}_{\mathbf{F}}}$, the initial guess $\mathbf{x}_n^0$ and the time increment Δt_n, are among the most influencing factors that can be easily modified. The motivation and the rather advanced mechanisms behind their determination are given with more details in the following subsections dedicated to each of them.

4.2. Choice of a Stopping Criterion

The **convergence criterion** is evaluated at each iteration i and indicates wether or not the current estimation $\mathbf{x}_n^i$ of the solution $\mathbf{x}_n^*$ is sufficiently accurate. As soon as it is satisfied for an iterate i^*, the *NR* algorithm is stopped and the result from the current iterate $\mathbf{x}_n^{i^*}$ is saved as the solution $\mathbf{x}_n$ for time step n.

Since for the exact solution $\mathbf{F}(\mathbf{x}_n^*)$ is zero, in practice, a natural convergence criterion aims to stop the iterations as soon as a sufficiently small residual value is calculated over all the system functions with some norm, such as

$$\left\|\mathbf{F}(\mathbf{x}_n^i)\right\| < \epsilon_{\text{abs}}\,, \qquad \frac{\left\|\mathbf{F}(\mathbf{x}_n^i)\right\|}{\left\|\mathbf{F}(\mathbf{x}_n^0)\right\|} < \epsilon_{\text{rel}}\,, \tag{5.42, 5.43}$$

where the absolute and relative tolerances, ϵ_{abs} and ϵ_{rel}, are small numbers; the latter being dimensionless as compared to the ratio between residuals, calculated with the current and the initial iterates. The notation $r(\mathbf{x}_n^i)$, or even r_n^i, is generally used to denote the system residual value $\left\|\mathbf{F}(\mathbf{x}_n^i)\right\|$.

Another stopping criterion can be based on the increments between two iterates, $\Delta\mathbf{x}_n^i = \mathbf{x}_n^i - \mathbf{x}_n^{i-1}$, and be activated, for examples, when

$$\left\|\Delta\mathbf{x}_n^i\right\| < \epsilon_{\text{abs}}\,, \qquad \frac{\left\|\Delta\mathbf{x}_n^i\right\|}{\left\|\mathbf{x}_n^i\right\|} < \epsilon_{\text{rel}}\,. \tag{5.44, 5.45}$$

A more general stopping criterion can be defined as follow. For each component j of a quantity of interest $(u_j)_n^i$, an error ratio $(q_j)_n^i$ can be calculated at iteration i, at time step n, by

$$(q_j)_n^i := \frac{\left|(\Delta u_j)_n^i\right|}{\epsilon_{\text{abs}} + \epsilon_{\text{rel}}\left|(u_j)_n^i\right|}\,, \qquad \mathbf{q} = \begin{pmatrix} q_1 \\ \vdots \\ q_{N_j} \end{pmatrix}, \qquad \left\|\mathbf{q}_n^i\right\| < 1\,, \tag{5.46}$$

where $(\Delta u_j)_n^i = (u_j)_n^i - (u_j)_n^{i-1}$. This quantity of interest u_j can be, for example, associated to the *DOF*s of the system, such that u_j corresponds then to $x_{\text{dof}j}$, and the number of components N_j can be as high as M, such that all the *DOF*s used in the *FE* representation are taken into account to build the error ratio vector $\mathbf{q}$, which is thus of size M in that case. An overall error ratio can then be assessed by applying some norm on this vector. The *NR* method is stopped as soon as this vector norm $\left\|\mathbf{q}_n^i\right\|$ becomes smaller than 1. Building $\mathbf{q}$ with *DOF*s $\mathbf{x}_n^i$ in (5.46) gives a stopping criterion that is a kind of combination of (5.44) and (5.45), where both absolute and relative tolerances are taken into account simultaneously.

In the generic expression (5.46), the quantity $(u_j)_n^i$ can mean anything. It can be related to post-processing quantities, global quantities, energy terms, field components value of $\mathbf{h}$, ϕ, $\mathbf{b}$ or $\mathbf{a}$, as examples. The *NR* method is assumed to have converged as soon as the considered quantity no longer varies significantly from one iteration to another. In order to compare fairly the rate of convergence of the *NR* method between

different types of *FE* formulations, either **h**-conform or **b**-conform, it is necessary to use the same stopping criterion in both cases. For that reason, when a comparison between numerical performance of complementary formulations is achieved, it has been chosen to use the stopping criterion of (5.46) and to build the error based on the magnetic field components $(h_j)_n^i$ that generate the magnetic field in the discretized *FE* meshed domain. These quantity values are extracted and used both with **b**-conform and **h**-conform formulations. Using then a mean L^2-norm, the following stopping criterion is adopted by default in the following:

$$\tilde{r}_n^i := \sqrt{\frac{1}{N_j}\sum_{j=1}^{N_j}\left(\frac{|(\Delta h_j)_n^i|}{\epsilon_{\text{abs}}+\epsilon_{\text{rel}}|(h_j)_n^i|}\right)^2} < 1\,, \tag{5.47}$$

where $\tilde{r}_n^i$ is a dimensionless residual. The choice of the magnetic field components $(h_j)_n^i$ rather than another field is motivated by the typical magnetization curve shape. In general, but more precisely in saturation, large variations of **h** only cause smaller changes on **b**. Therefore, at equal tolerances, a criterion based on the components of **h** is stricter in nature than one based on **b**.

Other possible choices for the type of the error norm that can be used are:

$$\|\mathbf{q}\|_{L^1} = \sum_{j=1}^{N_j}|q_j|\,, \qquad \|\mathbf{q}\|_{L^2} = \sqrt{\sum_{j=1}^{N_j}|q_j|^2}\,, \qquad \|\mathbf{q}\|_{\infty} = \max(|q_j|)\,,$$

$$\|\mathbf{q}\|_{\text{Mean}L^1} = \frac{1}{N_j}\sum_{j=1}^{N_j}|q_j|\,, \qquad \|\mathbf{q}\|_{\text{Mean}L^2} = \sqrt{\frac{1}{N_j}\sum_{j=1}^{N_j}|q_j|^2}\,.$$

In order to go over problematic situations where the *NR* method struggles to satisfy the criterion, a **maximum number of iterations** i_{max} is also set. If this limit is reached, the result calculated at the last iteration, $\mathbf{x}_n^{i_{max}}$, is still saved as the solution for the current time step n, hoping that the error made is not problematic for the following time steps. With hysteretic material laws, this case is all the more dangerous as the solution of a time step depends on the magnetization states from the previous one, even in a static formulation. If the *NR* method fails to converge properly at a given time, an error of uncontrolled amplitude occurs and it may more or less seriously affect the solutions found for later times.

4.3. Computation of an Optimal Relaxation Factor

The introduction of a **relaxation factor** γ applied between two iterates, with

$$\mathbf{x}_n^i = \mathbf{x}_n^{i-1} + \gamma\Delta\mathbf{x}_n^i\,, \tag{5.48}$$

helps avoiding cycles or too large jumps between subsequent iterates with the aim to ensure convergence, but sometimes at the cost of a reduced convergence rate. The relaxation factor is usually chosen between $\gamma \in]0,1]$, and its value is the same for all the

unknowns. It can be fixed to a certain value for all the simulations or be determined specifically at each *NR* iteration so as to minimize the total residual r_n^i expressed with this new relaxed iterate value (5.48), such that

$$r_n^i(\gamma) \equiv r(\mathbf{x}_n^{i-1} + \gamma \Delta \mathbf{x}_n^i) = \left\| \mathbf{F}(\mathbf{x}_n^{i-1} + \gamma \Delta \mathbf{x}_n^i) \right\| . \tag{5.49}$$

This can be seen as an optimization problem of a one-dimensional objective function $r_n^i(\gamma)$ in terms of the relaxation factor γ.

Line search methods such as the golden section, or any other similar techniques can be investigated, but this takes significant additional computational time to evaluate the residual at each new tested factor, as discussed in [82]. However, a residual evaluation with (5.49) remains in any cases faster than a complete system resolution from (5.41). So sometimes, it is worth taking some computational time to determine a good relaxation factor, if it then saves some, by making the *NR* iterations more effective in getting closer to the solution faster. Nevertheless, finding the exact value γ_{opt} that minimizes the residual is not needed and a compromise between improving the *NR* convergence without excessively increasing the computation cost is desired. Therefore, different simple strategies have been adopted in the search of sufficiently appropriate γ values.

- **Standard Search Technique**
  This is a very naive technique, similar to the naive line search used in the *var* approach (Fig. 3.6 (left)), which consists in searching a relaxation factor γ that minimizes the residual $r_n^i(\gamma)$, testing different factors following a decreasing geometric progression

  $$\gamma_{[m]} = \frac{1}{\varphi^m} , \tag{5.50}$$

  with $m = 0, 1, \ldots, m_{\max}$ and the factor φ is the common ratio of the progression, generally chosen equal to the golden ratio or to $\varphi = 2$ as in [82, 91]. The strategy starts to evaluate the residual with $\gamma_{[0]} = 1$, and then with the following factors in the order given by (5.50). The algorithm is stopped as soon as the objective function $r_n^i(\gamma_{[m]})$ finishes to decrease and that an increase is detected between two subsequent tested factors, $r_n^i(\gamma_{[m+1]}) > r_n^i(\gamma_{[m]})$, as illustrated in Fig. 5.1 (left) with $\varphi = 2$, and where $\gamma_{[2]} = 0.25$ is selected at the end of the procedure. A maximum number $m_{\max}$ can be fixed to stop the algorithm if no increase is detected in the discrete range of values tested.

  A possible variant consists in a decreasing arithmetic progression for the relaxation factors instead of (5.50), such as

  $$\gamma_{[m]} = 1 - d\,m , \tag{5.51}$$

  with $m = 0, 1, \ldots, m_{\max}$. The factor d is the common difference of the progression, and one must have $d\,m_{\max} < 1$ to always have $\gamma > 0$. Using this evolution with $d = 0.1$, on the second example of Fig. 5.1 (right), the procedure would stop at the first detected local minima and select $\gamma_{[2]} = 0.8$.

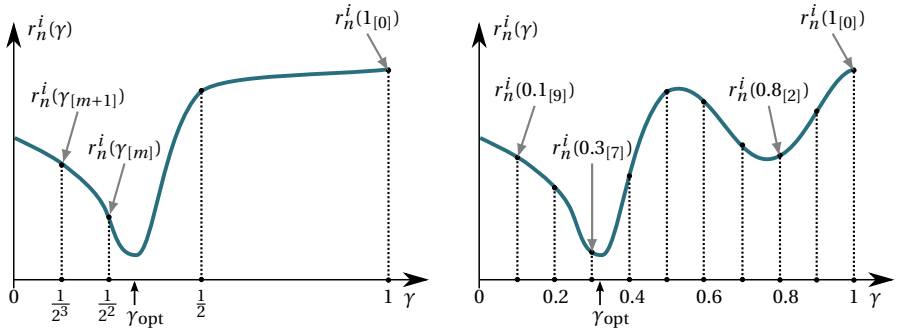

Figure 5.1: *Illustration of $r_n^i(\gamma)$ curves and search of suitable relaxation factors γ. (left): Standard search technique with a division by two between succesive tested factors $\gamma_{[m]}$, started from $\gamma_{[0]} = 1$, until an increase in $r_n^i(\gamma_{[m]})$ is detected. The final value with $m = 2$, that is $\gamma_{[2]} = 0.25$, is found here. (right): Heavy search technique with 10 evenly spaced factors tested from 1 to 0.1, and the optimal one among them is taken, thus $\gamma_{[7]} = 0.3$ here. Conversely, with a standard search technique spanning the same $\gamma_{[m]}$ values, starting from $\gamma_{[0]} = 1$ and decreasing linearly by step of 0.1, the algorithm would stop faster but at the less optimal value $\gamma_{[2]} = 0.8$ instead.*

- **Heavy Search Technique**
  Another less ingenious strategy consists in calculating the residuals for a whole set of chosen relaxation factors distributed between $]0, 1]$. These points can be separated, for examples, logarithmically as in (5.50) or linearly as in (5.51). The procedure tries all the $m_{\max} + 1$ relaxation factors from the given list and calculates the corresponding residual value for all of them. Then, the factor $\gamma_{[m]}$ that gives the smallest residual value among the others is kept. Applying this heavy search technique on the example of Fig. 5.1 (right), by trying 10 relaxation factors equally spaced between 1 and 0.1, allows to find $\gamma_{[7]} = 0.3$, which is rather close to the exact optimal value γ_{opt} in that example.

  Compared to the standard one, this technique can thus be more robust in general, with a better chance of approaching the global minimum by probing all the relaxation factors without stopping prematurely, but requires of course much more computational effort.

- **Accelerated Search Technique**

  Instead of looking for the relaxation factor γ that minimizes simply the residual, this technique aims to find the maximum relaxation factor for which the residual still decreases. Starting from an initial factor $\gamma_{[0]}$, the method works as follow:

  – The relaxation factor is multiplied by a ratio, $\gamma_{[m]} = \varphi\gamma_{[m-1]}$, as long as the corresponding residual decreases, i.e. $r_n^i(\gamma_{[m]}) < r_n^i(\gamma_{[m-1]})$.

  – On the other hand, if the objective function increases with a ratio-multiplied factor, i.e. $r_n^i(\varphi\gamma_{[m-1]}) > r_n^i(\gamma_{[m-1]})$, the factor cannot be increased, and is instead divided by the same ratio, $\gamma_{[m]} = \frac{\gamma_{[m-1]}}{\varphi}$, until a decreasing residual is found between two subsequent steps, such that $r_n^i(\gamma_{[m]}) < r_n^i(\gamma_{[m-1]})$.

Contrary to the heavy search technique, the relaxation factors are deduced quite rapidly here, without requiring too much residual evaluations. With this accelerated search technique, the relaxation factor can sometimes take values higher than 1, leading to over-relaxation of the *NR* method. The increments between two *NR* iterations are thus generally bigger in average than with the two other search techniques. The solution of a given time step is then expected to be approached in less *NR* iterations with such relaxation factors, but at the cost of a loss of general robustness, due to the favoring of large increments that may be too brutal in some situations. In other word, the accelerated relaxation factor search technique allows convergence to be achieved more quickly but it reduces the stability of the *NR* method.

4.4. Evaluation of a Jacobian Matrix

There is some freedom in the choice of the **Jacobian matrix** $\underline{\boldsymbol{J}_{\mathbf{F}}}(\mathbf{x})$ of the *FE* system (5.41), which can be replaced by other approximated matrices if the exact Jacobian derivation proves impossible or computationally inefficient since at the end, only the convergence of the iterative process matters. The analytical and numerical Jacobian determinations are distinguished here after and some approximated Jacobian matrix updates strategies are mentioned.

- **Analytical Jacobian Matrix**
  The Jacobian matrix $\underline{\boldsymbol{J}_{\mathbf{F}}}(\mathbf{x})$ in (5.41) relies on partial derivatives of the nonlinear functions $\mathbf{F}(\mathbf{x})$ In the classical *NR* approach, it is assumed that the analytical expressions of these derivatives are made available based on the functions $\mathbf{F}(\mathbf{x})$, so that the Jacobian matrix can be evaluated analytically. The Chapter 4 showed that, provided that standard analytical laws are used for the anhysteretic curve, analytical expressions can be deduced for the derivatives involved in the construction of the Jacobian matrix, even with the *EB* hysteresis model.

- **Numerical Jacobian Matrix**
  If analytical expressions do not exist, it is still possible to estimate numerically the Jacobian matrix components by finite differences. Moreover, as discussed in Chapter 4, such approximations can be interesting for simulations with hysteresis since, in this situation, the functions $\mathbf{F}(\mathbf{x})$ present angular points so that the exact derivatives could lead to oscillations of the classical *NR* method without relaxation. On the other hand, approximating the derivatives by finite differences can help to average out the slopes changes around angular points and thus may improve the convergence behavior of the iterative process.

  Numerical differentiations techniques of the Jacobian matrix components can be based, for example, either on forward or central difference formulae. They require additional evaluations of the functions $\mathbf{F}(\mathbf{x})$, which are time consuming, especially in presence of computationally costly hysteresis models. Central differences require more functions evaluations than forward differences. Nevertheless, it has been observed in practice that the use of the former instead of the

latter is essential with the *EB* hysteresis model, as it offers better stability for the *NR* method.

Moreover, in general, the choice of the step value to calculate the differences is delicate. A too small step size can introduce numerical cancellation errors while a too large one increases the truncation error of the derivative approximation [86]. The determination of an optimal step size for a given problem is computationally expensive and the resulting benefits are unjustifiable since small deviations in the Jacobian elements values have, most of the times, minor impacts on the *NR* process. Therefore, the adaptation of the step size of the finite difference approximations is not attempted here and a constant step size is used with numerical Jacobian evaluations. The size is chosen empirically in such a way to be satisfactory to the problem characteristics.

- **Approximated Jacobian Matrix Updates**

  There exist other variations of the classical *NR* method which are based on different evaluations of the Jacobian matrix.

  For example, since an exact Jacobian evaluation is not mandatory, the matrix can be updated only at the first iteration and then kept unchanged for the following iterations. This allows thus to reduce the cost of the Jacobian determinations for a given time step, but may increase the number of iterations needed before convergence.

  Quasi-Newton methods update schemes, such as those from the Broyden family presented in Chapter 4, can be generalized at the *FE* system level to approximate the current Jacobian matrix at each iteration based on the value from the previous one, making its construction lighter by reducing also the number of model function calculations needed. This can be more stable in some situations, but may also reduce the convergence rate.

  In [53], it is proposed to use, as a substitute for the Jacobian matrix, an identity matrix multiplied by the mean value of the maximum and minimum diagonal elements values of the standard Jacobian matrix. The matrix is updated only at the beginning of each time step and then remains unchanged for the following iterations. In appropriate conditions, it can produce stable solutions, requiring more iterations but consuming relatively the same total computational time than a classical *NR* method.

  The update strategies mentioned here have not been, or only partially, investigated in presence of the *EB* hysteresis model. Yet, in some preliminary tests with the *EB* model, these light update methods have shown some limits by diverging fairly quickly. Further study is required to draw conclusions and this is why they are not discussed further in this thesis.

4.5. Initialization using a Prediction of the Solution

The choice of the **initial guess** $\mathbf{x}_n^0$ is, finally, of high importance. A first estimate closer to the solution helps reducing the number of iterations needed to reach a given level of

accuracy. Sufficiently close to the exact solution, the *NR* method converges quadratically. On the other hand, if selected too far from the solution, the first iterate of the *NR* method may then lead to a sequence that fails to converge.

The most obvious way to initialize the *NR* method for a given time step is to start directly from the result of the previous time step. However, it is possible to envisage more advanced predictions based on the interpolation of several previous time solutions, and to extrapolate to the current time, in order to draw more information on the evolution trend of the unknown field.

To this end, Lagrange interpolating polynomials are built based on the previous time step solutions. In this description, initializations based on the previous time step only, i.e. $\mathbf{x}_n^0 = \mathbf{x}_{n-1}$, are seen as extrapolations of zero-degree polynomial (constant), as illustrated in Fig. 5.2 (left) for a given *DOF* of the *FE* system. A first-degree polynomial (linear) can be built from the last two previous time solutions, $\mathbf{x}_{n-1}$ and $\mathbf{x}_{n-2}$, from which it is possible to deduce, by linear extrapolation, a first guess of the current solution $\mathbf{x}_n^0$, as shown with Fig. 5.2 (middle). Continuing in the same idea, a second-order polynomial (quadratic) can be formed based on the three previous time solutions, $\mathbf{x}_{n-1}$,$\mathbf{x}_{n-2}$ and $\mathbf{x}_{n-3}$, and give, by quadratic extrapolation, another initial estimation for $\mathbf{x}_n^0$ to begin the current time step, as represented on Fig. 5.2 (right).

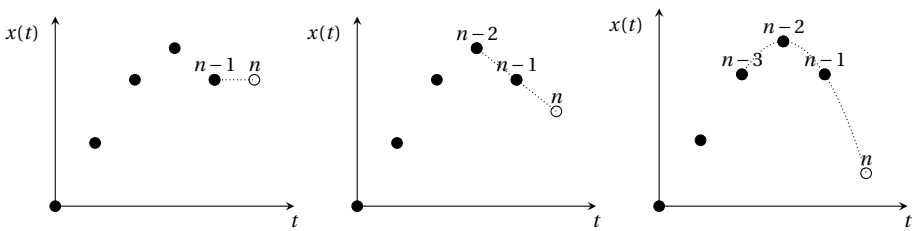

Figure 5.2: *Extrapolating predictions with polynomial of different degrees for a given DOF x(t). Black nodes represent previous time solutions and white nodes are the initial estimate of the current time step. to begin the NR method (left): Degree 0: initialization at the previous time solution. (middle): Degree 1: linear extrapolation from the two previous time solutions. (right): Degree 2: quadratic extrapolation from the three previous time solutions.*

Naturally, quadratic extrapolations are expected to generate initial estimations much closer to the exact solutions, so that the *NR* method converges in fewer iterations than if started from the last time step solution only.

Interpolations of higher degrees, with more previous data solutions, can still be considered but are not interesting in practice since the higher the degree of these polynomials, the greater the oscillations they will exhibit between the data points, and thus the poorest their extrapolating predictions will be.

4.6. Use of an Adaptive Time Increment

The **time increment** between two time steps, $\Delta t_n = t_n - t_{n-1}$, also affects the initial guess of the *NR* method, as it is related, at least, to the previous time step solution

$n-1$, and thus impact the convergence rate.

The smaller the time increment, the smaller the variations of the external sources in the formulation, and thus the smaller the change in the solution between two time steps, such that the *NR* method is likely to converge in less iterations for a given level of accuracy. In the limit case where changes become linear between sufficiently small time steps, the *NR* method is expected to converge in one iteration in regular conditions. However, the smaller the time increment, the larger the number of time steps that have to be calculated to reach a given final time in the simulation.

Therefore, it is possible to adopt an adaptive time increment strategy in order to modify the time increment for certain time steps, such that Δt_n are not necessarily constant, leading to not equidistant time steps.

This modification can be applied interactively during the simulation. For example, if the *NR* method fails for a given time step, it may be salutary to start again from the solution of the previous time step and to reduce the current time increment in order to calculate the solution at a time closer to the previous known solution, with the idea of facilitating the convergence of the *NR* method. If this new time increment is still problematic for the *NR* method, the strategy can be repeated by restarting from the last converged solution, decreasing the time increment again, and trying to recalculate a solution, thus even closer to the previous one.

Naturally this strategy has some limitations since it cannot be repeated indefinitely if the *NR* remains unsuccessful after several attempts because the time increment becomes always smaller and smaller. Without any lower time increment limit set, the simulation can thus hardly advance any further in time and stagnate.

Conversely, for time steps where the *NR* method converged sufficiently fast, i.e. with a fairly small number of iterations, this indicates that the evolution of the unknown field between the two previous time steps has been practically linear. Since there is no reason in sampling in time the field more than necessary in such circumstances, it may be wise to increase the time increment for the current time step. With larger time steps, the simulation can thus be completed more quickly. One again, this can be repeated for the next time steps, by continuing to increase the time increments, as long as the *NR* method converge without difficulty.

Of course these time increments should not become too large in order to keep a correct time discretization, especially with the influence of derivatives in the formulation or in presence of hysteresis models that depend on the magnetization states of the previous time steps. A maximum limit for the time increments is therefore mandatory.

In summary, the flexibility of the time increments Δt_n is a wonderful tool that allows to influence dynamically on the convergence of the *NR* method, and, more generally, on the resolution speed of time-stepping simulations.

CHAPTER

6 Parameter Identification

THIS chapter illustrates how the statistical distribution of pinning fields in a ferromagnetic material can be identified straightforwardly from standard magnetic measurements, i.e. Epstein frame [106] or single sheet tester (*SST*) [107]. An automatic discretization technique of the statistical distribution is then presented in order to extract the cell parameters to construct the energy-based (*EB*) hysteresis model associated to the material. Measurements and *EB* model predictions are then compared for validation purposes.

1. Identification of the Pinning Field Probability Density

In the continuous decomposition of the multi-cells *EB* model discussed in Chapter 2-Section 5, the memory of the material can be represented by the distribution of the reversible magnetic field $\mathbf{h}^*_{\text{rev}}(\lambda)$. It is remarkable that the pinning field probability density, denoted by $\zeta(\lambda)$, can actually be identified from standard Epstein (or *SST*) measurements. As the loading is always unidirectional in such measurements, it is the modulus of the fields $h = |\mathbf{h}|$ and $h^*_{\text{rev}} = |\mathbf{h}^*_{\text{rev}}|$ that are used throughout this section.

Starting from the demagnetized state (wiped-out memory state), being the state with $h^*_{\text{rev}}(\lambda) = 0, \forall \lambda$, a unidirectional magnetic loading from $h = 0$ until $h = h_{\text{A}}$ is first applied to the material. As the magnetization behavior of each individual cell verifies (2.29) and behaves similarly as in Fig. 2.4 (left) for unidirectional loading, the microscopic λ-regions whose magnetic state is modified by this increasing loading are those for which $\kappa^*(\lambda) < h_{\text{A}}$ and one has for them, at the end of the loading, $h^*_{\text{rev}}(\lambda) = h_{\text{A}} - \kappa^*(\lambda)$, the other $h^*_{\text{rev}}(\lambda)$ remaining zero. The homogenized macroscopic reversible field, based on (2.33), is then

$$h_{\text{rev}}(0 \rightarrow h_{\text{A}}) = \int_0^\infty \zeta(\lambda)\ \max(h_{\text{A}} - \kappa^*(\lambda), 0)\, d\lambda\,. \tag{6.1}$$

Note that this is the homogenization by the magnetic field (Chapter 2-Section 5.2) which is exploited here, whereas the homogenization by the energy balance (Chapter 2-Section 5.1) has been used behind the *EB* model in all the calculations presented

so far. This alternative homogenization strategy is chosen here in order to express the homogenized reversible field as an integral of each weighted reversible field contribution as in (6.1), which is a starting point in the proposed parameter identification procedure.

Writing $\kappa^*(\lambda) = \lambda\kappa_{\text{unit}}$, where κ_{unit} is a constant factor expressed in units of the magnetic field, introduced for units consistency, and which can be arbitrary fixed at $\kappa_{\text{unit}} = 1\,\text{A/m}$, one can proceed to a variable substitution in the integral (6.1) and write

$$h_{\text{rev}}(0 \to h_{\text{A}}) = \int_0^\infty \omega(\kappa^*)\ \max(h_{\text{A}} - \kappa^*, 0) d\kappa^*\,, \tag{6.2}$$

where $\omega(\kappa^*) = \frac{\zeta(\kappa^*/\kappa_{\text{unit}})}{\kappa_{\text{unit}}}$ is a weighting function equivalent to the probability density function $\zeta(\lambda)$, but expressed in terms of the pinning field values κ^* instead of the dimensionless factor λ. The function $\omega(\kappa^*)$ has then the units of the inverse of the magnetic field (m/A). Additionally, the expression in (6.2) can be rewritten simply by

$$h_{\text{rev}}(0 \to h_{\text{A}}) = F(h_{\text{A}})\,,$$

with the definition of an auxiliary function

$$F(h) := \int_0^h \omega(\kappa^*)\ (h - \kappa^*) d\kappa^*\,, \tag{6.3}$$

measured in A/m, whose first and second derivatives with respect to the magnetic field give respectively

$$\partial_h F(h) = \int_0^h \omega(\kappa^*) d\kappa^*, \qquad \partial_h^2 F(h) = \omega(h)\,, \tag{6.4, 6.5}$$

where the former is dimensionless and the latter is expressed in m/A.

6

Starting over from the state at field h_{A}, the material is now unloaded until the magnetic field reaches $h_{\text{B}} < h_{\text{A}}$, always along the same direction. The microscopic λ-regions involved in the unloading are those such that $h_{\text{B}} + \kappa^*(\lambda) < h_{\text{A}} - \kappa^*(\lambda)$, i.e. $\kappa^*(\lambda) < (h_{\text{A}} - h_{\text{B}})/2$. Integrating directly over all κ^* values, the homogenized reversible field at the end of the loading process can then be expressed by

$$\begin{aligned}
h_{\text{rev}}(0 \to h_{\text{A}} \to h_{\text{B}}) &= \int_0^\infty \omega(\kappa^*) \min(h_{\text{B}} + \kappa^*, \max(h_{\text{A}} - \kappa^*, 0))\ d\kappa^* \\
&= \int_0^{\frac{h_{\text{A}} - h_{\text{B}}}{2}} \omega(\kappa^*)(h_{\text{B}} + \kappa^*)\ d\kappa^* + \int_{\frac{h_{\text{A}} - h_{\text{B}}}{2}}^{h_{\text{A}}} \omega(\kappa^*)(h_{\text{A}} - \kappa^*)\ d\kappa^* \\
&= \int_0^{h_{\text{A}}} \omega(\kappa^*)(h_{\text{A}} - \kappa^*)\ d\kappa^* - 2\int_0^{\frac{h_{\text{A}} - h_{\text{B}}}{2}} \omega(\kappa^*)\Big(\frac{h_{\text{A}} - h_{\text{B}}}{2} - \kappa^*\Big)\ d\kappa^* \\
&= F(h_{\text{A}}) - 2F(\frac{h_{\text{A}} - h_{\text{B}}}{2}).
\end{aligned}$$

The auxiliary function F, whose second derivative is the sought distribution $\omega(\kappa^*)$, as depicted by (6.5), plays thus a central role here. If F can be identified, then ω is also determined in principle.

The virgin curve of the material, which can be assimilated to the first magnetization curve as discussed in Chapter 1-Section 1.4, is simply the composition of the anhysteretic curve with F, based on (2.35), from the homogenization by the magnetic field:

$$J_{\text{virgin}}(h) = J_{\text{an}}\Big(h_{\text{rev}}(0 \to h)\Big) = J_{\text{an}}\Big(F(h)\Big). \tag{6.6}$$

This relationship could serve as a basis for the identification of F. However, the anhysteretic curve is not part of standard magnetic measurement setups (Epstein or *SST*) and its determination is discussed in Chapter 6-Section 3. Therefore, an identification strategy independent of J_{an} is preferable. To find one, it is first noted that the coercive field $h_c(h)$ of a hysteresis loop of magnitude h is characterized by

$$J_{\text{an}}\Big(h_{\text{rev}}(0 \to h \to -h_c(h))\Big) = 0,$$

which implies

$$F(h) - 2F\Big(\frac{h + h_c(h)}{2}\Big) = 0. \tag{6.7}$$

The coercive field characteristic $h_c(h)$ can be obtained from the measurement of a series of symmetric hysteresis loop of increasing amplitude in unidirectional conditions. Fig. 6.1 depicts the measured $h_c(h)$ characteristics for five different non-grain-oriented (*NGO*) electrical steel grades. The measurements have been realized with the standard Epstein frame protocol [106], where the magnetic core is a stack of strips taken alternatively in the rolling direction (*RD*) and the transverse direction (*TD*), so as to average out the material's anisotropy. During the measurements, the magnetizing field is changed in a continuous fashion with a $\frac{\mathrm{d}b}{\mathrm{d}t}$ rate below 100 mT/s, as slowly as reasonable to avoid eddy-current effects and to produce quasi-static hysteresis loops.

Remarkably enough, the $h_c(h)$ characteristics of a material contains enough information to completely identify the function F, and hence the pinning field probability density $\omega(\kappa^*)$ of the material.

From a mathematical point of view, the coercive field characteristic has the following properties:

i $h_c(0) = 0$,
ii $\exists h_s : h_c(h) = h_{c,\max}\ \forall h > h_s$,
iii $h_c(h) < h$.

Property (i) tells indeed that $F(0) = 0$. From (ii), one sees that $F(h) = h - h_{c,\max}, \forall h > h_s$. Finally, (iii) implies that the series defined by

$$x^n = \frac{x^{n-1} + h_c(x^{n-1})}{2} < x^{n-1} \tag{6.8}$$

is strictly decreasing. Starting from an arbitrary initial value $x^0 > h_s$, for which it is known that $F(x^0) = x^0 - h_{c,\max}$, the value of F for all subsequent terms of the series is

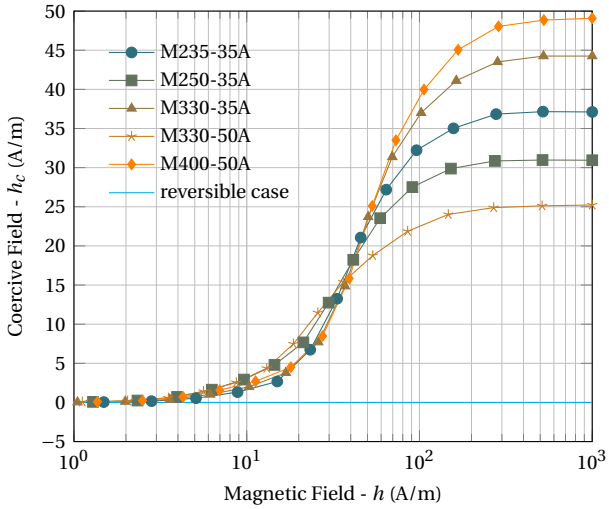

Figure 6.1: *Coercive field $h_c(h)$ of symmetrical hysteresis loops measured for five different non-oriented electrical steel grades.*

recursively given by $F(x^n) = F(x^{n-1})/2$, exploiting (6.7). Clearly, the series converges towards $F(0) = 0$.

The coercive field characteristic and the series $F(x^n)$ are detailed for the material M235-35A in Fig. 6.2. The coercive field characteristic is interpolated linearly in the measurement range $[h_{\min}, h_{\max}]$, and it is extrapolated as follows

$$h_c(h) = h_{c,\max} \quad \text{if} \quad h > h_{\max}\,,$$
$$h_c(h) = h_{c,\min}\left(\frac{h}{h_{\min}}\right)^2 \quad \text{if} \quad h < h_{\min}\,,$$

for field values outside the measurement range. The quadratic extrapolation at low fields is the one that has been observed to give the best results. One sees in Fig. 6.2 (left) that it prolongates reasonably the general shape of the characteristic, which was measured from $h_{\min} = 5.11\,\text{A/m}$.

With a properly inter- and extrapolated $h_c(h)$ characteristic, the iteration (6.8) can be carried out in order to produce the curve $F(h)$ in Fig. 6.2 (right). As it is a geometric progression, the points of the series are more or less equidistant in a logarithmic scale. One sees that the function $F(h)$ is rather smooth and its asymptotic behavior is also perfectly well defined

$$F(h) = h - h_{c,\max} \quad \text{if} \quad h > h_{\max}\,,$$
$$F(h) = \alpha h \quad \text{if} \quad h < h_{\min}\,,$$

where α is a scalar material-dependent constant. In between these two asymptotic behaviors, the curve $F(h)$ contains all information about the pinning field probability density $\omega(\kappa^*)$.

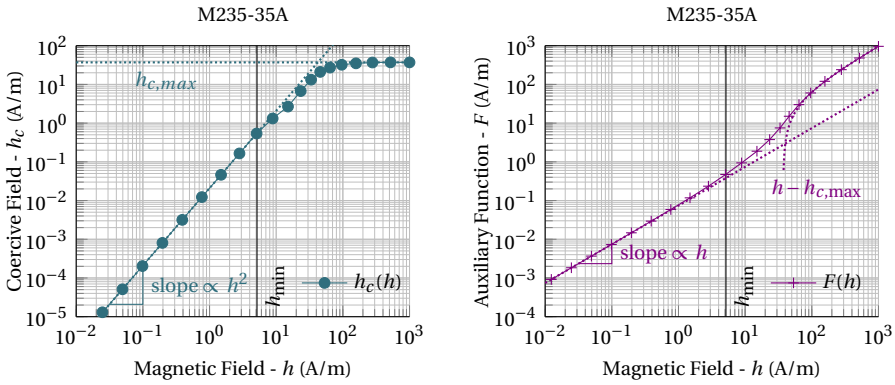

Figure 6.2: *Coercive field characteristic $h_c(h)$ (left) and function $F(h)$ (right) for the steel grade M235-35A, in logarithmic scale. The asymptotic behaviors are indicated with dotted lines for both curves. The vertical line at $h_{\min}$ indicates the lower bound of the measurement range.*

The constructed auxiliary function $F(h)$ for the material M235-35A is also plotted in linear scale in Fig. 6.3 (left). The reversible case, for which there is no remaining coercive field by defintion, is also drawn. It corresponds naturally to a straight line of unitary slope since the homogenized reversible field $F(h)$ coincides simply to h in this situation. The hysteresis irreversibility has the effect of delaying the increase of $F(h)$, before reaching the same evolution rate as the reversible curve at higher fields, but lowered by $h_{c,\max}$ for a given h.

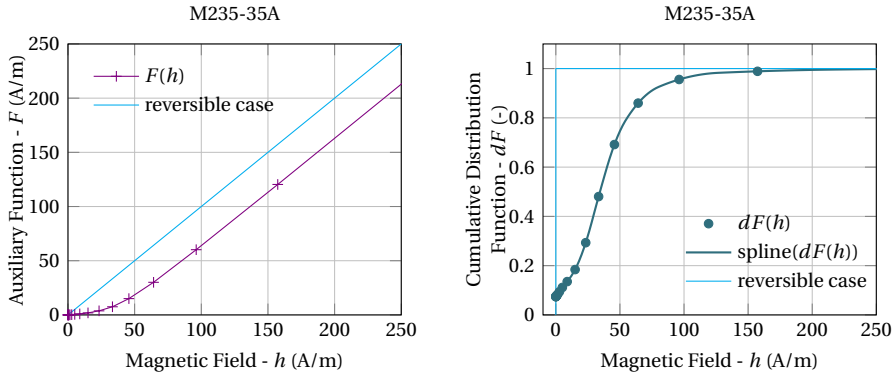

Figure 6.3: *(left): Function $F(h)$ for the steel grade M235-35A, in linear scale; (right): Corresponding pinning field cumulative distribution function $\partial_h F(\kappa)$, with, for illustration purpose, its spline interpolation based on the points $\partial_h F(x^j)$.*

As the curve is smooth, the first and second derivatives of $F(h)$ can be evaluated at the

series points x^k by finite differences with sufficient accuracy.

$$\partial_h F(x^j) = F(x^j)\frac{\Delta_2 - \Delta_1}{\Delta_1 \Delta_2} + F(x^{j+1})\frac{\Delta_1}{\Delta_2 \Delta_3} - F(x^{j-1})\frac{\Delta_2}{\Delta_1 \Delta_3}$$
$$\partial_h^2 F(x^j) = 2\left(\frac{F(x^{j-1})}{\Delta_1 \Delta_3} - \frac{F(x^j)}{\Delta_1 \Delta_2} + \frac{F(x^{j+1})}{\Delta_2 \Delta_3}\right)$$

with

$$\Delta_1 = x^j - x^{j-1} \quad , \quad \Delta_2 = x^{j+1} - x^j \quad , \quad \Delta_3 = x^{j+1} - x^{j-1}$$

and

$$\partial_h F(x^0) = 1 \quad , \quad \partial_h^2 F(x^0) = 0.$$

Fig. 6.3 (right) presents a spline interpolation of the derivative of F based on the points $\partial_h F(x^j)$ deduced by such finite differences. This function is the primitive of $\omega(\kappa^*)$, (6.4), and hence the cumulative distribution function of the pinning field, which means that $\partial_h F(\kappa^*)$ indicates the probability that the pinning field is lower than h. It reaches the asymptotic value one for $\kappa^* \approx 200\,\mathrm{A/m}$ in this example, which means that all pinning fields in the material are weaker than that value. Interestingly, the non-zero value at zero magnetic field indicates that about 10 % of the microscopic regions have a zero pinning fields, i.e. behave reversibly. The cumulative distribution function of a pure reversible material is indeed $\partial_h F = 1$ and is also shown in Fig. 6.3 (right).

The identification procedure has been applied to five *NGO* electrical steel grades, which are, namely, M235-35A (3.2 wt% Si), M250-35A (3.2 wt% Si), M330-35A (2.4 wt% Si), M330-50A (3.2 wt% Si), and M400-50A (3.2 wt% Si). Their measured coercive field characteristics $h_c(h)$ have already been shown in Fig. 6.1, while their associated pinning field cumulative distribution functions $\partial_h F(\kappa^*)$, and their pinning field probability densities $\omega(\kappa^*)$ are depicted in the following Fig. 6.4 and Fig. 6.5, respectively.

In Fig. 6.4, all cumulative distribution functions $\partial_h F(\kappa^*)$ start with a non-zero reversible component associated to a zero pinning strength and then tend to the unitary value at high field, when all pinning fields become unlocked. In Fig. 6.5, each grade has its own characteristic pinning field distribution $\omega(\kappa^*)$. They all include a non-zero amount $\omega(0)$ of reversible nature and present a maximal probability density for some specific pinning field quantity, before reducing to zero for higher pinning fields. The peak values and the standard deviations in the probability densities vary from one material to another.

Actually, these differences find their origin in the microstructure of the materials [23, 68]. The material characteristics are influenced in particular by the grain size, the dislocation density in the material structure, and the lamination thickness, among other factors. For example, a decrease in the average grain size affects the domain wall movement and thus the coercive force, as discussed at the end of Chapter 1-Section 1.3 and in Appendix B-Section 2. Basically, the pinning field distribution of a magnetic material can be seen as the identity card of its irreversible nature which is correlated with its internal composition [104, 120].

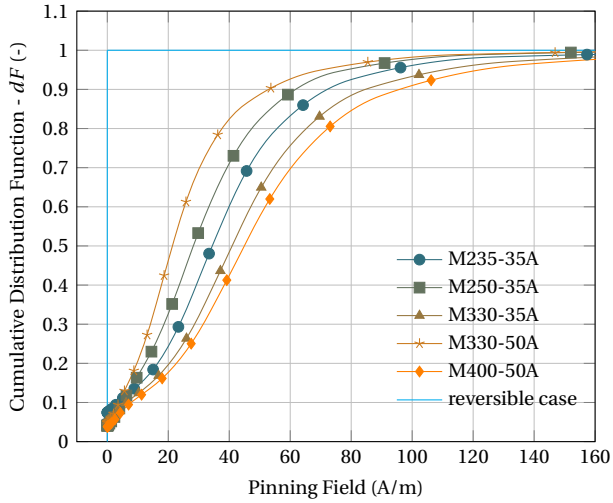

Figure 6.4: *Pinning field cumulative distribution function $\partial_h F(\kappa^*)$ for five different steel grades.*

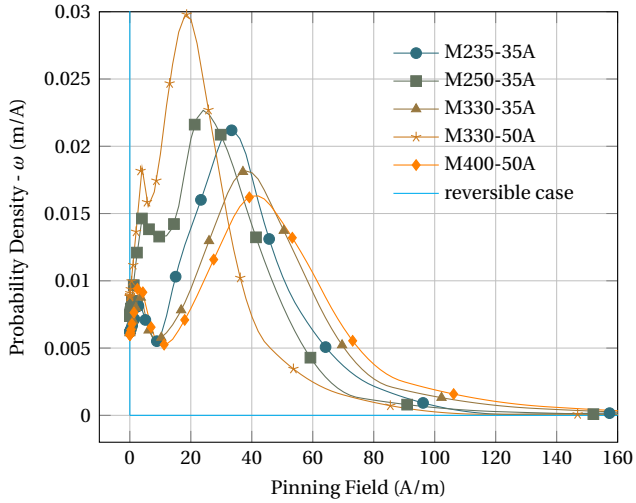

Figure 6.5: *Identified pinning field probability density $\omega(\kappa^*)$ for five different steel grades.*

More specifically, for the five electrical steel grades considered here, which are M235-35A (●), M250-35A (■), M330-35A (▲), M330-50A (★) and M400-50A (◆), it has been experimentally observed in [120] that they are made up of average grain size of about 100 µm, 109 µm, 87.5 µm, 122 µm and 70 µm, for each material respectively. Moreover, in the standardized steel nomenclature, the last two digits of the name denote the rated thickness of the electrical sheet in mm multiplied with one hundred, such that the three first lamination materials are 350 µm thick, and the two last are 500 µm thick.

For instance, M235-35A (●) and M250-35A (■) materials have the same alloy and same

thickness but the former has grains of slightly smaller size in average than the latter, such that its pinning field probability density is shifted to higher pinning field values in Fig. 6.5. Indeed, a structure with small grains cumulates a larger grain boundary surface where local impurities can preferably settle with the effect of increasing the local coercive forces [17, 127]. This statement is also verified with the M330-50A material (⋆), which has the largest average grain size and a homogeneous grain structure that tend to reduce the pinning field strengths and the width of the distribution curve in Fig. 6.5. A decrease in lamination thickness, which influences somehow the dislocation densities, leads to additional effects on the coercive force. For example, M330-35A (▲) has the same alloy, but a reduced thickness and a reduced average grain size than M330-50A (⋆). Its pinning field distribution has thus a larger standard deviation due to an inhomogeneous grain structure, with a wider variety in grain sizes. In general, the richness of the grain size spectrum in the microstructure is correlated with the spreading of the pinning field distribution. Similar observations can be done for the material M400-50A (◆), which have the smallest average grain size, and thus a displacement of its pinning field distribution peak to the highest pinning field values.

Even if the anisotropy of the *EB* hysteresis model has not been studied in this thesis, it is interesting to analyze the influence of the different stacking methods to see the modifications in the pinning field distribution function along *RD* or *TD*. Due to the rolling process, the grains are enlarged or stretched in *RD*. Therefore, for the same M235-35A material, one can measure in *RD* an average grain size of about 105 µm, with a small standard deviation, whereas in *TD*, one gets 89 µm, with a larger standard deviation [120]. According to the previous observations, this microstructure variation is expected to be reflected in the different peak values and shapes of the pinning field distribution functions.

For that purpose, the Epstein frame can be prepared with all strips in *RD*, or all strips in *TD*. The results depicted in Fig. 6.6 and Fig. 6.7 are then obtained, and compared with those obtained with the standard alternate *RD*-*TD*-*RD*-*TD* setup, already used by default previously, and here labeled with *RTD*. This example illustrates that the identified pinning field probability density can be strongly influenced by the anisotropy, despite the material is *NGO* basically. In combination with an orientation distribution function, which describes the magneto-crystalline texture, the direction-dependence can be taken into account in the model parameters to develop an anisotropic *EB* vector hysteresis model. Such extension of the *EB* model is attempted in [198], but is not discussed further here.

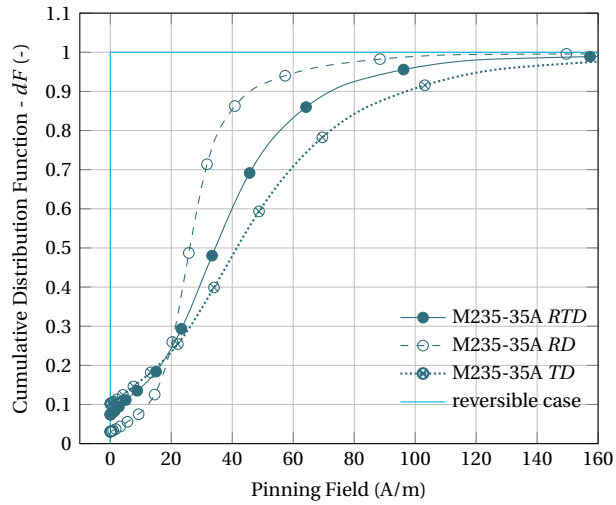

Figure 6.6: *Spline interpolation of the pinning field cumulative distribution function $\partial_h F(\kappa)$ based on the points $\partial_h F(x^j)$ for M235-35A in RD, TD and the standard alternate Epstein stacking (RTD).*

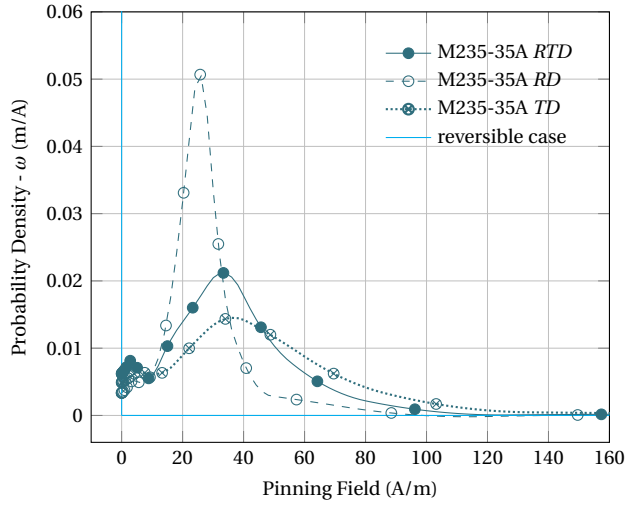

Figure 6.7: *Identified pinning field probability density for M235-35A and different stacking methods.*

2. Automatic Discretization of the Pinning Field Distribution

With the Bergqvist model, the probability density functions $\zeta(\lambda)$ are in general represented phenomenologically by Gaussian [13, 182], Lorentzian [17], or Rayleigh distributions [14], which have all appropriate shapes with adjustable parameters. They are eventually completed with a Dirac delta function to give a reversible contribution associated to the frictionless case. It is remarkable that the procedure presented here allows to follow a more physical approach to identify the model parameters, relying

on the direct visualization of the pinning field probability density curves. For information, a similar but different identification approach, also based on an experimental representation of the distribution curve, is also addressed in [132] for the Bergqvist model.

In any case, as already mentioned in Chapter 3-Section 1, the continuous pinning field distribution, represented here by $\omega(\kappa^*)$, has to be approximated by a discrete representation for the purposes of numerical implementation and inclusion in finite element (*FE*) formulation. This is achieved here by partitioning the pinning field spectrum into N regions, with delimitating values $h^0 = 0 < h^1 < \cdots < h^{N-1} < h^N = \infty$ of the magnetic field. Each region $k = 1, \ldots, N$ of the decomposition corresponds to a specific cell of the *EB* model, also named pseudo-particle. Each of them is characterized by its own weight ω^k and own pinning strength κ^k. These values can be calculated from the integral expressions (3.1) and (3.2) which can be rewritten, after substitution to pinning field variables $\kappa^*(\lambda) = \lambda\kappa_{\text{unit}}$, in terms of the pinning field distribution $\omega(\kappa^*)$, whose primitive is known from the auxiliary function definition $F(h)$, such that

$$\omega^k = \int_{h^{k-1}}^{h^k} \omega(\kappa^*)\, d\kappa^* = \partial_h F(h^k) - \partial_h F(h^{k-1}), \tag{6.9}$$

$$\kappa^k = \frac{\displaystyle\int_{h^{k-1}}^{h^k} \omega(\kappa^*)\kappa^*\, d\kappa^*}{\displaystyle\int_{h^{k-1}}^{h^k} \omega(\kappa^*)\, d\kappa^*} = \frac{\Big[h\partial_h F(h) - F(h)\Big]_{h^{k-1}}^{h^k}}{\omega^k}. \tag{6.10}$$

The discrete quantities ω^k are dimensionless whereas κ^k are expressed in A/m.

One can see that $\sum_{k=1}^{N} \omega^k = 1$ is verified with (6.9), assuming $\partial_h F(h^N) = 1$ and $\partial_h F(h^0) = 0$. With only one subdivision, i.e. $N = 1$, one has $\omega^1 = 1$ and $\kappa^1 = h_{c,\max}$. With more subdivisions, there is some freedom in the delimitation of the field range $[h^{k-1}, h^k]$ corresponding to each cell k. Besides $h^0 = 0$ and $h^N = \infty$ which remain fixed, the intermediate $N-1$ values $h^1 < \cdots < h^{N-1}$, which split the integrals in several pieces, can be selected by hand, as done in [103], or separated equidistantly, for example.

Here, an automatic discretization is adopted in order to find the best partitioning of the pinning field spectrum. This problem can be seen as the search for the best piecewise linear representation of the cumulative distribution function $\partial_h F(h)$ with N segments, which amounts to looking for the best decomposition of the area below the pinning field distribution function $\omega(h)$ with N rectangles. For that purpose, a strictly increasing piecewise linear function $y(x)$ composed of $N+1$ movable points (x^k, y^k) with $k = 0, 1, \ldots, N$, is considered. As $x^0 = h^0$ and $x^N = h^N$ are fixed a priori, it leaves $2N$ coordinate parameters to determine. An optimization process allows to find by least square fitting method the best positionning of the points (x^k, y^k) that approximates the data curve $\partial_h F(h)$. Once the optimal coordinates (x^k, y^k) are found, the parameters ω^k and κ^k associated to each cell can be deduced directly by adapting (6.9) and (6.10) as

$$\omega^k = y^k - y^{k-1}, \tag{6.11}$$

$$\kappa^k = \frac{\left(x^k y^k - F(x^k)\right) - \left(x^{k-1} y^{k-1} - F(x^{k-1})\right)}{\omega^k}. \tag{6.12}$$

A fitting result is shown in Fig. 6.8 (left) where a discretization with 3 cells, and thus with 3 segments, is done for the cumulative distribution function of material M235-35A. The corresponding discretization in 3 rectangles for the pinning field distribution is illustrated in Fig. 6.8 (right). Each rectangle has an area of ω^k and a width of $(x^k - x^{k-1})$. The height of each rectangle is equal to the slope of the corresponding segment in the polyline approximation of Fig. 6.8 (left).

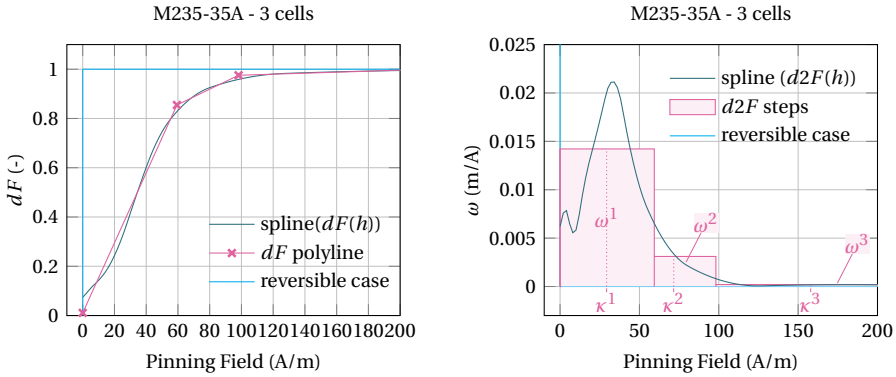

Figure 6.8: *Discrete representation with* 3 *cells for the cumulative distribution function* $\partial_h F(\kappa^*)$ *(left) and the pinning field distribution* $\omega(\kappa^*)$ *(right) of material M235-35A.*

It can be seen in Fig. 6.8 (left) that the reversible contribution with zero-pinning field is not properly taken into account with this discrete decomposition. In order to improve this representation, a cell purely dedicated to the reversible effect can be considered, for which $\omega^1 = \partial_h F(0)$ and $\kappa^1 = 0$. The other cell parameters can still be determined by exploiting the fitting technique to get the optimal decomposition of the cumulative distribution curve with $N-1$ remaining segments. For the same total number of cells, this involves thus less adjustable coordinates than previously, since $y^0 = 0$, $y^1 = \partial_h F(0)$ and $x^1 = 0$ are now frozen to characterize fully the reversible cell $k = 1$ in this context. Basically, this amounts to introducing a Dirac delta function in the pinning field distribution.

The fitting obtained with 3 cells, with one of them being specifically devoted to the reversible response, is shown in Fig. 6.9 for the M235-35A material. The cumulative distribution function is now well represented by the discretization at zero field and is approximated by only two segments for the remaining field range. The pinning field distribution is discretized by a Dirac delta function at $\kappa^1 = 0$, associated to cell $k = 1$, and by two rectangles which stand for the two remaining cells.

Naturally, the discretization can be further improved by increasing the number N of cells taken. For instance, the identification of the cell parameters based on this pro-

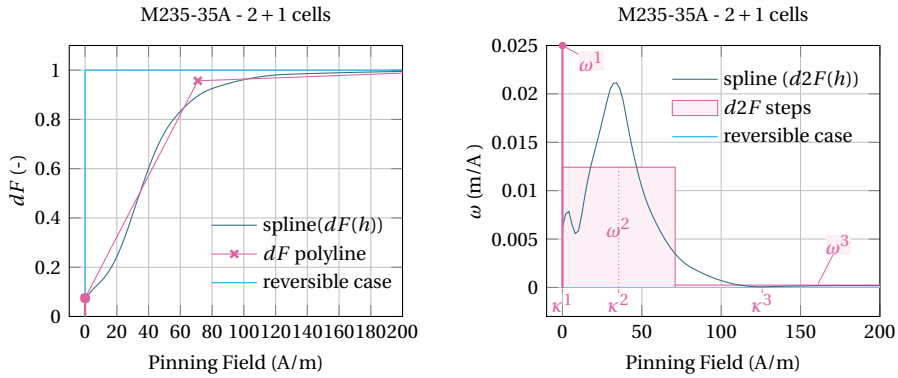

Figure 6.9: *Discrete representation with* 3 *cells (one of which being purely reversible) for the cumulative distribution function* $\partial_h F(\kappa^*)$ *(left) and the pinning field distribution* $\omega(\kappa^*)$ *(right) of material M235-35A.*

cedure for the M235-35A material data with a decomposition in 6 and 15 pseudo-particles are illustrated in Fig. 6.10 and Fig. 6.11, respectively.

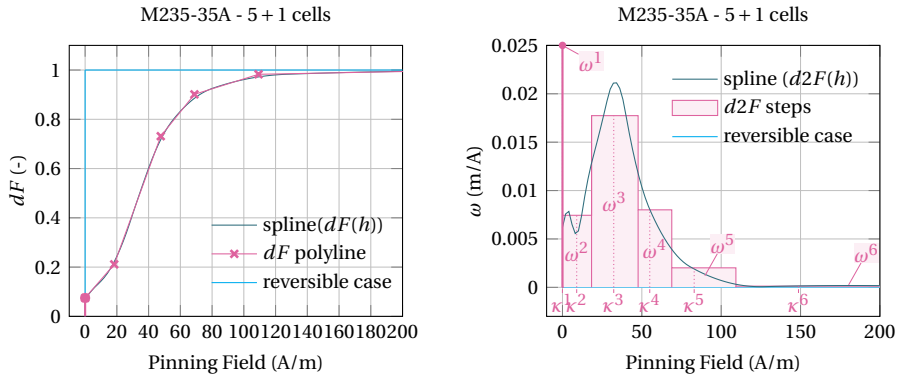

Figure 6.10: *Discrete representation with* 6 *cells (one of which being purely reversible) for the cumulative distribution function* $\partial_h F(\kappa^*)$ *(left) and the pinning field distribution* $\omega(\kappa^*)$ *(right) of material M235-35A.*

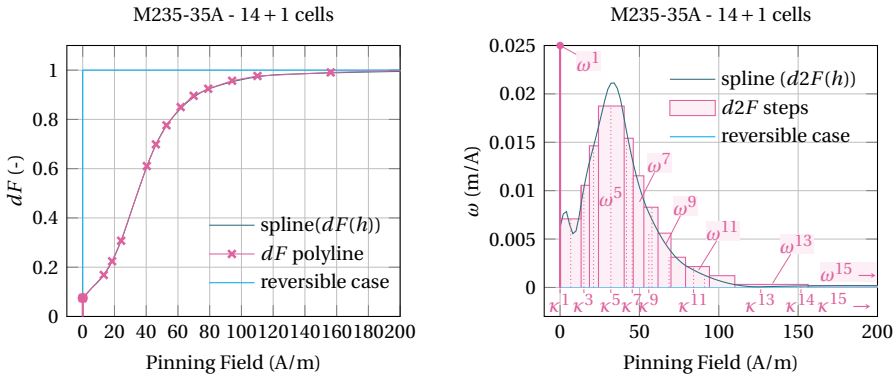

Figure 6.11: *Discrete representation with* 15 *cells (one of which being purely reversible) for the cumulative distribution function* $\partial_h F(\kappa^*)$ *(left) and the pinning field distribution* $\omega(\kappa^*)$ *(right) of material M235-35A.*

3. Identification of the Anhysteretic Curve

It remains to explain the strategy to identify the anhysteretic curve. As already mentioned in the previous section, the anhysteretic curve is not part of standard magnetic measurement procedure. On the other hand, the initial magnetization curve can be evaluated easily from hysteresis loops measurements by joining the reversal points of each cycle, as illustrated by Fig. 1.6 (left), or be determined experimentally by monotonically increasing the magnetic field strength from zero to the maximum field strength, starting from the demagnetized state. Then, based on the first magnetization curve measurement and the knowledge of the auxiliary function F, it is possible to deduce the anhysteretic curve by application of (6.6), without any additional measurement.

Experience shows that anhysteretic curves can be represented accurately by a double Langevin function [103]

$$J_{\text{an}}(h_{\text{rev}}) := J_a L\left(\frac{h_{\text{rev}}}{h_a}\right) + J_b L\left(\frac{h_{\text{rev}}}{h_b}\right), \tag{6.13}$$

with $L(x) = \coth x - \frac{1}{x}$, as already encountered with (1.11). The term indexed with a b represents the magnetic polarization due to the motion of Bloch walls, whereas the term indexed with an a represents the magnetic polarization, occurring at high field intensity, that is associated with the rotation of the magnetic moments relative to their preferred easy-magnetization axis, as discussed in Chapter 1-Section 1.3. Once the function F is known for a material, the four parameters J_a, h_a, J_b, h_b of the double Langevin representation (6.13) can be determined by simply matching the measured virgin curve $J_{\text{virgin}}(h)$ with $J_{\text{an}}(F(h))$, in order to verify (6.6). This is illustrated in Fig. 6.12 (left) with the steel M235-35A data only. It is an evidence of the consistency of the proposed identification procedure that the curve $J_{\text{an}}(F(h))$, which combines two unrelated nonlinear functions, is indeed, as expected, linear at the origin.

Comparatively, a similar fitting has been attempted with a hyperbolic tangent function

in Fig. 6.12 (right), as used with (3.33). As can be seen, the double Langevin function allows a better agreement with the anhysteretic data points deduced from the procedure, whereas the fitting with the hyperbolic tangent function is of poor quality at high field intensity. These two curves are also displayed in a linear scale plot in Fig. 6.13. The linear behavior at small fields remains consistent with both functions. Practically, the anhysteretic function can also be determined from interpolation between data points for an even better representation over the entire measured field range.

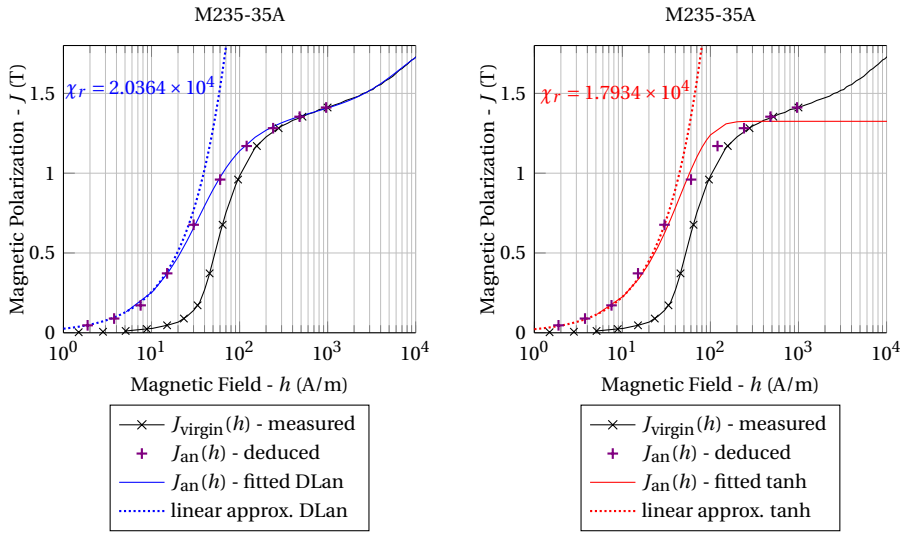

Figure 6.12: *Virgin curve and the identified double Langevin anhysteretic curve (left) or the identified hyperbolic tangent anhysteretic curve (right) of the steel grade M235-35A, in logarithmic scale. The asymptotic linear behavior of the anhysteretic curves at the origin is represented by dotted lines.*

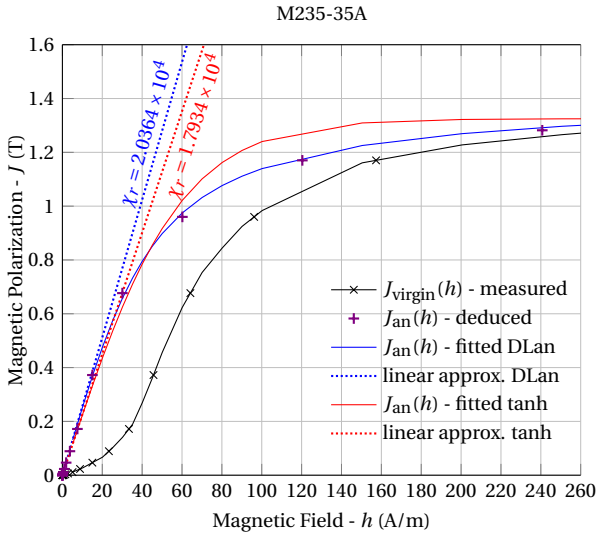

Figure 6.13: *Virgin curve and the identified anhysteretic curve with either a double Langevin or a hyperbolic tangent function of the steel grade M235-35A. The asymptotic linear behavior of the anhysteretic curves at the origin is represented by dotted lines.*

4. Validation on Material Measurements

The identification procedure for the *EB* model parameters is now tested on the *NGO* Fe-Si 3.2 wt% 0.48 mm thick lamination, which is the material used in the test electromagnetic analysis methods (*TEAM*) Problem Number 32 [33], whose complete study with the full device modeling is investigated in more detail in Chapter 7-Section 5.

The *TEAM* 32 provides the material data shown in Fig. 6.14, measured on an Epstein yoke cutting strips along different directions with respect to the *RD* or the *TD*. The characterization has been achieved in each direction by means of several symmetrical minor loops under controlled flux conditions with magnetic flux density reaching maximum value ranging from 0.5 to 1.6 T. It can be seen that, despite the fact that material is non-oriented, they are substantial differences between measurement along the *RD* or the *TD*, with an easier saturation in the former configuration and slightly larger coercive fields in the latter one. This allows eventually to incorporate anisotropic effects in vector hysteresis models. However, the anisotropy has not been taken into account for the *EB* model in this thesis, and only the data associated to the *RD* is considered here.

The information gathered in the symmetrical minor loops given by Fig. 6.14 is sufficient to fully determine the *EB* model parameters based on the identification procedure presented in this chapter. Indeed, the $h_c(h)$ characteristics can be deduced by extracting the coercive field associated to the maximal magnetic field amplitude of each cycle, while the virgin curve, $J_{\text{virgin}}(h)$, can be evaluated by drawing the curve passing through the maximum and minimum reversal points of each symmetrical loops.

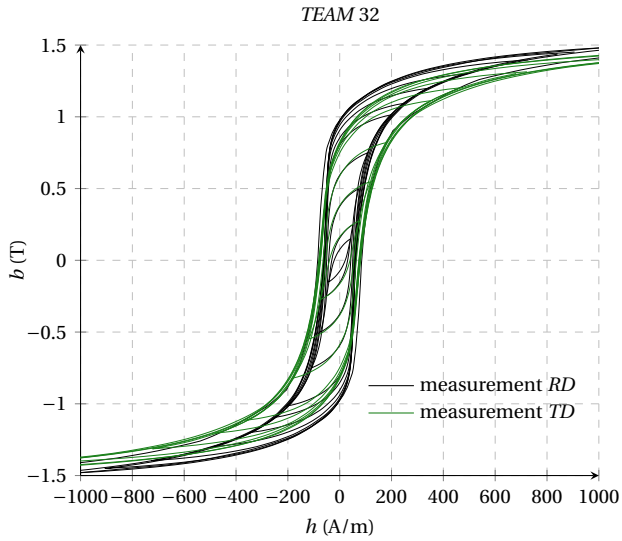

Figure 6.14: *Measurements on the Fe-Si 3.2 wt% material provided by the TEAM 32 benchmark problem.*

It is chosen to represent the anhysteretic curve of the *EB* model by a double Langevin function (6.13). The identification procedure proposed in Chapter 6-Section 3 produces the parameters $J_a = 0.792\,\mathrm{T}$, $h_a = 9.082\,\mathrm{A/m}$, $J_b = 0.791\,\mathrm{T}$, and $h_b = 137.121\,\mathrm{A/m}$ for the *TEAM* 32 material. Furthermore, the *EB* model is considered to be composed of $N = 3$ cells in a first approach. At the end of the automatic discretization technique described in Chapter 6-Section 2, the cell parameters obtained from the *TEAM* 32 data are set to $[\omega^1 = 0.03; \kappa^1 = 0 A/m], [\omega^2 = 0.92; \kappa^2 = 55 A/m], [\omega^3 = 0.05; \kappa^3 = 199 A/m]$.

In order to enrich the comparison, a representation with a classical Jiles-Atherton (*JA*) hysteresis model is also examined. The model parameters for the *TEAM* 32 material have been identified for each *RD* and *TD* in [7, 6] through a real coded genetic algorithm detailed in [136], that minimizes the mean squared error between experimental and simulated magnetic field curves. As attention is focused on the *RD* here, only the parameters associated to that direction are retained for the *JA* model, which are thus $c = 0.652$, $m_s = 1.33 \times 10^6\,\mathrm{A/m}$, $a = 172.856\,\mathrm{A/m}$, $\alpha = 417 \times 10^{-6}$, and $k = 232.562\,\mathrm{A/m}$. Hereafter, the measurement of the *TEAM* 32 material can then be compared with simulation results achieved with the *EB* and the *JA* models.

First, the field evolution described by the major loop that reaches a maximum amplitude of $b_{\max} = 1.5\,\mathrm{T}$ is analyzed. The details of the magnetic field and the flux density variations measured at each time step during this cycle is given in Fig. 6.15. The measurement of the magnetic field, drawn in Fig. 6.15 (left), is used as an input source for the 3-cell *EB* model and the *JA* hysteresis model. The flux densities which are then calculated as output by each hysteresis model are compared with the measured values in Fig. 6.15 (right).

The averaged accuracy of the hysteresis model prediction can be quantified thanks to

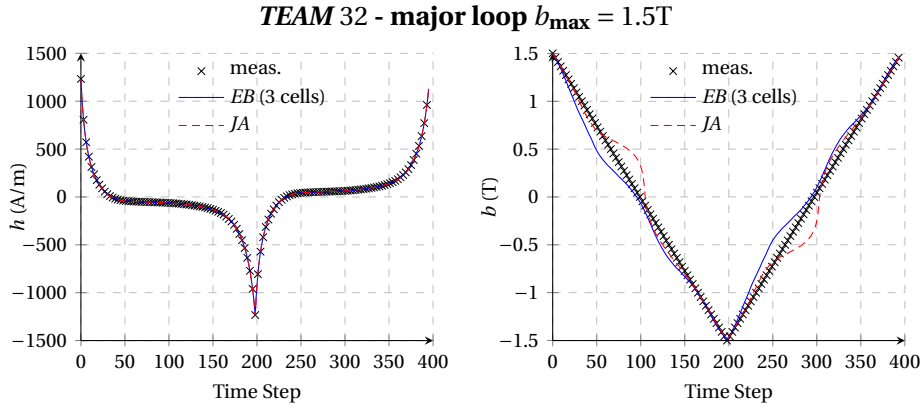

Figure 6.15: *Evolution of the magnetic field (left) and the induction field (right) obtained at each time step measurement for the major loop (b_{max} = 1.5 T) of the TEAM 32 material. The magnetic field obtained from measurement (left) is used as a source for the simulations with a 3-cell EB model and a JA hysteresis model to produce the output induction field (right).*

the definition of a root mean square deviation (*RMSD*) factor, based on the differences between the computed and the measured flux densities over all the N^t time steps of the simulation and the corresponding N^t measurement data points,

$$\mathrm{RMSD} = \sqrt{\frac{1}{N_t}\sum_{n=1}^{N_t}\left(b_n - b_n^{\mathrm{meas}}\right)^2}, \qquad \mathrm{RMSD}_r = 100 \times \frac{\mathrm{RMSD}}{b_{\max}}\%, \tag{6.14}$$

where the relative root mean square deviation (*RMSD*$_r$) is the dimensionless equivalent factor, expressed in %, obtained by dividing the previous factor with the maximum flux density $b_{\max}$ among the measurement data.

The simulations with the *EB* or the *JA* models are in rather good agreement with the measured signal of the major loop in Fig. 6.15 (right), considering the simplicity of their implementation. Both models have similar level of accuracy in average over the entire cycle, with *RMSD*$_r$ values of about 8 % for each simulation, but the *JA* model leads to the highest deviation from the measured values for some time steps, with a maximum error of 0.35 T, whereas the deviation is of 0.26 T at most with the *EB* model in the worst case.

The results can also be discussed by representing the $b-h$ curves for the major loop, obtained from the measurement and the simulations, as done in Fig. 6.16. From that perspective, one can see that the measured $b-h$ curve shape is well approximated by the *EB* model during saturation, but less during desaturation of the material. As a consequence, the magnetic energy dissipated over each cycle, which corresponds to the area enclosed by the hysteresis loop (1.15), tends to be underestimated by the *EB* model. Indeed, the area obtained from the measurement data is 477 J/m^3, whereas the *EB* model underestimates this value to 347 J/m^3 only (deviation of 27 %). This highlights one limitation of the original *EB* hysteresis model, which can only produce

perfectly symmetric loops that have the same shape for the positive and the negative branches. However, this does not seem to be always the case in practice for some materials, as visible with the *TEAM* 32 electrical steel measurement, since the curve bendings are not necessary the same between saturation and desaturation, where an asymmetric enlargement of the major loop appears for the descending branch.

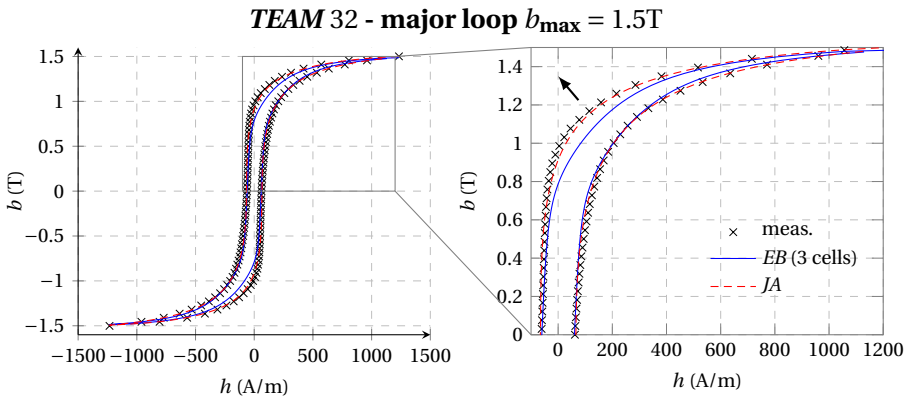

Figure 6.16: *$b-h$ curves comparison between measurement and results obtained with a 3-cell EB model and a JA hysteresis model for the major loop (b_{max} = 1.5 T) of the TEAM 32 material.*

There are various physical interpretations that may explain this asymmetry between ascending and descending branches in the measurement. First, based on the magnetization principles presented in Chapter 1-Section 1.3 and dissected in Fig. 1.4, it appears that the discrepancy occurs mainly in the saturation knee, which corresponds to the part of the hysteresis loop where irreversible domain wall motion takes place, but mostly domain rotation dominates. During saturation, all magnetic domains are forced to be oriented in the magnetic field direction, which is not necessary along an easy magnetization axis at the grain scale, because the grains are in general randomly oriented relative to each other, especially in *NGO* material. During desaturation, the domain rotation may thus behave differently due to the influence of local magnetocrystalline anisotropy [130] that modifies thus the shape and the bending of the descending curve from the ascending one. This phenomenon is refered as asymmetric domain rotation in [183], even if the domain wall movement has certainly also an influence in the process as well. Secondly, the asymmetry may be due to nucleation phenomena which happen when domains of reversed magnetization are formed inside a saturated region, at the moment of desaturation [26]. Actually, the nucleated domains can even lead to reentrant hysteresis curve with strong asymmetric shape in specific experimental setup [90]. Nevertheless, the hysteresis by nucleation has not been considered in this thesis, but its distinction from wall motion hysteresis is neither obvious nor rigorous as it can be interpreted as the sudden expansion of small preexisting reversed domains [26]. Thirdly and lastly, this asymmetric enlargement of the $b-h$ loop can find its origin in dynamic effects if the measurements are not made exactly at the same constant rate during saturation and desaturation of the material. Although it is ensured in [33] that the *TEAM* 32 material is characterized under con-

trolled flux conditions at a frequency of 10 Hz, which guarantees good accuracy of the experimental data with negligible dynamic effects, this statement is yet not illustrated based on measurements of the major loop in the paper. Knowing the difficulty to experimentally control the symmetry of a flux source with high amplitudes at small frequency, the possibility of slight discrepancies in the rate between the increasing or the decreasing regime during the measurement should not be discarded. Furthermore, such asymmetric enlargement can be successfully reproduced by simulation thanks to the dynamic lamination model described in the next Chapter 7-Section 1, by simply introducing a slight asymmetry in the triangular flux density signal, whose influence is notable, even at 10 Hz.

Anhyhow, it is obvious that the *EB* model is not able to develop such asymmetry with its standard static implementation.

Concerning the *JA* model adopted here, although it only allows to generate symmetric major loops as well, the produced curve seems in better agreement than the *EB* one compared to the measurement for the desaturation branch, according to Fig. 6.16 (right). This is because the *JA* parameters have been fitted in order to represent at best the entire experimental major loop curve, resulting in a compromise to reduce the mean-square error from the measurement on both the saturation and the desaturation branches, whereas the identification strategy used for the *EB* model relies on physical principles. Nevertheless, it is worth recalling that the *EB* model is at the end as accurate as the *JA* model over the entire major loop representation, as already mentioned by comparing their $RMSD_r$ factor and as emphasized in Fig. 6.15 (right).

Increasing the number of cells in the *EB* model does not improve the accuracy of the major loop representation. Actually, a single-cell model that gathers all the pinning strengths with $\omega^1 = 1$ and $\kappa^1 = h_{c,\max}$, that is $h_{c,\max} = 61\,\mathrm{A/m}$ for the material studied here, is even enough to produce a result as satisfying as Fig. 6.15 for the major loop. Indeed, the shape of the ascending and descending branches depends essentially on the choice of the anhysteretic curve representation because in the standard *EB* model operation illustrated in Fig. 2.4, these two main branches are, at the end, equivalent to the anhysteretic curve, but with a horizontal translation in the $b-h$ diagram of $\pm h_{c,\max}$. This is confirmed in Fig. 6.17 (left) which plots the $RMSD_r$ factors calculated for simulations of the major loop with the *EB* model in function of different number of cells taken in the discretization. One can see that the $RMSD_r$ factors remain constant, at about 8 %, independently of the number of cells, and that it corresponds to the *JA* level of accuracy with respect to the measurement for all the *EB* simulations.

Actually, the discretization into a greater number of cells finds its interest for the modeling of distorted signals or even simply for the representation of minor loops, where a finer description of the pinning field is then required. This is clearly illustrated by Fig. 6.17 (right) which quantifies the ability of the simulations to reproduce the minor loop associated to $b_{\max} = 0.5\,\mathrm{T}$ of the *TEAM* 32 material measurement data. When the number of cells is increased, the $RMSD_r$ factors of the simulations with the *EB* model reduce until reaching a precision of about 8 % with respect to the measurement for a model made-up of at least 7 cells. Beyond this number, the $RMSD_r$ factors remain

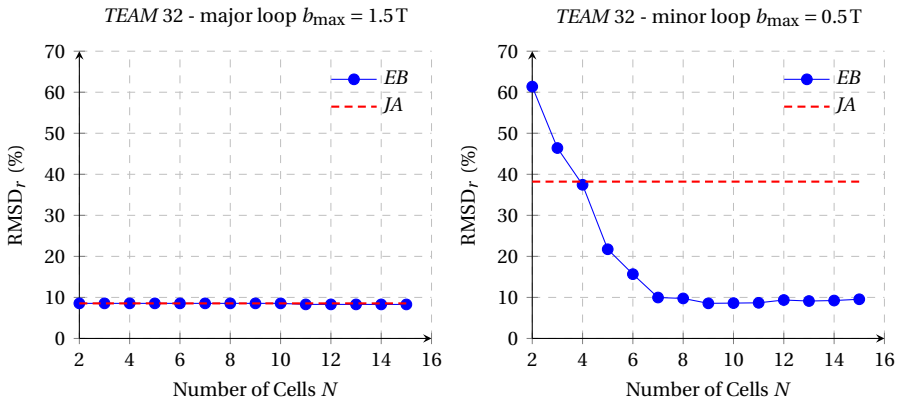

Figure 6.17: *Evolution of the deviation, quantified by a RMSD$_r$ factor (%), between the measurement and the EB model prediction in function of the number of cells N taken, for major loop (left) and minor loop (right) of TEAM 32 material. The deviation of the JA model with parameters fitted on the major loop with respect to the measurement is also given, for comparison.*

then mostly constant and there is thus no longer any advantage in taking more cells to improve the prediction for this specific measured minor loop. In other word, an equivalent accuracy of 8 % can be realized with the *EB* model, as well for the major loop as for the minor loops, as long as an appropriate number of cells is taken in the latter case.

On the other hand, the simulation with the *JA* model, whose parameters are basically determined to fit the major loop curve, is far from reaching such a level of precision for the minor loop since it only has a *RMSD$_r$* factor of 38 % compared to the measurement in that case. In order to improve the prediction with the *JA* model, it would be necessary to calculate other parameters associated specifically to the minor loop this time, but at the risk to deteriorate the approximation on the major loop. The standard *JA* model does not enjoy the flexibility of the *EB* model to adapt its modeling accuracy for different signal shapes. This highlights the main advantage of the *EB* model compared to other conventional hysteresis models.

The $b-h$ curves produced by the *EB* model, with various number of cells N = 3, 6, 9, 12, 24, 48, for the simulation of the minor loop b_{max} = 0.5 T, are displayed in Fig. 6.18, and compared with the measurement and the result obtained with the *JA* model. The refinement of the *EB* model outputs towards the measurement with an increase of the number of cells is clearly visible. The field response becomes smoother and the predicted dissipation becomes more accurate as the number of cells grows. According to the measurements, the loop area is 68 J/m^3. The area of the hysteresis cycle produced by a 3 cell *EB* model gives the poorest result of 97 J/m^3 (deviation of 43 %). However, this calculated quantity becomes closer to the measured one as the number of cells is increased, leading to 84 J/m^3 (deviation of 24 %), 79 J/m^3 (deviation of 16 %), 78 J/m^3 (deviation of 15 %), 77 J/m^3 (deviation of 13 %) and 76 J/m^3 (deviation of 12 %), with 6, 9, 12, 24 and 48 cells respectively, from the examples provided in Fig. 6.18. In compari-

son, the poor quality of the *JA* model simulation results is obvious. It produces a value of 42 J/m^3 for the loss of magnetic energy, which corresponds to a deviation of 38 % compared to the measurement. Moreover, the well known failure of the *JA* model in its inability to close minor loops can also be observed in Fig. 6.18. Such problems do not exist with the *EB* model.

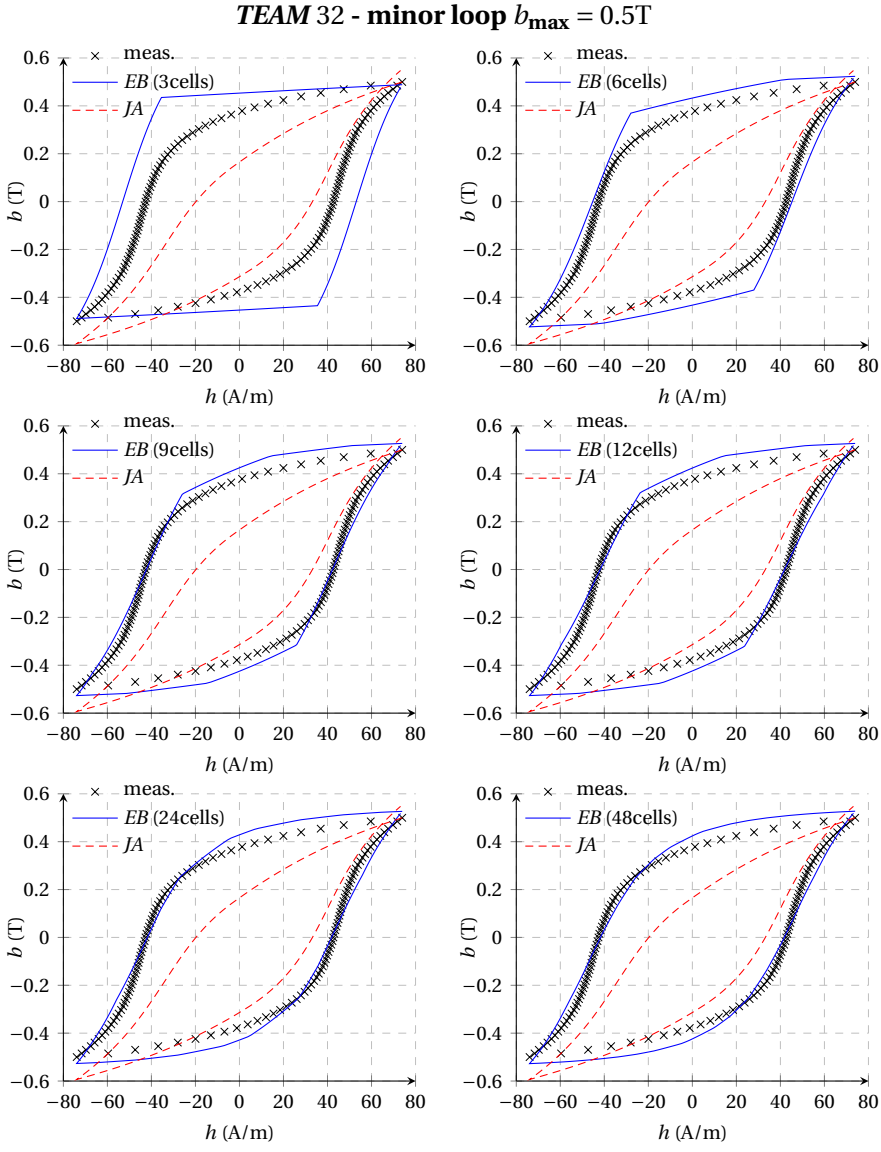

Figure 6.18: *Improvement of the EB model representation with an increasing number of cells N = 3, 6, 9, 12, 24, 48, compared to measurement for the minor loop (b_{max} = 0.5 T) of the TEAM 32 material. The results of the JA model with parameters fitted on the major loop are also given.*

In order to improve furthermore the accuracy of the *EB* model and thus minimize the reachable $RMSD_r$ value from the measurement with a better prediction of the magnetic energy loss, it is inevitable to go through a complexification of the model. A first modification, already mentioned in Chapter 6-Section 3, consists in using an anhysteretic curve constructed by interpolation on the measurement points, rather than using an analytical law. This is the most correct approach to define the anhysteretic curve, but also probably, the least suitable for a numerical implementation since it can lead to irregularities that reduce the curve smoothness, yet such essential to facilitate the convergence in a Newton-Raphson (*NR*) algorithm. On the other hand, the fitting on measurements can be improved by the use of an effective field, $\mathbf{h}_e = \mathbf{h} + \alpha\mu_0^{-1}\mathbf{J}$, experienced by each cell. In this case, pseudo-particles are no more independent of one another, complicating thus also the model implementation. This would offer the opportunity to generate a correct slope for the anhysteretic curve both at low and high fields, by modifying the added material-dependent parameter α. Such artificial concept, borrowed from the Weiss theory (A.18), is commonly used in other hysteresis models, as in the *JA* model for example, but also in the so-called moving Preisach model [205], or even in the Bergvist model [17, 16, 183]. Furthermore, a method that can be investigated to palliate the limitation of the original *EB* model in order to model the asymmetric domain rotation phenomenon previously mentioned, consists in using variable pinning strength κ^k that would be dependent on the applied magnetic field instead of staying constant for all magnetizations. Such idea is actually already explored for the Bergqvist model, presented as a series-distributed vector play hysterons model, with improved vector play operators whose threshold values vary with the field intensity. Such dependence can be identified from the half width separation between the main ascending and descending branches along with different magnetizations [145, 146], or be defined with an appropriate parametric function [147, 183]. Therefore, the model can generate different slopes during saturation and desaturation, and eventually produce asymmetric major loop, probably more in line with the experimental measurements, as seen in Fig. 6.16 (right). In the same way, the degree of reversibility, which corresponds to the weight ω^1, associated to the pinning-free cell $\kappa^1 = 0\,\mathrm{A/m}$, and so far assumed constant in the original *EB* implementation, can also be expressed as a function of the magnetization or the applied field [5, 203, 183]. Indeed, the degree of reversibility can possibly vary for different magnetization levels. Ultimately, the anisotropy is another important characteristics that needs to be included somehow in the model. A first strategy has already been investigated to this end for the *EB* model in [198].

Neverthless, it is worth recalling that the interest of the *EB* model lies in its original simplicity and its ability, despite everything, to produce results of satisfactory precision. The improvements possibilities listed above for the *EB* model are only suggested here, but not explored further in this thesis. Therefore, regarding the deliberately unchanged simplicity of the considered *EB* model and according to the quality of the results produced in this section, the identification strategy detailed previously is estimated to be validated.

CHAPTER

7 Finite Element Simulations

In this last chapter, finite element (*FE*) simulations with the energy-based (*EB*) hysteresis model are conducted on various test cases of increasing geometric complexity, namely a one-dimensional (*1D*) representation of a ferromagnetic sheet, a simple square where rotational sources are experienced, a planar cross-section of a perfectly flux-confining T-joint slab, a complete three-phase transformer modeled in two-dimensional (*2D*) configuration and finally, a transformer application from the test electromagnetic analysis methods (*TEAM*) Problem 32 benchmark to compare with experimental results.

1. Infinite Ferromagnetic Sheet - *1D*

As a first illustration of the hysteresis model implementations within a *FE* context, the case of an infinite ferromagnetic sheet as shown in Fig. 7.1 (left) is studied. A tangential uniform magnetic field $\mathbf{h}_{\text{app}}$ is applied on both lateral surfaces along the direction $\mathbf{z}$. Moreover, given that the sheet is assumed infinite in the $\mathbf{y}$ and $\mathbf{z}$ directions, the magnetic field $\mathbf{h}$, as well as the induction field $\mathbf{b}$ and the magnetic state variables $\mathbf{X}^k$, are also restricted to be parallel to the direction $\mathbf{z}$ in the whole domain, varying only with the spatial coordinate x. Accounting for the symmetries, it is sufficient to work with a *FE* model that consists of a *1D* formulation of the eddy current problem applied on a line parallel to $\mathbf{x}$, across half the thickness $d/2$ of the sheet, as illustrated in Fig. 7.1 (right).

Simulations are performed using the $\mathbf{h}-\phi$ formulation (5.25) including the direct hysteresis model on a line domain of thickness $d/2 = 0.15\,\text{mm}$, meshed by 100 elements. The point corresponding to the surface at $x = 0$ is excited by a time-varying essential boundary condition $\mathbf{h}\big|_{x=0} = h_{app}(t)\mathbf{z}$ while a natural boundary condition $(\mathbf{curl}\,\mathbf{h} \times \mathbf{n})\big|_{x=d/2} = \mathbf{0}$ holds at the middle of the lamination, with $\mathbf{n}$ the normal vector pointing outward the studied domain, and thus parallel to $\mathbf{x}$ at $x = d/2$. An electric conductivity of $\sigma = 1.57 \times 10^6\,\text{S/m}$ is considered in the whole domain and the previously used parameters for the 3-cell hysteresis model from Chapter 3-Section 5 are adopted again. Due to the *1D* configuration, the various *EB* hysteresis implementations lead to

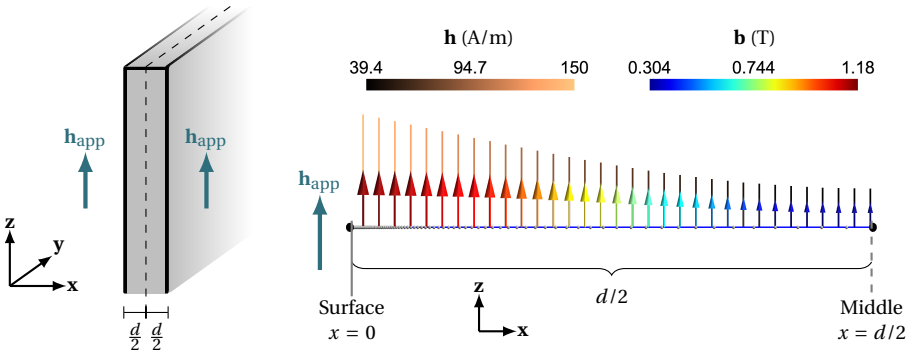

Figure 7.1: *Schematic representation of a lamination with the unidirectional FE configuration.*

the same outputs, such that the simplest Vector Play Model (*vpm*) approach is chosen here.

This rather simple *FE* application is readily able to give a first glance on the complex nature of iron losses which result from the interplay of nonlinear characteristics, irreversible phenomena, eddy currents and skin effects. All these physical effects are taken into account in this *FE* model. Irreversible phenomena introduced by the rate-independent hysteresis model contribute to add another dissipation source to the classical induced currents.

To illustrate this, global integrated quantities corresponding to power definitions are analyzed and compared. The sample is excited by an applied field of sinusoidal waveform of magnitude 150 A/m at different frequencies f. Fig. 7.2 presents for $f = 50$ Hz and $f = 500$ Hz, the evolution during one period of the eddy current losses P_{ec}, and the rate-of-change of the magnetic field energy P_{mag}, calculated respectively by

$$P_{\text{ec}} = 2\int_0^{d/2} \sigma^{-1}|\mathbf{j}|^2\,dx = 2\int_0^{d/2} \sigma^{-1}|\mathbf{curl}\,\mathbf{h}|^2\,dx,, \qquad P_{\text{mag}} = 2\int_0^{d/2} \mathbf{h}\cdot\dot{\mathbf{b}}\,dx,, \quad (7.1, 7.2)$$

and expressed in watts per unit area (W/m^2). Thanks to its energy equilibrium foundation (3.4), the hysteresis model allows to split at any time the magnetic specific power in a reversible and irreversible parts, $P_{\text{mag}} = P_{\text{rev}} + P_{\text{irr}}$, with

$$P_{\text{rev}} = 2\int_0^{d/2} \left(\mu_0 \mathbf{h}\cdot\dot{\mathbf{h}} + \sum_k \mathbf{h}_{\text{rev}}^k \cdot \dot{\mathbf{J}}^k\right) dx, \quad P_{\text{irr}} = 2\int_0^{d/2} \left(\sum_k \mathbf{h}_{\text{irr}}^k \cdot \dot{\mathbf{J}}^k\right) dx, \qquad (7.1, 7.2)$$

where the first term, P_{rev}, takes the permeability of vacuum contribution μ_0 into account, but which is negligible compared to the $\mathbf{h}_{\text{rev}}^k$ contributions; and the last term P_{irr}, corresponds to the power actually dissipated by the hysteresis phenomenon. The reversible part corresponds to the reversible magnetic energy that is stored in the material and that can be totally retrieved at the end of a time period. Therefore, the mean value of P_{rev} during a cycle, noted $\overline{P}_{\text{rev}}$, is zero. On the other hand, the irreversible part gives the amount of energy that is lost through hysteresis, and it is relevant to note

that this quantity is available at any time, thus not only at the end of a period or after the completion of minor loops as it is usually the case with other hysteresis models or with simpler iron loss models. This is an interesting property of the *EB* model which allows to know the losses distribution at all times for any applied fields, even for the most sophisticated. At the end, the mean value of P_{irr} over one period, denoted by $\overline{P}_{\text{irr}}$, corresponds to the mean value $\overline{P}_{\text{mag}}$.

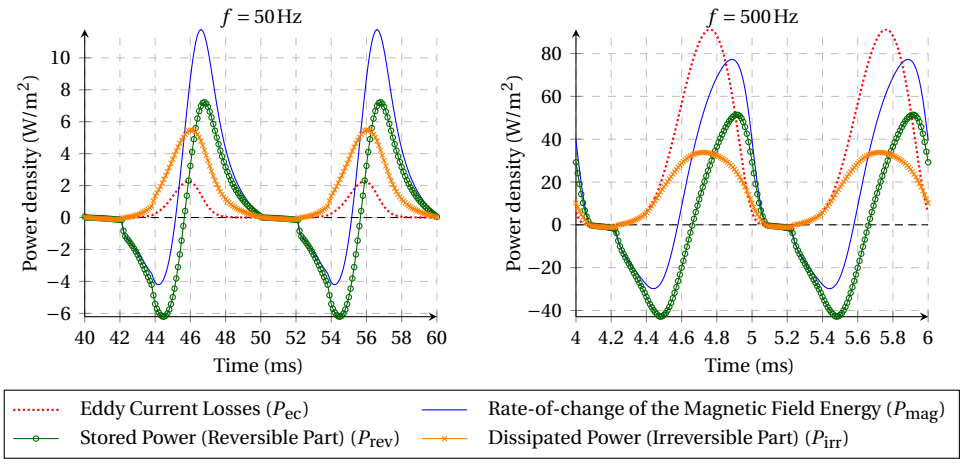

Figure 7.2: *Energy analysis of the lamination sheet, during one cycle.*

As can be seen in Fig. 7.2, the magnetic dissipated power P_{irr} is predominant at low frequency 50 Hz, compared to the eddy current losses P_{ec} while the situation inverses at the higher frequency 500 Hz.

The evolution in function of the frequency of the mean value over a period for these two types of losses is summarized in Fig. 7.3. The total iron losses per unit surface correspond to the sum of both contributions $P_{\text{tot}} = P_{\text{ec}} + P_{\text{irr}}$. These total losses are also given by the flux of the Poynting vector $\mathbf{P}$ across the lamination surfaces, which are assimilated to a point in the *FE* model in Fig. 7.1 (right), thus

$$P_{\text{tot}} = -2\,(\mathbf{P}\cdot\mathbf{n})\,\big|_{x=0}\,, \tag{7.5}$$

where the Poynting vector is defined by

$$\mathbf{P} = \mathbf{e}\times\mathbf{h} = \sigma^{-1}\mathbf{curl}\,\mathbf{h}\times\mathbf{h}\,. \tag{7.6}$$

At 50 Hz, the hysteresis losses constitute more than 75 % of the total losses in this example. The eddy current losses become the predominant above 200 Hz. The proportionality with f and f^2 for the hysteresis and the eddy current losses respectively are visible in Fig. 7.3 (left) for low frequencies, likewise predicted in classical loss separation models [20], as discussed in Chapter 1-Section 2.2. The curves start to deviate further from

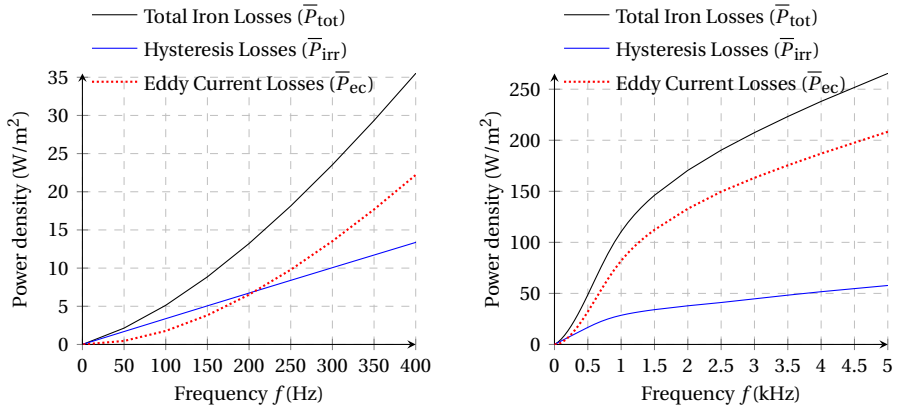

Figure 7.3: *Frequency dependences of the classical eddy current and hysteresis losses, averaged over a period. Classical evolutions at low frequencies (left); Influence of the skin effect at higher fields (right).*

these proportional relations at higher frequencies, shown in Fig. 7.3 (right), due to the increasing influence of skin effects.

A rather more complex excitation $\mathbf{h}_{app}$ of the lamination model is investigated with a 100 Hz magnetic field of magnitude 150 A/m superimposed with a 7-th harmonic of magnitude 75 A/m in Fig. 7.4 (left). It shows the local $b-h$ relations at the surface and at the center of the sheet. The loop and inner cycles are slightly smaller in the middle of the lamination because the magnetic field variations felt inside are lower than on the surface due to eddy currents shielding. The hysteresis model is rate-independent so that the constitutive law is not influenced by the frequency, and there is no additional loop enlargement compared to the quasi-static case.

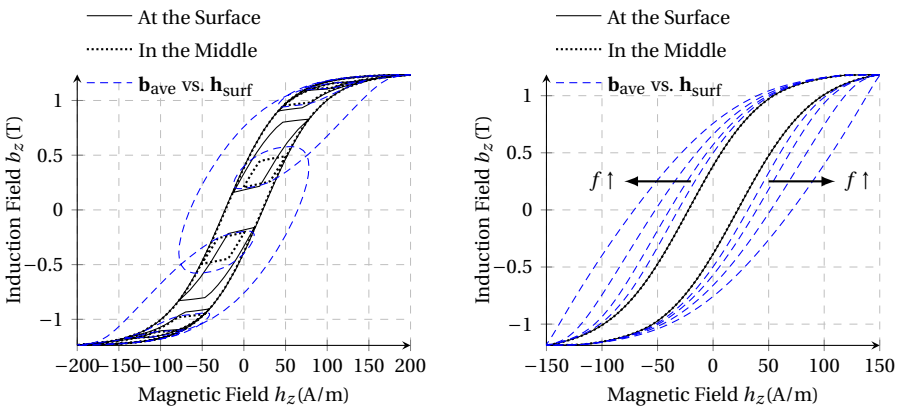

Figure 7.4: *(left): Local $b-h$ curves at the surface and at the the middle of the lamination, with the law $\mathbf{b}_{ave}$ vs. $\mathbf{h}_{surf}$, averaged over the lamination, for $f = 100Hz$ with a 7-th harmonic. (right): Expansion with the frequency of the $\mathbf{b}_{ave}$ vs. $\mathbf{h}_{surf}$ curve illustrated for sinusoidal applied fields at $f = 50, 100, 200, 400$ Hz.*

Despite being very simple, this *FE* model configuration is already appropriate to simulate measurements in Epstein frames or Single Sheet Testers, for example, provided the joints in lamination corners can be neglected. In this practical situation, the measured quantities are thus currents and fluxes that are related to the surface magnetic field $\mathbf{h}_{\text{surf}} = \mathbf{h}\big|_{x=0} = \mathbf{h}_{\text{app}}$, and the flux density averaged over the lamination thickness $\mathbf{b}_{\text{ave}} = 2d^{-1}\int_0^{d/2}\mathbf{b}\,dx$, respectively. Actually, at low frequency, the flux density $\mathbf{b}$ is approximately uniform over the thickness of the lamination when the skin effect is negligible. From Maxwell's equations, a relation between the surface field $\mathbf{h}_{\text{surf}}$ and the magnetic field $\mathbf{h}_{\text{ave}}$ associated to the average flux density $\mathbf{b}_{\text{ave}}$ can be derived [26]:

$$\mathbf{h}_{\text{surf}} = \mathbf{h}_{\text{ave}} + \frac{\sigma d^2}{12}\frac{\partial\,\mathbf{b}_{\text{ave}}}{\partial t}, \tag{7.7}$$

where $\mathbf{h}_{\text{ave}}$ and $\mathbf{b}_{\text{ave}}$ are the fields related through the quasi-static magnetic constitutive law of the material, thus where the static *EB* hysteresis model applies. The hysteresis loop in terms of the quantities that are observable from outside the lamination, i.e. $\mathbf{b}_{\text{ave}}$ vs. $\mathbf{h}_{\text{surf}}$, is shown in Fig. 7.4, produced by the *FE* model. This curve takes up the influence of the eddy currents, as suspected with the second term contribution in (7.7), in addition to the static hysteresis, such that the relation becomes rate-dependent. This lamination model considers thus the dynamic enlargement of the hysteresis loops with the frequency, as can be observed experimentally, reminding Fig. 1.8 in Chapter 1-Section 1.5. Increasing the frequency of the applied field in the *FE* model expands the loops of the latter curve. This is highlighted in Fig. 7.4 (right) in the case of a simple sinusoidal applied field for different frequencies. This $\mathbf{b}_{\text{ave}}$ vs. $\mathbf{h}_{\text{surf}}$ relation can be seen as a global constitutive law associated to the entire lamination, with the incorporation of the eddy currents contribution. This law characterises thus the magnetodynamic behavior of the lamination sheet at a larger scale than where the local static *EB* hysteresis model applies.

Regarding the standard loss decomposition from (1.19) (Chapter 1-Section 2.2), this lamination model takes thus the static hysteresis losses and the eddy-current losses into consideration. Eventually, the third contribution, called excess losses, can be included as well if the chosen microscopic hysteresis mechanism goes beyond the simple friction force analogy of the *EB* model and tries to include additional dynamic (or rate-dependent) effects [187, 98]. However, the physical justification of this excess loss term is less clear so it has been decided to disregard it in the context of this thesis. Such dynamic extensions for the *EB* hysteresis model have been proposed in [102, 197].

2. Square - *2D*

The inversion of the various *EB* hysteresis model approaches are experimented in a magnetostatic $\mathbf{a}$-formulation (5.40), with a very simple *2D* square *FE* domain Ω of ferromagnetic material represented in the $\mathbf{xy}$-plane in Fig. 7.5 (left). The direction of the vector potential $\mathbf{a} = a_z\mathbf{e}_z$ is fixed a priori along the $\mathbf{z}$ axis, perpendicular to the studied domain. In that simplified case, the normal component a_z is sufficient to describe the magnetic vector potential, which reduces the computational complexity. The fields $\mathbf{b}$

and **h** lie necessarily in the **xy**-plane in that configuration. The model is only excited from the boundary source term $\langle \mathbf{n} \times (\mathbf{h}_s)_n, \mathbf{a}' \rangle_{\Gamma_h}$ of (5.40), where the tangential component of the magnetic field $(\mathbf{h}_s)_n$ is imposed on all the boundary Γ_h of the square, with values changing with time step n. This mimics a time-varying current layer imposed on the contour, in a perpendicular direction to the **xy**-plane, which induces a uniform distribution of the field **b** and **h**.

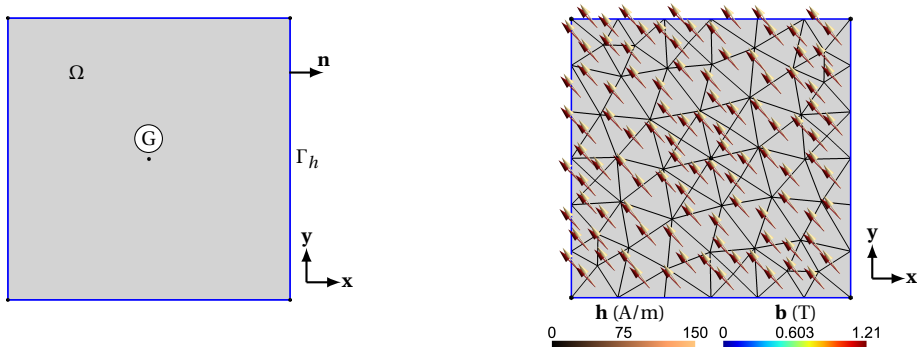

Figure 7.5: *(left): Simple square domain geometry; (right): Meshed domain with the fields distribution result displayed for a given time step ($n = 130$) during a clockwise rotational excitation ($h_{max} = 150\,\mathrm{A/m}, \Phi = 90°$). The delay between the field **b** and the field **h** is a manifestation of the hysteresis.*

This academic square model allows to test several types of excitations, similar to those investigated in Chapter 3-Section 5, but this time in a *FE* context, with in addition the difficulty of the inversion of the material law at each degree of freedom (*DOF*) of the *FE* system. There is a local Newton-Raphson (*NR*) method applied for the model inversion at the material law level with (4.3), for each discretized unknown value in the mesh, and a global *NR* method used to solve the magnetostatic problem (5.40) at the *FE* system level. Therefore, this simple example already provides a sufficiently developed study framework for comparing the influence at the two resolution levels of different implementations with the *EB* hysteresis model. There are indeed several implementations that have been introduced throughout this thesis, from the three direct *EB* model approaches of Chapter 3, with the various inversion techniques of the material law presented in Chapter 4, now included in a *FE* system environment whose resolution by a global *NR* method is also influenced by the implementation choice of several factors, as discused in Chapter 5, such as the way the *FE* Jacobian matrix can be calculated or the selection technique for relaxation factors, to name some but a few.

The goal of this section is not to present all the implementation combinations that exist, but to show some of them which cover a sufficiently wide variety of possibilities, to compare their performance and try to find the association of numerical techniques that provide the most efficient overall implementation, from the point of view of global robustness and computational speed, for the total *FE* magnetostatic square model with the *EB* hysteresis model. It is chosen to limit the model construction to the following implementation choices only:

- The three direct *EB* model approaches at the material law level:
  - the Vector Play Model (*vpm*),
  - the variational approach (*var*),
  - the differential approach (*diff*);
- The inversion techniques of the *EB* model at the material law level:
  - the Newton-Raphson with Jacobian matrix evaluated numerically (NR_{num}),
  - the Newton-Raphson with Jacobian matrix evaluated analytically (NR_{ana}),
  - the Good Broyden–Fletcher–Goldfarb–Shanno algorithm (*GoodBFGS*);
- The evaluation types of the Jacobian matrix in the *NR* method of the *FE* system:
  - the Jacobian matrix evaluated numerically by finite differences (JAC_{num}),
  - the Jacobian matrix evaluated analytically (JAC_{ana});
- The search techniques for the relaxation factors in the *NR* of the *FE* system:
  - the standard search technique (*standard*),
  - the heavy search technique (*heavy*),
  - the accelerated search technique (*accelerated*).

However, the JAC_{num} case is used with the NR_{num} inversion technique exclusively, which comes down to adopt simultaneously numerical Jacobian approximations for both the global and the local *NR* methods. Conversely, the JAC_{ana} case is taken with the NR_{ana} and the *GoodBFGS* inversion techniques only. At the end, all the remaining combinations give $3\times3\times3=27$ varieties of implementations that can be experimented for the magnetostatic **a** formulation with the *EB* hysteresis model.

Each of the 27 implementation diversities are compared on their ability to simulate a series of test cases, with different excitation field sources. In terms of material characteristics, the same 3-cell hysteresis model parameters from Chapter 3-Section 5 are still adopted here. In order to probe as many various magnetization paths as possible and to identify the state changes for which a given magnetostatic system resolution becomes challenging, a set of simulations are excited with various imposed boundary source fields $\mathbf{h}_s(t)\big|_{\Gamma_h}$, of similar characteristics to those used in Fig. 3.13 and Fig. 3.14, i.e. $\mathbf{h}_s(t)|_{\Gamma_h} = h_{\max}\big[\cos(2\pi f t), \cos(2\pi f t - \Phi), 0\big]$, with various maximal amplitude field value components $h_{\max}$, and various phase shifting angles Φ. In that way, a set of 40 different excitation source fields is built, made of 4 different amplitudes, $h_{\max} = 50, 100, 150, 200\,\mathrm{A/m}$, associated with 10 different Φ values, taken between 0° (unidirectional case) and 90° (circular case), by step of 10°. Note that the frequency f has no impact on the final results since the hysteresis model is rate-independent and the magnetic formulation is static here. By default, each simulation includes two periods of 200 time steps each. As the simulations start from the demagnetized state, the source fields $\mathbf{h}_s(t)\big|_{\Gamma_h}$ are smoothly increased in amplitude from 0 to $h_{\max}$ during the 50 first steps, and then reach their typical evolution regimes. The stopping criterion

in the *NR* of the *FE* system is based on a mean L^2-norm of the expression (5.46), using the exported nodal quantities a_z as quantity of interest, and with $\epsilon_{\text{abs}} = 10^{-5}\,\text{T m}$, $\epsilon_{\text{rel}} = 10^{-5}$.

Fig. 7.5 (right) illustrates on a meshed domain the computed fields **b** and **h** obtained with one of the 27 implementation forms at time step $n = 130$, with a purely circular excitation ($\Phi = 90°$) of $h_{\text{max}} = 150\,\text{A/m}$. The **b** and **h** fields distributions are uniform over the square domain. Actually, the vector **h** calculated inside the domain Ω by the magnetostatic system resolution is such that it is the same as the one imposed on the boundary. Thus, it is useless to consider as many triangles as in Fig. 7.5 (right) to mesh the square, since there is no spatial variations of the physical quantities here. This mesh is just used for illustration purpose. Both **b** and **h** vector fields rotate counterclockwise through time, and **b** lags slightly behind **h** due to hysteresis influence.

Each of the 27 implementations of the magnetostatic problem are submitted to the set of 40 simulation test cases, which allow to compare the different implementations over a sufficiently broad spectrum and to draw conclusions on their average overall efficiency. To quantify the quality of an implementation choice, the total central processing unit (*CPU*) time needed to complete a simulation is recorded with the number of iterations required by the *NR* method of the *FE* system to converge per time step. The number of relaxation factors tested per each *NR* iteration at the *FE* system level is also reported.

All the gathered information is summarized in Table 7.1, Table 7.2 and Table 7.3, which are associated to *standard*, *heavy* and *accelerated* relaxation techniques respectively. Each line of these tables corresponds to one combination type of the implementation choices discussed before. Each table contains thus 9 lines, themselves divided into three subsets associated with each choice of model approach. Each subset includes then three lines related to each of the investigated inversion techniques of the *EB* material law model. As decided, the Jacobian determination of the *FE* system is here limited to one specific type for a given inversion technique, thus not requiring the addition of other lines in the tables. By counting all the rows of the three tables, the 27 types of implementations previously mentioned are then well referenced. The values indicated in the last three columns give information on the *FE* convergence characteristics of the implementations. They are derived from the average of the values obtained over all the set of 40 simulation test cases, that is run with every implementation.

As expected, all the simulations gathered in Table 7.3, which rely on the *accelerated* search technique for the relaxation factors, are completed in less time than their counterparts with the *standard* or the *heavy* search techniques, listed in Table 7.1 or Table 7.2, respectively. This can be seen by comparing the average calculation times of each simulation indicated in the fourth columns of the tables. The *accelerated* search gives a speed up between 2 and 4 compared to the *standard* technique, and between 3 and 5 with regard to the *heavy* one. Indeed, when determined by the *accelerated* technique, the relaxation factors allow to reduce the mean number of *NR* iterations that solve the *FE* system at each time step, as shown by the fith column. In addition, there are less relation factors that are tested per *NR* iteration to find a suitable value, as the

Table 7.1: *Simulations with standard search technique for relaxation factors in NR of FE systems.*

approach	inversion method at material level	jacobian type for *FE* systems	*CPU* time (s) per simulation	mean (max) *NR* iterations on *FE* system/time step	mean number of relaxation factors tested/*NR* iter
vpm	*NRnum*	*JACnum*	7.47	9.30 (13)	7.39
	NRana	*JACana*	7.41 (▼)	9.64 (15)	7.26
	GoodBFGS	*JACana*	7.71 (✗)	9.28 (43)	6.93
var	*NRnum*	*JACnum*	25.87 (▲)	4.31 (41)	3.34
	NRana	*JACana*	10.73 (▼)	5.12 (12)	3.28
	GoodBFGS	*JACana*	11.89	5.12 (12)	3.28
diff	*NRnum*	*JACnum*	18.24 (▲)	9.39 (13)	7.43
	NRana	*JACana*	10.4 (▼)	9.78 (14)	7.30
	GoodBFGS	*JACana*	10.89	9.80 (14)	7.29

Table 7.2: *Simulations with heavy search technique for relaxation factors in NR of FE systems.*

approach	inversion method at material level	jacobian type for *FE* systems	*CPU* time (s) per simulation	mean (max) *NR* iterations on *FE* system/time step	mean number of relaxation factors tested/*NR* iter
vpm	*NRnum*	*JACnum*	8.99 (✓)	9.30 (13)	10
	NRana	*JACana*	9.07	9.65 (17)	10
	GoodBFGS	*JACana*	11.69 (✗)	9.58 (32)	10
var	*NRnum*	*JACnum*	58.75 (▲)	4.30 (12)	10
	NRana	*JACana*	24.27 (▼)	5.12 (16)	10
	GoodBFGS	*JACana*	27.52	5.12 (16)	10
diff	*NRnum*	*JACnum*	22.48 (▲)	9.39 (13)	10
	NRana	*JACana*	12.79 (▼)	9.79 (14)	10
	GoodBFGS	*JACana*	13.32	9.80 (14)	10

Table 7.3: *Simulations with accelerated search technique for relaxation factors in NR of FE systems.*

approach	inversion method at material level	jacobian type for *FE* systems	*CPU* time (s) per simulation	mean (max) *NR* iterations on *FE* system/time step	mean number of relaxation factors tested/*NR* iter
vpm	*NRnum*	*JACnum*	2.21	4.65 (31)	2.50
	NRana	*JACana*	1.65 (▼)	3.75 (30)	2.09
	GoodBFGS	*JACana*	1.94	3.90 (37)	2.16
var	*NRnum*	*JACnum*	15.7 (▲)	4.03 (11)	2.12
	NRana	*JACana*	7.27 (▼)	4.66 (31)	2.09
	GoodBFGS	*JACana*	7.74	4.67 (31)	2.09
diff	*NRnum*	*JACnum*	4.24 (▲)	4.76 (33)	2.65
	NRana	*JACana*	2.88 (▼)	5.14 (23)	2.34
	GoodBFGS	*JACana*	2.94	5.13 (25)	2.34

last column numbers are smaller in Table 7.3 than in the two other tables. Thus, this contributes also to reduce the total computational time. Nevertheless, care must be taken that the maximum number of iterations reached per time step is higher with the *accelerated* technique. This indicates that, for some time steps, the *NR* method converges with greater difficulty. With this simple *FE* square geometry example, this does not tend to be more of a problem in the limit of the considered excitations, but for more complicated situations, the *accelerated* technique may lead to non-convergence issues of the *NR* method, more quickly than with the *standard* or the *heavy* techniques,

which are generally more robust.

With the *heavy* search technique, an optimal relaxation factor is selected between 10 linearly spaced values, between 1 and 0.1. At each *NR* iteration, there are always 10 residuals that are thus calculated during the procedure, one with each tested factor, as can be seen with the last column values of Table 7.2. This is why the longest *CPU* time per simulations are encountered with this costly technique.

On the other hand, the *standard* search technique is lighter as it stops as soon as a suitable relaxation factor is found while scanning the same discrete interval from 1 to 0.1 by step of 0.1. Moreover, by looking at the fifth columns of Table 7.1 and Table 7.2, both *standard* and *heavy* techniques practically lead to the same numbers of mean *NR* iterations. It actually means that, most of the times, both techniques lead to the same choice of relaxation factor. This can be explained easily for this relatively simple example. Indeed, the nonlinearity comes here only from the material law that derives somehow from a convex function. However, any local minimum of a convex function is a global minimum. Therefore, the factor found by the *standard* technique which aims to locally minimize the residual is conditioned to be identical to that obtained with the *heavy* technique. Actually, factors tested beyond a minimizing one with the latter technique has no interest in this example. Yet, this is done here to illustrate the additional cost associated with the *heavy* procedure, which may prove useful in other circumstances.

Discussion is now focused on the comparison between the implementation types grouped in a given table. About the choice of the *EB* model approach, the simulations are completed more quickly with the *vpm* approach than with the *var* or the *diff* approaches naturally, as already observed previously. However, the speedup provided by the *vpm* approach is not as significant here as the one observed when comparing at the material law level only in Chapter 3 or Chapter 4. Indeed, the *CPU* times given in the fourth column of the tables are the total simulation times. Thus, they take also the assembling and the resolution times of *FE* systems into account, not only the calculation times of the system components which are those that depend a priori on the hysteresis model approach chosen. In this example, the system is rather small and its construction is not the operation that takes the most time. Therefore, total time ratios between model approaches in this *FE* context have other values compared to ratios encountered in previous chapters. Nevertheless, the fact that *vpm* is faster than *diff* which is itself faster than *var* is still visible here, although to a lesser extent. The *vpm* approach allows speedups between 1.1 and 2.5 with respect to *diff*, and between 1.4 and 7 compared to *var* approach, depending on the other implementation choices.

It is interesting to note that in Table 7.1 and Table 7.2, *FE* simulations including the *var* approach require almost half as many *NR* iterations per time step as with the two other approaches. No real explanation has been found to justify this numerical observation in this example. In theory, *diff* and *var* approaches provide the same solutions with the exception of numerical approximations, and one would expect the number of iterations to be more or less similar, since the stopping criterion is always the same in all simulations. Yet, it is true that the analytical Jacobian (JAC_{ana}) is calculated slightly

differently since it is expressed either in terms of $\mathbf{J}^k$ or $\mathbf{h}^k_{\text{rev}}$, but this remark does not apply for the case with numerical Jacobians (JAC_{num}). The differences in the mean iteration numbers may then be due to numerical approximations in the *var* approach, as it is more subject to cancellation errors, which can thus have an influence in the satisfaction of the stopping criterion of the *NR* method. However, this has not been studied in more detail and no further conclusion can be drawn.

Continuing the analysis of the tables values, the results are now compared by considering the effect of the inversion method choice for the material law on the overall implementation performances. First of all, it can be seen that, for a same combination of global relaxation factor search technique and *EB* model approach, there are few differences brought between NR_{ana} and *GoodBFGS* inversion techniques, either in terms of total computational times or in the numbers of mean *NR* iterations at the *FE* system level. More precisely, one can say however that the NR_{ana} inversion is preferable to the *GoodBFGS* one, as it generally induces slightly shorter *CPU* times per simulation (marked by ▼) in the tables. This is especially true when the *vpm* approach is considered because in that case, the *GoodBFGS* is the least adapted inversion technique that can be chosen, as evident in Table 7.1 and Table 7.2, where it leads to the longest *CPU* times (indicated by ✗), and to the largest maximum numbers of global *NR* iterations, reflecting the difficulties of convergence for certain time steps. This is not surprising since, as seen in Chapter 4, the *GoodBFGS* is suited for symmetric Jacobian matrices while this property is not guaranteed with the local differential reluctivity tensors of the *vpm* approach.

Both *GoodBFGS* and NR_{ana} inversion techniques are always combined with an analytical evaluation of the global Jacobian matrix associated to the *FE* system, denoted by JAC_{ana}. One can now look at the case where a pure numerical approximation of the Jacobians is considered, both locally with a NR_{num} inversion technique, and globally with a JAC_{num} evaluation. The Jacobian matrix components are thus deduced by central finite differences. In the NR_{num}, at the material level, the step for the finite differences varies between subsequent local iterations as the tenth of the last increment on $\mathbf{h}$, to calculate the magnetic permeability tensors. The reluctivity tensors are then deduced by taking the inverse of the latter. In the *NR* method at the global *FE* system level, the JAC_{num} is based on a fixed step of 10^{-2} A/m, which is chosen beforehand by trial and error so as to obtain satisfactory results on this *FE* example.

As expected, compared to the corresponding JAC_{ana} cases, the complete numerical estimation of the Jacobians with the NR_{num}-JAC_{num} association causes a significant increase in the total simulation times for the *var* and the *diff* approaches, by a factor 2 in average, as can be seen with the *CPU* time values (indicated by ▲) in Table 7.1, Table 7.2 and Table 7.3. This happens even if the JAC_{num} cases improve slightly the convergence by needing a little less iterations on the *FE* system to find the solution per time step than the analogous JAC_{ana} cases. This is due to the fact that the NR_{num}-JAC_{num} combination requires additional *EB* model evaluations at each iteration to calculate the finite differences. However, these updates are very costly with the *var* approach, and to a lesser extent, with the *diff* approach. On the other hand, the update of the material law is very fast with the *vpm* approach, such that simulations based on

finite differences do not take necessarily more time than with an analytical evaluation of the Jacobian with this model approach. Therefore, the *vpm*-NR_{num}-JAC_{num} association is not much slower than the alternative implementations *vpm*-NR_{ana}-JAC_{ana} or *vpm*-*GoodBFGS*-JAC_{ana}. Actually, it is even the *vpm*-NR_{num}-JAC_{num} implementation (marked by ✓) that is the fastest between the three variants in Table 7.2. The advantage of the NR_{num}-JAC_{num} type is that it can sometimes make the *NR* process more robust and require fewer mean iterations to converge. On the other hand, it is necessary to determine an adequate step for the calculation of the finite differences and this is not always easy to find a satisfactory one for the *FE* problem.

It should be remembered that the values given in the summarizing tables are averaged over 40 test cases. Details of the *CPU* times and the mean *NR* iterations values obtained for each of the 40 simulations with the 27 implementations are shown in the 9 following Figures (3 implementations per Figure), from Fig. 7.6 to Fig. 7.14.

All these Figures reveal that, mostly with *standard* and *heavy* relaxation techniques (from Fig. 7.6 to Fig. 7.11), the *CPU* times and the mean *NR* iterations on *FE* system per time step have the global tendency to increase in function of the maximal amplitude $h_{\max}$, and the rotational nature Φ, of the excitation that is used in the simulation.

The *CPU* times measured with the *var* approach (Fig. 7.7, Fig. 7.10, Fig. 7.13) are less predictable as they do not behave as smoothly with respect to $h_{\max}$ and Φ. Updating the *var* approach seems to be sometimes more complicated for specific excitation test cases than others, but the understanding of this behavior is very empirical. Some test cases are also more difficult to solve than others with the inappropriate *vpm*-*GoodBFGS* association. They are distinguished by higher computational time values than with the corresponding *vpm*-NR_{ana} combination cases, as can be observed by comparing in Fig. 7.6, Fig. 7.9 and Fig. 7.12, the bottom middle and the bottom right *CPU* time curves.

With the *accelerated* relaxation technique (Fig. 7.12, Fig. 7.13 and Fig. 7.14), the mean *NR* iteration numbers and the *CPU* times remain rather small over all the various excitation characteristics $h_{\max}$ and Φ, except with the *var* approach (Fig. 7.13) or with the *vpm*-*GoodBFGS* combination (Fig. 7.12 (right)), where some discrepancies appear for some test cases, as already mentioned earlier.

In conclusion of this section, a rather large set of different implementations of the *EB* model in a simple *FE* framework has been studied. The proposed implementation choices intervene at different levels, either at the level of the magnetic material law, or at the level of the global *FE* system. The choice of one implementation rather than another can be guided by performance motivations but also by robustness needs. Thus, it is clear that the *accelerated* relaxation technique gives the shortest simulation times, but risk-taking with overly large relaxation factor selection can be fatal in other more complex situations where the *heavy* relaxation can then be helpful. The extra cost associated with this latter choice has been quantified for this example. At the material level, the *vpm* approach remains the fastest compared to the *diff* approach, and even more with regard to the *var* approach. However, the speedups are less significant than

expected due to the inclusion in this *FE* context. About the model inversion, the technique that stands out the most is the NR_{ana} technique which remains one of the best choices in all circumstances, compared to NR_{num} or *GoodBFGS*. Finally, the numerical evaluation of the Jacobians based on finite differences should be avoided as much as possible with the *var* or the *diff* approaches, because the model update calls are then computationally costly with these approaches and must be limited. The analytical evaluations of the Jacobian matrices based on the developments of Chapter 4 find then all their interest here. This does not apply for the *vpm* approach, whose resolution is straightforward and thus lends itself well to a finite difference approximations of the deriatives. A numerical evaluation of the Jacobian matrices, if determined by an appropriate choice of discretization step, can further improve the robustness of the iterative process. In the end, the problem of choice always comes down to a compromise between speed and robustness.

Search Technique for Relaxation Factors in *NR* of *FE* Systems: *standard*.
Hysteresis Model Approach: *vpm*.

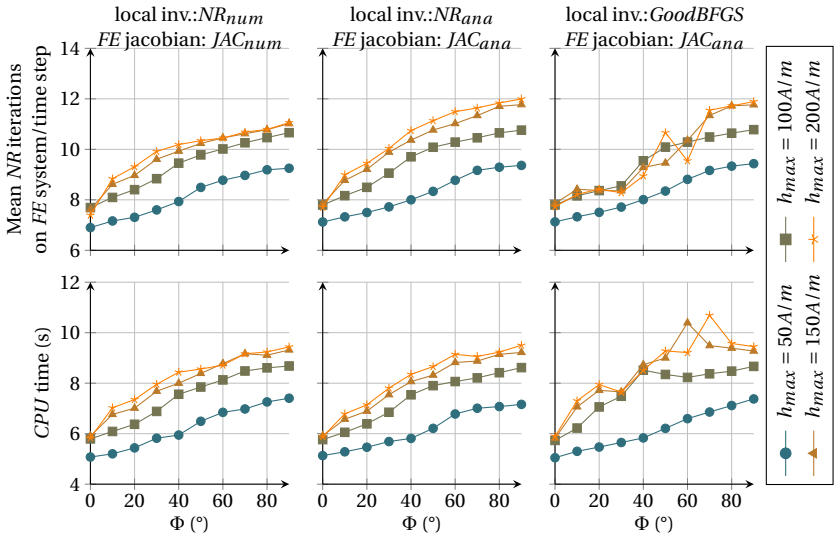

Figure 7.6: *Details on performances with standard relaxation & vpm approach over* 40 *simulation test cases.*

Search Technique for Relaxation Factors in *NR* of *FE* Systems: *standard*. Hysteresis Model Approach: *var*.

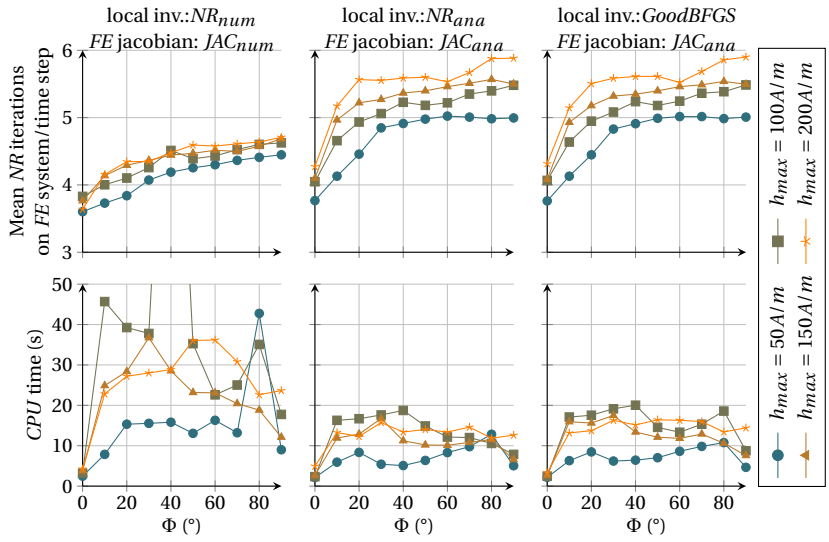

Figure 7.7: *Details on performances with standard relaxation & var approach over* 40 *simulation test cases.*

Search Technique for Relaxation Factors in *NR* of *FE* Systems: *standard*. Hysteresis Model Approach: *diff*.

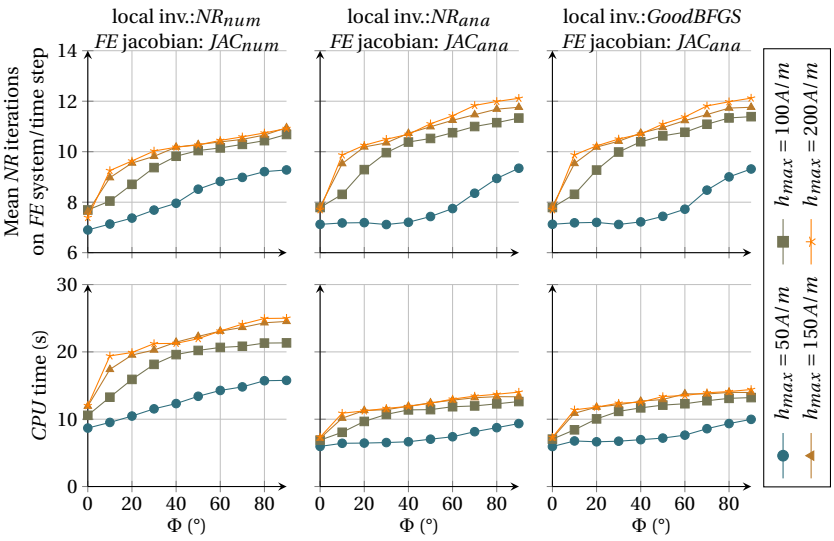

Figure 7.8: *Details on performances with standard relaxation & diff approach over* 40 *simulation test cases.*

Search Technique for Relaxation Factors in *NR* of *FE* Systems: *heavy*.
Hysteresis Model Approach: *vpm*.

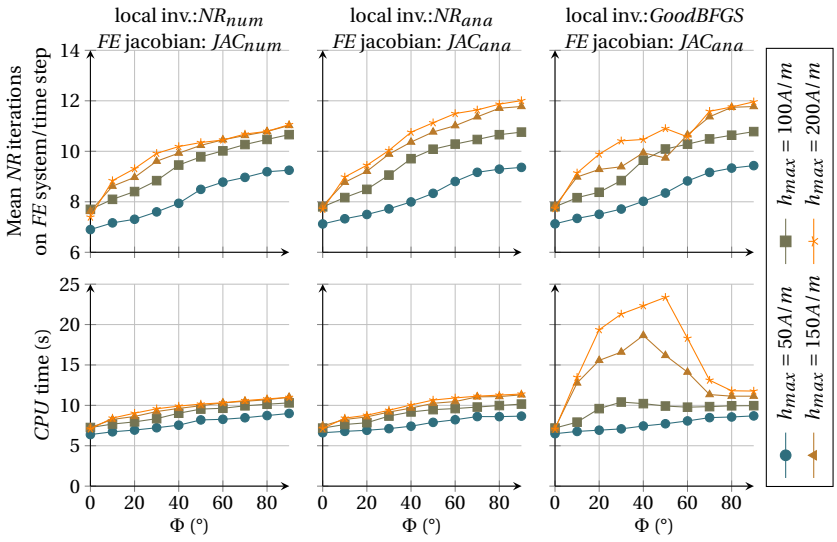

Figure 7.9: *Details on performances with heavy relaxation & vpm approach over 40 simulation test cases.*

Search Technique for Relaxation Factors in *NR* of *FE* Systems: *heavy*.
Hysteresis Model Approach: *var*.

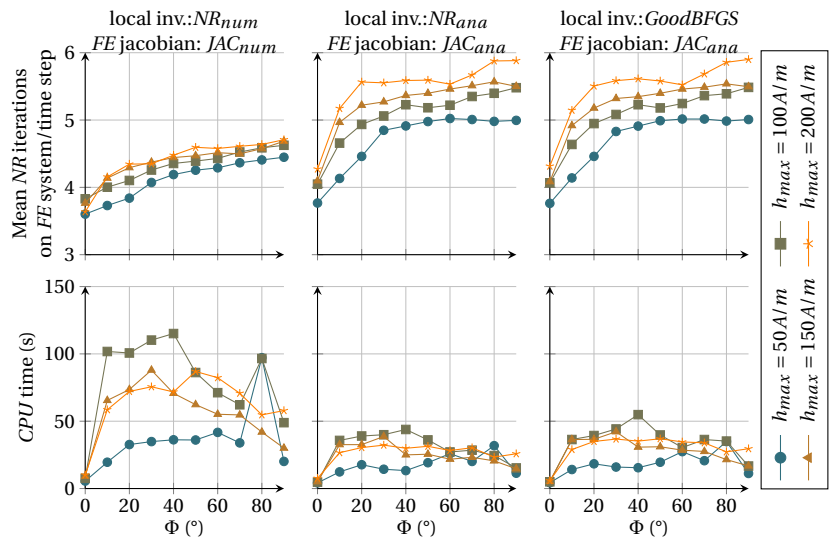

Figure 7.10: *Details on performances with heavy relaxation & var approach over 40 simulation test cases.*

Search Technique for Relaxation Factors in *NR* of *FE* Systems: *heavy*.
Hysteresis Model Approach: *diff*.

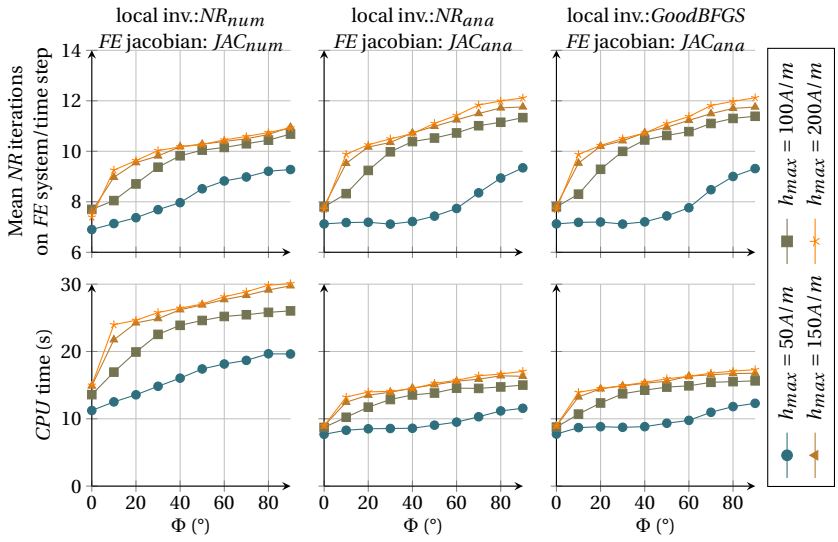

Figure 7.11: *Details on performances with heavy relaxation & diff approach over* 40 *simulation test cases.*

Search Technique for Relaxation Factors in *NR* of *FE* Systems: *accelerated*.
Hysteresis Model Approach: *vpm*.

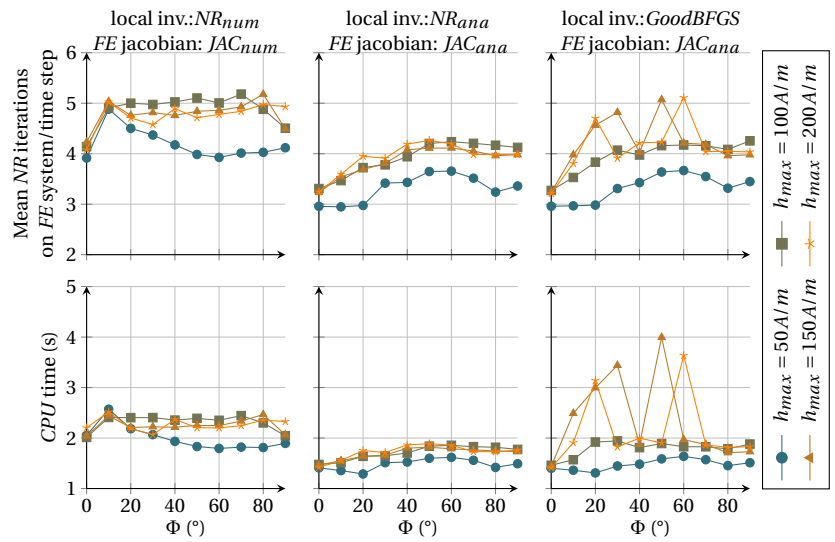

Figure 7.12: *Details on performances with accelerated relax. & vpm approach over* 40 *simulation test cases.*

Search Technique for Relaxation Factors in *NR* of *FE* Systems: *accelerated*. Hysteresis Model Approach: *var*.

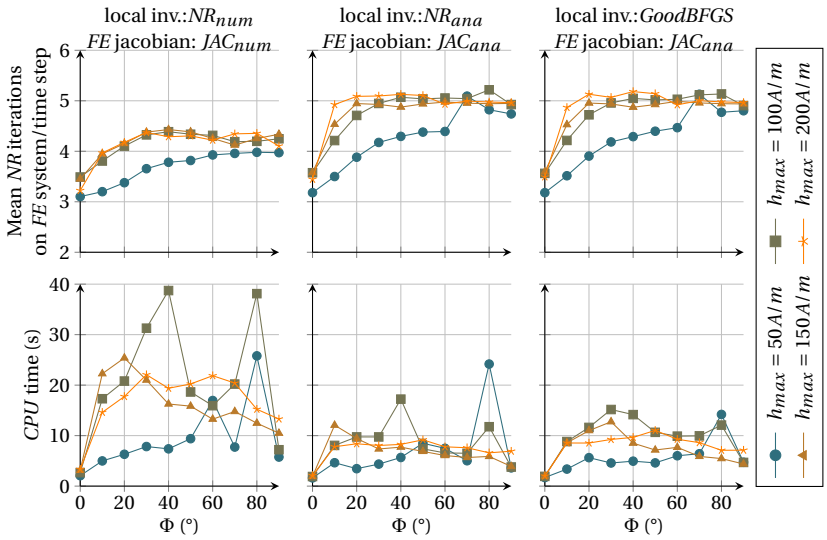

Figure 7.13: *Details on performances with accelerated relax. & var approach over* 40 *simulation test cases.*

Search Technique for Relaxation Factors in *NR* of *FE* Systems: *accelerated*. Hysteresis Model Approach: *diff*.

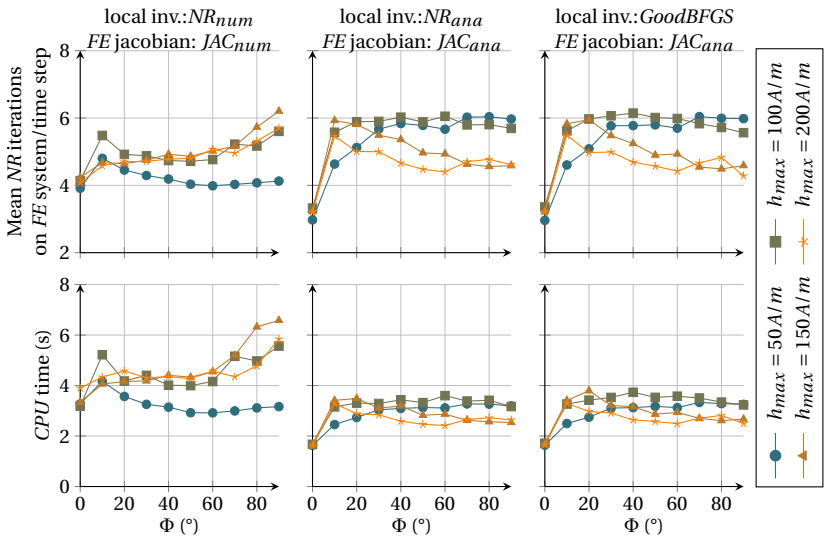

Figure 7.14: *Details on performances with accelerated relax. & diff approach over* 40 *simulation test cases.*

3. T-joint - *2D*

In this section, *FE* simulations with the magnetostatic **a** formulation (5.40), which includes thus the inverse **b**-based hysteresis model, are compared with those realized with the complementary magnetostatic ϕ formulation (5.29), which relies on the direct **h**-based hysteresis model instead. This comparison is conducted with the idea of validating the inversion of the *EB* hysteresis model and measuring its computational cost in a *FE* context.

The complementary formulations are applied to a simple *2D FE* domain, shown in Fig. 7.15, which is a T-shaped magnetic circuit exhibiting rotational flux [97], which can be assimilated to a T-joint of a three-phase transformer.

For the **a** formulation, since the problem is *2D*, the magnetic vector potential **a** can once again be represented by its normal component to the studied domain only. Thus, the scalar notation a is employed to denote the nodal value of the vector component of **a** along the **z** axis, which is sufficient for its representation.

The boundary Γ of the studied T-joint domain Ω is considered as an alternating series of flux walls Γ_{wj} and flux gates Γ_{gj} [97]. By definition, flux walls Γ_{wj} are magnetically impermeable interfaces, on which $\mathbf{n}\cdot\mathbf{b}=0$ holds, with $\mathbf{n}$ the outward unit normal on Γ. The related magnetomotive forces are expressed by $\mathscr{F}_j = \langle \mathbf{n}\times\mathbf{h}, 1\mathbf{e_z}\rangle_{\Gamma_{wj}}$. On the other hand, flux gates Γ_{gj} correspond to perfectly permeable interfaces, on which $\mathbf{n}\times\mathbf{h}=\mathbf{0}$ is verified. The magnetic fluxes flowing through the gates, inward Ω, are given by $\Phi_j = -\langle \mathbf{n}\cdot\mathbf{b}, 1\rangle_{\Gamma_{gj}}$. Therefore, the sum of the magnetomotive forces $\mathscr{F}_j$ is zero, and so does the sum of the fluxes Φ_j.

In the **a** formulation, a has a constant value A_{wj} along each flux wall Γ_{wj}. Gate fluxes between two walls can be strongly imposed by fixing the two associated A_{wj} values as $\Phi_j = A_{wj} - A_{wk}$. Otherwise, an A_{wj} value can be considered as a floating potential unknown of the problem. In that case, the linked magnetomotive force $\mathscr{F}_j$ is weakly imposed through the contour integral in (5.40). To this end, a specific basis function is

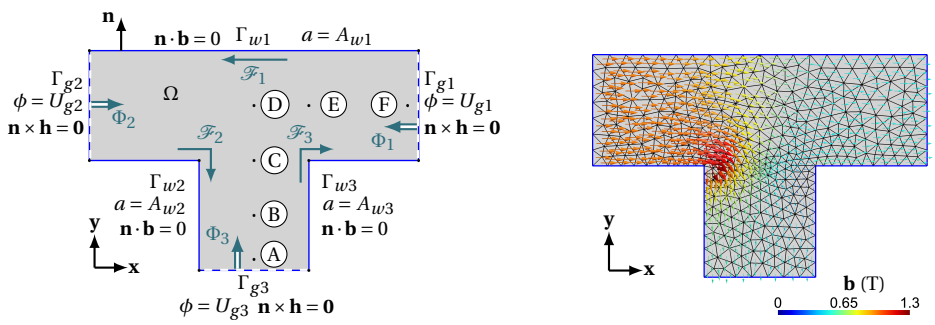

Figure 7.15: *(left): Schematic representation of a 2D model of a T-joint of a three-phase transformer with, as boundary, a sequence of three flux walls $\Gamma_{w1},\Gamma_{w2},\Gamma_{w3}$ and three flux gates $\Gamma_{g1},\Gamma_{g2},\Gamma_{g3}$, and the location of 6 points A, B,..., F. (right): Induction field obtained during a simulation at $t = 1s$ (time step 1000).*

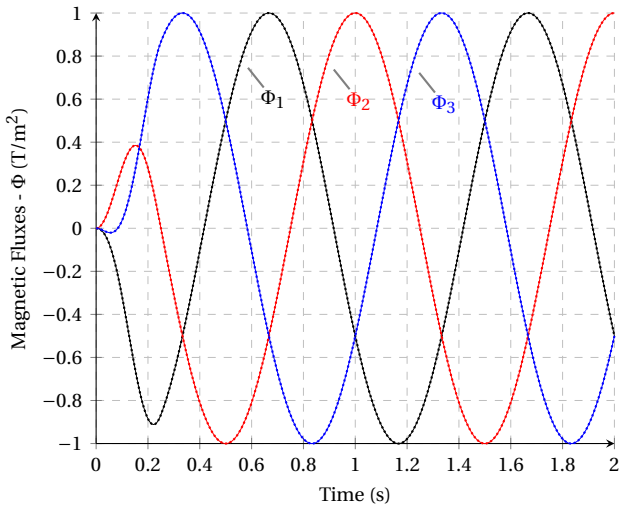

Figure 7.16: *Magnetic fluxes imposed in the three flux gates with soft start.*

used which decreases element-wise linearly from 1 on Γ_{wj} to 0 in the layer of elements around Γ_{wj}. Equivalently, in the ϕ formulation, ϕ can either be fixed *a priori* or constitutes a floating potential $\phi = U_{gj}$ on the corresponding flux gates Γ_{gj}. Therefore, in the latter case, the associated magnetic flux Φ_j is weakly imposed via the contour integral in (5.29).

The same 3-cell material hysteresis model used since Chapter 3-Section 5 is still considered. A rotational field is effected by imposing strongly in the **a** formulation and weakly in the ϕ formulation the gate fluxes $\Phi_1 = \cos(2\pi f t + 2\pi/3)$ and $\Phi_2 = \cos 2\pi f t$, with a frequency arbitrary fixed to $f = 1\,\text{Hz}$. Two periods are sampled with 1000 time steps each. In order to start smoothly through the first magnetization curve of the hysteretic material, the fluxes Φ_1 and Φ_2 are multiplied during the first quarter of a period by the function $(1 - \cos(\pi t / t_{\text{relax}}))/2$, with $t_{\text{relax}} = 0.25\,\text{s}$. The evolution of the two imposed magnetic fluxes conditions the third one which are shown in Fig. 7.16.

For both formulations, the chosen stopping criteria of the *NR* method for the *FE* system resolutions is defined by (5.47), with $\epsilon_{\text{abs}} = 10^{-6}\,\text{A/m}$ and $\epsilon_{\text{rel}} = 10^{-6}$. At each *NR* iteration, a *heavy* search technique is adopted with an optimal relaxation factor selected between 10 evenly spaced values between 1 and 0.1. The Jacobian is computed analytically. The first iterate is approximated by quadratic extrapolation from the three previous time solutions, as in Fig. 5.2 (right).

The *FE* mesh is made of 843 triangles and yields 403 and 442 *DOFs*, for **a** and ϕ respectively after the application of constraints. Fig. 7.15 (right) shows the look of the induction field obtained during a simulation at $t = 1\,\text{s}$ (time step 1000), when the inward magnetic flux Φ_2, from gate Γ_{g2}, is maximal. The field rotates in and out of the different gates over time and takes the largest values in the corners of the T-joint.

Simulations are performed with the three model approaches, *vpm*, *var* or *diff*, which are used either in their direct or inverse form depending of the *FE* formulation chosen, **a** or ϕ. To have time references for both formulations, simulations are also realized without using an *EB* hysteresis model, but using a restricted anhysteretic law (*anhy*) approach for the magnetic constitutive law, built by interpolation on a database of a one-to-one $b-h$ curve, which corresponds to the same anhysteretic curve that is exploited in the hysteresis model.

The information on convergence characteristics of the different formulations of the T-joint problem is given in Table 7.4.

Table 7.4: *Convergence characteristics of different FE formulations for the T-joint problem.*

FE formulation	approach	total *CPU* time (minute)	mean (max) *NR* iterations on *FE* system/time step	*CPU* time per *NR* iteration (s)	number of non-converged time steps
a	*anhy*	7.3	3.00 (3)	$7.26\cdot10^{-2}$	0
a	*(inv) vpm*	28.5	3.68 (13)	0.23	0
a	*(inv) var*	610.6	6.93 (50)	2.64	3
a	*(inv) diff*	46	4.13 (13)	0.33	0
ϕ	*anhy*	5.1	2.03 (3)	$7.56\cdot10^{-2}$	0
ϕ	*(dir) vpm*	28.7	4.11 (14)	0.21	0
ϕ	*(dir) var*	91.4	3.95 (50)	0.69	3
ϕ	*(dir) diff*	38.4	4.02 (14)	0.29	0

Naturally, the *anhy* approaches require less *CPU* time to finish the simulation than with an *EB* hysteresis model inclusion. Actually, in this example, the *vpm* approach, which is the fastest *EB* model implementation, takes about 3.9 and 5.6 times more total *CPU* time than the respective *anhy* cases, in the **a** and ϕ formulations. However, since the total number of iterations is not exactly the same for the different formulations, it is also interesting to compare *CPU* times taken per *NR* iteration, reported in the fifth column of Table 7.4. Then, it appears that the *vpm* approach is about 3.1 or 2.8 times as long per *NR* iteration as in the *anhy* cases, in the **a** and ϕ formulations respectively. It seems logical to find a ratio of around 3 since it is a 3-cell *EB* hysteresis model that is considered here.

For all the *EB* model approaches, the *CPU* time cost per *NR* iteration is always slightly higher with the **a** formulation than with the ϕ formulation due to the additional inversion of the hysteresis model needed at the material law level. In this example, this additional inversion cost is not very visible for the *vpm* and *diff* approaches, which take only about 1.09 and 1.13 more *CPU* times per *NR* iteration in the **a** formulation compared to the ϕ formulation. Moreover, with the *vpm* approach, this is not even noticeable on the total *CPU* times reported in the third column because the ϕ formulation requires a little more *NR* iterations than the **a** formulation. Generally speaking, the *diff* approach is slower than the *vpm* approach but at a reasonable cost here, knowing that each cell update with the *diff* approach is complicated by an additional angle search problem while the *vpm* updates are straightforward, such as with the *anhy* cases.

On the other hand, the *var* approach remains the most complicated *EB* model implementation. It takes the most *CPU* time to complete a simulation as it is 3.3 times as long per *NR* iteration as with the *vpm* approach in the ϕ formulation and, even worse, up to 11.4 as long in the **a** formulation, which leads to a total *CPU* time longer than 10 hours to solve this rather simple *FE* problem, while only 7 minutes are required with an *anhy* approach in the same conditions. All the complexity of the *var* implementation structure worth to be recalled here: there is the problem of loss of significance that can occur during the minimization update at each cell level, which adds to the approximation of the material law inversion with the local *NR* method needed in the **a** formulation, which is itself encompassed in the global *NR* method of the *FE* system. It must be mentioned that, given all these sources of imprecision that are involved at all levels of the implementation, the chosen stopping criterion (5.47), with $\epsilon_{\text{abs}} = 10^{-6}$ A/m and $\epsilon_{\text{rel}} = 10^{-6}$ seems to be very strict for the *var* approach. As a result, it is not surprising to find that the *NR* method of the *FE* system does not manage to satisfy that stopping criterion for 3 on the 2000 time steps of the simulations both in the **a** and ϕ formulations[1]. Nevertheless, although the maximum number of iterations, set at 50, has been reached for those time steps, the *FE* model has not been destabilized for the cause and the subsequent time steps were successfully calculated.

The computed evolution for the magnetomotive forces $\mathscr{F}_1(t), \mathscr{F}_2(t)$ and $\mathscr{F}_3(t)$, associated to flux walls Γ_{w1}, Γ_{w2} and Γ_{w3} respectively, are shown in Fig. 7.17, obtained with the inverse or direct *var* approaches in the **a** or ϕ formulations, respectively. A very good agreement is observed between the results of both formulations on these global quantities. The same correspondence is obtained with the *vpm* or the *diff* approaches, which produce the same curves as in Fig. 7.17.

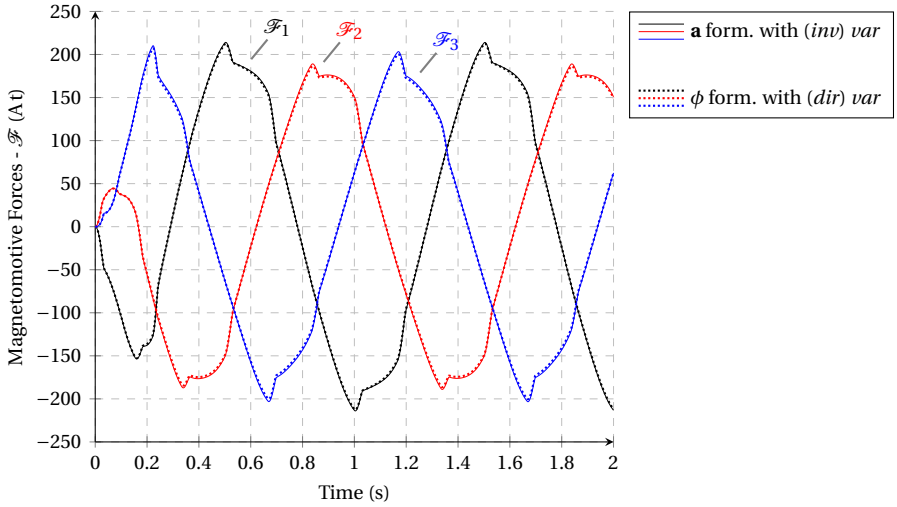

Figure 7.17: *Agreement between the magnetomotive forces (global quantities) obtained via the* **a** *formulation, including the inverse var approach; and the* ϕ *formulation, including the direct var approach.*

[1] not necessarily at the same time steps however.

Still focusing on the results from the *var* approach with both the **a** and ϕ formulations, the produced b-loci and h-loci, in addition with the $b_x - h_x$ and $b_y - h_y$ loops are given in Fig. 7.18, at the six points indicated in Fig. 7.15 (left). As can be observed, from the point of view of local quantities, the difference between the results provided for the **b** or **h** field values by the two formulations is more pronounced for certain points. However, this difference is more related to the quality of the mesh size than to an effect due to the inversion of the hysteresis model. Indeed, a similar gap occurs when considering an *anhy* approach. The results can be improved by refining the mesh size, but for an obviously higher computational cost. For the local fields, both formulations produce then outputs that are also very similar.

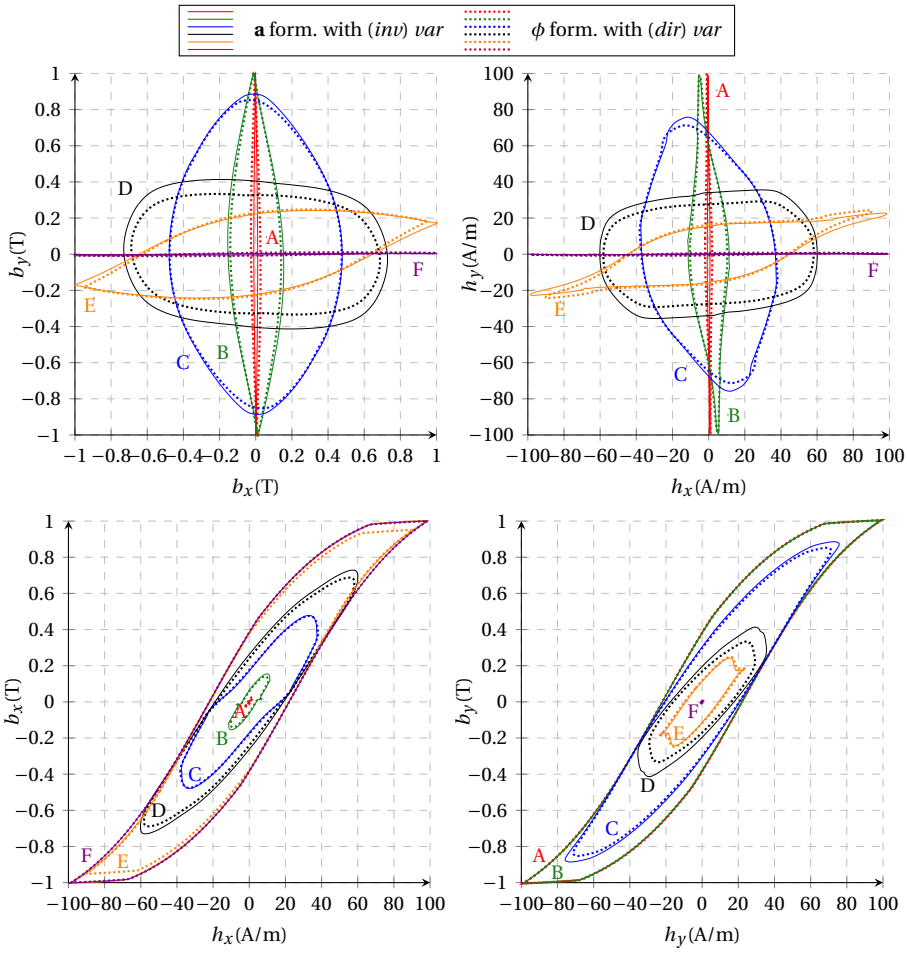

Figure 7.18: ***b****-loci (top left),* ***h****-loci (top right),* $b_x - h_x$ *curves (bottom left),* $b_y - h_y$ *curves (bottom right), obtained at the 6 points A,B,...,F of the T-joint, either via the* **a** *formulation with the inverse var approach (continuous lines), or via the* ϕ *formulation with the direct var approach (dotted lines).*

The *vpm* approach is still a very good approximation in this T-joint example as the local

curves in Fig. 7.19 highlight. At the level of the **b** and **h** fields, obtained at the 6 points of the T-joint, the simulation results obtained with the *vpm* are indeed relatively close to those obtained with the *diff* approach, the two simulations having been conducted in the **a** formulation, using the inverse models. The *diff* and *var* approaches give similar results with the exception of numerical approximations.

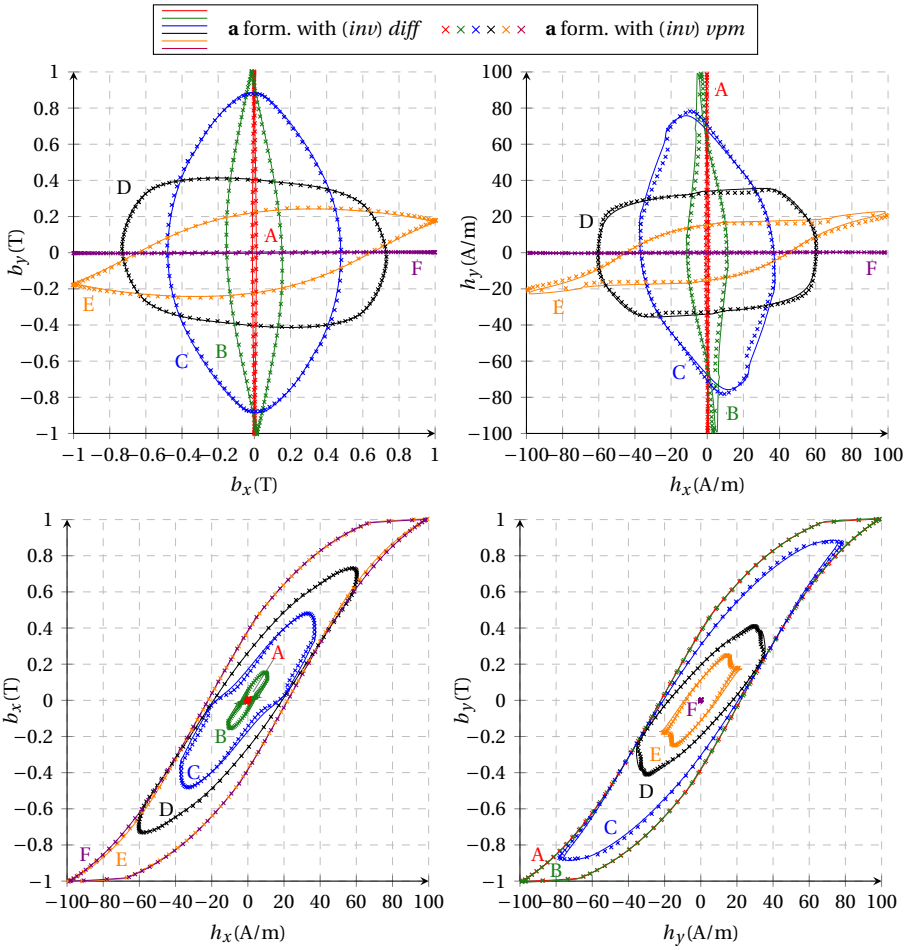

Figure 7.19: ***b****-loci (top left),* ***h****-loci (top right),* $b_x - h_x$ *curves (bottom left),* $b_y - h_y$ *curves (bottom right), obtained at the 6 points A,B,...,F of the T-joint, via the* **a** *formulation by including either the inverse diff approach (in continuous lines) or the inverse vpm approach (cross marks).*

In summary, **a** and ϕ formulations including the *EB* hysteresis model converge to the same results, both globally and locally. The additional cost due to the inversion of the material law is not significant for the *vpm* or *diff* approaches. The choice is thus more or less free to adopt one or the other *FE* implementation, either **b**-conform or **h**-conform, according to the regularity needs, independently of the hysteresis model, whether it is direct or inverse, since inversion does not have a preponderant influence

on the efficiency of one formulation compared to the other. The implementation with the *var* approach is the most complicated to make it work and should not be recommended in practice, unless to accept a relaxation of the stopping criterion. The *vpm* approach allows once again a fast implementation of the *EB* hysteresis model, as fast as an *anhy* approach, regarding the multi-cell aspect. Moreover, it remains an excellent approximation in this *FE* example, giving results visually very close to those obtained with the *diff* and *var* approaches.

4. Three-Phase Transformer - *2D*

In this section, the simulations of a three-phase transformer, originally studied in [100], aims to be conducted using either the $\mathbf{a}-v$ or $\mathbf{h}-\phi$ *FE* formulations, i.e. (5.36) or (5.25), with the *EB* hysteresis model embedded in either its inverse or direct form respectively. Furthermore, the *vpm*, *var* and *diff* implementations of the hysteresis model are compared in this context. Finally, the mesh influence and the computational times are analyzed between the different *FE* formulations with the *vpm* hysteresis model, and contrasted with the nonlinear *anhy* material law case.

Fig. 7.20 (left) shows the cross-section of the three-phase transformer. The laminated ferromagnetic core is the region where the 3-cell *EB* hysteresis model is employed, still with the same material parameters as before. Each phase has one primary and two secondary windings. In the *FE* formulations, the windings are seen as stranded inductors Ω_s. Electric global quantities are employed in these regions for the coupling with circuit equations and for defining voltage sources [60]. Hereby, only the primary windings are supplied by voltage sources. The transformer representation is surrounded by air even if in no-load operation the leakage flux is negligible, so that it may be sufficient to only model the magnetic core as done in [100]. A *FE* mesh shown in Fig. 7.20 (right) with 1770 first-order triangles is used by default. The number of triangles is controlled by a mesh scale factor (*MSF*) fixed at 2 for this case. The description of the device is restricted to a *2D* case in which the fields **h** and **b** lie in the **xy**-plane, and the current density **j** is assumed perpendicular to the study domain.

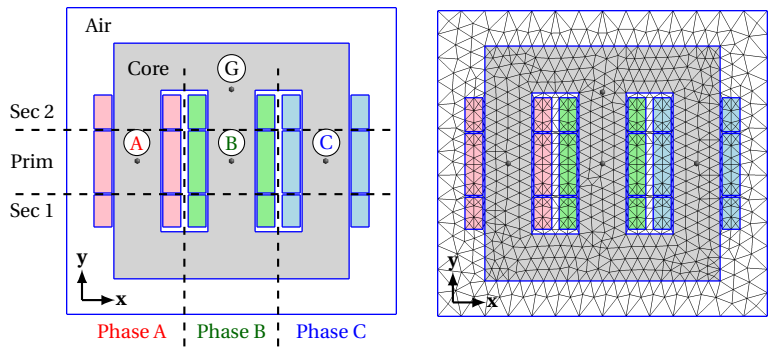

Figure 7.20: *2D FE model of the three-phase transformer (left); meshed by* 1770 *triangles,*788 *of them belonging to the core region - [mesh scale factor=* 2 *(MSF2)] (right).*

The eddy currents in the laminations, mainly flowing parallel to the plane of the laminations, cannot thus be modeled straightforwardly in this *2D* case. Yet, they exist techniques [96, 63, 169] to include the eddy current losses in the laminated core with both *FE* formulations (5.36) or (5.25). One of them, being very simple at least for the $\mathbf{a}-v$ formulation, consists in introducing, based on (7.7), an additional conductivity matrix dedicated to the lamination into the *FE* equations [100, 98], which yields the correct losses, assuming the skin and edge effects are negligible. However, because the implementation of this contribution in the dual $\mathbf{h}-\phi$ formulation is not as straightforward, the laminated core is assumed non conductive Ω_c^C in both formulations. With this simplification, the formulations are thus still limited to a magnetostatic case actually, as studied in the T-joint example of the previous section. The novelty of this section is that the model, although still rather academic given these assumptions, becomes a little more realistic by the introduction of coupling with external circuits in the *FE* description which allows imposition of more appropriate voltage-driven sources.

Furthermore, the *2D* restriction allows to express the $\mathbf{a}-v$ formulation in terms of a vector potential $\mathbf{a}$ whose direction can be fixed a priori along the $\mathbf{z}$ axis and of which only the normal component constitutes then the unknown. With this assumption, the gauge condition $\mathrm{div}\,\mathbf{a}=0$ is automatically ensured. The same applies for the electric potential gradient, $\mathbf{grad}\,v$, where only the component along $\mathbf{z}$ can be considered[2]. The function spaces of these potentials are thus adapted in consequence, simplifying the resolution of the problem.

On the other hand, for the $\mathbf{h}-\phi$ formulation, a source magnetic field $\mathbf{h}_s$ has to be calculated for each active stranded inductor. Each inductor is represented in the cross-section by two rectangle regions around a core leg and have to be linked together with the introduction of cuts in order to make the complementary domain simply connected for the correct definition of the potential ϕ. These source magnetic fields and associated cuts are generated a priori through the technique developed in [58] which projects a known distribution $\mathbf{j}_s$ to a function space of $\mathbf{h}_s$ associated with co-tree edges of the mesh.

Eventually, the $\mathbf{a}-v$ formulation is more commonly used in *2D* problems before the $\mathbf{h}-\phi$ formulation, because the former can be solved more easily in this case, simplifying from vector to scalar unknowns, while the latter requires additional processing, particularly for multiply connected domains. However, the $\mathbf{h}-\phi$ formulation should not be forsaken because it has its own advantages at the discrete level. It allows to satisfy exactly the Ampere law (5.11), instead of the Faraday law (5.12) with the dual $\mathbf{a}-v$ formulation, so that the choice of the formulation can be made according to the type of desired conformity. Most notably, the *EB* hysteresis model can be included in a direct way (direct form (*dir*)) in the $\mathbf{h}-\phi$ formulation, without the inversion operation (inverse form (*inv*)) that may take slightly additional computation time in the dual formulation, as already discussed in the previous section. It is interesting to compare these dual formulations also in this three-phase transformer modeling context. Nonetheless, *FE* simulations on electromagnetic devices taking any hysteresis model

[2] Anyhow, the electric potential v equals zero everywhere in this example, following the simplifications.

into account are usually based on the **a** formulation in the literature [94, 8, 51, 149, 91], even if the hysteresis model is in general natively driven by the magnetic field **h**. This is why the two formulations are considered and compared in this practical example.

The transformer is studied in case of three-phase no-load operation starting from the demagnetised state of the ferromagnetic core. The three primary windings are connected in star and supplied at 50 Hz by 220 V root mean square (*RMS*) value voltages whose amplitudes gradually increase from zero to the nominal value [100], as in Fig. 7.21. The time-stepping simulations include 6 periods of 300 time steps each and steady

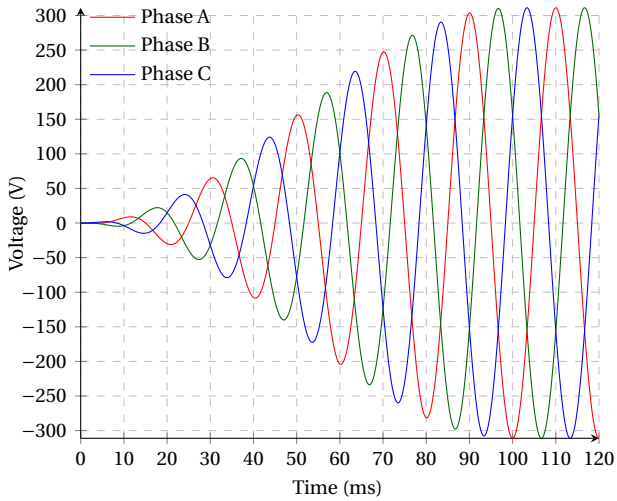

Figure 7.21: *Smooth start of the Voltages imposed in the three primary windings.*

state is reached after say 5 periods.

Fig. 7.22 shows the calculated current waveforms for the last period obtained with both formulations including either the *vpm* or the *diff* hysteresis model implementations, in their *dir* or *inv* forms, depending on the *FE* formulation. Each simulation produces globally the same evolution for the primary currents in the three phases. Note that the results with the *var* implementation are intentionally not depicted in Fig. 7.22 for a better visibility, because they would overlap the *diff* approach results. As a general remark, it can be seen that the steady-state is not totally reached in Fig. 7.22 because there is still a remaining direct current (*DC*) offset between phases. Due to the core asymmetry, the magnetizing current of phase *B* is lower than the current obtained for the two outer phases. There are slight differences between the results from the four different simulation cases. The discrepancies in the currents are more pronounced between **a**−ν and **h**−ϕ formulations than by the choice between *vpm* or *diff* hysteresis model approaches. Indeed, the calculated maximal value of the current in phase *A*, for example, is more affected by the formulation than by the hysteresis model approach that is used. There is a variance in the extreme value of about 0.07 A (8.5 %) between the *FE* formulations while there is only 0.01 A (1.6 %) change linked to the hysteresis

model approach chosen[3].

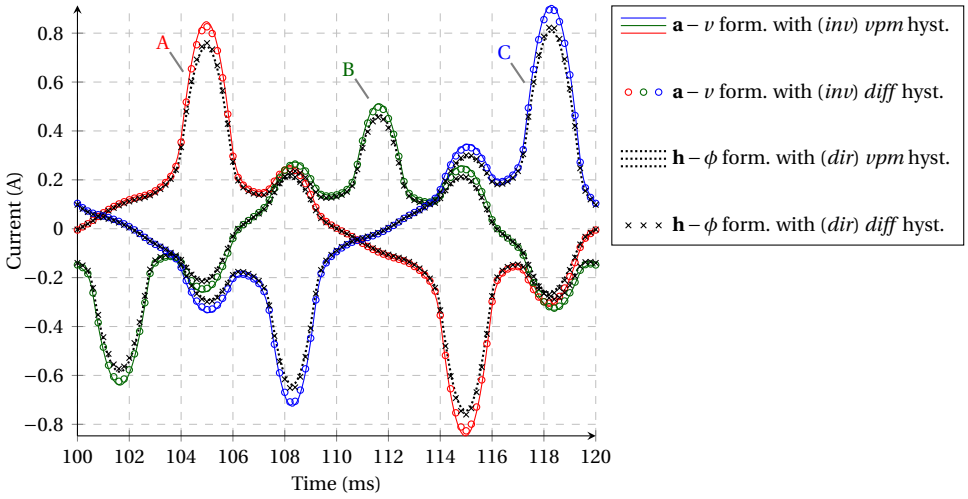

Figure 7.22: *Currents in the primary windings with each simulation configuration, for the last period.*

The local $b-h$ quasi-static hysteresis loops, produced by the four simulation cases at points A, B and C during the last period, are presented in Fig. 7.23 (left). The three legs of the transformer are alternately subjected to an equivalent flux producing, at these central points, similar hysteresis loops which overlap visually in the presented figures. There is a great agreement between the curves obtained from the different simulations. Actually, at these points, the magnetic polarization is unidirectional such that *vpm* with *var* and *diff* approaches are totally identical, as there is no additional approximation coming from the *vpm* version. Likewise, the choice between $\mathbf{a}-\nu$ or $\mathbf{h}-\phi$ formulations do not bring any significant modification in the output fields at these locations.

Fig. 7.23 (right) illustrates, for the various investigated simulation cases, the loci of the rotating induction field $\mathbf{b}$ at the point G situated in the T-joint of the transformer. In this place, the local behavior is completely different than in the middle of the leg, with almost a circular polarization. The variations between the simulation field outputs are more pronounced than previously. In this example, the differences induced by the formulation selection are more important than those introduced by the hysteresis model approach choice. Indeed, as the induction pattern is almost circular in this region, the approximated *vpm* approach leads to nearly the same results as with the exact *diff* or *var* approach. The *var* approach results are once again not represented for clarity in Fig. 7.23, and they are identical to the *diff* approach results. The average deviation of the induction field over one period between the *vpm* and the exact *diff* or

[3]The median value between the compared results is used as reference to evaluate the relative deviation in %.

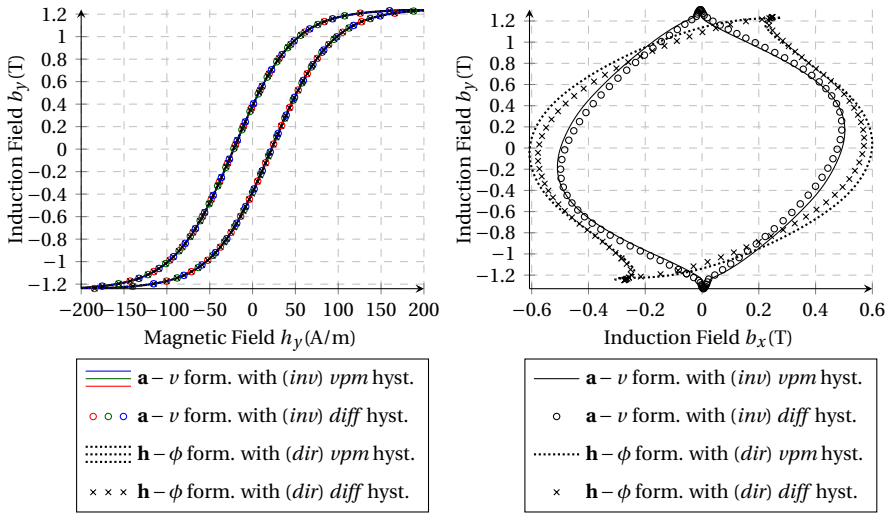

Figure 7.23: *$b-h$ curves at Points A,B,C (left); **b** loci at Point G (right).*

var hysteresis approaches is of only 0.02 T (2.3 %). On the other hand, the formulation selection has a huge influence here, resulting in variations on the local induction field of about 0.23 T (25 %). In this situation, there is absolutely no interest in using the more accurate but much more costly *diff* or *var* approach compared to the *vpm* approach because the benefit of a higher quality hysteresis representation is lost in the numerical approximation introduced by the *FE* formulation choice.

However, the differences linked to the *FE* formulations are related to the density of the mesh that is used and this disparity can be reduced either by using higher order *FE* or by increasing the number of elements used to mesh the studied domain.

Fig. 7.24 and Fig. 7.25 illustrate how the results from **a** – ν and **h** – ϕ *FE* formulations including the *vpm* approach, vary with a progressive mesh refinement through the increase of the *MSF* that controls the number of triangle density. More particularly, in Fig. 7.24 (left), one can see how the waveforms of the primary current in phase A obtained with each *FE* formulation are getting closer, when the number of triangles increases from the coarsest mesh (*MSF*1) with 562 elements to the finest one (*MSF*4) with 25288 elements. The variation on the peak value of the current is reduced from 0.21 A (28 %) with the *MSF*1 to 0.01 A (1.7 %) with the *MSF*4, as detailed by Fig. 7.24 (right).

The same convergence behavior appears on the local fields calculated at Point *G* and is visible in Fig. 7.25. The *b* loci from **a** – ν and **h** – ϕ *FE* formulations are getting closer to each other for finer meshes. The mean deviation over one period related to the *FE* formulations on the local induction field at Point *G* reduces from 0.35 T (38 %) to 0.05 T (5 %) with the highest mesh density.

In summary, it appears that the approximation introduced by the *FE* formulations and

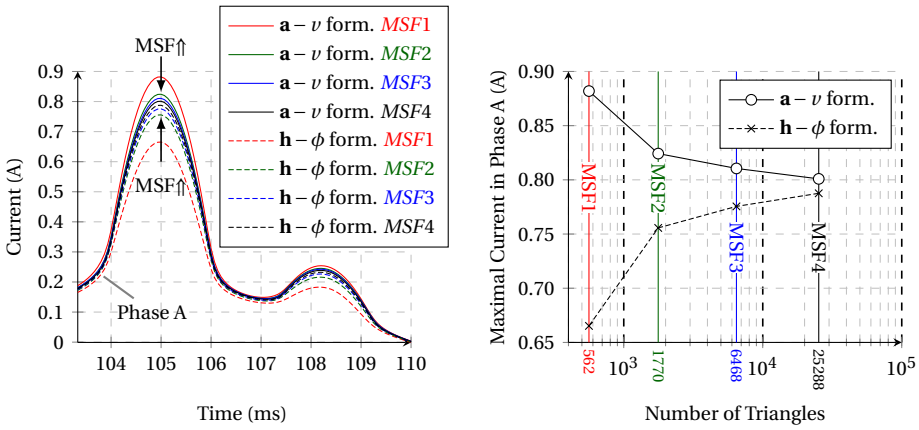

Figure 7.24: *Influence of the MSF on simulation results with the vpm approach; convergence of the phase current waveform in phase A (left) and of the peak value (right) with the mesh refinement.*

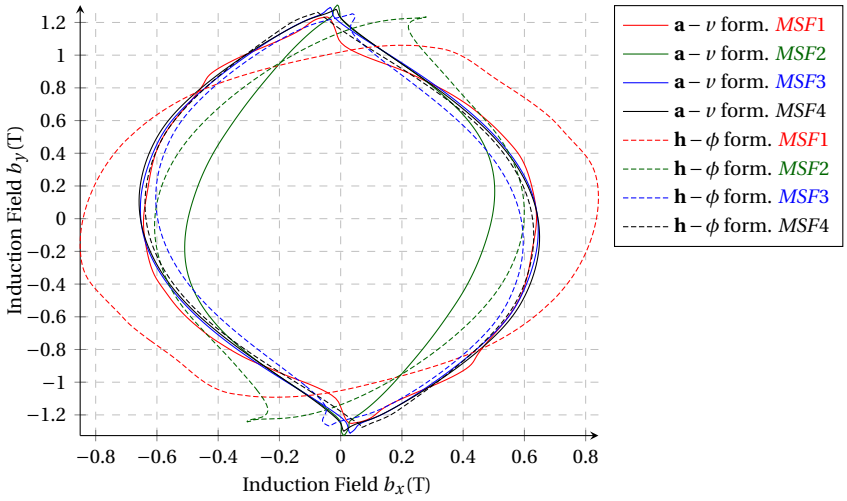

Figure 7.25: *Influence of the MSF on simulation results with the vpm approach; convergence of the flux density* ***b*** *at Point G, with the mesh refinement.*

the one from the simplified *vpm* approach start to be at the same order of magnitude only for the finest mesh considered (*MSF*4).

Indeed, in this three-phase transformer example, the polarization induction patterns are mostly purely unidirectional in the bulk of the three core limbs and circular in T-joints, with intermediate elliptical behavior assumed in the core regions in between. The simplified *vpm* approach predicts thus the same magnetization as the exact *diff* and *var* approaches in most of the core domain and remains an excellent approximation for all the ferromagnetic core in general, leading to relatively small deviations on the local fields and global quantities. It is therefore not surprising that a rather impor-

tant mesh refinement is needed to make the *FE* formulations sufficiently sensitive to capture the deviation introduced by the *vpm* hysteresis approach. The exact *diff* or *var* hysteresis approaches are only useful for mesh quality at least higher than *MSF*4, in this example. It is worth noting that more important deviations may be encountered between the approximated *vpm* predictions and the results from the *var* and *diff* approaches if magnetic anisotropy is taken into account, as discussed in [177]. In that situation, the *diff* approach may therefore be useful to improve the prediction compared to the *vpm* approach, even with coarse meshes.

Once again, the *var* approach is computationally very expensive and more subjected to convergence issues compared to the *vpm* one. The new proposed *diff* approach allows a significant improvement of the convergence behavior to derive the same solution as the *var* approach, but remains naturally slower than the approximative *vpm* version. The simulations in this section were run on a single core of an Intel E5-2650 processor with the clock frequency 2.0 GHz on NIC4, a High Performance Computing massively parallel cluster of the University of Liège. In fact, quantitatively, even with the coarse mesh (*MSF*2) presented in Fig. 7.20 (right), the time-stepping simulations of one period made by 300 time steps take already about 1 or 2 hours with the *var* hysteresis model approach in its *dir* form within the $\mathbf{h}-\phi$ formulation, or in its *inv* version within the $\mathbf{a}-\nu$ formulation respectively, while it lasts about 35 minutes and 40 minutes with the *dir* and *inv* forms of the *diff* approach respectively. On the other hand, the *vpm* approach needs only around 15 minutes to simulate one period. The inversion of the *var* approach, and to a much lesser extent of the *diff* approach, is more time consuming than their direct counterpart, while for the *vpm* approach there is nearly no difference in the observed computational time between its *dir* and *inv* implementations in this example. These observations are finally very similar to those obtained with the T-joint case in the previous section.

In all simulations, the same residual $\tilde{r}_n^i$ as described by (5.47) is chosen as stopping criterion again, which is based on all the magnetic field components of each element of the *FE* mesh, at iteration i of time step n of the *NR* process at the *FE* system level. As before, the absolute and relative tolerances ϵ_{abs} and ϵ_{rel} in (5.47) are fixed to 10^{-6} A/m and 10^{-6} respectively. The *NR* process is thus stopped as soon as $\tilde{r}_n^i < 10^0$ is verified or if a maximal iteration number fixed at 50 is reached. At each *NR* iteration i, an optimal relaxation factor γ^i is selected between 10 evenly spaced values between 1 and 0.1 to facilitate the convergence. The Jacobian is computed analytically. The first iterate is simply initialized by the values from the previous time solution, as in Fig. 5.2 (left).

Fig. 7.26 illustrates, for each investigated simulations, how the *NR* residual at the *FE* system level evolves for all the 1800 time steps. The *NR* procedure remains convergent with the *vpm* and *diff* approaches while, with the *var* approach, for some time steps, the stopping criterion precision fails to be satisfied. Even if this does not prevent computing the following time steps, this highlights once again the numerical lack of robustness of the *var* approach. Indeed, despite the application of the relaxation scheme, the stopping criterion is not satisfied with the *var* hysteresis approach for 40 out of the 1800 time steps with the *inv* form in the $\mathbf{a}-\phi$ formulation and for 83 time steps with the *dir* form in the $\mathbf{h}-\phi$ formulation. In Fig. 7.26 (top), the residual curves

associated to these specific time steps never go below the horizontal line 10^0 representing the stopping criterion. The *NR* process enters in a cycling behavior without being able to reduce furthermore the residual after reaching the final 50-th iteration. This is obviously an illustration of the *var* approach limitations due to its ill-conditioned nature, in addition with the numerical loss of significance that may occur during the minimization process of the magnetic energy density and which is hard to handle. Yet, in this example, the residuals $\tilde{r}_n^i$ (5.47) remain confined below 10^2 (relative tolerance of 10^{-4}), for the more delicate time steps, which is usually still a reasonable tolerance for highly nonlinear simulated problems. The non-converged time steps contribute to increasing the mean iteration numbers per time step for the *var* approach, with the $\mathbf{a}-\nu$ and the $\mathbf{h}-\phi$ formulations needing both around 8 iterations per time step in this case. On the other hand, there is no such convergence problem with the proposed *diff* approach as can be seen in Fig. 7.26 (middle). There are more critical time steps appearing with the $\mathbf{h}-\phi$ formulation for which the stopping criterion is harder to satisfy and the residual, while mostly still decreasing, converges slower, needing more than 50 iterations for 17 time steps out of 1800 in this example. The *diff* approach remains stably convergent with 8.9 and 7.8 average *NR* iterations for the $\mathbf{h}-\phi$ and $\mathbf{a}-\nu$ formulations respectively. This is a relatively fast convergence to the exact solution predicted by the *EB* hysteresis model, competitive with the variational implementation presented in [177]. Finally, the fastest convergence is achieved with the *vpm* hysteresis approach here. Fig. 7.26 (bottom) shows the residuals evolution with the *vpm* approach for the two complementary *FE* formulations. The NR methods converge in average with 5.5 iterations for the $\mathbf{a}-\phi$ formulation with the *inv* form and with 4.8 for the $\mathbf{h}-\phi$ formulation with the *dir* form.

As a general remark on Fig. 7.26, one may observe that the higher the involved fields for the last time steps, and the more the number of iterations required increases.

Finally, for a practical *FE* usage, the *vpm* approach remains recommended to use whenever the accurate representation of the *EB* hysteresis model brought by the *diff* or *var* approach is not worth the additional computational effort and the greater risk of confronting convergence issues with the latter one. In any case, the *diff* approach should be preferred over the *var* approach.

Of course, investigating finer meshes for reducing the errors from the *FE* formulations has also a computational cost. The computational times taken with the *vpm* approach for the different *MSF* are displayed in Fig. 7.27 and compared with simulations using only a simple *anhy* material law in order to get a reference on how the two *FE* formulations confront without the hysteresis model. All computational times increase linearly with the number of triangles used.

On the anhysteretic case first, it appears that a nonlinear iteration with the $\mathbf{a}-\nu$ formulation is slightly faster than with the $\mathbf{h}-\phi$ formulation, about 5 s for 7 s in average with the finest mesh (*MSF*4). The mean number of iterations per time step does not depend on the mesh, and is about 2.4 for the $\mathbf{a}-\phi$ formulation and 2.1 for the $\mathbf{h}-\phi$ formulation, for all the meshes. The total computational times with each formulation are at the end quite similar, with yet a slight advantage for the $\mathbf{a}-\nu$ formulation, which

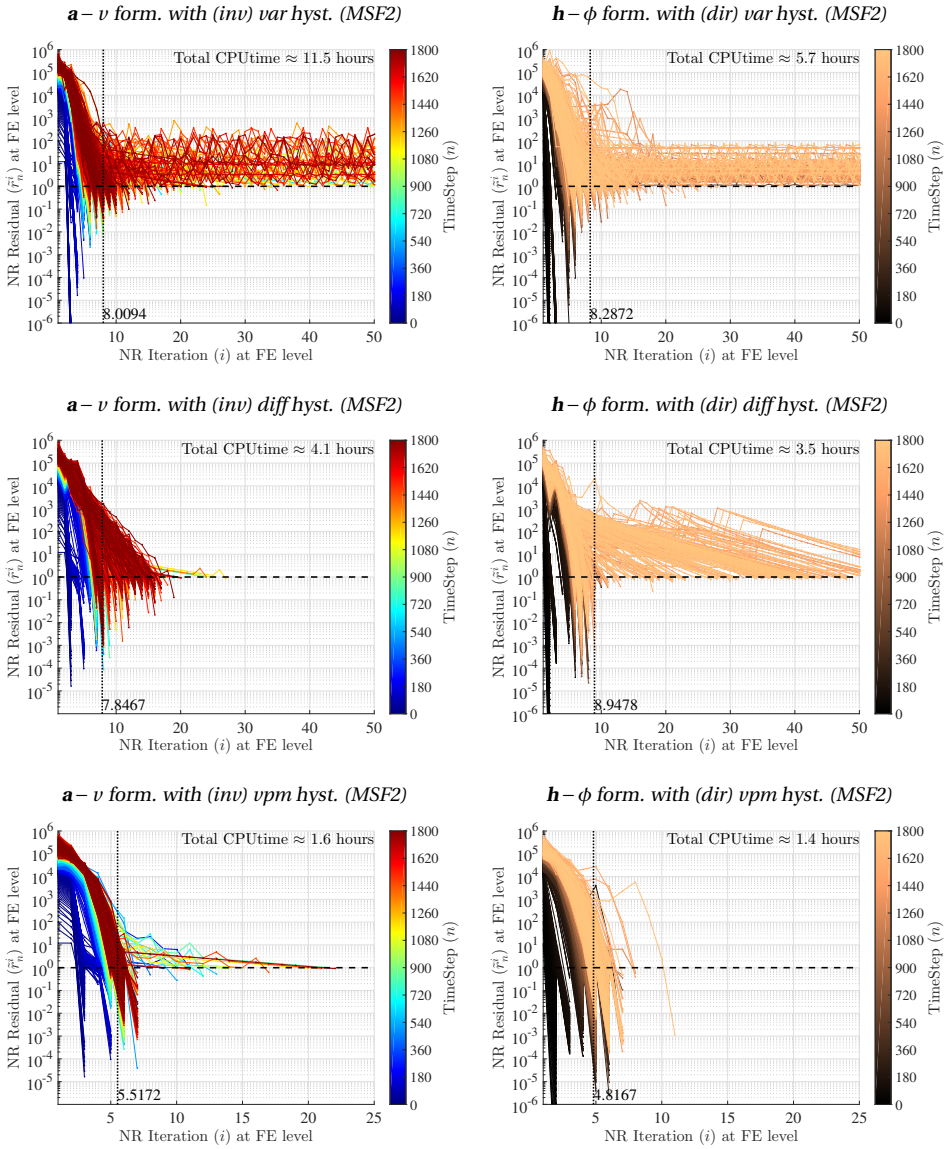

Figure 7.26: *Evolution of the residual* $\tilde{r}_n^i$ (5.47) *in the NR scheme used at the FE system level in function of the iteration number* i*, for each time step* n*, each step* n *having a specific color. The NR process is stopped when* $\tilde{r}_n^i < 10^0$ *or if* $i > i_{max} = 50$.

remains faster, about 20%, with 9:30 hours compared to 11:30 hours with *MSF*4.

With the *νpm* hysteresis case, there is no much differences between the *FE* formulations on the total computational times. The additional inversion of the hysteresis model at each *NR* iteration compared to the *anhy* case, does slow down more the **a** – ν

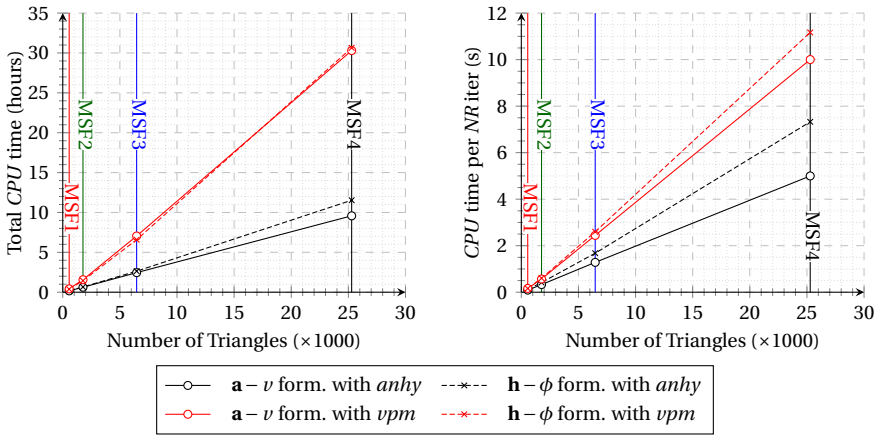

Figure 7.27: *CPU times with both FE formulations, with the vpm approach or the anhysteretic (anhy) constitutive law, for various MSF associated to different meshes.*

formulation, as the inversion required about 25% of the computational time per *NR* iteration. Nevertheless, the $\mathbf{h}-\phi$ formulation, even with a direct application of the *vpm* approach, remains slightly slower per *NR* iteration than the $\mathbf{a}-\nu$ formulation, with 11 s vs. 10 s respectively, for the finer mesh case (*MSF*4), as seen in Fig. 7.27 (right). Because the $\mathbf{h}-\phi$ formulation needs in average a little less number of *NR* iterations per time step, the total computational times balance out at the end, with around 30 hours taken for both *FE* formulations with the mesh *MSF*4. In other words, the benefit of the *dir* hysteresis form in the $\mathbf{h}-\phi$ formulation does not allow to improve the speed performance in this example with the *vpm* hysteresis model.

The simulations with the *vpm* hysteresis model are about 3 times as long as with the anhysterestic material law. It is worth reminding here that a 3-cell hysteresis model has been adopted and that the computational time depends of course on the chosen complexity of the multi-cell model. As the cells are independent of one another, parallelization on several clusters would be interesting to investigate in order to speed up the *EB* hysteresis inclusion.

Finally, it is interesting to note that, considering the median value between the two *FE* formulations as an absolute reference, the refinement of the mesh from *MSF*3 to *MSF*4 for an accuracy gain from 4% to 1.7% on a global quantity (Fig. 7.24) or from 7.5% to 5% on a local field (Fig. 7.25), comes with an increase of the total computational time by a factor 5 (Fig. 7.27). Further refinements would lead to subsequently less relative improvements on the true solution but with an ever-growing computer resources needed. The last small discrepancies are always the more costly to remove and this is a usual trade-off between accuracy and complexity which extends beyond the hysteresis modeling.

5. Transformer from *TEAM* Problem 32 Benchmark - *2D*

As a final example, the *TEAM* Problem Number 32, described in [33], is considered. The interest of this benchmark problem is that it provides reliable measurements for checking the numerical procedures developed in this thesis. Indeed, the *TEAM* Problem 32 proposes a test case for validating magnetic field analysis codes, including vector hysteresis, and makes available several measurements of local and global output quantities, under various operating conditions.

The experimental setup is schematized in Fig. 7.28. It consists of a three-limbed ferromagnetic core made of five Fe-Si 3.2 wt%, 0.48 mm thick laminations, with a specific electrical conductivity of $\sigma = 1.78 \times 10^6$ S/m. Two windings of 90 turns each are placed on the external limbs.

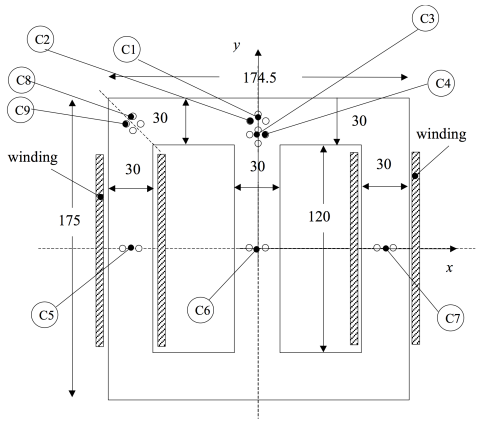

Figure 7.28: *2D structure of the three-limb transformer with pick-up coils [33]; Dimensions are in* mm.

This problem has four different variations depending on the supplied conditions of the windings. They are either connected in series, fed by a controlled sinusoidal voltage source, without or with harmonics, or both subjected to two sinusoidal waveforms in quadrature, or eventually, only the first coil is fed while the second one is closed on an external resistor.

Pick-up coils, referred to as C1 to C9 in Fig. 7.28, are placed in several locations in the core in order to measure local magnetic flux densities. In regions where rotational flux densities are expected, a pair of orthogonal pick-up coils is used to get field measurements in both directions.

In *FE* simulations, the *TEAM* problem 32 can be calculated as a *2D* case. Moreover, only half of the transformer cross-section can be considered due to symmetry. The geometry and the mesh that are used for this problem are shown in Fig. 7.29. The location of points 1,2,3, which are associated to pick-up coils C1-C2, C3-C4 and C6 respectively, are indicated in Fig. 7.29 (left). The mesh in Fig. 7.29 (right) is made of 2242 triangle elements and 1175 nodes.

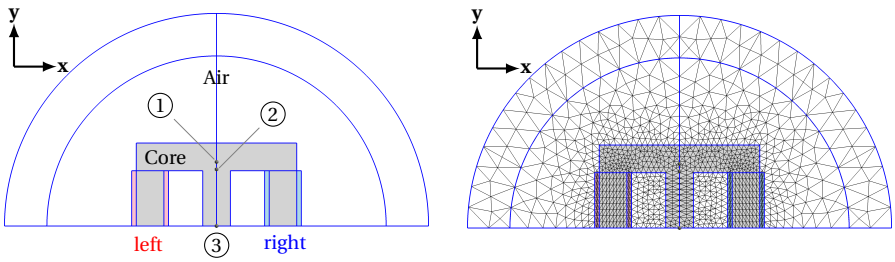

Figure 7.29: *Geometry of the TEAM problem* 32 *with the location of* 3 *points related to pick-up coils positions (left); and the mesh considered for FE simulations (right).*

The calculations in this section are performed with the $\mathbf{a}-v$ formulation given by (5.36). As in the previous *FE* examples, the *2D* restriction allows to use a nodal representation for the vector $\mathbf{a}$, where only the component along the $\mathbf{z}$ axis constitutes the unknown. The $\mathbf{b}$ and $\mathbf{h}$ fields lie thus as before in the $\mathbf{xy}$-plane. In order to take the eddy currents in the laminated core into account, one can investigate the low frequency lamination model, which consists in introducing an additional conductivity matrix based on the expression (7.7) in the *FE* formulation, as detailed in [100, 98, 51]. However, this addition has little impact on the simulation results here. Indeed, the analysis in this benchmark problem is developed at a frequency of 10 Hz. This guarantees relatively good accuracy of the experimental data while the influence of skin effect is negligible and, mainly, there is no dynamic effect observed in the signal amplitudes at this low frequency value, as mentioned in [33]. Therefore, the lamination model contribution is not required in the following study, which focuses in reproducing by simulation global and local measured quantities.

Fe-Si 3.2 wt% electrical steel sheets have been characterized through the usual Epstein frame by the authors in [33]. They provide a set of measured unidirectional symmetric $b-h$ loops, along different directions with respect to the rolling direction (*RD*) or transverse direction (*TD*). This allows to apply the identification procedure as described in Chapter 6 to determine the material parameters for the *EB* model. However, as the hysteresis model studied in this thesis is only described for isotropic magnetic materials, the same hysteresis data is used for all directions and only the parameters corresponding to the *RD* is then adopted. The one-to-one scalar anhysteretic curve is represented by a double Langevin function with $J_a = 0.792\,\mathrm{T}$, $h_a = 9.082\,\mathrm{A/m}$, $J_b = 0.791\,\mathrm{T}$, and $h_b = 137.121\,\mathrm{A/m}$; while a 3-cell discretization is considered with $[\omega^1 = 0.03; \kappa^1 = 0A/m][\omega^2 = 0.92; \kappa^2 = 55A/m][\omega^3 = 0.05; \kappa^3 = 199A/m]$, as deduced by the procedure presented in Chapter 6 for the *TEAM* 32 data along the *RD*. Only the *vpm* approach of the *EB* model is considered here. Moreover, in the $\mathbf{a}-v$ formulation, it is the inverse form of the *EB* model that is used.

In addition to the comparison with experimental measurements, simulations are also conducted with a vector Jiles-Atherton (*JA*) model for the magnetic constitutive law of the ferromagnetic core. This allows to confront furthermore results deduced with the *EB* hysteresis model to those obtained with a more widely used hysteresis model. In [7, 6], simulations for the *TEAM* 32 are realized with an anisotropic vector *JA* model

and the parameters are determined using optimizing procedures described in [136]. Here, the representation is restricted to an isotropic material law and the same *JA* coefficients found for the *RD* are adopted for all directions, as in [91]. The considered parameters for the *JA* model are thus: $c = 0.652$, $m_s = 1.33 \times 10^6\,\mathrm{A/m}$, $a = 172.856\,\mathrm{A/m}$, $\alpha = 417 \times 10^{-6}$, and $k = 232.562\,\mathrm{A/m}$. Note that, to be included in the $\mathbf{a}-\nu$ formulation, a $\mathbf{b}$-based version of the *JA* model is employed.

In all simulations, the stopping criterion for the *NR* method at the *FE* system level is fixed by $\tilde{r}_n^i$ from (5.47) with $\epsilon_{\mathrm{abs}} = 10^{-5}\,\mathrm{A/m}$, $\epsilon_{\mathrm{rel}} = 10^{-5}$. A *heavy* relaxation procedure with 10 linearly spaced values between 1 and 0.1 is used to ensure convergence. The initial *NR* iterate is approximated by a second degree polynomial extrapolation based on the three previous time solutions. Two periods with 1000 time steps each are considered in all simulations, with a smooth start from the demagnetized state, and the steady state is reached at the second cycle.

As already mentioned, the *TEAM* 32 problem has four different test cases, but attention will be paid only to CASE2 and CASE3 here, as denoted by the authors. CASE2 is convenient for checking distorted multi-harmonic signals under unidirectional flux, whereas CASE3 is appropriate for checking vector hysteresis modeling, with rotational flux.

CASE2

In the configuration of CASE2, the two windings are connected in series, with an additional resistance of $R_s = 11.1\,\Omega$, and supplied by a voltage source that consists of a 10 Hz fundamental and a fifth harmonic component, each with a peak value of 11.8 V.

Comparison between the current obtained in the windings from the simulations, either with the *EB* model or with the *JA* model, is shown in Fig. 7.30, with, in addition, the current observed during the measurement over one period. Both predictions from the simulations give the same output for the current and are in agreement with the measured quantity.

In Fig. 7.31, the local magnitude of the induction field calculated at point 3 for the *EB* and the *JA* hysteretic data is compared with the measured data obtained at pick-up coil C6. Moreover, a simulation has also been realized by considering only the double Langevin function as magnetic constitutive law, thus removing any hysteresis influence. The resulting output, denoted by *anhy*, is also drawn in Fig. 7.31.

The simulation in the *anhy* case produces clearly the least accurate signal, with peak magnitudes furthest from the measurement. Additionally, there is a slight phase shift that arises between the measured value and the anhysteretic approach result. This highlights the requirement for the inclusion of the hysteresis effects if detailed design of a device behavior has to be performed. About simulations with hysteresis models, it appears that the *JA* model generates slightly higher fifth harmonic content than the *EB* model. In this example, although the *EB* model is made of only 3 cells, it allows already to predict with a better accuracy the measured signal than the classical *JA* model,

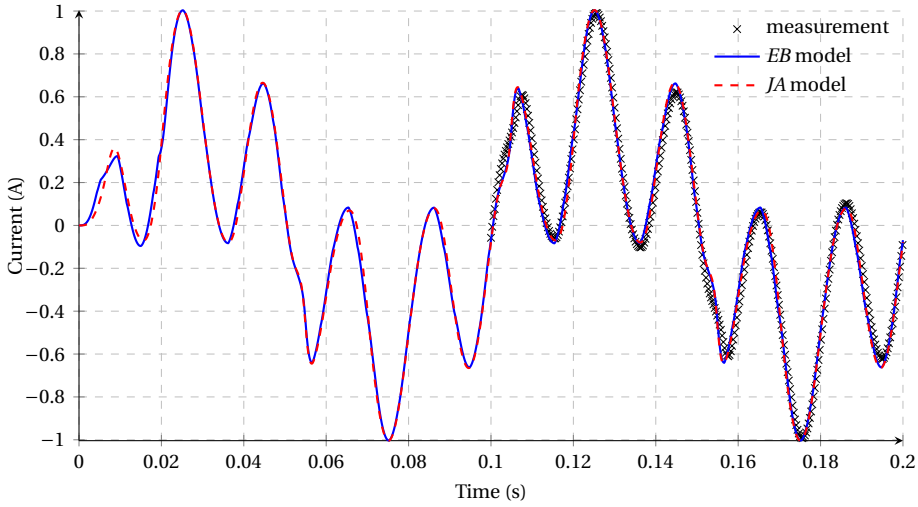

Figure 7.30: *Comparison of the current in the windings from simulations with the EB or the JA hysteresis models, with respect to the current obtained from measurement.*

which is known for not behaving well with distorted signals in presence of harmonics. This underlines the predictive power of the *EB* model compared to the *JA* model in a practical situation.

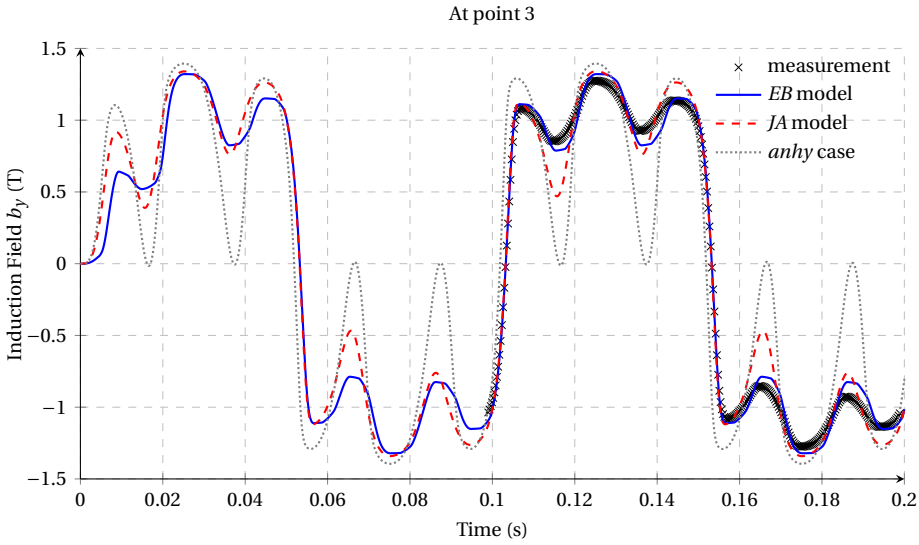

Figure 7.31: *Comparison of the y-component of the magnetic flux density at point 3 from simulations with the EB or the JA hysteresis models, with respect to the magnetic flux density measured at pick-up coil C6. Simulation result obtained with a corresponding anhysteretic material law is also depicted.*

CASE3

In the configuration of CASE3, the two windings are supplied with two sinusoidal voltage waveforms in quadrature, with, for both, a peak amplitude of 14.5 V at frequency of 10 Hz, each being connected in series with a 11.1 Ω resistance. The phase shift of 90° between the two excitation sources generates thus a rotating flux in the T-joints of the device.

Fig. 7.32 presents the established currents on the left and right windings. The numerical results, either with the *EB* or the *JA* model, are in excellent agreement with the experimental results for these global quantities.

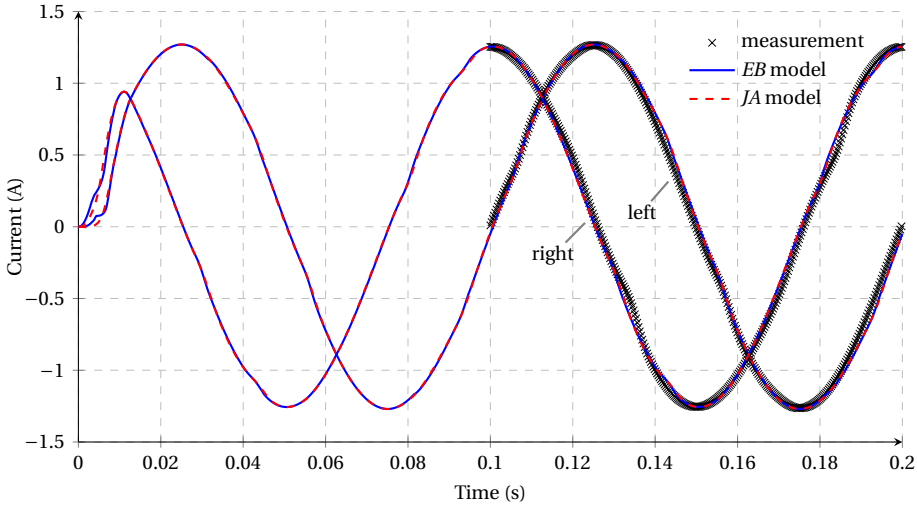

Figure 7.32: *Currents in the left and right windings obtained from simulations with the EB or the JA models, compared to those obtained from measurements.*

For local quantities, the flux density is evaluated on points 1 and 2, where measurements along the **x** or **y** directions are collected with dedicated pick-up coils. In Fig. 7.33, the magnetic induction values taken at point 1 along the **x** axis, from simulations and from the corresponding pick-up coil in the experimental set-up, are presented. In Fig. 7.34, similar results are displayed for the **y** direction at the same point. The resulting **b** loci constructed from Fig. 7.33 and Fig. 7.34 are shown in Fig. 7.35. In the same way, measured and simulated flux density results obtained at point 2 are depicted in the following Fig. 7.36, Fig. 7.37 and Fig. 7.38, with details of signal shapes in each direction, and their corresponding **b**-loci.

Analyzing first the results at point 1, a good agreement is observed between the simulations and the experimental data along the **x** direction, with a slightly better prediction for the *EB* model compared with the *JA* model, as visible on Fig. 7.33. There are more pronounced differences between computed results and measurements along the **y** direction at point 1, as can be seen on Fig. 7.34. Improving the hysteresis models by

taking account of the anisotropy nature of the magnetic material would have reduced this difference. The authors in [6] are using an anisotropic vector *JA* model and they seem to have a lower loss of accuracy of their simulation regarding their results from one direction to the other one. Nevertheless, knowing that the simulations are here only valid for isotropic material, the measured and computed evolution curves have similar shapes, despite the magnitude discrepancy. It can thus be estimated that the simulations remain consistent. The signal waveform seems a little bit better represented by the *EB* model than with the *JA* model. This is also true regarding the **b**-loci in Fig. 7.35.

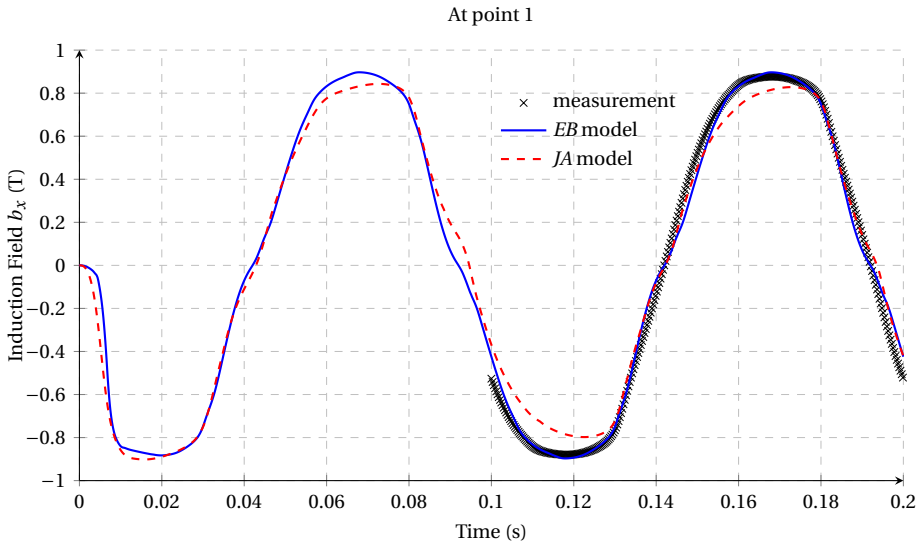

Figure 7.33: *Comparison of the x-component of the magnetic flux density at point* 1 *from simulations with the EB or the JA hysteresis models, with respect to measured values.*

The same comparison can be applied based on the results localized at point 2. The anisotropy seems to affect less the field values at this location since they are in rather good agreement for both directions, either along **x** or **y** axis, by looking at Fig. 7.36 and Fig. 7.37, respectively. The prediction with the *EB* model is not always better than with the *JA* model at each time instant but remains of satisfactory accuracy, taking into account the model approximations. The same remark applies by comparing the **b**-loci illustrated in Fig. 7.38.

As conclusion, the *TEAM* 32 benchmark provides a valuable tool for the validation of numerical methods to model hysteretic magnetic materials in a practical application. A *2D FE* model of the device including the inverse *EB* hysteresis model has been simulated at different load cases and compared with results obtained with a vector *JA* model, on their ability to represent accurately the measured data given by the *TEAM* 32 problem. First, it is worth noting that good convergence of the *NR* algorithm has been observed at any time steps in every simulation thanks to the relaxation proce-

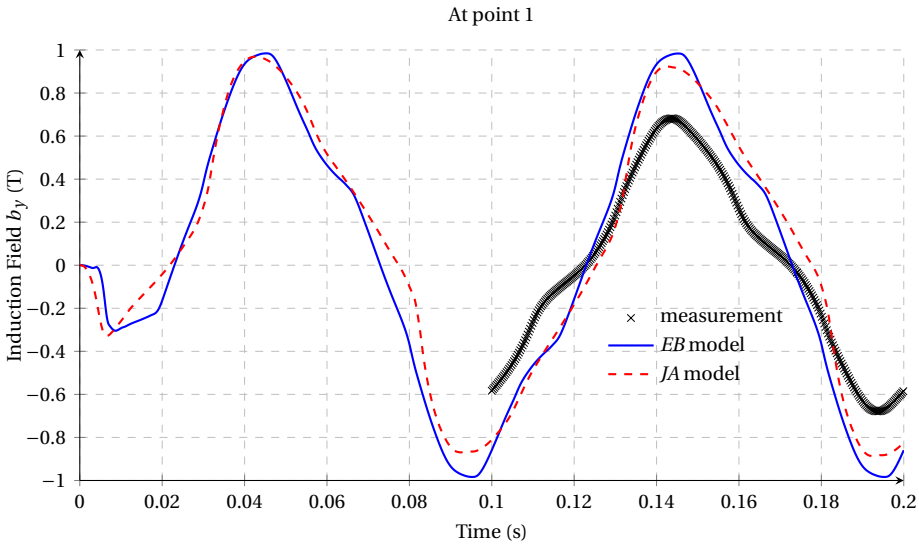

Figure 7.34: *Comparison of the y-component of the magnetic flux density at point* 1 *from simulations with the EB or the JA hysteresis models, with respect to measured values.*

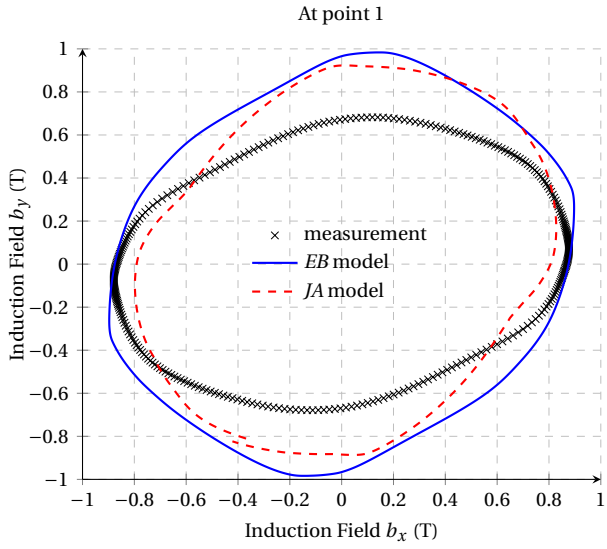

Figure 7.35: ***b****-loci at point* 1 *from simulations with the EB or the JA models, and from measurement.*

dure and the initialization technique. The use of the *EB* model has proven crucial for accurate representation of local distorted values in presence of harmonics whereas the *JA* model is by nature less adapted for such situation. Considering the earlier analysis, and despite some result differences, the *EB* model has also been able to reproduce local rotating flux density measurements with rather good accuracy, knowing the

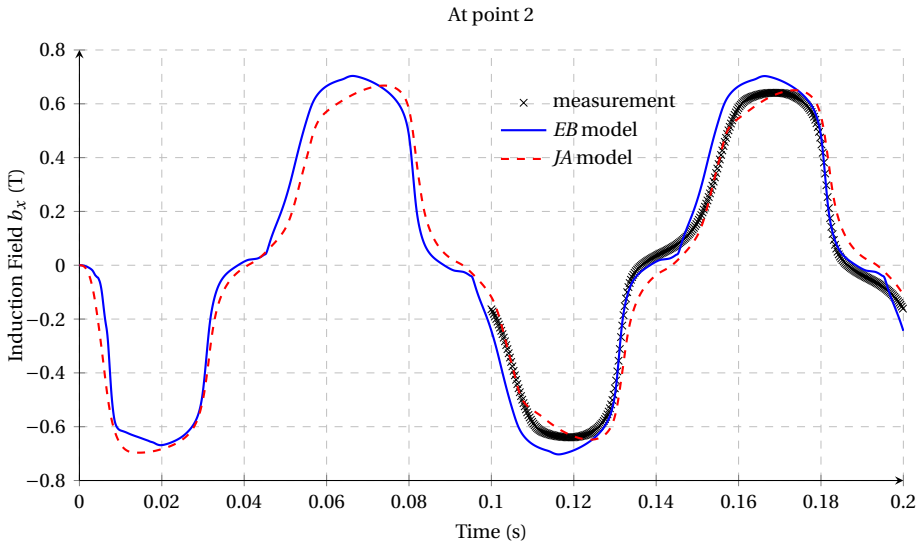

Figure 7.36: *Comparison of the x-component of the magnetic flux density at point 2 from simulations with the EB or the JA models, with respect to measured values.*

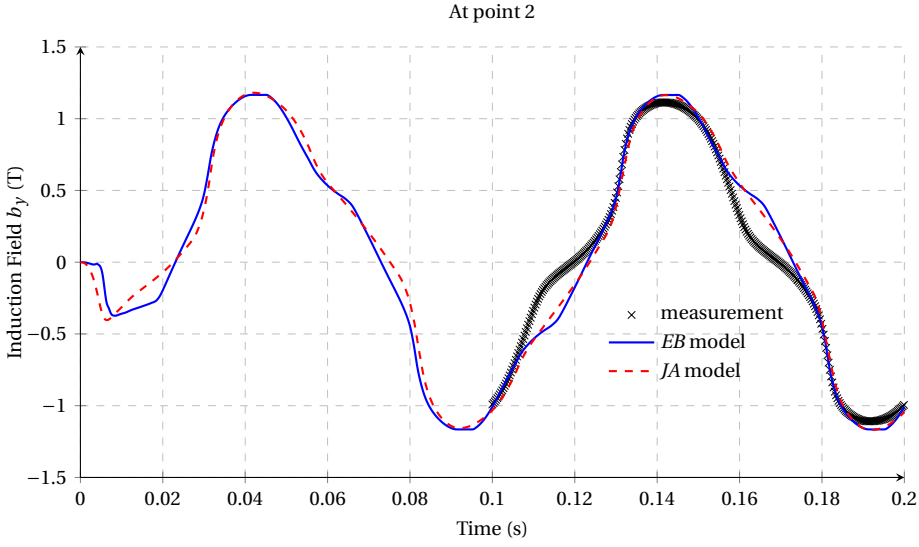

Figure 7.37: *Comparison of the y-component of the magnetic flux density at point 2 from simulations with the EB or the JA hysteresis models, with respect to measured values.*

approximations behind the hysteresis model construction. Extensions to anisotropic materials and three-dimensional (*3D*) analysis have to be investigated in future work.

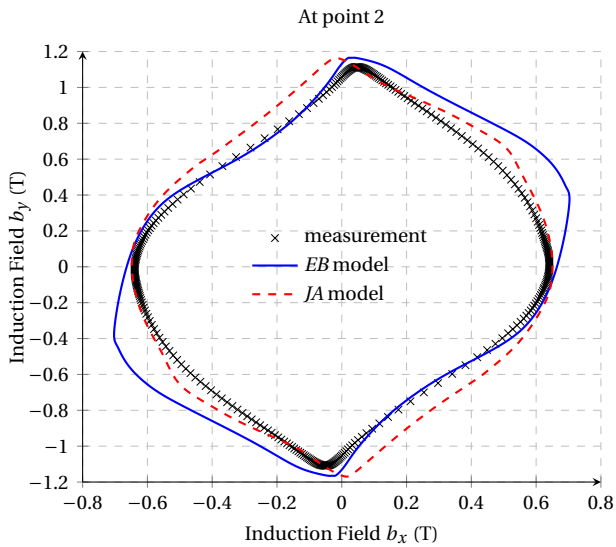

Figure 7.38: ***b****-loci at point* 2 *from simulations with the EB or the JA models, and from measurement.*

Conclusion

Main Achievements and Conclusions

This thesis focused on the development of a highly accurate quasi-static energy-based (*EB*) hysteresis model. The model relies on an explicit representation of the pinning force as a dry friction-like force acting on the magnetic polarization. Unlike Preisach and Jiles-Atherton models, this model is vectorial from the beginning and derives from thermodynamic first principles.

Three approaches have been considered: the first one, called Vector Play Model (*vpm*), relies on a simplification that allows an explicit, and thus fast, update rule, while the two others, the variational approach (*var*) and differential approach (*diff*), avoid this simplification, but require a non-linear equation to be solved iteratively. The *vpm* and *var* approaches were already used by other researchers, whereas the *diff* approach introduced in this thesis, is a new, more efficient, exact implementation, which combines the efficiency of the *vpm* with the accuracy of the *var*. The three hysteresis implementations lead to the same result for purely unidirectional or rotational excitation cases, and give a rather good approximation in all situations in-between, at least in isotropic material conditions [177].

These hysteresis modeling approaches can be incorporated into a finite element (*FE*) code as a local constitutive relation with memory effect. The inclusion in two complementary **b**-conform and **h**-conform *FE* formulations has been investigated in detail, the former requiring the inversion of the vector hysteresis model, naturally driven by **h**, for which the Newton-Raphson (*NR*) method can be used. Then, at the *FE* level, once again, the *NR* technique has been adopted to solve the nonlinear *FE* equations, leading to the emergence of the discontinuous differential reluctivity and permeability tensors, requiring a relaxation technique in the *NR* scheme. To the best of our knowledge, the inclusion of an *EB* hysteresis model had never been successfully achieved in a **b**-conform *FE* formulation before.

The one-dimensional (*1D*) *FE* simulation of an infinite ferromagnetic lamination has been studied for its ability to predict both stored and dissipated magnetic energy at

any moment in time, in parallel with the classical dynamic eddy current losses, also taken into account through the *FE* model. This property constitutes one of the substantial advantages of the *EB* model. The hysteresis implementations have then been used under their inverse form (*inv*) and direct form (*dir*) respectively in the two complementary *FE* formulations for the two-dimensional (*2D*) *FE* time-stepped simulations of the no-load operation of a three-phase transformer. Matching results between both hysteretic *FE* formulations have been observed, with a convergence of the results correlated with the refinement of the mesh. Moreover, because the ferromagnetic domain, assumed isotropic in this example, is essentially submitted to unidirectional or elliptical field patterns, in the legs or in the T-joints of the core respectively, with intermediate behaviours in the transition regions, the approximate *vpm* approach leads to results very close to the *var* and *diff* approaches, as observed on global and local quantities. The mesh has to be sufficiently refined in order to make the *FE* model sensitive to the approximation introduced by the *vpm* approach. About the *NR* scheme at the *FE* level, it is well known that it is difficult to obtain good convergence of iterations with highly nonlinear materials, as it is the case here. Nevertheless, thanks to the relaxation technique, the outer *NR* cycle reached convergence in a reasonable number of iterations per time step with the *vpm* approach. However, the simulations with the *var* approaches have shown to have limitations in their ability to converge for some critical time steps. The new *diff* approach allows to improve the convergence performance compared to the *var* approach without loss of accuracy. Surprisingly, there was no significant gain in the total computational time between the *vpm* approach in the **h**-conform formulation or the **b**-conform formulation, despite the additional inversion of the model for the latter.

Finally, the *FE* simulations with the *EB* model have been successfully validated by means of available measurements of a practical transformer application, with satisfactory agreement for both global and local quantities with regard to the actual simplicity of the *EB* model. The consideration of the hysteresis effect is required in order to calculate with better accuracy the flux pattern generated inside the device. The *EB* model has better prediction capabilities than the Jiles-Atherton (*JA*) model, especially in presence of distorted field waveforms with higher harmonics. Therefore, the *EB* model appears has an elegant solution to improve further the design of efficient electromagnetic energy converters.

Future Prospects

Several suggestions for future work are listed hereafter.

First, one can consider improvements to the *EB* model in order to increase its ability to predict material measurements:

1. The saturation law used inside the hysteresis model could be easily constructed from interpolation of points deduced from measurement data, instead of being approximated by a best fitting technique with an analytical function, even if the double Langevin function gives already satisfactory results in general.

2. The anisotropy of the magnetic properties is an important characteristic of the material that needs to be taken into account in order to represent accurately the material behavior in both the rolling direction (*RD*) and transverse direction (*TD*). It has been shown that significant differences can be observed along different magnetization directions, even in the case of non-grain-oriented (*NGO*) electrical sheets. This is therefore a crucial aspect, which can be incorporated in the *EB* model by considering, as a first attempt, symmetric positive definite second-rank tensors to represent the pinning field $\underline{\boldsymbol{\kappa}}^k$ instead of scalar values κ^k, as seen in [177]. However, this contradicts the initial postulate that the irreversible magnetic field $\mathbf{h}_{\text{irr}}^k$ should be parallel to the variation of the magnetic polarization $\dot{\mathbf{J}}^k$. One can thus instead consider a scalar pinning force to be a function of the angle between $\dot{\mathbf{J}}^k$ and a fixed direction, such as attempted in [199, 198]. Furthermore the saturation law used in the model can also be adapted in such a way to vary in function of the direction.

3. There is the current limitation in the classical *EB* model related to its inability to obey the rotational loss property that the magnetic hysteresis loss tend to zero for a rotating magnetic field when the magnitude of the applied field is saturated [1]. This is a known problem for ordinary vector play models [157, 40, 39], which have led to the development of modified vector play models [17, 3, 145]. Similar adaptations could be introduced for the *EB* model by considering a variable pinning strength, dependent on the reversible magnetic field, such that its value would be reduced in saturation in order to satisfy the rotational loss property. A variable pinning strength dependent on the magnetic field itself would also be appropriate to model the asymmetric domain rotation which causes the saturation and desaturation branches to have different shapes. However, it is worth noting that there is no real physical interpretation behind this correction, which seems artificial. A better understanding of the origin of these observed phenomena would be required to integrate them properly in the *EB* hysteresis model.

4. The standard *EB* model is a static hysteresis model which is thus rate-independent. A viscosity term could be added in the model so as to obtain a dynamical vector model, like in [102]. This is like introducing a dash pot in parallel with the nonlinear spring in the mechanical analogy of the *EB* model. In the loss separation representation, this additional contribution would correspond to the so-called excess loss, which may possibly become significant at high frequency.

5. The model could also be integrated in multiphysical problems where the coupling with mechanical or thermal effects would affect the magnetic properties, for example. It is thus important to know the impact of magnetostriction or the temperature influence on the *EB* model parameters. The temperature-dependence is considered in [14, 196, 195] for equivalent vector play models. This is a crucial point if one is interested in the thermal demagnetization of permanent magnets, for instance.

6. It would be interesting to investigate other mechanisms that may be involved in hysteresis loops, such as by nucleation phenomena. At the moment, only the

pinning effect is assumed to be responsible of the hysteresis curve with the *EB* hysteresis model. This would certainly be mandatory to represent somehow this mechanism to be able to model correctly nucleation-type permanent magnet with the *EB* hysteresis model.

7. Naturally, the parameter identification strategy must be rethought accordingly to determine any additional parameters that would have been introduced to make the *EB* hysteresis model more sophisticated.

Linked to the above perspectives for improvement or generalization, one should investigate further modifications that affect the numerical implementation aspects of the *EB* model:

1. An easy improvement would be to parallelize the pseudo-particle updates of the *EB* model on different threads, or processors, in order to calculate them simultaneously during a simulation. This is relatively straightforward in the sense that the computation of each cell is already independent from one another, as soon as the current magnetic field is known. The updated fields need then to be gathered to compute the new magnetic field or the new flux density. This strategy is certainly interesting to accelerate the central processing unit (*CPU*) time of simulations in the case where there is a large number of cells and a refined *FE* mesh with many degrees of freedom.

2. The generalization to three-dimensional (*3D*) applications can be examined. Actually, the *EB* model is already ready to be used in the *3D* case under its *vpm* and *var* approaches. The *diff* approach needs the introduction of an additional angle search to find the updated position of the magnetic reversible field on a spherical surface.

3. The hysteresis model can be combined in a multi-scale approach with a computational homogenization technique [170, 168, 171], allowing the lamination of magnetic materials and the microstructure of synthetic materials to be taken into account. This approach combines the energy consistency of the *EB* hysteresis model, applied to representative elementary volumes, without going down to the level of extremely expensive micromagnetic calculations.

Finally, one can study other applications where *FE* simulations with the *EB* model can be experimented:

1. The *FE* method can be applied for the simulations of rotational electrical machines, where the movement of the device would be an additional complication, and the analysis of the results obtained with the *EB* hysteresis model in such circumstances would be interesting.

2. Despite this thesis being focused exclusively on ferromagnetic materials, the *EB* model is sufficiently general to be used also for ferrimagnetic materials. Therefore, the *FE* modeling for the design of devices with ferrimagnetic cores, such as those encountered in switched-mode power supplies, for instance, can also be investigated with the *EB* hysteresis model. It has been shown that the model can work even in presence of sharp signal waveforms, such as those delivered in power electronics.

3. The study of the magnetization and demagnetization of permanent magnets is another important field where the *EB* hysteresis model can be exploited. The analysis of fault simulation, short circuit demagnetization and hysteresis loss risk in machines with permanent magnets can then be addressed.

APPENDIX

A Ferromagnetism at the Microscopic Scale

THE theory of ferromagnetism due to Weiss is based on the formalism developed by Langevin in the case of paramagnetism.

1. Classical Langevin Theory of Paramagnetism

In the Langevin theory of paramagnetism, a paramagnetic domain is represented by a medium containing N_m atoms per unit volume, each carrying a magnetic moment $\mathbf{m}_0$. The distance between the moments is large enough so that there is no interaction between them, and they are free to rotate in any direction. Submitted to an external field $\mathbf{h}$, each moment possesses a potential energy W_pot, measured in joule (J), which tends to orient them in parallel with the field,

$$W_\mathrm{pot} = -\mu_0 \mathbf{m}_0 \cdot \mathbf{h} = -\mu_0 m_0 h \cos\gamma\,, \tag{A.1}$$

where γ is the angle between $\mathbf{m}_0$ and $\mathbf{h}$, measured from $\mathbf{h}$ whose orientation serves as reference.

Since the moments are independent of each other, it is reasonable to assume that their energy distribution is given by Boltzmann's law. Let $n(\gamma)d\gamma$ be the number of moments per unit volume making an angle between γ and $\gamma + d\gamma$ with $\mathbf{h}$, and let $d\Omega = 2\pi \sin\gamma d\gamma$ be the differential solid angle they occupy, as in Fig. A.1 (left). Obeying Maxwell-Boltzmann statistics, the magnetic moments are distributed for a given temperature T measured in kelvin (K), as

$$n(\gamma)d\gamma = n_0 \exp\left(-\frac{W_\mathrm{pot}}{k_\mathrm{B}T}\right) d\Omega = n_0 \exp\left(\frac{\mu_0 m_0 h \cos\gamma}{k_\mathrm{B}T}\right) 2\pi \sin\gamma d\gamma\,, \tag{A.2}$$

where $k_\mathrm{B} = 1.3807 \times 10^{-23}\,\mathrm{J/K}$ is the Boltzmann constant. This equation translates the competition between the potential energy and the thermal agitation which tends to destroy any preferential alignment to the field. The factor n_0 is a normalization constant defined by the condition

$$\int_0^\pi n(\gamma)d\gamma = N_\mathrm{m}\,. \tag{A.3}$$

The total magnetization m is obtained by summing the projections of all moments $\mathbf{m}_0$ on $\mathbf{h}$:

$$m = \int_0^\pi n(\gamma) m_0 \cos\gamma d\gamma , \tag{A.4}$$

which can be rewritten in the following form

$$m = N_\mathrm{m} m_0 \frac{\displaystyle\int_0^\pi \cos\gamma \sin\gamma \exp\left(\frac{\mu_0 m_0 h \cos\gamma}{k_\mathrm{B} T}\right) d\gamma}{\displaystyle\int_0^\pi \sin\gamma \exp\left(\frac{\mu_0 m_0 h \cos\gamma}{k_\mathrm{B} T}\right) d\gamma} . \tag{A.5}$$

By posing the dimensionless parameter α, given by the expression

$$\alpha = \frac{\mu_0 m_0 h}{k_\mathrm{B} T} , \tag{A.6}$$

and changing the variable

$$\cos\gamma = x , \tag{A.7}$$

the integration of (A.5) is easy provided:

$$m = N_\mathrm{m} m_0 \frac{\displaystyle\int_{-1}^{1} x \exp(\alpha x) dx}{\displaystyle\int_{-1}^{1} \exp(\alpha x) dx} = N_\mathrm{m} m_0 \left(\coth\alpha - \frac{1}{\alpha}\right) := N_\mathrm{m} m_0 L(\alpha) . \tag{A.8}$$

In this final expression, the function $L(\alpha)$ is called the Langevin function. It's bevavior as a function of h/T is shown in Fig. A.1 (right). This function has a horizontal asymp-

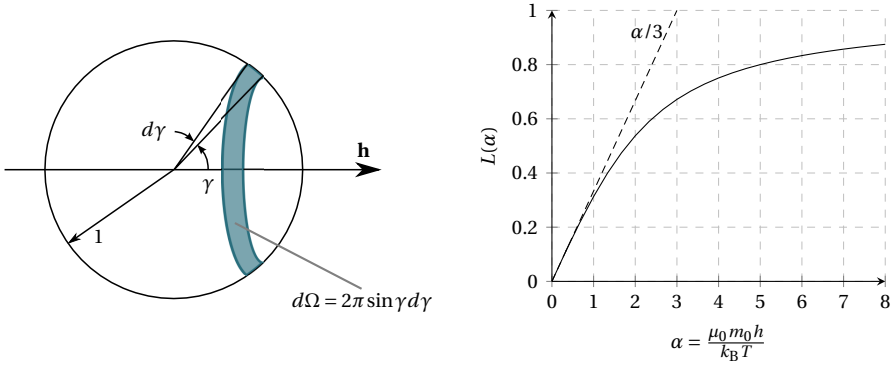

Figure A.1: *Langevin function*

tote predicting the saturation phenomenon corresponding to the perfect alignment of the moments on $\mathbf{h}$, with a maximum possible magnetization of $m_\mathrm{sat} = N_\mathrm{m} m_0$. Around the origin, $L(\alpha)$ can be approached by $L(\alpha) \approx \alpha/3$.

A

2. Quantum Mechanical Theory of Paramagnetism

It is interesting to present the quantum description of the problem since it brings modification to the characteristic law in satisfactory agreement with experiments.

Contrary to Langevin's classical description which takes into account a continuum of states, quantum theory only tolerates that the atomic magnetic moment module varies by discrete values and that its orientation in space, measured from an external field **h** taken as reference, is restricted to certain quantified angles γ.

The integral (A.4) in which all orientations of $\mathbf{m}_0$ in space are allowed must therefore be replaced by a sum of the allowed values of γ. From quantum mechanics, the component of the magnetic moment along the field **h** can only take the discrete values

$$m_{0h} = \tilde{J} g_{\tilde{J}} m_{\mathrm{B}} \left(\frac{M_{\tilde{J}}}{\tilde{J}} \right), \tag{A.9}$$

where $M_{\tilde{J}}$ is a quantum number that can have $2\tilde{J}+1$ values, varying by unit steps in the interval

$$-\tilde{J} \leq M_{\tilde{J}} \leq \tilde{J}, \tag{A.10}$$

while $\tilde{J}$ is the total angular momentum quantum number having only integer or half integer values. In the expression (A.9), m_{B} refers to the Bohr magneton, a universal constant which is the natural atomic unit of magnetic moments, $m_{\mathrm{B}} \approx 9.27 \times 10^{-24}\,\mathrm{A\,m^2}$. The factor $g_{\tilde{J}}$ corresponds to the Landé factor, a dimensionless quantity, typically of order unity, which, based on the relative contribution of the orbital and spin angular momentum, weights the total angular momentum, whose component along the quantization axis is equivalent to $M_{\tilde{J}}$. The ratio $\frac{M_{\tilde{J}}}{\tilde{J}}$ in (A.9) plays thus the same role as $\cos\gamma$ in the continuous description and m_{0h} is limited to a maximum value of $\tilde{J} g_{\tilde{J}} m_{\mathrm{B}}$, as illustrated by Fig. A.2 (left). At the end, the total magnetization expression (A.5) becomes in quantum formalism

$$m = N_{\mathrm{m}} \tilde{J} g_{\tilde{J}} m_{\mathrm{B}} \frac{\sum_{M_{\tilde{J}}=-\tilde{J}}^{M_{\tilde{J}}=+\tilde{J}} \left(\frac{M_{\tilde{J}}}{\tilde{J}} \right) \exp\left(\frac{\mu_0 \tilde{J} g_{\tilde{J}} m_{\mathrm{B}} \left(\frac{M_{\tilde{J}}}{\tilde{J}} \right) h}{k_{\mathrm{B}} T} \right)}{\sum_{M_{\tilde{J}}=-\tilde{J}}^{M_{\tilde{J}}=+\tilde{J}} \exp\left(\frac{\mu_0 \tilde{J} g_{\tilde{J}} m_{\mathrm{B}} \left(\frac{M_{\tilde{J}}}{\tilde{J}} \right) h}{k_{\mathrm{B}} T} \right)}, \tag{A.11}$$

Using again the dimensionless parameter α, expressed in this context by

$$\alpha = \frac{\mu_0 (\tilde{J} g_{\tilde{J}} m_{\mathrm{B}}) h}{k_{\mathrm{B}} T}, \tag{A.12}$$

the quotient of sums appearing in (A.11) can be rewritten as a function $B_{\tilde{J}}(\alpha)$, known as the Brillouin function

$$B_{\tilde{J}}(\alpha) := \frac{2\tilde{J}+1}{2\tilde{J}} \coth\left(\frac{2\tilde{J}+1}{2\tilde{J}} \alpha \right) - \frac{1}{2\tilde{J}} \coth\left(\frac{1}{2\tilde{J}} \alpha \right), \tag{A.13}$$

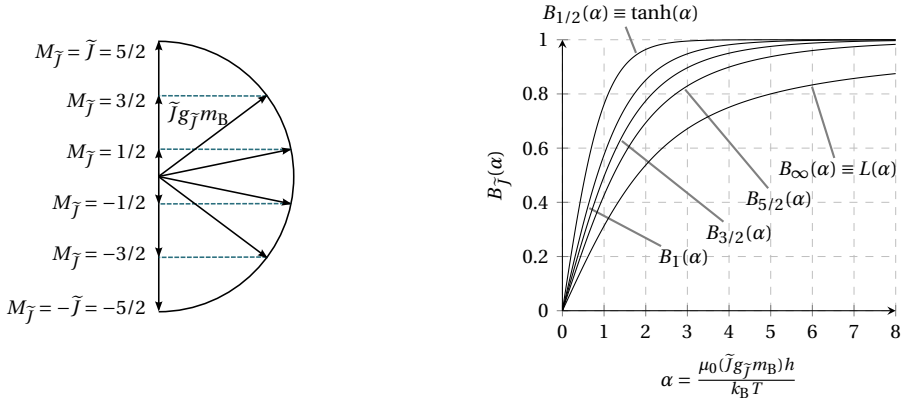

Figure A.2: *Brillouin function*

such that, the expression of magnetization (A.11) becomes

$$m = N_m \tilde{J} g_{\tilde{J}} m_B B_{\tilde{J}}(\alpha)\,. \tag{A.14}$$

From (A.8) and (A.14), it appears that quantum consideration has the effect of replacing Langevin function by Brillouin function in the expression of magnetization. The Brillouin functions are illustrated in Fig. A.2 (right) for different $\tilde{J}$ values. However in general, only the portion around the origin of the functions has to be considered because the dimensionless parameter α rarely exceeds 10^{-2}. Indeed, at room temperature, where $k_B T \approx 4 \times 10^{21}$ J, and taking $m_0 \approx m_B$, the parameter α varies according to the applied magnetic field as $\alpha = (2.5 \times 10^{-9})h$, which means that even subjected to relatively high magnetic field strengths, e.g. $h = 10^6$ A/m, the α value remains small, e.g. $\alpha \approx 2.5 \times 10^{-3}$. Under standard condition, the energy transmitted by **h** to align the magnetic moments is in general insufficient to defeat the thermal agitation, that is in adequacy with the properties of paramagnetism.

For small α, $B_{\tilde{J}}(\alpha)$ can be replaced by its first order approximation near the origin

$$B_{\tilde{J}}(\alpha) \approx \frac{\tilde{J}+1}{3\tilde{J}}\alpha\,. \tag{A.15}$$

A

The magnetization is then proportional to the field, $m = \chi_r h$, and the paramagnetic susceptibility can be deduced from (A.14) and (A.15):

$$\chi_r = \frac{\tilde{J}+1}{3\tilde{J}} \frac{\mu_0 N_m \left(\tilde{J} g_{\tilde{J}} m_B\right)^2}{k_B} \frac{1}{T}\,. \tag{A.16}$$

This last relationship expresses the Curie's law: the susceptibility of paramagnetic materials varies proportionally to the inverse of absolute temperature.

3. Weiss Theory of Ferromagnetism

The Langevin theory and its quantum correction are based on the fundamental assumption that there is no interaction between magnetic moments, which is suitable for paramagnetic description.

In the case of ferromagnetism, this hypothesis is no longer verified: the moments are extremely close and strongly coupled to each other.

The Weiss theory for ferromagnetism resolves this problem by considering a ferromagnetic medium as a paramagnetic substance where the mutual influence between all the neighboring moments is attributed to the existence of a strong interaction field, called the Weiss molecular field $\mathbf{h}_\mathrm{W}$.

This internal molecular field is very intense. Referring to Fig. A.2 (right), at room temperature and for $m \approx m_\mathrm{B}$, a field strength as high as $h_\mathrm{W} \geq 10^9$ A/m is required to lead the parameter α to $\alpha \geq 2.5$, and land into the beginning of the saturation region.

This interaction field favors the alignment of the magnetic moments along a common direction. As the magnetization indicates the average importance of this alignment, it is reasonable to postulate a proportional relation between the magnetization and the molecular field

$$\mathbf{h}_\mathrm{W} = \lambda_\mathrm{W} \mathbf{m}\,, \tag{A.17}$$

where λ_W is a dimensionless material characteristic constant.

In the theory developed by Weiss, each magnetic moment appears to be independent of the others, and the coupling manifests only through the postulation of this additional interaction field $\mathbf{h}_\mathrm{W}$. Under these conditions, the Langevin theory and its quantum correction still apply, provided that each magnetic moment experiences now an effective field that is the sum of the applied field with the molecular field, such that

$$\mathbf{h}_\mathrm{eff} = \mathbf{h} + \mathbf{h}_\mathrm{W} = \mathbf{h} + \lambda_\mathrm{W} \mathbf{m}\,. \tag{A.18}$$

The equations (A.8) or (A.14) are thus still valid, but the parameter argument α ((A.6) or (A.12)) has to be adapted accordingly, by replacing h by h_eff:

$$\alpha = \frac{\mu_0 m_0}{k_\mathrm{B} T} \left(h + \lambda_\mathrm{W} m\right). \tag{A.19}$$

The presence of the magnetization in the function argument leads to a transcendental equation for the magnetization expression, which writes with the quantum consideration,

$$m = m_\mathrm{sat} B_{\tilde{J}}\left(\frac{\mu_0 m_0}{k_\mathrm{B} T} \left(h + \lambda_\mathrm{W} m\right)\right), \tag{A.20}$$

where $m_\mathrm{sat} = N_\mathrm{m} m_0 = N_\mathrm{m} \left(\tilde{J} g_{\tilde{J}} m_\mathrm{B}\right)$, is the maximal possible magnetization. It is known, by rewriting (A.19), that the solution, if one exists, must satisfy also

$$m = \frac{k_\mathrm{B} T}{\mu_0 m_0 \lambda_\mathrm{W}} \alpha - \frac{h}{\lambda_\mathrm{W}}\,. \tag{A.21}$$

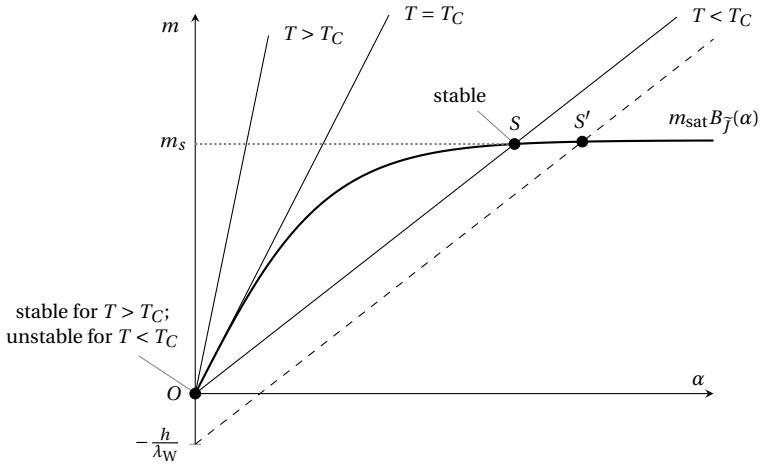

Figure A.3: *Weiss Theory*

Therefore, one can proceed to a graphical resolution of the equations (A.20) and (A.21), illustrated on Fig. A.3. In the absence of a magnetic field $h = 0$, and for temperatures $T < T_C$, the straight line (A.21) intersects the curve (A.20) in O and S. The solution $\alpha = 0$ is unstable and should not be considered because as soon as an interaction between magnetic moments develops, the molecular field that is created will force the alignment of all moments, and thus a transition to the solution S. The solution S represents a stable state where the system spontaneously acquires a non-zero magnetization m_s, even without external magnetic field. Temperature changes affect the slope of the line (A.21), and thus the position of S. If the temperature decreases, S moves further towards saturation and the spontaneous magnetization tends to the maximal value, $m_s \to m_{\text{sat}}$. Conversely, When the temperature increases, the line straightens up and the spontaneous magnetization decreases, until reaching the limit case where the line (A.21) becomes tangent to the curve (A.20) at point O. This situation happens when the Curie temperature $T = T_C$ is reached, whose value

$$T_C = \frac{\widetilde{J}+1}{3\widetilde{J}} \frac{\mu_0 m_0 \lambda_{\text{W}} m_{\text{sat}}}{k_{\text{B}}}, \tag{A.22}$$

can be deduced from the slopes equality. Beyond the Curie temperature $T > T_C$, the only remaining valid stable solution is the zero-state point O. Spontaneous magnetization is no longer possible $m_s = 0$, because thermal agitation becomes more effective and randomizes the atomic moments orientations. The ferromagnetic coupling disappears and the material behaves like a paramagnetic medium.

The application of a magnetic field in the direction of the magnetization induces a downward translation of h/λ_{W} of the line (A.21) in Fig. A.3. Accordingly, the stable point S moves towards the point S'. However, this displacement is very small in general, even for intense magnetic fields, because the constant λ_{W} which characterizes the molecular field through (A.17), remains several orders of magnitude larger, since

$h_W \approx 10^9$ A/m in standard conditions. Consequently, the applied field has a negligible influence on the magnetization.

To finish, it should be noted that expanding (A.20) to first order around the origin with (A.15) ends up again with a linear relation, $h = \chi_r m$, where the susceptibility writes this time

$$\chi_r = \frac{\widetilde{J}+1}{3\widetilde{J}} \frac{\mu_0 m_0 m_{\text{sat}}}{k_B} \frac{1}{T - T_C}, \tag{A.23}$$

which is known to be the Currie-Weiss law.

The Weiss molecular field theory allows to give a simple explanation on the spontaneous magnetization processes encountered in ferromagnetism, and a valid approximation on its temperature dependence. Despite satisfactory agreements with experimental measurements, which demonstrate the value of the Weiss model, the phenomenological character of the molecular field approach must not be forgotten. Indeed, the existence of the molecular field is only postulated and its definition is based on the averaged value of the magnetization, through (A.17), thus without any insight the microscopic arrangement of the magnetic moments. A microscopic description of the molecular field can only be depicted on the basis of quantum theory. Heisenberg gave a quantum theoretical justification of the molecular field, introducing the notions of the so-called exchange energy between neighboring magnetic moments and the overlapping of crystalline orbitals. The details of this much more complex approach is beyond the scope of this thesis. Nevertheless, it should be emphasized that Weiss theory and spontaneous magnetization processes are only valid at a localized scale in space, the scale of a Weiss domain, also called magnetic domain.

APPENDIX

B Ferromagnetism at the Mesoscopic Scale

1. Magnetic Domain Structure in a Monocrystalline Sample

The existence of magnetic domains and the prediction of their spatial disposition can be described, in principle, by the micromagnetic approach. To give an overview on the origin of magnetic domains, the qualitative concept of micromagnetics is briefly presented.

Under this approach, magnetic domains result from the complex balance of several energy terms. The domain structure of a material is one of which minimizes the total energy W_{tot} of the system

$$W_{tot} = W_{in} + W_h \,, \tag{B.1}$$

where W_h is the energy coming from the action of an external field h, while W_{in} corresponds to the internal energy. The internal energy, W_{in}, is decomposed in 4 terms:

$$W_{in} = W_{an} + W_{ms} + W_{ex} + W_{me} \,, \tag{B.2}$$

where W_{an} is the anisotropy energy, W_{ms} the magnetostatic energy, W_{ex} the exchange energy and W_{me} the magnetoelastic energy.

The impact of each of these terms is schematized in Fig. B.1, in the case of a parallelepipedic sample of perfect single crystal iron. The crystalline axes of the reference crystal are parallel to the edges of the sample.

The magnetocrystalline anisotropy energy, W_{an}, comes from the interactions of the magnetization with the crystal lattice, which favors the orientation of the magnetization vector along certain preferred directions. For example, in iron, the atomic magnetic moments preferably align with the edges of the cubic crystal. As shown by Fig. B.2, these correspond to the crystallographic directions $\langle 100 \rangle$, which denotes the set of all the six directions $[100], [\bar{1}00], [010], [0\bar{1}0], [001]$ and $[00\bar{1}]$, that are equivalent by symmetry. When a magnetic field is applied parallel to the axis $\langle 100 \rangle$, the magnetic polarization reaches rapidly the saturated region, with small excitation amplitude of the applied field. These directions are thus called easy axis of magnetization. In contrast,

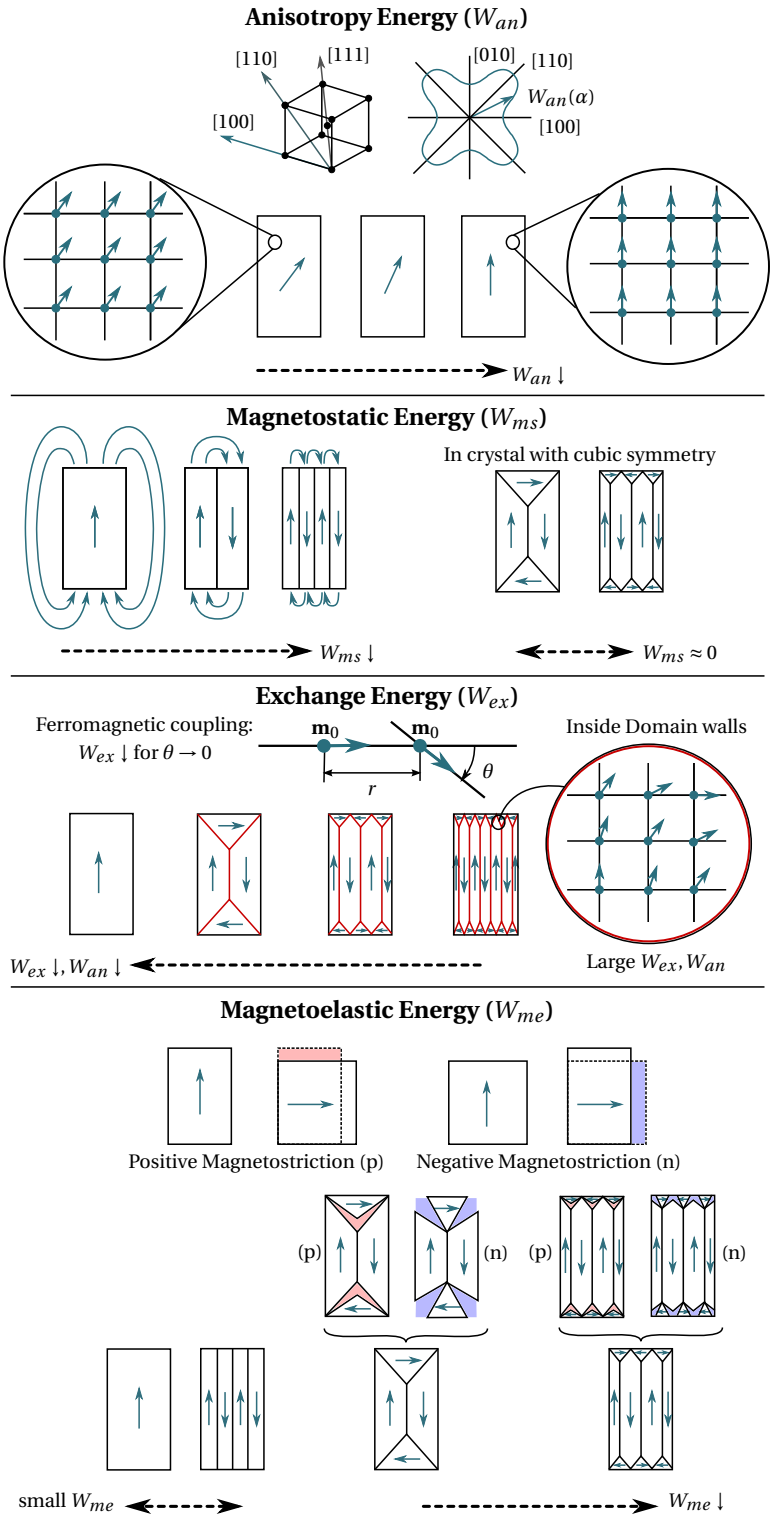

Figure B.1: *Complex balance of four energy terms in the magnetic domain structure.*

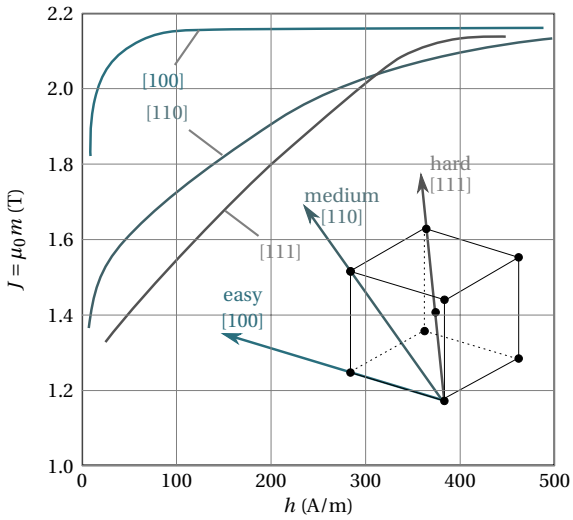

Figure B.2: *Magnetocrystalline anisotropy.*

the magnetization is increasingly more difficult along the crystal directions ⟨110⟩ and ⟨111⟩, which are called medium and hard axis of magnetization respectively, as can be seen on Fig. B.2. The energy W_{an} is mimimum along the easy direction of magnetization and maximum along the hard one. In Fig. B.1, under the effect of W_{an} alone, the spontaneous magnetization tends therefore to align itself parallel to the easy axis of the reference crystal, since they are energetically favorable directions.

The magnetostatic energy, W_{ms}, brings an opposite tendency in the energy balance since it favors magnetic configurations which cancels the average magnetic moment. This energy corresponds to the potential energy acquired by the magnetic moments due to the magnetic field that they generate upon themselves. This field is called demagnetizing field because its effect opposes to the magnetization, trying to reduce the total magnetic moment. The origin of the demagnetizing field is in general explained by means of the presence of magnetic charge density on the surface of ferromagnets. These magnetic poles, which reflect the magnetic flux lines mapped outside the sample, also generate inside the magnet a so-called demagnetizing field, whose orientation is opposed to magnetization. The energy of the demagnetizing field decreases for magnetic configurations that minimize magnetic charge density on the surface, and thus reduce the spatial extension of the field outside the sample. In particular, it favors the magnetization field to be parallel to the surface, along the edges of the sample. Therefore, magnetostatic energy has the effect of dividing the reference crystal into as many lamellar domains as possible, since W_{ms} is approximately inversely proportional to the number of lamellae. When magnetocrystalline anisotropy has cubic symmetry, it is possible to devise domain arrangements such as in Fig. B.1, with specific triangular prism domains, called flux closure domains. In this configuration, the sample does not produce any fields outside, no poles are formed and there is no demagnetizing field, such that W_{ms} is zero.

The exchange energy, W_{ex}, is the energy concept discovered by Heisenberg to give a theoretical justification to Weiss molecular field which favors uniform magnetization configurations, as already mentioned in the previous section. This energy results from the exchange interaction between magnetic moments. This interaction is purely quantum in nature since it relies fundamentally on the angular momentum of electronic spin of two neighboring atoms whose quantum wave functions overlap. The exchange interaction is a local phenomenon because these quantum wave functions decrease exponentially over the distance separating the moments. Therefore, only the contribution from the closest neighbors is taken into account. The associated energy depends on the relative orientation of these moments. For ferromagnetic coupling, this energy is minimum when their orientation is along the same direction. The exchange energy tends thus to keep adjacent magnetic moments parallel to each other. Within the transition zone between two magnetic domains of different magnetization directions, the magnetic moments change gradually their orientation, from one direction to the other, thus increasing the exchange energy W_{ex} inside the domain walls. Moreover, the magnetocrystalline anisotropy energy W_{an} also increases within domain walls since, inside them, the moments take less favorable directions between two easy axis of magnetization. The sum of these two contributions, W_{ex} and W_{an}, represents the energy associated to the domain walls. Minimizing W_{ex} and W_{an} energies favors thus the limitation of the total surface area of the domain walls. In particular, as illustrated by Fig. B.1, the division of the reference crystal into more and more lamellar domains will stop when the decrease obtained in magnetostatic energy W_{ms} is compensated by the increase in exchange energy W_{ex} and anisotropy energy W_{an} in the domain walls.

The magnetoelastic energy, W_{me}, is the energy contribution due to the effect of magnetostriction, which is a property that causes slight changes in the shape and the dimensions of magnetic materials under the process of magnetization. The magnetostriction is said to be positive, when the sample lengthens in the magnetization direction, and negative if it contracts in the magnetization direction. This causes deformations and elastic stresses in the crystal lattice. The magnetoelastic energy favors directions of magnetization that minimize these tiny mechanical stresses originating from magnetostriction. In the reference crystal, this energy varies according to the structure of the magnetic domains as illustrated by Fig. B.1. The energy tends to be minimized when the direction of magnetization of the domains are in parallel configuration because the crystal deformation affects only one direction in that case. It requires higher energy W_{me} to form flux closure domains on the edge because the constraints exerted by the domains on each other are stronger in that configuration. These constraints can be represented graphically by cutting by thought the crystal along each domain walls, and exaggerating the deformation of each domain under positive (p) or negative (n) magnetostriction effects, as shown in Fig. B.1. The increase in magnetoelastic energy represents the work that would be required to deform the pieces until they can be reassembled. Reducing the size of these closure domains lower the energy W_{me}.

At no field, the domain structure results thus from the compromise by which the material tries to satisfy all these competing internal requirements, as summarized by Fig. B.1.

Under the effect of an external magnetic field, the magnetic sample receive an addi-

tional energy contribution W_h, which influences the total energy of the system (B.1), and thus the domain structure. The term W_h, called Zeeman energy, corresponds to the potential energy acquired by the magnetic body submitted to an outer magnetic field. This energy favors domains magnetized in the direction of the applied field. Fig. B.3(a) shows a typical domain structure pattern of an iron single crystal,

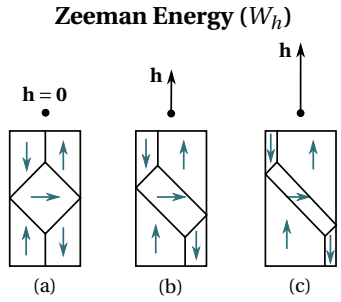

Figure B.3: *Zeeman Energy*

with no external magnetic energy provided. When an external field is applied, the energy balance is modified and a reorganization of the domain structure take place, mostly through the displacement of the domain walls. The energy W_h decreases in domains with magnetization pointing approximately in the direction of the applied field and, conversely, increases in the others. Therefore, according to the general minimum principle, the former domains, which are favored energetically, grow at the expenses of the surrounding domains, which reduce and eventually disappear. With an increasing field, the domain structure evolves successively as the sequence shown by Fig. B.3(a)→(b)→(c). At high field, the material is everywhere magnetized in the direction of the field, with nearly only one remaining big domain covering the whole sample, and the average magnetization of the crystal becomes close the spontaneous magnetization. By removing the field h, the sample returns in its initial state Fig. B.3(a). The magnetization process is here reversible because the motion of the domain wall is perfectly free in this ideal single crystal example.

2. Magnetic Domain Structure in Polycrystalline material

The previous section describes the magnetic domain arrangement in a perfect crystal lattice. However, most magnetic materials are polycrystalline in the sense that they are composed of many microscopic crystalline grains of varying size and orientation. Each grain can be seen as small single crystal, such as the one studied in the previous section, but the orientation of the crystal lattice changes from one grain to another, and so do the easy axes of magnetization. When the grains are oriented completely at random, a sufficiently large volume of polycrystalline material appears as isotropic, by averaging out the magnetocrystalline anistropy.

The general principle that the intrinsic magnetic domain structure corresponds to a minimum of the internal energy remains valid. By considering each grain separately,

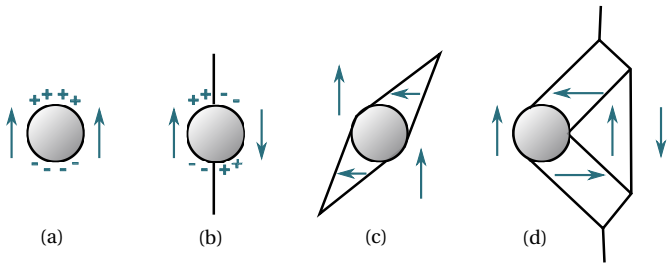

Figure B.4: *Pinning effect around a non-magnetic cavity.*

one can say that the division into magnetic domains inside each grain, is likely to present similar patterns that those seen about the reference crystal in Fig. B.1, with a main orientation favored in the easy directions of magnetization, specific to each grain. However, this only gives a general picture because the minimization cannot be applied by reducing the internal energy of each individual grain, considered as isolated from the others.

This is particularly true due to the magnetostatic energy, which is strongly influenced by the environment surrounding each grain. While the shape of the sample has a huge impact in the case of single crystal, this is the structure of the grains that has predominant effect in the study of polycrystalline material.

Moreover, the magnetic domain structure is also influenced by the presence of relatively punctual defects, such as cavities, non-magnetic inclusions or dislocations in the crystallographic structure. The interface between grains, called grain boundaries, corresponds to thin layers of amorphous solid, ensuring imperfect junctions between crystal lattices of different orientations. Grain boundaries are thus the preferential sites for location of impurities and defects in the overall polycrystalline structure.

The presence of a cavity gives rise to a large amount of magnetostatic energy linked to the formation of magnetic poles on opposite faces of the cavity, as illustrated in Fig. B.4(a). This energy is reduced when a domain wall is passing through the inclusion, giving a better balance between the magnetic poles, as in Fig. B.4(b). Therefore, the domain wall tend to be retained by the inclusion as it corresponds in a local energy minimum. A certain amount of energy is required to unlock the domain wall from its position. This phenomenon is called the domain wall pinning effect and it has a direct influence on the macroscopic properties of a magnetic material and the shape of its magnetization curve. In the absence of domain walls near the cavity, local blade domain structure such as that shown in Fig. B.4(c) can form around the inclusion, reducing the magnetostatic energy at the cost of increasing the wall energy. This configuration can further reduce its magnetostatic energy by indirect pinning of a domain wall, through secondary domains connections, as in Fig. B.4(d).

Bibliography

[1] C. Appino, C. Ragusa, and F. Fiorillo. “Can rotational magnetization be theoretically assessed?” In: *International Journal of Applied Electromagnetics and Mechanics* 44.3,4 (2014), pp. 355–370.

[2] M. d´ Aquino, G. Rubinacci, A. Tamburrino, and S. Ventre. “Efficient Numerical Solution of Magnetic Field Problems in Presence of Hysteretic Media for Non-destructive Evaluation”. In: *IEEE Trans. Magn.* 49.7 (July 2013), pp. 3167–3170.

[3] M. d´ Aquino, C. Serpico, C. Visone, and A. A. Adly. “A new vector model of magnetic hysteresis based on a novel class of Play hysterons”. In: *IEEE Transactions on Magnetics* 39.5 (Sept. 2003), pp. 2537–2539.

[4] K. Atallah and D. Howe. “Calculation of the rotational power loss in electrical steel laminations from measured H and B”. In: *IEEE Transactions on Magnetics* 29.6 (Nov. 1993), pp. 3547–3549.

[5] D. L. Atherton and M. Schonbachler. “Measurements of reversible magnetization component”. In: *IEEE Transactions on Magnetics* 24.1 (Jan. 1988), pp. 616–620.

[6] J. P. A. Bastos, N. Sadowski, J. V. Leite, N. J. Batistela, K. Hoffmann, G. Meunier, and O. Chadebec. “A Differential Permeability 3-D Formulation for Anisotropic Vector Hysteresis Analysis”. In: *IEEE Trans. Magn.* 50.2 (Feb. 2014), pp. 341–344.

[7] J. P. A. Bastos. *Magnetic Materials and 3D Finite Element Modeling*. CRC Press, 2013.

[8] A. Benabou, S. Clénet, and F. Piriou. “Comparison of Preisach and Jiles-Atherton models to take into account hysteresis phenomenon for finite element analysis”. In: *Journal of Magnetism and Magnetic Materials* 261.1 (2003), pp. 139–160.

[9] A. Benabou, J. Leite, S. Clénet, C. Simão, and N. Sadowski. “Minor loops modelling with a modified Jiles–Atherton model and comparison with the Preisach model”. In: *Journal of Magnetism and Magnetic Materials* 320.20 (2008), e1034–e1038.

[10] A. Benabou. “Contribution à la caractérisation et à la modélisation de matériaux magnétiques en vue d’une implantation dans un code de calcul de champ”. PhD thesis. Université de Lille, 2002.

[11] A. Bergqvist. “On Magnetic Hysteresis Modeling”. PhD thesis. Stockholm: Royal Institute of Technology, 1994.

[12] A. J. Bergqvist. “A simple vector generalization of the Jiles-Atherton model of hysteresis”. In: *IEEE Trans. Magn.* 32.5 (Sept. 1996), pp. 4213–4215.

[13] A. Bergqvist and G. Engdahl. “A model for magnetomechanical hysteresis and losses in magnetostrictive materials”. In: *J. Appl. Phys.* 79.8 (1996), pp. 6476–6478.

[14] A. Bergqvist, D. Lin, and P. Zhou. “Temperature-Dependent Vector Hysteresis Model for Permanent Magnets”. In: *IEEE Transactions on Magnetics* 50.2 (Feb. 2014), pp. 345–348.

[15] A. Bergqvist, A. Lundgren, and G. Engdahl. “Experimental testing of an anisotropic vector hysteresis model”. In: *IEEE Trans. Magn.* 33.5 (Sept. 1997), pp. 4152–4154.

[16] A. Bergqvist, A. Lundgren, F. Stillesjö, and G. Engdahl. “Statistical modeling of magnetic and magnetostrictive properties due to domain wall motion”. In: *J. Appl. Phys.* 85.8 (Apr. 1999), p. 5190.

[17] A. Bergqvist. “Magnetic vector hysteresis model with dry friction-like pinning”. In: *Physica B: Condensed Matter* 233.4 (1997), pp. 342–347.

[18] G. Bertotti. “Physical interpretation of eddy current losses in ferromagnetic materials. I. Theoretical considerations”. In: *Journal of Applied Physics* 57.6 (1985), pp. 2110–2117.

[19] G. Bertotti. “Physical interpretation of eddy current losses in ferromagnetic materials. II. Analysis of experimental results”. In: *Journal of Applied Physics* 57.6 (1985), pp. 2118–2126.

[20] G. Bertotti. “General properties of power losses in soft ferromagnetic materials”. In: *IEEE Transactions on Magnetics* 24.1 (Jan. 1988), pp. 621–630.

[21] G. Bertotti. “Generalized Preisach model for the description of hysteresis and eddy current effects in metallic ferromagnetic materials”. In: *J. Appl. Phys.* 69.8 (1991), pp. 4608–4610.

[22] G. Bertotti. “Dynamic generalization of the scalar Preisach model of hysteresis”. In: *IEEE Transactions on Magnetics* 28.5 (Sept. 1992), pp. 2599–2601.

[23] G. Bertotti. “Connection between microstructure and magnetic properties of soft magnetic materials”. In: *Journal of Magnetism and Magnetic Materials* 320.20 (2008), pp. 2436–2442.

[24] G. Bertotti, A. Boglietti, M. Chiampi, D. Chiarabaglio, F. Fiorillo, and M. Lazzari. “An improved estimation of iron losses in rotating electrical machines”. In: *IEEE Transactions on Magnetics* 27.6 (Nov. 1991), pp. 5007–5009.

[25] G. Bertotti, G. Di Schino, A. Ferro Milone, and F. Fiorillo. “On the Effect of Grain Size on Magnetic Losses of 3% Non-Oriented SiFe”. In: *Journal de Physique Colloques* 46.C6 (1985), pp. 385–388.

[26] G. Bertotti. *Hysteresis in Magnetism*. Academic Press, 1998.

[27] S. Bobbio, G. Milano, C. Serpico, and C. Visone. “Models of magnetic hysteresis based on play and stop hysterons”. In: *IEEE Trans. Magn.* 33.6 (Nov. 1997), pp. 4417–4426.

[28] A. Bossavit. “A rationale for edge-elements in 3-D fields computations”. In: *IEEE Transactions on Magnetics* 24.1 (Jan. 1988), pp. 74–79.

[29] A. Bossavit. *Électromagnétisme, en vue de la modélisation*. Mathématiques et Applications. Springer Berlin Heidelberg, 2004.

[30] A. Bossavit. “Two dual formulations of the 3-D Eddy-currents problem”. In: *COMPEL* 4 (Dec. 1985), pp. 103–116.

[31] A. P. V. den Bossche, D. M. V. de Sype, and V. C. Valchev. “Ferrite Loss Measurement and Models in Half Bridge and Full Bridge Waveforms”. In: *2005 IEEE 36th Power Electronics Specialists Conference*. June 2005, pp. 1535–1539.

[32] A. V. den Bossche, V. C. Valchev, and G. B. Georgiev. “Measurement and loss model of ferrites with non-sinusoidal waveforms”. In: *2004 IEEE 35th Annual Power Electronics Specialists Conference (IEEE Cat. No.04CH37551)*. Vol. 6. June 2004, 4814–4818 Vol.6.

[33] O. Bottauscio, M. Chiampi, C. Ragusa, L. Rege, and M. Repetto. “Description of TEAM Problem: 32 A test-case for validation of magnetic field analysis with Vector hysteresis”. In: *compumag* (2013).

[34] R. P. Brent. *Algorithms for Minimization without Derivatives*. Englewood Cliffs, N.J.: Prentice-Hall, 1973.

[35] L. Brillouin. “Les moments de rotation et le magnétisme dans la mécanique ondulatoire”. In: *J. Phys. Radium* 8.2 (1927), pp. 74–84.

[36] M. Brokate. “Some mathematical properties of the Preisach model for hysteresis”. In: *IEEE Transactions on Magnetics* 25.4 (July 1989), pp. 2922–2924.

[37] C. G. Broyden. “A class of methods for solving nonlinear simultaneous equations”. In: *Math. Comput.* 19 (1965), pp. 577–593.

[38] C. G. Broyden. “The Convergence of a Class of Double-rank Minimization Algorithms”. In: *IMA Journal of Applied Mathematics* 6.1 (1970), pp. 76–90.

[39] E. Cardelli. “A General Hysteresis Operator for the Modeling of Vector Fields”. In: *IEEE Transactions on Magnetics* 47.8 (Aug. 2011), pp. 2056–2067.

[40] E. Cardelli, E. D. Torre, and A. Faba. “A General Vector Hysteresis Operator: Extension to the 3-D Case”. In: *IEEE Transactions on Magnetics* 46.12 (Dec. 2010), pp. 3990–4000.

[41] K. Carpenter. “A differential equation approach to minor loops in the Jiles-Atherton hysteresis model”. In: *IEEE Trans. Magn.* 27.6 (Nov. 1991), pp. 4404–4406.

[42] K. Chen. “Iron-Loss Simulation of Laminated Steels Based on Expanded Generalized Steinmetz Equation”. In: *2009 Asia-Pacific Power and Energy Engineering Conference*. Mar. 2009, pp. 1–3.

[43] T. Chevalier, A. Kedous-Lebouc, B. Cornut, and C. Cester. “A new dynamic hysteresis model for electrical steel sheet”. In: *Physica B: Condensed Matter* 275.1 (2000), pp. 197–201.

[44] K. Chwastek. “Modelling of dynamic hysteresis loops using the Jiles–Atherton approach”. In: *Mathematical and Computer Modelling of Dynamical Systems* 15.1 (2009), pp. 95–105.

[45] J. Coey. *Magnetism and Magnetic Materials*. Magnetism and Magnetic Materials. Cambridge University Press, 2010.

[46] M. Crisfield. “A fast incremental/iterative solution procedure that handles “snap-through””. In: *Computers & Structures* 13.1 (1981), pp. 55–62.

[47] B. D. Cullity and C. D. Graham. *Introduction to Magnetic Materials*. 2nd ed. Wiley, 2008.

[48] L. Daniel. “Multi-scale modelling of the magneto-mechanical behaviour of ferromagnetic textured materials”. Theses. École normale supérieure de Cachan - ENS Cachan, Sept. 2003.

[49] R. Dautray, A. Craig, M. Artola, M. Cessenat, J. Lions, and H. Lanchon. *Mathematical Analysis and Numerical Methods for Science and Technology: Volume 5 Evolution Problems I*. Mathematical Analysis and Numerical Methods for Science and Technology. Springer Berlin Heidelberg, 1999.

[50] W. Davidon. “Variable Metric Method for Minimization”. In: *SIAM Journal on Optimization* 1.1 (1991), pp. 1–17.

[51] O. Deblecker, J. Lobry, and C. Broche. “Core loss estimation in three-phase transformer using vector hysteresis model and classical loss model incorporated in 2D magnetodynamics”. In: *European Transactions on Electrical Power* 13.2 (2003), pp. 91–103.

[52] F. Delincé. “Modélisation des régimes transitoires dans les systèmes comportant des matériaux magnétiques non-linéaires et hystérétiques”. PhD thesis. Université de Liège, 1994.

[53] E. Dlala and A. Arkkio. “Analysis of the Convergence of the Fixed-Point Method Used for Solving Nonlinear Rotational Magnetic Field Problems”. In: *IEEE Transactions on Magnetics* 44.4 (Apr. 2008), pp. 473–478.

[54] É. Du Trémolet de Lacheisserie and M. Cyrot. *Magnétisme: Matériaux et applications. II*. Collection Grenoble sciences. EDP Sciences, 2000.

[55] P. Dular. “Dual Magnetodynamic Finite Element Formulations with Natural Definitions of Global Quantities for Electric Circuit Coupling”. In: *Scientific Computing in Electrical Engineering: Proceedings of the 3rd International Workshop, August 20–23, 2000, Warnemünde, Germany*. Berlin, Heidelberg: Springer Berlin Heidelberg, 2001, pp. 367–377.

[56] P. Dular, C. Geuzaine, F. Henrotte, and W. Legros. “A general environment for the treatment of discrete problems and its application to the finite element method”. In: *IEEE Trans. Magn.* 34.5 (Sept. 1998), pp. 3395–3398.

[57] P. Dular, J. Gyselinck, F. Henrotte, W. Legros, and J. Melkebeek. “Complementary finite element magnetodynamic formulations with enforced magnetic fluxes”. In: *COMPEL* 18.4 (1999), pp. 656–667.

[58] P. Dular, F. Henrotte, F. Robert, A. Genon, and W. Legros. “A generalized source magnetic field calculation method for inductors of any shape”. In: *IEEE Trans. Magn.* 33.2 (Mar. 1997), pp. 1398–1401.

[59] P. Dular, J. Y. Hody, A. Nicolet, A. Genon, and W. Legros. “Mixed finite elements associated with a collection of tetrahedra, hexahedra and prisms”. In: *IEEE Transactions on Magnetics* 30.5 (Sept. 1994), pp. 2980–2983.

[60] P. Dular, P. Kuo-Peng, C. Geuzaine, N. Sadowski, and J. P. A. Bastos. “Dual magnetodynamic formulations and their source fields associated with massive and stranded inductors”. In: *IEEE Trans. Magn.* 36.4 (July 2000), pp. 1293–1299.

[61] P. Dular. “Modélisation du champ magnétique et des courants induits dans des systèmes tridimensionnels non linéaires”. PhD thesis. Université de Liège, 1996.

[62] P. Dular. “The benefits of nodal and edge elements coupling for discretizing global constraints in dual magnetodynamic formulations”. In: *J. Comput. Appl. Math.* 168.1 (2004), pp. 165–178.

[63] P. Dular. “A time-domain homogenization technique for lamination stacks in dual finite element formulations”. In: *J. Comput. Appl. Math.* 215.2 (2008), pp. 390–399.

[64] L. R. Dupré, G. Bertotti, and J. A. A. Melkebeek. “Dynamic Preisach model and energy dissipation in soft magnetic materials”. In: *IEEE Transactions on Magnetics* 34.4 (July 1998), pp. 1168–1170.

[65] L. R. Dupré, J. J. Gyselinck, and J. A. Melkebeek. “Complementary finite element methods in 2D magnetics taking into account a vector Preisach model”. In: *IEEE Trans. Magn.* 34.5 (Sept. 1998), pp. 3048–3051.

[66] L. R. Dupré, R. V. Keer, and J. A. A. Melkebeek. “On a magnetodynamic model for the iron losses in non-oriented steel laminations”. In: *Journal of Physics D: Applied Physics* 29.3 (1996), p. 855.

[67] L. R. Dupré, R. Van Keer, and J. A. A. Melkebeek. “Complementary 2-D finite element procedures for the magnetic field analysis using a vector hysteresis model”. In: *Int. J. Numer. Methods Eng.* 42.6 (1998), pp. 1005–1023.

[68] L. Dupré, M. J. Sablik, R. V. Keer, and J. Melkebeek. “Modelling of microstructural effects on magnetic hysteresis properties”. In: *Journal of Physics D: Applied Physics* 35.17 (2002), p. 2086.

[69] L. Dupré, R. Van Keer, and J. Melkebeek. “Modelling the electromagnetic behaviour of sife alloys using the Preisach theory and the principle of loss seperation”. In: *Mathematical Problems in Engineering* 7.2 (2001), pp. 113–128.

[70] G. Emiel. “Méthodes d’optimisation non differentiable pour la résolution de grands problèmes. Applications à la gestion à moyen-terme de la production.” Theses. Université Panthéon-Sorbonne - Paris I, Nov. 2008.

[71] M. Enokizono, T. Suzuki, J. Sievert, and J. Xu. “Rotational power loss of silicon steel sheet”. In: *IEEE Transactions on Magnetics* 26.5 (Sept. 1990), pp. 2562–2564.

[72] M. Fafard and B. Massicotte. “Geometrical interpretation of the arc-length method”. In: *Computers & Structures* 46.4 (1993), pp. 603–615.

[73] P. Ferrouillat. “Développement de formulations éléments finis 3D en potentiel vecteur magnétique : application aux machines asynchrones en mouvement”. PhD thesis. 2015.

[74] F. Fiorillo and A. Novikov. “An improved approach to power losses in magnetic laminations under nonsinusoidal induction waveform”. In: *IEEE Transactions on Magnetics* 26.5 (Sept. 1990), pp. 2904–2910.

[75] F. Fiorillo and A. M. Rietto. “Rotational versus alternating hysteresis losses in nonoriented soft magnetic laminations”. In: *Journal of Applied Physics* 73.10 (1993), pp. 6615–6617.

[76] F. Fiorillo and A. Rietto. “Rotational and alternating energy loss vs. magnetizing frequency in SiFe laminations”. In: *Journal of Magnetism and Magnetic Materials* 83.1 (1990), pp. 402–404.

[77] R. Fletcher. “A new approach to variable metric algorithms”. In: *The Computer Journal* 13.3 (1970), pp. 317–322.

[78] R. Fletcher. *Practical Methods of Optimization; (2Nd Ed.)* New York, NY, USA: Wiley-Interscience, 1987.

[79] V. François-Lavet, F. Henrotte, L. Stainier, L. Noels, and C. Geuzaine. “An energy-based variational model of ferromagnetic hysteresis for finite element computations”. In: *J. Comput. Appl. Math.* 246 (2013), pp. 243–250.

[80] A. Frias. “Minimization of iron losses of traction electric machines by modeling and optimization”. Theses. Université de Grenoble, Mar. 2015.

[81] G. Friedman and I. D. Mayergoyz. “Hysteretic energy losses in media described by vector Preisach model”. In: *IEEE Transactions on Magnetics* 34.4 (July 1998), pp. 1270–1272.

[82] K. Fujiwara, T. Nakata, N. Okamoto, and K. Muramatsu. “Method for determining relaxation factor for modified Newton-Raphson method”. In: *IEEE Transactions on Magnetics* 29.2 (Mar. 1993), pp. 1962–1965.

[83] E. Furlani. *Permanent Magnet and Electromechanical Devices: Materials, Analysis, and Applications*. Electromagnetism. Elsevier Science, 2001.

[84] T. Gautreau. “Iron Losses Prediction in Electrical Motors. Loss Surface Hysteresis Model and Application to Synchronous Permanent Magnet Machines.” Theses. Institut National Polytechnique de Grenoble - INPG, Dec. 2005.

[85] C. Geuzaine and J.-F. Remacle. “Gmsh: A 3-D finite element mesh generator with built-in pre- and post-processing facilities”. In: *International Journal for Numerical Methods in Engineering* 79.11 (), pp. 1309–1331.

[86] P. Gill, W. Murray, and M. Wright. *Practical optimization*. Academic Press, 1981.

[87] M. S. Gockenbach. *Newton s method*. 2003.

[88] D. Goldfarb. “A Family of Variable-Metric Methods Derived by Variational Means”. In: *Mathematics of Computation* 24.109 (1970), pp. 23–26.

[89] A. Goldman. *Magnetic Components for Power Electronics*. Springer US, 2002.

[90] W. Grosse-Nobis. “Frequency spectrum of the Barkhausen noise of a moving 180° domain wall”. In: *Journal of Magnetism and Magnetic Materials* 4.1 (1977), pp. 247–253.

[91] C. Guérin, K. Jacques, R. V. Sabariego, P. Dular, C. Geuzaine, and J. Gyselinck. “Using a Jiles-Atherton vector hysteresis model for isotropic magnetic materials with the finite element method, Newton-Raphson method, and relaxation procedure”. In: *International Journal of Numerical Modelling: Electronic Networks, Devices and Fields* 30.5 (2017), e2189.

[92] Y. Guo, J. G. Zhu, J. Zhong, H. Lu, and J. X. Jin. “Measurement and Modeling of Rotational Core Losses of Soft Magnetic Materials Used in Electrical Machines: A Review”. In: *IEEE Transactions on Magnetics* 44.2 (Feb. 2008), pp. 279–291.

[93] O. Gutfleisch, M. A. Willard, E. Brück, C. H. Chen, S. G. Sankar, and J. P. Liu. “Magnetic Materials and Devices for the 21st Century: Stronger, Lighter, and More Energy Efficient”. In: *Advanced Materials* 23.7 (2011), pp. 821–842.

[94] J. J. C. Gyselinck, L. Vandevelde, D. Makaveev, and J. A. A. Melkebeek. “Calculation of no load losses in an induction motor using an inverse vector Preisach model and an eddy current loss model”. In: *IEEE Transactions on Magnetics* 36.4 (July 2000), pp. 856–860.

[95] J. Gyselinck, P. Dular, N. Sadowski, J. Leite, and J. Bastos. “Incorporation of a Jiles-Atherton vector hysteresis model in 2D FE magnetic field computations: Application of the Newton-Raphson method”. In: *COMPEL* 23.3 (Sept. 2004), pp. 685–693.

[96] J. Gyselinck, R. V. Sabariego, and P. Dular. “A nonlinear time-domain homogenization technique for laminated iron cores in three-dimensional finite-element models”. In: *IEEE Trans. Magn.* 42.4 (Apr. 2006), pp. 763–766.

[97] J. Gyselinck, L. Vandevelde, J. Melkebeek, and P. Dular. “Complementary two dimensional finite element formulations with inclusion of a vectorized Jiles-Atherton model”. In: *COMPEL* 23.4 (Dec. 2004), pp. 959–967.

[98] J. Gyselinck, L. Vandevelde, J. Melkebeek, P. Dular, F. Henrotte, and W. Legros. “Calculation of eddy currents and associated losses in electrical steel laminations”. In: *IEEE Trans. Magn.* 35.3 (May 1999), pp. 1191–1194.

[99] J. Gyselinck. “Twee-Dimensionale Dynamische Eindige-Elementenmodellering van Statische en Roterende Elektromagnetische Energieomzetters”. PhD thesis. Universiteit Gent, 2000.

[100] J. Gyselinck, M. De Wulf, L. Vandevelde, and J. Melkebeek. “Incorporation of vector hysteresis and eddy current losses in 2D FE magnetodynamics.” In: *6th Int. Conf. ELECTRIMACS, Sept. 14-16, Lisboa, Portugal, 1999*. 1999, pp. 37–44.

[101] R. F. Harrington. *Time-Harmonic Electromagnetic Fields*. IEEE-Press, 2001.

[102] F. Henrotte and K. Hameyer. “A dynamical vector hysteresis model based on an energy approach”. In: *IEEE Transactions on Magnetics* 42.4 (Apr. 2006), pp. 899–902.

[103] F. Henrotte, A. Nicolet, and K. Hameyer. “An energy-based vector hysteresis model for ferromagnetic materials”. In: *COMPEL* 25.1 (Jan. 2006), pp. 71–80.

[104] F. Henrotte, S. Steentjes, K. Hameyer, and C. Geuzaine. “Iron Loss Calculation in Steel Laminations at High Frequencies”. In: *IEEE Trans. Magn.* 50.2 (Feb. 2014), pp. 333–336.

[105] G. Houlsby and A. Puzrin. “A thermomechanical framework for constitutive models for rate-independent dissipative materials”. In: *International Journal of Plasticity* 16.9 (2000), pp. 1017–1047.

[106] IEC-60404-2. *Magnetic materials - Part 2: Methods of measurement of the magnetic properties of electrical steel strip and sheet by means of an Epstein frame*. 2008.

[107] IEC-60404-3. *Magnetic materials - Part 3: Methods of measurement of the magnetic properties of electrical steel strip and sheet by means of a single sheet tester*. 2009.

[108] D. M. Ionel, M. Popescu, S. J. Dellinger, T. J. E. Miller, R. J. Heideman, and M. I. McGilp. “On the variation with flux and frequency of the core loss coefficients in electrical machines”. In: *IEEE Transactions on Industry Applications* 42.3 (May 2006), pp. 658–667.

[109] D. M. Ionel, M. Popescu, M. I. McGilp, T. J. E. Miller, S. J. Dellinger, and R. J. Heideman. “Computation of Core Losses in Electrical Machines Using Improved Models for Laminated Steel”. In: *IEEE Transactions on Industry Applications* 43.6 (Nov. 2007), pp. 1554–1564.

[110] J. Jackson. *Classical Electrodynamics*. Wiley, 2012.

[111] S. Jacobs, F. Henrotte, M. Herranz Gracia, K. Hameyer, P. Goes, and D. Hectors. “Magnetic material optimization for hybrid vehicle PMSM drives”. In: *World electric vehicle journal* 3 (2009), 9 S.

[112] K. Jacques, C. Geuzaine, and J. Gyselinck. “Using an Energy-Based Hysteresis Model in Magnetodynamic Finite Element Simulations of a Three-Phase Transformer”. In: *10th International Symposium on Electric and Magnetic Fields (EMF)*. Lyon, France, Apr. 2016.

[113] K. Jacques, C. Geuzaine, F. Henrotte, and J. Gyselinck. “Comparison between differential and variational forms of an energy-based hysteresis model”. In: *IEEE International Energy Conference (ENERGYCON)*. Belgium, Apr. 2016, pp. 1–6.

[114] K. Jacques, C. Geuzaine, F. Henrotte, and J. Gyselinck. “Comparison between differential and variational forms of an energy-based hysteresis model”. In: *IEEE International Energy Conference (ENERGYCON)*. Leuven, Belgium, Apr. 2016.

[115] K. Jacques, R. V. Sabariego, C. Geuzaine, and J. Gyselinck. “Inclusion of a Direct and Inverse Energy-Consistent Hysteresis Model in Dual Magnetostatic Finite-Element Formulations”. In: *20th International Conference on the Computation of Electromagnetic Fields (COMPUMAG)*. Montréal, Canada, July 2015.

[116] K. Jacques, R. V. Sabariego, C. Geuzaine, and J. Gyselinck. “Inclusion of a Direct and Inverse Energy-Consistent Hysteresis Model in Dual Magnetostatic Finite-Element Formulations”. In: *IEEE Transactions on Magnetics* 52.3 (Mar. 2016), pp. 1–4.

[117] K. Jacques, P. Dular, C. Geuzaine, and J. Gyselinck. “Dual Magnetodynamic Finite Element Formulations with Inclusion of an Energy-Based Hysteresis Model”. In: *17th Biennal Conference on Electromagnetic Field Computations (CEFC)*. Miami, FL, United States, Nov. 2016.

[118] K. Jacques, F. Henrotte, C. Geuzaine, and J. Gyselinck. “Improved Energy-Based Hysteresis Model and Parameter Identification for Magnetic Hysteresis Materials”. In: *The 11th International Symposium on Electric and Magnetic Fields (EMF)*. Darmstadt, Germany, Apr. 2018.

[119] K. Jacques, F. Henrotte, J. Gyselinck, R. V. Sabariego, and C. Geuzaine. “Comparison between The Energy-Based Hysteresis Model and The Jiles-Atherton Model in Finite Element Simulations”. In: *The 18th International Symposium on Applied Electromagnetics and Mechanics (ISEM)*. Chamonix, Mont-Blanc, France, Sept. 2017.

[120] K. Jacques, S. Steentjes, F. Henrotte, C. Geuzaine, and K. Hameyer. “Representation of microstructural features and magnetic anisotropy of electrical steels in an energy-based vector hysteresis model”. In: *AIP Advances* 8.4 (2018), p. 047602.

[121] D. C. Jiles. “Frequency dependence of hysteresis curves in ’non-conducting’ magnetic materials”. In: *IEEE Transactions on Magnetics* 29.6 (Nov. 1993), pp. 3490–3492.

[122] D. C. Jiles, J. B. Thoelke, and M. K. Devine. “Numerical determination of hysteresis parameters for the modeling of magnetic properties using the theory of ferromagnetic hysteresis”. In: *IEEE Transactions on Magnetics* 28.1 (Jan. 1992), pp. 27–35.

[123] D. Jiles. “A self consistent generalized model for the calculation of minor loop excursions in the theory of hysteresis”. In: *IEEE Trans. Magn.* 28.5 (Sept. 1992), pp. 2602–2604.

[124] D. Jiles. *Introduction to Magnetism and Magnetic Materials, Second Edition*. Taylor & Francis, 1998.

[125] D. Jiles and D. Atherton. “Theory of ferromagnetic hysteresis”. In: *J. Magn. Magn. Mater.* 61.1-2 (1986), pp. 48–60.

[126] H. Jordan. “Die ferromagnetischen konstanten für schwache wechselfelder”. In: *Elektr. Nach. Techn.* 1 (1958), p. 8.

[127] K. H. J. Buschow and F. R. de Boer. *Physics of Magnetism and Magnetic Materials*. 1st ed. Springer US, 2003.

[128] J. Kitao, K. Hashimoto, Y. Takahashi, K. Fujiwara, Y. Ishihara, A. Ahagon, and T. Matsuo. “Magnetic Field Analysis of Ring Core Taking Account of Hysteretic Property Using Play Model”. In: *IEEE Transactions on Magnetics* 48.11 (Nov. 2012), pp. 3375–3378.

[129] C. Kittel. *Introduction to Solid State Physics*. Wiley, 2004.

[130] C. Kittel. *Physique de l’état solide: cours et problèmes*. Sciences sup. Dunod, 2005.

[131] T. Kochmann. “Relationship between rotational and alternating losses in electrical steel sheets”. In: *Journal of Magnetism and Magnetic Materials* 160 (1996), pp. 145–146.

[132] J. Krah and A. Bergqvist. “Numerical optimization of a hysteresis model”. In: *Physica B: Condensed Matter* 343.1-4 (2004), pp. 35–38.

[133] P. Krejci. “Hysteresis and periodic solutions of semilinear and quasilinear wave equations”. In: 193 (Jan. 1986), pp. 247–264.

[134] A. Krings. “Iron Losses in Electrical Machines - Influence of Material Properties, Manufacturing Processes, and Inverter Operation”. PhD thesis. KTH, Electrical Energy Conversion, 2014.

[135] P. Langevin. “Sur la théorie du magnétisme”. In: *J. Phys. Theor. Appl.* 4.1 (1905), pp. 678–693.

[136] J. V. Leite, S. L. Avila, N. J. Batistela, W. P. Carpes, N. Sadowski, P. Kuo-Peng, and J. P. A. Bastos. “Real coded genetic algorithm for Jiles-Atherton model parameters identification”. In: *IEEE Transactions on Magnetics* 40.2 (Mar. 2004), pp. 888–891.

[137] J. V. Leite, M. V. F. da Luz, N. Sadowski, and P. A. da Silva. “Modelling Dynamic Losses Under Rotational Magnetic Flux”. In: *IEEE Transactions on Magnetics* 48.2 (Feb. 2012), pp. 895–898.

[138] J. V. Leite, N. Sadowski, P. Kuo-Peng, and J. P. A. Bastos. “A new anisotropic vector hysteresis model based on stop hysterons”. In: *IEEE Transactions on Magnetics* 41.5 (May 2005), pp. 1500–1503.

[139] J. V. Leite, N. Sadowski, P. Kuo-Peng, N. J. Batistela, J. P. A. Bastos, and A. A. de Espindola. “Inverse Jiles-Atherton vector hysteresis model”. In: *IEEE Transactions on Magnetics* 40.4 (July 2004), pp. 1769–1775.

[140] J. V. Leite, A. Benabou, and N. Sadowski. “Accurate minor loops calculation with a modified Jiles-Atherton hysteresis model”. In: *COMPEL* 28.3 (2009), pp. 741–749.

[141] A. S. Lewis and M. L. Overton. *Nonsmooth optimization via BFGS*. Tech. rep. 2008.

[142] A. S. Lewis and M. L. Overton. “Nonsmooth optimization via quasi-Newton methods”. In: *Mathematical Programming* 141.1-2 (2013), pp. 135–163.

[143] J. Li, T. Abdallah, and C. R. Sullivan. “Improved calculation of core loss with nonsinusoidal waveforms”. In: *Conference Record of the 2001 IEEE Industry Applications Conference. 36th IAS Annual Meeting (Cat. No.01CH37248)*. Vol. 4. Sept. 2001, 2203–2210 vol.4.

[144] L. Li, A. Kedous-Lebouc, A. Foggia, and J. C. Mipo. “An iron loss model (loss surface) for FeCo sheet and its application in machine design”. In: *The XIX International Conference on Electrical Machines - ICEM 2010*. Sept. 2010, pp. 1–6.

[145] D. Lin, P. Zhou, and A. Bergqvist. “Improved Vector Play Model and Parameter Identification for Magnetic Hysteresis Materials”. In: *IEEE Trans. Magn.* 50.2 (Feb. 2014), pp. 357–360.

[146] D. Lin, P. Zhou, and M. A. Rahman. “A Practical Anisotropic Vector Hysteresis Model Based on Play Hysterons”. In: *IEEE Transactions on Magnetics* 53.11 (Nov. 2017), pp. 1–6.

[147] D. Lin, P. Zhou, and N. Chen. “A New Vector Hysteresis Model Based on Series-Distributed Play Hysterons”. In: *COMPUMAG*. Montreal, 2015.

[148] J. Lubliner. *Plasticity Theory*. Dover books on engineering. Dover Publications, 2008.

[149] M. V. F. da Luz, J. V. Leite, A. Benabou, and N. Sadowski. “Three-Phase Transformer Modeling Using a Vector Hysteresis Model and Including the Eddy Current and the Anomalous Losses”. In: *IEEE Transactions on Magnetics* 46.8 (Aug. 2010), pp. 3201–3204.

[150] R. Marion, R. Scorretti, N. Siauve, M. A. Raulet, and L. Krahenbuhl. “Identification of Jiles-Atherton Model Parameters Using Particle Swarm Optimization”. In: *IEEE Transactions on Magnetics* 44.6 (June 2008), pp. 894–897.

[151] A. V. P. Mark A. Krasnosel’skii. *Systems with Hysteresis*. 1st ed. Springer-Verlag Berlin Heidelberg, 1989.

[152] T. Matsuo. “Rotational Saturation Properties of Isotropic Vector Hysteresis Models Using Vectorized Stop and Play Hysterons”. In: *IEEE Transactions on Magnetics* 44.11 (Nov. 2008), pp. 3185–3188.

[153] T. Matsuo. “Comparison of Rotational Hysteretic Properties of Isotropic Vector Stop Models”. In: *IEEE Transactions on Magnetics* 45.3 (Mar. 2009), pp. 1194–1197.

[154] T. Matsuo. “Anisotropic Vector Hysteresis Model Using an Isotropic Vector Play Model”. In: *IEEE Transactions on Magnetics* 46.8 (Aug. 2010), pp. 3041–3044.

[155] T. Matsuo and M. Shimasaki. “Identification of a Generalized 3-D Vector Hysteresis Model Through the Superposition of Stop- and Play-Based Scalar Models”. In: *IEEE Transactions on Magnetics* 43.6 (June 2007), pp. 2965–2967.

[156] T. Matsuo and M. Shimasaki. “Two Types of Isotropic Vector Play Models and Their Rotational Hysteresis Losses”. In: *IEEE Transactions on Magnetics* 44.6 (June 2008), pp. 898–901.

[157] I. D. Mayergoyz. *Mathematical Models of Hysteresis and Their Applications*. Elsevier Science, 2003.

[158] G. Meunier. *The Finite Element Method for Electromagnetic Modeling*. ISTE. Wiley, 2010.

[159] L. Michalowsky and J. Schneider. *Magnettechnik : Grundlagen, Werkstoffe, Anwendungen*. Essen, 2006.

[160] D. Miljavec and B. Zidaric. “Introducing a domain flexing function in the Jiles-Atherton hysteresis model”. In: *J. Magn. Magn. Mater.* 320.5 (2008), pp. 763–768.

[161] N. Mohan, T. M. Undeland, and W. P. Robbins. *Power Electronics. Converters, Applications and Design*. third. John Wiley and Sons, Inc, 2003.

[162] A. J. Moses. “Importance of rotational losses in rotating machines and transformers”. In: *Journal of Materials Engineering and Performance* 1.2 (Mar. 1992), pp. 235–244.

[163] A. J. Moses. “Energy efficient electrical steels: Magnetic performance prediction and optimization”. In: *Scripta Materialia* 67.6 (2012), pp. 560–565.

[164] J. Muhlethaler, J. Biela, J. W. Kolar, and A. Ecklebe. “Improved Core-Loss Calculation for Magnetic Components Employed in Power Electronic Systems”. In: *IEEE Transactions on Power Electronics* 27.2 (Feb. 2012), pp. 964–973.

[165] W. Murray. “Newton-Type Methods”. In: *Wiley Encyclopedia of Operations Research and Management Science*. American Cancer Society, 2011.

[166] M. Nayfeh and M. Brussel. *Electricity and Magnetism*. Dover Publications, 2015.

[167] J. C. Nedelec. “Mixed Finite Elements in R3”. In: *Numer. Math.* 35.3 (Sept. 1980), pp. 315–341.

[168] I. Niyonzima, R. V. Sabariego, P. Dular, and C. Geuzaine. “Nonlinear Computational Homogenization Method for the Evaluation of Eddy Currents in Soft Magnetic Composites”. In: *IEEE Transactions on Magnetics* 50.2 (Feb. 2014), pp. 61–64.

[169] I. Niyonzima, R. V. Sabariego, P. Dular, F. Henrotte, and C. Geuzaine. “Computational Homogenization for Laminated Ferromagnetic Cores in Magnetodynamics”. In: *IEEE Transactions on Magnetics* 49.5 (May 2013), pp. 2049–2052.

[170] I. Niyonzima, R. V. Sabariego, P. Dular, F. Henrotte, and C. Geuzaine. “Computational Homogenization for Laminated Ferromagnetic Cores in Magnetodynamics”. In: *IEEE Trans. Magn.* 49.5 (May 2013), pp. 2049–2052.

[171] I. Niyonzima, R. Sabariego, P. Dular, K. Jacques, and C. Geuzaine. “Multiscale Finite Element Modeling of Nonlinear Magnetoquasistatic Problems using Magnetic Induction Conforming Formulations”. In: *Multiscale Modeling & Simulation* 16.1 (2018), pp. 300–326.

[172] J. Nocedal and S. J. Wright. *Numerical Optimization*. second. New York, NY, USA: Springer, 2006.

[173] R. O'Handley. *Modern Magnetic Materials: Principles and Applications*. Wiley, 2000.

[174] W. A. Pluta. "Some Properties of Factors of Specific Total Loss Components in Electrical Steel". In: *IEEE Transactions on Magnetics* 46.2 (Feb. 2010), pp. 322–325.

[175] M. Popescu and D. M. Ionel. "A Best-Fit Model of Power Losses in Cold Rolled-Motor Lamination Steel Operating in a Wide Range of Frequency and Magnetization". In: *IEEE Transactions on Magnetics* 43.4 (Apr. 2007), pp. 1753–1756.

[176] F. Preisach. "Über die magnetische Nachwirkung". In: *Zeitschrift für Physik* 94.5 (May 1935), pp. 277–302.

[177] L. Prigozhin, V. Sokolovsky, J. W. Barrett, and S. E. Zirka. "On the Energy-Based Variational Model for Vector Magnetic Hysteresis". In: *IEEE Trans. Magn.* 52.12 (Dec. 2016), pp. 1–11.

[178] R. H. Pry and C. P. Bean. "Calculation of the Energy Loss in Magnetic Sheet Materials Using a Domain Model". In: *Journal of Applied Physics* 29.3 (1958), pp. 532–533.

[179] A. Puzrin and G. Houlsby. "Fundamentals of kinematic hardening hyperplasticity". In: *Int. J. Solids Struct.* 38.21 (2001), pp. 3771–3794.

[180] S. Ramo, J. Whinnery, and T. Van Duzer. *Fields and Waves in Communication Electronics*. Wiley-India, 2008.

[181] J. Reinert, A. Brockmeyer, and R. W. A. A. D. Doncker. "Calculation of losses in ferro- and ferrimagnetic materials based on the modified Steinmetz equation". In: *IEEE Transactions on Industry Applications* 37.4 (July 2001), pp. 1055–1061.

[182] D. Ribbenfjard and G. Engdahl. "Modeling of Dynamic Hysteresis With Bergqvist's Lag Model". In: *IEEE Trans. Magn.* 42.10 (Oct. 2006), pp. 3135–3137.

[183] D. Ribbenfjärd. "Electromagnetic transformer modelling including the ferromagnetic core". PhD thesis. KTH, Electromagnetic Engineering, 2010, p. 183.

[184] E. Riks. "An incremental approach to the solution of snapping and buckling problems". In: *International Journal of Solids and Structures* 15.7 (1979), pp. 529–551.

[185] P. Robert. *Matériaux de l' électronique*. Traité de l' électricité. Presses polytechniques romandes, 1999.

[186] U. Römer. *Numerical Approximation of the Magnetoquasistatic Model with Uncertainties: Applications in Magnet Design*. Springer Theses. Springer International Publishing, 2016.

[187] L.-L. Rouve, F. Ossart, T. Waeckerle, and A. Kedous-Lebouc. "Magnetic flux and losses computation in electrical laminations". In: *IEEE Transactions on Magnetics* 32.5 (Sept. 1996), pp. 4219–4221.

[188] R. V. Sabariego. “The fast multipole method for electromagnetic field computation in numerical and physical hybrid systems”. PhD thesis. Université de Liège, 2004.

[189] J. Saitz. “Computation of the core loss in an induction motor using the vector Preisach hysteresis model incorporated in finite element analysis”. In: *IEEE Transactions on Magnetics* 36.4 (July 2000), pp. 769–773.

[190] J. Saitz. “Magnetic field analysis of electric machines taking ferromagnetic hysteresis into account”. G4 Monografiaväitöskirja. Helsinki University of Technology; Teknillinen korkeakoulu, 2001, p. 123.

[191] D. F. Shanno. “Conditioning of Quasi-Newton Methods for Function Minimization”. In: *Mathematics of Computation* 24.111 (1970), pp. 647–656.

[192] W. Shen, F. Wang, D. Boroyevich, and C. W. Tipton. “Loss Characterization and Calculation of Nanocrystalline Cores for High-frequency Magnetics Applications”. In: *APEC 07 - Twenty-Second Annual IEEE Applied Power Electronics Conference and Exposition*. Feb. 2007, pp. 90–96.

[193] N. Shor. *Minimization Methods for Non-Differentiable Functions*. Springer Series in Computational Mathematics, 1985.

[194] J. Sievert, H. Ahlers, M. Birkfeld, B. Cornut, F. Fiorillo, K. Hempel, T. Kochmann, A. Kedous-Lebouc, T. Meydan, A. Moses, and A. Rietto. “European intercomparison of measurements of rotational power loss in electrical sheet steel”. In: *Journal of Magnetism and Magnetic Materials* 160 (1996), pp. 115–118.

[195] F. Sixdenier, O. Messal, A. Hilal, C. Martin, M. A. Raulet, and R. Scorretti. “Temperature-Dependent Extension of a Static Hysteresis Model”. In: *IEEE Transactions on Magnetics* 52.3 (Mar. 2016), pp. 1–4.

[196] F. Sixdenier and R. Scorretti. “Numerical model of static hysteresis taking into account temperature”. In: *10th International Symposium on Electric and Magnetic Fields (EMF 2016)*. Lyon, France, Apr. 2016.

[197] S. Steentjes, D. Eggers, and K. Hameyer. “Application and Verification of a Dynamic Vector-Hysteresis Model”. In: *IEEE Transactions on Magnetics* 48.11 (Nov. 2012), pp. 3379–3382.

[198] S. Steentjes, F. Henrotte, and K. Hameyer. “Energy-based ferromagnetic material model with magnetic anisotropy”. In: *Journal of Magnetism and Magnetic Materials* 425 (2017), pp. 20–24.

[199] S. Steentjes, F. Henrotte, K. Jacques, and K. Hameyer. “Energy-Based Ferromagnetic Material Model with Magnetic Anisotropy and Magnetostriction”. In: *Conf. Proc. 1st IEEE Conference Advances in Magnetics (AIM)*. Bormio, Italy, Mar. 2016.

[200] C. P. Steinmetz. “On the law of hysteresis (originally published in 1892)”. In: *Proceedings of the IEEE* 72.2 (Feb. 1984), pp. 197–221.

[201] N. Stranges and R. D. Findlay. “Measurement of rotational iron losses in electrical sheet”. In: *IEEE Transactions on Magnetics* 36.5 (Sept. 2000), pp. 3457–3459.

[202] J. Stratton. *Electromagnetic theory*. International series in pure and applied physics. McGraw-Hill book company, inc., 1941.

[203] J. Szpunar, D. Atherton, and B. Szpunar. "Analysis of the irreversible processes of magnetization in steel". In: *IEEE Transactions on Magnetics* 23.1 (Jan. 1987), pp. 300–304.

[204] M. Toman, G. Stumberger, and D. Dolinar. "Parameter Identification of the Jiles-Atherton Hysteresis Model Using Differential Evolution". In: *IEEE Transactions on Magnetics* 44.6 (June 2008), pp. 1098–1101.

[205] F. Vajda and E. D. Torre. "Efficient numerical implementation of complete-moving-hysteresis models". In: *IEEE Transactions on Magnetics* 29.2 (Mar. 1993), pp. 1532–1537.

[206] K. Venkatachalam, C. R. Sullivan, T. Abdallah, and H. Tacca. "Accurate prediction of ferrite core loss with nonsinusoidal waveforms using only Steinmetz parameters". In: *2002 IEEE Workshop on Computers in Power Electronics, 2002. Proceedings.* June 2002, pp. 36–41.

[207] A. Visintin. *Differential Models of Hysteresis*. 1st ed. Applied Mathematical Sciences 111. Springer-Verlag Berlin Heidelberg, 1994.

[208] R. Wait and A. Mitchell. *Finite element analysis and applications*. A Wiley-Interscience publication. J. Wiley, 1985.

[209] P. Weiss. "L' hypothèse du champ moléculaire et la propriété ferromagnétique". In: *J. Phys. Theor. Appl.* 6.1 (1907), pp. 661–690.

[210] P. R. Wilson, J. N. Ross, and A. D. Brown. "Optimizing the Jiles-Atherton model of hysteresis by a genetic algorithm". In: *IEEE Transactions on Magnetics* 37.2 (Mar. 2001), pp. 989–993.

[211] K. Yamazaki and N. Fukushima. "Iron-Loss Modeling for Rotating Machines: Comparison Between Bertotti's Three-Term Expression and 3-D Eddy-Current Analysis". In: *IEEE Transactions on Magnetics* 46.8 (Aug. 2010), pp. 3121–3124.

[212] C. Yicheng and P. Pillay. "An improved formula for lamination core loss calculations in machines operating with high frequency and high flux density excitation". In: *Conference Record of the 2002 IEEE Industry Applications Conference. 37th IAS Annual Meeting (Cat. No.02CH37344)*. Vol. 2. Oct. 2002, 759–766 vol.2.

[213] H. Ziegler. *An Introduction to Thermomechanics*. 2ed. North-Holland in Applied Mathematics and Mechanics. Elsevier, 1983.

[214] S. E. Zirka and Y. I. Moroz. "Hysteresis modeling based on similarity". In: *IEEE Transactions on Magnetics* 35.4 (July 1999), pp. 2090–2096.

[215] S. E. Zirka, Y. I. Moroz, P. Marketos, and A. J. Moses. "Congruency-based hysteresis models for transient simulation". In: *IEEE Transactions on Magnetics* 40.2 (Mar. 2004), pp. 390–399.

[216] S. E. Zirka, Y. I. Moroz, P. Marketos, and A. J. Moses. "Viscosity-based magnetodynamic model of soft magnetic materials". In: *IEEE Transactions on Magnetics* 42.9 (Sept. 2006), pp. 2121–2132.

[217] S. E. Zirka, Y. I. Moroz, R. G. Harrison, and K. Chwastek. “On physical aspects of the Jiles-Atherton hysteresis models”. In: *Journal of Applied Physics* 112.4 (2012), p. 043916.